The effects of zinc oxide nanoparticle interface on conformational dynamics of protein models from different structural hierarchies

Shreyasi Asthana

Department of Life Science
National Institute of Technology Rourkela

The effects of zinc oxide nanoparticle interface on conformational dynamics of protein models from different structural hierarchies

Dissertation submitted in partial fulfilment

of the requirements of the degree of

Doctor of Philosophy

in

Life Science

By

Shreyasi Asthana

(Roll Number: 513LS6008)

based on research carried out

under the supervision of

Dr. Suman Jha

December 2018

Department of Life Science

National Institute of Technology Rourkela

Dedicated to my Parents

and family…

Department of Life Science
National Institute of Technology Rourkela

December 2018

Certificate of Examination

Roll Number: 513LS6008

Name: Ms. Shreyasi Asthana

Title of Dissertation: "The effects of zinc oxide nanoparticle interface on conformational dynamics of protein models from different structural hierarchies". We, the below signed, after checking the dissertation mentioned above and the official record book(s) of the student, hereby state our approval of the dissertation submitted in partial fulfillment of the requirement of the degree of ***Doctor of Philosophy*** **in** ***Life Science*** **at** ***National Institute of Technology, Rourkela.*** We are satisfied with the volume, quality, correctness, and originality of the work.

Suman Jha
Principal Supervisor

S. Paul
External, DSC

H. Sahoo
Member, DSC

B. Mallick
Member, DSC

External

Chairperson, DSC

Head of the Department

Department of Life Science
National Institute of Technology Rourkela

Dr. Suman Jha
Assistant Professor

December 2018

Supervisor's Certificate

This is to certify that the work presented in this dissertation entitled **"The effects of zinc oxide nanoparticle interface on conformational dynamics of protein models from different structural hierarchies"** by ***Ms. Shreyasi Asthana***, Roll Number **513LS6008**, is a record of original research carried out by her under my supervision and guidance in partial fulfillment of the requirements of the degree of ***Doctor of philosophy*** **in** ***Life Science***. Neither this dissertation nor any part of it has been submitted for any degree or diploma to any institute or university in India or abroad.

Dr. Suman Jha

Declaration of Originality

I, Ms. Shreyasi Asthana, Roll Number: 513LS6008, hereby, declare that this dissertation entitled ***"The effects of zinc oxide nanoparticle interface on conformational dynamics of protein models from different structural hierarchies"*** presents my original work carried out as a doctoral student of NIT Rourkela and, to the best of my knowledge, it contains no material previously published or written by another person, nor any material presented for the award of any degree or diploma of NIT Rourkela or any other institution. Any contribution made to this research by others, with whom I have worked at NIT Rourkela or elsewhere, is explicitly acknowledged in the dissertation. Works of other authors cited in this dissertation have been duly acknowledged under the section "Bibliography". I have also submitted my original research records to the scrutiny committee for evaluation of my dissertation.

I am fully aware that in case of my non-compliance detected in the future, the Senate of NIT Rourkela may withdraw the degree awarded to me on the basis of the present dissertation.

December 2018
NIT Rourkela

Ms. Shreyasi Asthana

Acknowledgment

I would first like to express my heartfelt thanks to my supervisor Dr. Suman Jha for his guidance and support throughout the course of my Ph.D. research work. I would also like to thank him for providing me the liberty to work and introducing me to this intriguing field of protein biology.

I would also like to extend my thanks to Prof. Animesh Biswas, Director, National Institute of Technology, Rourkela for making all the infrastructural facilities available to complete my work.

I am also thankful to the members of doctoral scrutiny committee Dr. Sujit Kumar Bhutia (chairman), Dr. Subhankar Paul (member), Dr. Harekrushna Sahoo (member), and Dr. Bibekananda Mallick (member) for their suggestions and encouragement during the course of my Ph.D. I would also like to acknowledge all the faculty members of our department for their constant encouragement at all times.

I wish to acknowledge Dr Surajit Das, Dr Vidya Devi Negi, Dr Rohan Dhiman and Dr. Bibekananda Mallick for providing the cell culture facilities. I would also like to thank Dr. Anupam Nath Jha and Mr. Zaved Hazarika (from Tezpur Univeristy) for the Molecular Dynamics Simulation study, Dr. Gopal Chakrabarti and Mr. Souvik Roy (from Calcutta University) for Isothermal Titration Calorimetry experiments, Dr. Hirak Chakraborty (Sambalpur University) for Time resolved fluorescence experiments and Dr. Harekrushna Sahoo (NIT, Rourkela) for Circular Dichroism facility. I also thank Mousumi for Molecular Dynamics Simulations.

I will be failing in my duty if I do not acknowledge the constant co-operation of all the academic staffs and technical staffs. I would like to thank Jyoti, Chahat, Sanjeev Bhaiya, Aniruddha Bhaiya and Jayanta Bhaiya for their support with the instruments. I would also like to thank Girish Sir, Murli mausa, Minz Sir and Majhi Sir for their kind cooperation for all the other official issues. I

extend my thanks to Mr. Arup Dey for his help with CD experiments and Mr. Subhabrata Chakraborty and Mr. Utpal for their patience during TEM image acquisition.

I would like to thank all my lab-mates, Parth, Manoranjan, Kanti, Jyoti, Ashutosh and Anuj for their help and support. I also wish to thank all the project students, Rajshri, Shwetambari, Rituparna, Stuti, Nandini, Kajal, Ajeet, Manish and Swati for helping me and bearing with me through their course of the dissertation.

Finally, I would like to thank my friends, Parth, Indira Di, Moumita Di, Namrata, Jaya Di, Niharika Di, Bhaskar, Dipta Da, Rajanya, Mousumi, Rituraj Bhaiya, Sonu, Shraddha, Garima Di, Bhakti and Supriya who stood by me through thick and thin, and made my days brighter at NIT Rourkela. I would also like to extend my thanks to my friends outside NIT, Saswati, Anmada, Mousumi, Bhumika, Sisir, Amandeep, Abhinav, Lipi, Khushman and Avro who have always supported me during this time.

I would like to thank and acknowledge Department of Biotechnology, Ministry of Human Resource and Development, and the National Institute of Technology Rourkela, India for the financial support for fellowship and grants for executing the thesis work and attending conferences & workshops.

Last but not the least, I would like to thank my parents and my entire family for always believing in me and encouraging me to pursue my goals and, above all, to the Almighty God for showering his never ending blessings on me.

Abstract

In recent years, nanoparticles and nanomaterials have found their far reaching applications in various fields including the field of biology and medicine. The consequences of these nanoparticles in biological milieu need to be properly assessed. As soon as a nanoparticle enters a biological milieu, a myriad of changes take place. Proteins present in milieu get adsorbed and desorbed over the nanoparticle interface in a dynamic process, resulting in a protein corona. Despite the advances made in nanosciences, our understanding of interactions between protein and nanoparticle interface is still limited. Nanoparticle interface behaviour is anticipated to change with change in accessible surface behaviour of the proteins present in biological milieu. Hence, it becomes essential to study the impact of nanoparticle interface on conformational and amyloidogenic properties of proteins with varying surfaces present in biological milieu. Thus, the thesis discusses the observed effects of zinc oxide nanoparticle (ZnONP) interface on conformational and amyloidogenic propensities of protein models belonging to structurally different hierarchies. Initially, the thesis shows changes in conformational and amyloidogenic propensities for an intrinsically disordered polypeptide (IDP), like IAPP, with change in the length of negatively charged polymeric surfaces, i.e. heparin fragments; diffusive binding of smaller heparin fragments through IAPP sequence is anticipated to delay the fibrillation, whereas interactions with longer fragments (> heparin heptamer) stabilize N- and C- terminus charged residues and expose IAPP self-recognition element resulting in enhanced fibrillation. On the other hand, ZnONP with negative surface potential interaction with monomeric IAPP found to inhibit the fibrillation and the fibril-mediated cytotoxicity. The second part of the thesis indicates the effect of ZnONP interface on another, relatively longer, IDP, i.e. α-synuclein. The results indicated that highly favorable interaction between the interface and protein forms thermodynamically stable complex resulting into amorphous aggregation, instead of fibrillation; the interaction must have raised the threshold barrier between the structures, complex and amyloid structures, resulting the complex to kinetically trap in amorphous aggregate. However, the interaction with globular protein like insulin showed opposite results, which is discussed in subsequent chapter of the thesis. The interaction of insulin with ZnONP interface results in protein conformational rearrangement into an amyloid-prone conformation. The conformation fibrillates relatively faster and causes enhanced fibril-mediated cell death on increasing the interface concentration in solution at physiological pH. Otherwise, the protein at higher concentrations only forms amorphous aggregate in physiological pH. The thesis ends with the discussion on the effects of interface interaction with quaternary protein, like Concanavalin A (ConA). Interestingly, ConA adopts different unfolding conformations upon interaction with different chaotropes, like SDS, guanidinium chloride etc. Guanidinium chloride completely unfolds the protein above 2 M, whereas sodium dodecyl sulfate took protein into all-α protein from an all-β protein. Additionally, ConA interaction with ZnONP interface causes conformational rearrangement with relatively more exposed hydrophobic patches, resulting into amorphous aggregation of the protein. Thus, the thesis findings, altogether, indicate that the interacting interfaces, like ZnONP with negative interfacial potential and protein interface, predominantly determine conformational changes in protein upon interaction, and its subsequent consequences like amyloidosis, flocculation.

Keywords: zinc oxide nanoparticles, amyloid, IAPP, α-synuclein, insulin, Concanavalin A.

CONTENTS

List of figures

List of tables

List of abbreviations

1-anilinonaphthalene-8-sulfonic acid	ANS
Alzheimer's disease	AD
Ampicillin	Amp
Basic Local Search Alignment Tool	BLAST
Bovine Serum Albumin	BSA
Carbon Nanotubes	CNT
Circular Dichroism	CD
Circular dichroism neural network	CDNN
Concanavalin A	ConA
Congo Red	CR
Critical Micelle Concentration	CMC
Degree of Polymerization	dp
Deoxyribonucleic Acid	DNA
Dulbecco's Minimal Eagle's Medium	DMEM
Epigallocatechin gallate	EGCG
Ethylene Diamine Tetra Acetic Acid	EDTA
Extracellular matrix	ECM
Fetal Bovine Serum	FBS
Food and Drug Administration	FDA
Fourier Transform Infrared Spectroscopy	FT-IR
Glycosaminoglycans	GAGs
Gold	Au
GROningen MAchine Chemical Simulation	GROMACS
Guanidine Hydrochloride	GdnHCl
Hexafluoroisopropanol	HFIP
High Angle Annular Dark Field	HAADF
Hydroxyapatite	HA
Immunoglobulin G	IgG
Intrinsically Disordered Proteins	IDP
Islet Amyloid Polypeptide	IAPP
Isoelectric point	pI
Isothermal Titration Calorimetry	ITC
Magnetite	Fe_3O_4
Molecular Dynamics	MD
Mouse Insulinoma 6	MIN6
Nanoparticle	NP
National Centre for Cell Science	NCCS
Nuclear Magnetic Resonance	NMR
Parkinson's Disease	PD
Penicillin Streptomycin	penstrep
Phosphate Buffered Saline	PBS
Polyacrylamide Gel Electrophoresis	PAGE

Poly Lactic Acid	PLA
Poly(lactic-co-glycolic) Acid	PLGA
Polystyrene	PS
Predictor of Natural Disordered Regions	PONDR
Protein Data Bank	PDB
Quantum Dots	QDs
Reactive Oxygen Species	ROS
Residue Wise Mean Fluctuations	RMSF
Ribonucleic Acid	RNA
Root Mean Square Deviations	RMSD
Rotations per minute	rpm
Rosewell park Memorial Institute Medium	RPMI
Selected-area electron diffraction	SAED
Scanning Transmission Electron Microscopy	STEM
Serum Amyloid P component	SAP
Silver Nanoparticle	AgNP
Silver	Ag
Sodium Dodecyl Sulfate	SDS
Soybean agglutinin	SBA
Standard Deviation	SD
Surface Plasmon Resonance	SPR
Thioflavin T	ThT
Time Resolved Fluorescence	TRF
Transmission Electron Microscopy	TEM
Type II Diabetes Mellitus	TIIDM
Ultra Violet-Visible	UV-Vis
World Health Organization	WHO
Zinc	Zn
Zinc Oxide	ZnO

Notations

Angstrom	Å
Association constant	K_a
Femtoseconds	fs
Gram	g
Hours	hrs
Isobaric-Isothermal	NVT
Kilocalorie/Mole	Kcal/mol
Kilojoule/Mole	KJ/mol
Mega Ohms	MΩ
Microgram	μg
Microliters	μL
Micromolar	μM
Milligram	mg
Millilitres	mL
Millimolar	mM
Minutes	mins
Nanoseconds	ns
Normal-Pressure-Temperature	NPT
Picomolar	pM
Picoseconds	ps
Potential of hydronium ion	pH
Seconds	secs
Stern-Volmer constant	K_{sv}
Volume by volume	v/v
Weight by volume	w/v

Chapter 1
Introduction

1. Introduction

1.1 Protein

Protein is one of the most important biomolecules in living organisms. It constitutes about two-thirds of the total cytosol, with cumulative concentrations approaching about 200 mg/mL. The human genome contains approximately 20,500 protein-coding genes [1]. These different proteins are composed from only 20 naturally occurring amino acids. All amino acids except proline have a common basic structure, differing only in their side chains (R-group) [2]. Proline has a secondary amine, which happens because the R-group forms covalent bond with the N-terminus of amino acid. The structure of proline is also helpful for exerting various structural effects in protein essential for their functions [3]. There are as many as seven different type R-groups found in amino acids, which are aliphatic, hydroxyl, acidic, basic, amine, sulfur-containing and aromatic functional groups. Almost all the proteins must adopt a unique tertiary or quaternary structure in order to carry out their specific functions. However, a new class of proteins known as Intrinsically Disordered Proteins (IDPs) are also present in cytosol, which adopt a conformation in presence of their native partner/substrate. IDPs do not have a native three-dimensional structure because of its high charge and absence of hydrophobic patches [4]. IDPs have been discussed in details in the following sections.

1.1.1 Protein classification on the basis of varying structural hierarchies

The primary structure is universally governed by protein coded by gene sequence, evolution, and is species specific. The peptide sequence co-translationally starts forming local interactions, mainly hydrogen bond interaction between peptide bonds. Following are the orders of protein folding from the protein structure point of view:

Primary structure refers to a linear sequence of amino acids held together through peptide bonds. This sequence is encoded within DNA, which is encrypted to mRNA followed by the translation on ribosome. As amino acids are being added to polypeptide chain through codon specific charged tRNAs, they are joined to each other by peptide bonds. The peptide bond is formed by a condensation reaction between the acidic group of one amino acid and the amino group of another amino acid, catalyzed by peptidyl transferase enzyme. The peptide bond is a planar structure with a partial double bond character because nitrogen shares its lone pair electron with oxygen in -C(=O)N(H)- peptide bond. The sequence of amino acid ultimately

determines the structure and conformation of the protein, depending upon the spatial arrangement of atoms in amino acid R groups of the polypeptide chain [5].

Secondary structure is organization of local contacts along the peptide backbone. Most important secondary structures in proteins comprise of α-helix, β-sheets and β-turns. Others, which do not have a specific secondary structure, fall under random coils. Secondary structures are established by intramolecular and intermolecular hydrogen bonding of amide groups mainly present in the polypeptide chain, giving rise to specific phi (φ) and psi (ψ) angles of peptide backbone [5].

The phi (φ) and psi (ψ) angles of an **α-helix** lie in the center of allowed regions in the Ramachandran plot **(Figure 1.1)**. Average dihedral angles for right-handed **α-helix** fall between φ = -64±7 and ψ = -41±7. Also in addition to the intramolecular hydrogen bonding, radius of the helix allows favorable van der Waals interactions across the helical axis [6, 7]. The resulting interactions make it the most abundant conformation present in globular proteins accounting for almost 32-38% of all residues in proteins [6, 8].

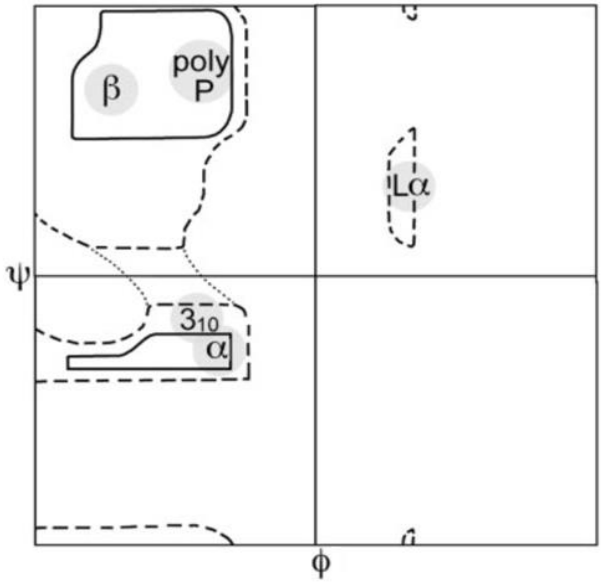

Figure 1.1. Ramachandran plot depicting the allowed secondary structure regions for a peptide chain. The ones with solid lines are generously allowed, followed by the dashed and the dotted lines adapted from [7].

Apart from α-helix, **β-sheets** are the second most important structural elements in globular proteins comprising 20-28% of all residues [6, 8]. A typical β-sheet contains a β-strand with

backbone dihedral angles φ= -120 and ψ = +120 with a separation of 3.2 and 3.4 Å per residue for residues in **antiparallel and parallel** strands, respectively. There are no intrachain hydrogen bonds, and the van der Waals interactions between atoms of neighboring residues are also insignificant due to the extended structure of the chain. Therefore, this extended conformation is stable only when there are contributions from hydrogen bonds and van der Waals interactions between aligned strands, which impart stability. Hence, β-sheet, in protein, is mostly found in more than one strands in either "**antiparallel" or "parallel"** arrangement of two interacting strands. Antiparallel β-sheets are believed to be more stable than parallel β-sheets because of the relatively more favorable orientation of interstrand hydrogen bonds and peptide bond dipoles. However, in parallel β-sheet arrangement, the components of different strands dipoles align and interact relatively unfavorably [9].

The third most important secondary structures found in proteins are turns **(reverse turns or loops)**. These also comprise approximately 30% of all the residues in proteins. These turns are responsible for reversing the direction of polypeptide chain microdipoles, and are responsible for the overall globular structure of proteins, like in **β-hairpins.** In β-hairpins motif, loops connect adjacent β-strands in an antiparallel arrangement, and are the most widely studied class of turns. Other commonly occurring turns are classical **β-turns,** wherein four residues those are not involved in hydrogen bonding with $C_{\alpha(i)}$ and $C_{\alpha(i+3)}$ placed at < 7Å. Afterβ-turns, second most common turn is **γ-turn**, which is further classified in classic (very rare γ-turn) and reverse gamma turn (produces a kink in structure, 91 % of all γ-turns) [6, 8, 9]. In γ-turn, out of three peptide bonds, first two forms the hydrogen bond. The conformation of short loops like the ones mentioned above, depending on the position of the amino acids like glycine, proline, and asparagine, facilitate the chain to adopt unusual conformation. However, large loops have less well-defined conformations, and are governed by interactions determined by rest of the protein structure [5, 6].

Tertiary structure on the other hand, is the overall arrangement of folded polypeptide chain with different orientations of secondary structural elements in three-dimension. For many proteins, the structural hierarchy ends here. However, in nature, many proteins exist as aggregates/complexes of two or more polypeptide chains which may be identical or different (homo- or hetero-) subunits connected together through non-covalent interactions and/or covalent disulfide bonds. They can be either a dimer, trimer, tetramer, hexamer or even

higher order structures [10, 11]. The association of discrete polypeptide chains, each with its independent tertiary structure, is known as **quaternary structure,** and has enhanced stability compared to its monomeric subunits or other globular proteins **(Figure 1.2).**

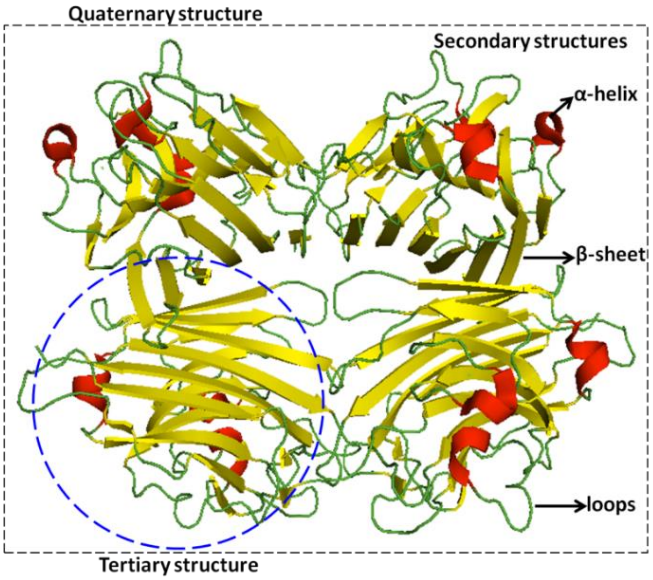

Figure 1.2. Structure of peanut agglutinin (PDB ID: 2DV9), depicting the structural hierarchy of proteins. Quaternary, tertiary and secondary structures are shown. The α-helix, β-sheets, and loops are colored in red, yellow and green, respectively [12].

1.1.2 Interactions governing the protein structure

In order to fold into a native conformation and exert its function, a polypeptide must overcome the large enthalpy and entropy barriers associated with it. For this, the protein interacts through intramolecular interactions within itself and intermolecular interactions with the solvent molecules to orient itself in a stable structure in that condition. All these interactions arise from some of the limited set of non-covalent interactions, which are discussed below:

Hydrogen bonding: Hydrogen bonds are formed when two electronegative atoms compete for the same hydrogen atom, where the hydrogen atom is covalently bonded to one of the electronegative atoms. The donors of hydrogen bond have a hydrogen atom covalently attached to an electronegative heteroatom, e.g. -NH, -OH, -SH, and the acceptor is another electronegative atom with lone pair electrons in atomic proximity, e.g. -C=O. The peptide backbone and the side chains of amino acids in a protein make many hydrogen bonds with

polar solvents, like water. During folding process, these hydrogen bonds are reshuffled till the end, while new intramolecular hydrogen bonds are formed, mostly in the secondary structures, as discussed in the structural hierarchies' section [6].

Hydrophobic interactions/effects: Although globular proteins exist in aqueous environments, many amino acid side chains present in protein are hydrophobic. The interactions of such non-polar surfaces with the aqueous environment are unfavorable but among themselves are highly favorable interactions. These favorable interactions between non-polar molecules are known as hydrophobic interactions/effects. The interaction is predominantly entropically driven and plays an indispensable role in the formation of the hydrophobic core of a protein to stabilize the protein structure [13, 14].

Van der Waals interactions: All atoms and molecules tend to attract to each other, even in the absence of charged groups, due to the mutual interactions related to the induced polarization effects. These ubiquitous interactions are known as van der Waals interactions. These are weak, close range forces prevailing between all atoms and molecules irrespective of their charges and affinities [6].

Electrostatic Interactions:

Salt bridges: The positive charges on side chains of amino acids, like arginine, lysine, histidine, and the negative charges on side chains of aspartate and glutamate when present in atomic proximity, the pair forms hydrogen bond along with the electrostatic interaction. Hence, the non-directional electrostatic interactions between opposite charges along with the directional hydrogen bond interaction are known as salt bridges. Charge-charge interactions on the protein surface are weaker due to solvent screening. Occasionally salt bridges are also found within the protein core, which is found to be far stronger than the pair found at solvent accessible protein surface [4, 15].

Dipole interactions: A molecule does not need to have a net charge to participate in electrostatic interactions. Sometimes, the unequal sharing of electrons between atoms of different negativities results in attaining a partial negative charge δ- at electronegative atoms and a partial positive charge at the covalently attached, relatively less electronegative atom. The perfect example of dipole interactions is the peptide bond, which has a partial double

bond character due to resonance within the bond, where the highly electronegative atom oxygen acquires a net negative charge and the amino group acquires a somewhat positive charge in the -C(=O)-N(-H)- group, and have a net dipole of 3.7 Debye per peptide bond [6].

Cation-π interactions: The π-electrons of the aromatic amino acids phenylalanine, tyrosine, and tryptophan are localized above and below the face of the benzene ring. The excess of electrons provides a small negative charge to the face, whereas the hydrogen atoms on edge gain a slight positive charge. The electrostatic interactions between these partial charges dominate interactions between aromatic rings [4, 16, 17]. Moreover, while the positively-charged side chains of arginine and lysine are mostly involved in salt bridges, they can also interact with the π-electrons of the aromatic amino acids phenylalanine, tyrosine, and tryptophan [17].

Disulfide bonds: The thiol (-SH) group of cysteine residues are oxidized to form disulfide (S-S) bond. These can be either intrachain as in lysozyme or interchain as in insulin. Disulfide bonds tend to stabilize the native structure by reducing the conformational entropy of the unfolded ensembles [18].

1.1.3 Protein Folding

Folding of proteins into its compact quaternary native structure is one of the most important features of biological self-assembly. The way evolutionary selection has influenced the structural and functional assembly is astonishing. Correctly folded proteins have long-term stability in crowded biological environments which interact favorably with their binding partners [19]. Therefore, proteins that do not fold correctly or remain in a correctly folded conformation are either degraded or are responsible for many pathological conditions.

A pioneering work in this field by Anfinsen suggested that the denatured state of ribonuclease could spontaneously refold to its correct native structure when the denaturing condition is removed. In absence of any known mechanism, he suggested that all the information required by a protein to fold to its native state is contained in its amino acid sequence. The statement was later known as **Anfinsen's Dogma or Anfinsen's Hypothesis** [20]. However, the central question as "How does a protein "know" its correct secondary, tertiary and quaternary structure based only on its amino acid sequence" remains elusive.

In 1969, Cyrus Levinthal argued that it would take an astronomical scale of time for a polypeptide chain to attain its native conformation, if the folding process was based on a random search [21]. However, in cells, proteins are continually synthesized and folded within a few seconds. This mismatch of timescales between estimated folding time and actual folding time was called as **"Levinthal's Paradox"**, and it provided the base for what is now called as the **"protein folding problem"**. Levinthal also stated that in order to achieve the native conformation in such a small time, there must be some predetermined pathways which come into play during protein folding [22]. Recent studies have proposed that folding process does not necessarily involve a sequence of predefined stepwise processes, but rather undefined stages of many conformations accessible to a polypeptide chain [19].

In order to understand the process of protein folding, three different mechanisms were put forward: The **framework** model suggests that local secondary structural elements are initially formed independently [23, 24]. These structural elements then collide into one another giving rise to its native tertiary structure. Other model proposed is **hydrophobic collapse** model suggesting that folding is initiated with a collapse of hydrophobic residues which form the hydrophobic core of the protein, followed by formation of secondary structural elements around it [25]. The **nucleation model** states that partial native secondary structures serve as suitable folding nuclei from which the correct folded structure can form [26].

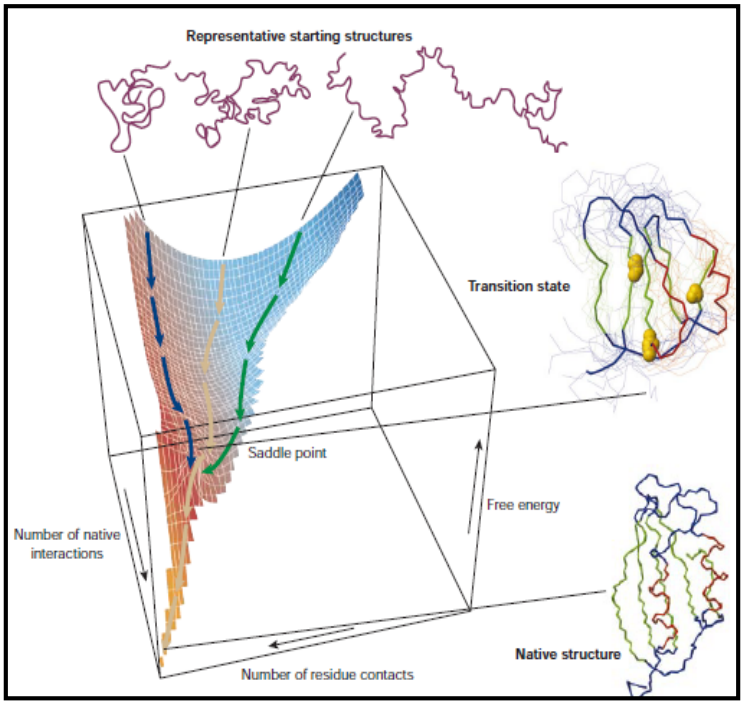

Figure 1.3. A typical protein folding funnel showing the energy landscape [19].

Although no general mechanism, which could be applicable to all proteins, has so far been achieved. All the three proposed models indicated existence of partially folded or intermediate conformations along the folding pathway. The current understanding of protein folding seems to be an extension of Leventhal's folding paradox which includes incorporation of multiple possible routes to many intermediate states finally leading to the native state [27]. The presence of many possible pathways those end in a native structure form the basis of the **folding funnel** model. Thus, it brings the concept of energy landscape **(Figure 1.3)** [28, 29]. The model proposes protein folding as a conformational search on an uneven free energy landscape inclined towards the native state with local free energy minima. Each conformation that a given protein can adopt is associated with its free energy content. The driving force for precise folding is generally believed to be the search for conformation with the lowest free energy. A plot of free energy versus the conformation creates an energy landscape on which the protein can fold adopting several pathways in its search for an energy minimum. The conformation with the lowest energy usually represents the native structure, and believed to be the most stable state in physiological conditions [19, 30].

However, the theory is being challenged by the recent discovery of a new class of protein known as **natively unfolded proteins or IDPs.** IDPs do not have a well-defined three-dimensional structure often function by binding to various partners, such as nucleic acids, due to their high flexibile nature. The last decade has seen the discovery of many proteins that lack a well-defined three-dimensional structure. Moreover, very recently it has been shown that about 30% of eukaryotic proteins have a stretch of the disordered region, around 30 amino acids long [31]. IDPs are dynamic in nature, which can interconvert into different ensembles like collapsed (as in molten globule conformation) or extended (as in coil or pre-molten globule conformation) [31]. The differences between structured protein and IDPs include differences in amino acid composition, sequence complexity, hydrophobicity, aromaticity and charge. Unlike proteins with well-defined structures, the IDP sequences are deficient in hydrophobic amino acid residues (Ile, Leu, and Val) and aromatic (Trp, Tyr, and Phe) amino acid residues. The absence of hydrophobic residues resists the formation of the hydrophobic core generally found in proteins. IDPs possess a low content of order-promoting amino acids, like Cys and Asn. On the other hand, IDPs are substantially enriched in polar (Arg, Gly, Gln, Ser, Pro, Glu, and Lys), structure-breaking (Gly and Pro), and disorder-promoting amino acid residues [32]. It has been therefore suggested that a lack of stable structure may facilitate a protein to have broader binding specificities [32, 33]. It has been

shown that the proteins involved in molecular recognition, binding and signaling have evolved to contain some intrinsically disordered regions [4]. The molecular recognition functions of IDPs include regulatory and signaling interactions, which usually involve multiple partners facilitating high specificity for recognition and low affinity providing higher flexibility simultaneously. IDPs often fold to carry out their functions brought about by the interaction with binding partners like proteins, nucleic acids, membrane, etc [31, 34].

1.1.4 Protein misfolding and amyloids

Dysfunction of proteins can result in various pathological conditions. A wide range of human diseases called as protein conformation/protein-misfolding diseases arise from when proteins tend to misfold. Apparent consequences of protein misfolding are aggregation (amorphous or amyloids), loss of normal function or gain of toxic function [19]. Some proteins have an intrinsic propensity to attain a pathologic conformation, which becomes evident with age or at high concentrations or in the presence of certain entities. Protein misfolding diseases may affect a single organ or can spread through multiple tissues. The major group of misfolding diseases, including several neurodegenerative disorders and the amyloidoses originate from the conversion of specific proteins from their soluble states into stable, highly ordered, filamentous protein aggregates with cytotoxic propensities, known as **amyloid fibrils**. Some of the most prevalent protein misfolding diseases are Alzheimer's disease caused by the misfolding of Aβ-42 [35], Parkinson's disease (PD) caused by the misfolding of α-synuclein [36], type II diabetes mellitus caused by the misfolding of amylin [37], injection localized amyloidoses caused due to misfolding of insulin in patients taking insulin injections [38] and dialysis-related amyloidosis [39]. Recent studies show that all proteins can fibrillate provided that the protein is suspended in an appropriate condition [40, 41]. The abundance of intrinsic disorder in proteins and conditions causing various misfolding diseases are an interesting area of research. The terminologies and characteristics associated with amyloidosis are discussed in the following section.

Typically, the term **amyloid** is used to indicate the presence of unbranched, 80 to 100 Å proteinaceous fibrillar (linear or concentric) deposits, having either Congo red birefringence or a β pleated sheet X-ray diffraction pattern [42]. Meanwhile, it was also suggested to be used only for abnormal *in vivo* proteinaceous fibril deposits [43]. The current understanding of amyloids defines as a general terminology for protein aggregation, resulting in cross β-sheet conformation, where each sheet is bound to the next sheet mainly through hydrogen bonds.

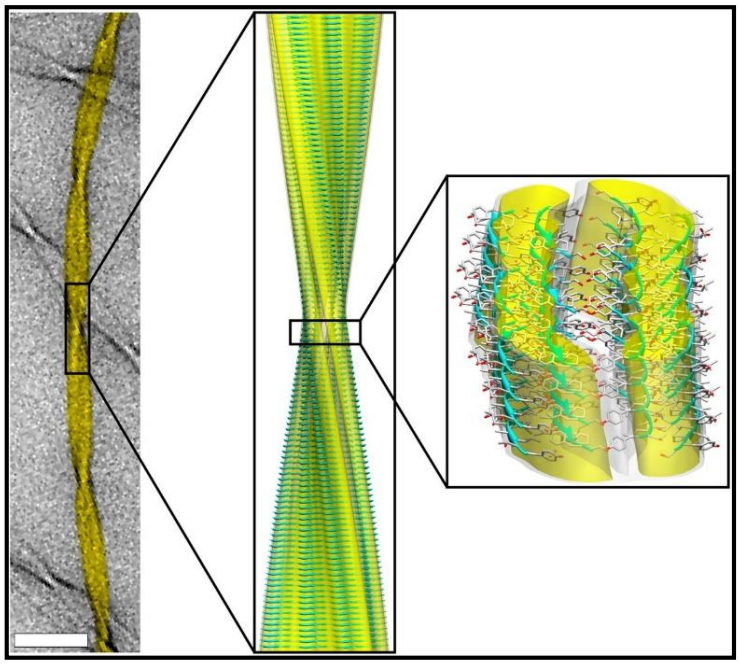

Figure 1.4. Structure of amyloid fibrils at atomic resolution [44].

The structures then form stable fibrils in which the β-strands are oriented perpendicular to the fibril elongation axis, named cross β-sheet structure, of indefinite lengths. The unique secondary structure formed in the process of fibrillation has a very peculiar binding site for dyes like Congo red, Thioflavin derivative (ThT) dyes [45]. These dyes stack in between the arrays of cross β-sheet structure, resulting in restricted rotational freedom along a plane, with a very high quantum jump compared to the unbound dye [46]. The information about the cross β sheet structure of an amyloid can be found out by X-ray fiber diffraction too. In this, the amyloid samples are exposed to X-ray beam with the long axis of the fibrils, more or less perpendicular to the direction of the beam, which then results in an amyloid-specific diffraction pattern. The X-ray reflections are then distinguished by their direction with reference to the fibre axis and their respective distances from the centre of the patterns; meridional reflections are defined as the ones lying parallel to the fibre axis, and equatorial reflections are those positioned at right angles to the fibre axis [47] and the structures of amyloid fibrils are also in line with the cross β sheet structure proposed by Pauling and Corey [48] and is represented in **Figure 1.4** [44].

It has now been widely established and accepted that the formation of amyloids follows a nucleated growth mechanism. In principle, it involves the formation of a nucleus first, and then fibrillar growth on the axial phase of nucleus takes place. This growth is characterized

by a short lag phase followed by rapid exponential phase. The lag phase is the time required for the accumulation of critical nuclei population needed to shoot-up the fibrillation process.

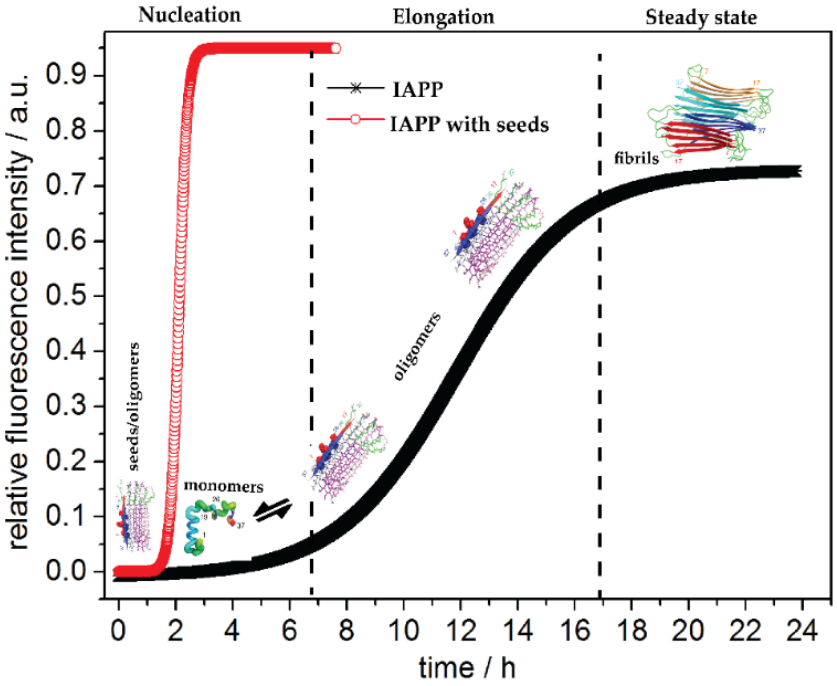

Figure 1.5. Mechanism of primary nucelated amyloid formation is represented with time on x-axis and the extent of fibrillation on y-axis. An initial nucleation phase is followed by a growth phase that reaches an apparent steady-state plateau (black). In presence of pre-formed seeds, serving as nucleation sites, the lag phase is circumvented (red) [49].

Addition of a pre-fibrillar species (oligomeric structure or nucleus), however, abolishes or shortens the lag phase, i.e. the time required for initial nucleation to happen [50, 51]. Once there is formation of the nucleus, an association of monomers and oligomers with nucleus take the fibrillization kinetics into exponential phase also known as elongation phase **(Figure 1.5)**. Experimental conditions like salt concentration, pH and peptide concentration are anticipated to alter the kinetics of amyloid formation [41]. The identification of oligomeric species and mounting evidence that these smaller oligomeric aggregates are more toxic than mature fibrils, have led extensive research in specifically elucidating their roles in (i) toxicity to cells bearing them only and/or to the cells in proximity too, and (ii) involvement in formation of well-structured amyloid fibrils on cell membrane. In the process of fibrillation, there are intermediate structures starting from partially folded/unfolded conformation to multimeric structure, commonly known as oligomers or nucleus which is assumed to be composed of poorly folded with flanking protein as intermediates [4, 40, 49].

The nucleus is thermodynamically as well as kinetically unstable, which probably leads to self-assembly of the structure into thermodynamically and kinetically stable structure known as protofilaments [52, 53]. Protofilaments vary in shape, ranging from small beads to the beaded strings, which circularize to form annular structures known as protofibrils [54]. The protofibrils come together to form the next hierarchical structure known as mature amyloid fibrils. The protofibrillar structures have been found in many amyloidogenic proteins including islet amyloid polypeptide (IAPP), and, as mentioned above, have a strong affinity for dyes like Congo Red (CR) and ThT [55]. In contrast, it has also been established that not every process of amyloid formation precedes with well-defined steps of fibrillation. In many cases, it has been found that amyloid is also formed by disordered protein aggregates following a mechanism wherein the protein aggregates interact with each other until a threshold is reached which is followed by conformational rearrangement into well-structured amyloid fibrils [55].

For some globular proteins that would otherwise not aggregate, their aggregation is linked to stress conditions like high temperature, pH variations, low concentration of organic solvents etc. The harsh conditions pose a possible risk of partial unfolding of globular proteins, giving rise to decreased conformational stability and increased the possibility of thermodynamically trapped amyloid-like fibrils [56, 57].

1.2 Nanoparticles

The word “nano” is coined from Latin word meaning dwarf. Nanotechnology deals with the processes that occur at a nanoscale range of size. The field of nanotechnology had made considerable progress since 1959 when Nobel laureate Richard P. Feynman delivered his famous talk on “There’s Plenty of Room at the Bottom” [58]. This multidisciplinary area of science has applications in varying disciplines like material sciences, biophysics, bioengineering, cancer, and radiation biology. Nanotechnology has also created its potential influence in medicine including immunology, cardiology, endocrinology, ophthalmology, oncology, etc. It is also highly utilized in specialized fields like tumor targeting, and gene and drug delivery [59]. In this context, different types of nanoparticles (NPs) have been synthesized and used. The following section discusses different types of NPs with wide applications.

1.2.1 Types of nanoparticles

Polymeric NPs

These are mostly composed of polymeric materials like Polylactic acid (PLA), Polylactic-co-glycolic acid (PLGA), alginate, dextran, etc. They are mostly spherical or capsular in shape. Due to their polymeric and high biocompatible properties, they have many applications in biology and medicine [60].

Lipid-based NPs

Lipid NPs contain lipid molecules and are referred to as liposomes and mostly spherical in shape. The core of the NP contains either single or a mixture of lipids, while, the surface contains soluble lipophilic molecules. They can be used as efficient carriers for lipophilic molecules and sometimes drugs. Surfactants or emulsifiers can be used to stabilize the core of these NPs. The most important application of lipid NPs is drug delivery [61].

Ceramics NPs

Ceramics NPs are synthesized from metals and metalloids through a process that involves high heating followed by a rapid cooling. They can be dense, amorphous, polycrystalline, hollow or porous in structure and can be applied in various fields like as catalysis and photocatalysis, photodegradation of dyes, imaging, etc. In recent research, biocompatible and bioactive ceramic NPs synthesized from titanium oxide (TiO_2), alumina (Al_2O_3), zirconia (ZrO_2), silica (SiO_2) and hydroxyapatite (HA), have also been proposed for the biological applications, like for drug delivery, treating bacterial infections, etc. [62].

Carbon derived NPs

Two major classes of carbon derived NPs are fullerenes and carbon nanotubes (CNTs). Fullerenes are nanomaterials made up of globular hollow cage similar to allotropic forms of carbon like graphene. They have a remarkable commercial importance due to their good electrical conductivity, electron affinity, and flexibility. CNTs are elongated and tubular structures, typically, 1–2 nm in diameter. These can be categorized as metallic or semiconducting according to their diameter. They structurally resemble graphite sheets rolled upon themselves, which can be single (SWNTs), double (DWNTs) or multiple walls (MWNTs) nanotubes [63].

Metal NPs

Metal NPs are extensively synthesized from metal salt precursors. Due to their well-known localized surface plasmon resonance (LSPR), these NPs possess unique electrical properties. NPs of the alkali and metals like Zn, Cu, Ag, and Au have a broad absorption band in the visible range of the electromagnetic spectrum and vary according to the size of the synthesized NPs. The size and shape-controlled synthesis of metal NPs is an important factor for their specific applications. Due to the advanced optical properties, metal NPs have found applications in many research areas. The reduction of metals in the presence of reducing and capping agents leads to the formation of metal NPs coated with the capping agents which also functions to stabilize and prevent it from agglomeration [64].

1.2.2 Capping and functionalization of nanoparticles

A combination of nanotechnology and biology for the synthesis of hybrid materials involves biomolecules such as DNA and proteins as functional groups for the assembly of NPs. In this context, biomolecules offer several advantages over inorganic materials for use in biology and medicine. The structural diversity of biomolecules may be used to devise novel nanomaterials. Despite the various advantages in the preparation of NPs, the coupling and functionalization of NPs with biological compounds is limited to only a small part of research till date [65, 66]. If the capping layers on the NPs consist of relatively less stable groups such as citrate, biomolecules may come to their rescue and may be linked directly with the metal NPs by exchange reactions with stronger binding ligands like polystyrene. This method has been previously applied to immobilize cysteine-containing proteins onto gold NP (AuNP) surfaces.

This is achieved by either chemical or genetic means which allows the site-directed modification of proteins containing thiol groups. If NPs are stabilized by non-protein charged ligands, then also proteins can be immobilized onto them through various noncovalent interactions like electrostatic interactions, hydrogen bonding, etc. Apart from this, a ligand containing functional groups such as amine, carboxyl or maleimide are also utilized to covalently link proteins to NPs by carbodiimide-mediated esterification and amidation reactions or reaction with thiol groups in proteins. This suggests that although some chemical strategies have been explored for linking inorganic NPs with biological materials. These coupling methods, especially, covalent conjugation of proteins, can lead to degradation and inactivation of their activity and functionality **(Figure 1.6)** [66].

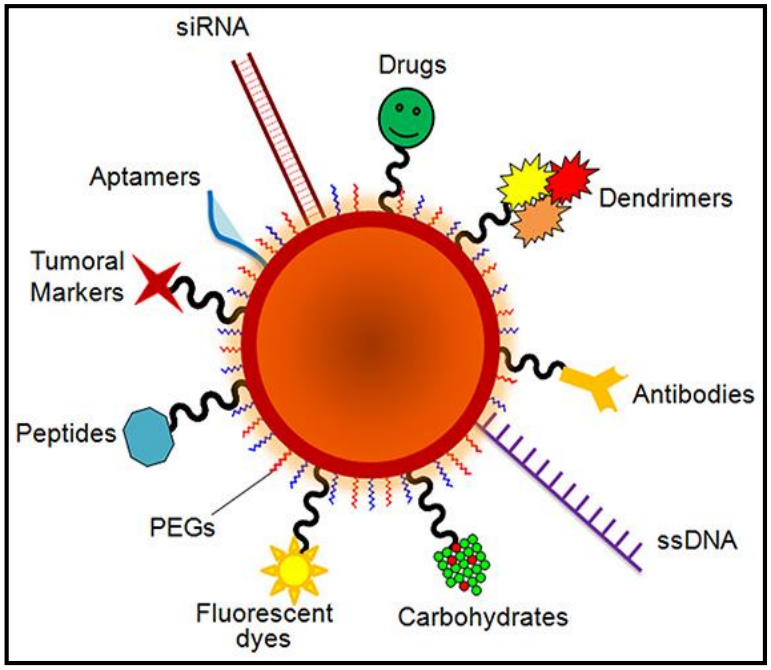

Figure 1.6. An illustration of NP surface functionalization with different biomolecules [66].

1.2.3 Physicochemical properties

Important physicochemical properties like large surface area, mechanical strength, optical activity and chemical reactivity provide NPs with unique advantages as compared to their material. Some of their important properties are discussed below

Electronic and optical properties

The optical and electronic properties of NPs are dependent on their size. They exhibit a strong UV–Visible absorption band that is absent in the spectrum of the bulk metal. The excitation band is a result of the incident frequency of photons in accoradance with the excitation of the electrons in the conduction band and is called as the LSPR. LSPR excitations produce absorption maxima with a tremendously high absorbance. This is approximately equivalent to that often more fluorophores and an enhanced local electromagnetic field near the surface of NPs. It is evident in the literature that the LSPR peak of a NP is dependent on the size, shape, and d-spacing of the NPs, as well as its dielectric properties of local environment including the substrate and solvents [64]. For example, colloidal AuNPs are responsible for the rusty colors and vary from colors red to blue depending on their shapes and sizes [67]. Similarly, the color of AgNP suspension varies from light yellow to grey according to their sizes and agglomeration propensities [68].

Magnetic properties

Magnetic NPs are composed of a magnetic element (nickel, iron, and cobalt) and a functional chemical component. They are of great interest to investigators in different fields like catalysis, biomedicine, magnetic fluids, data storage, magnetic resonance imaging (MRI), and bioremediation. At low sizes i.e. 10-20 nm, the magnetic properties come into play that makes these particles highly useful [69-71]. Uneven electronic distributions in NPs enhance the magnetic property. These properties are also dependent on the methods employed for synthesis like solvothermal, micro-emulsion, thermal decomposition, coprecipitation, and flame spray synthesis [70].

1.2.4 Applications of NPs in drugs and medications

Inorganic NPs display distinctive physical and chemical properties. Therefore, they have been suggested to be important materials for the development of novel nanodevices, drugs and injectable formulations for use in different chemical, biological and pharmaceutical applications [72, 73]. In the recent years, NPs have drawn interest in every area of medicine for their ability to deliver drugs in doses and site specificity ensuring increased therapeutic efficiency and low side effects [73, 74]. Iron oxide NPs, magnetite (Fe_3O_4) or maghemite (Fe_2O_3) is most commonly employed for their biomedical applications [75]. The selection of NPs for achieving efficient effects for biological and imaging applications relies on the physicochemical and optical properties of NPs. The development of hydrophilic NPs as successful drug carriers has been challenging. Among the different materials used, nano preparations polylactic acid (PLA) and polyethylene oxide (PEO) have been shown as promising systems for the intravenous administration of drugs [76]. Superparamagnetic iron oxide NPs with suitable surface characteristics may also be used for many *in vivo* applications like MRI contrast enhancement, detoxification of biological fluids, hyperthermia, drugs delivery, tissue repair and cell separation. These biomedical applications are based on high magnetization property, small size (<100 nm) and a narrow particle size distribution of the NPs [70]. The detection of analytes in tissue sections can be achieved through antigen-antibody interactions using fluorescently labeled antibodies, dyes tagged to AuNPs [77]. The last decade has seen a considerable research in developing biodegradable NPs as effective drug delivery agents [72, 78]. Different polymers are being used in drug delivery research owing to their property to effectively deliver the drugs to the target site thereby increasing its therapeutic benefits while minimizing side effects. Control release of pharmacologically relevant drugs at specific site with the therapeutically accurate levels and

doses has been a major goal in designing such systems. Liposomes have been used potential drug carriers because of their advantages including the ability to protect drugs from degradation and reducing side effects. However, developmental works on liposome drugs have been restricted due to inherent health issues such as squat encapsulation efficiency, poor storage, and stability. On the other hand, polymeric NPs promise some critical advantages over these materials i.e. liposomes [61, 72].

Many semiconductor and metallic NPs have a high potential for cancer diagnosis due to their SPR enhanced light scattering and absorption. AuNPs can effectively convert absorbed light to localized heat which can be exploited for the selective laser photothermal therapy for cancer [79]. The antineoplastic effects of different types of NPs are also efficiently employed to inhibit the tumor growth and progression. A particular study showed multihydroxylated NPs to have antineoplastic activity with efficiency and lower toxicity [80]. AgNPs are also applied in wound dressings, catheters and various household products in lieu of their antimicrobial activity [81, 82]. Antimicrobial agents are important in textile, medicine, water disinfection and food packaging industries. Therefore, antimicrobial properties of inorganic NPs add more value to this aspect, as compared to organic compounds, which are relatively toxic to the biological systems. TiO_2, ZnO, Cu- and Ni-based NPs have been exploited due to their antibacterial propensities [83, 84]. Some personal care products also contain NPs, like sunscreens which contain NPs like TiO_2 and ZnO. These NPs are excellent absorbers of ultraviolet (UV) radiation and protect skin cells against UV-rays. Both TiO_2 and ZnO are also used as additives in food industry for their anti-microbial effects [85, 86].

1.2.5 Toxicity of NPs

Besides the several industrial and medical applications, certain toxicity issues are also associated with NPs and other nanomaterials [87]. NPs can enter the environment through soil, water, air and other anthropological activities. In contrast, application of NPs for environmental remediation deliberately exposes NPs into the soil or aquatic systems. This has attracted increasing concern over the toxicity linked to them. The advantages of magnetic NPs such as their small size and high reactivity can also pose a potential threat by inducing adverse cellular toxic responses like the generation of reactive oxygen species (ROS), reactive nitrogen species (RNS), DNA damage, etc. [88, 89]. Studies have also demonstrated that NPs can enter organisms through ingestion or inhalation and can then translocate to various parts of the body to exert their toxic effects [90, 91].

The uses of AgNPs in numerous consumer products lead them to release their contents to the aquatic environment. This becomes a source of dissolved Ag in the aquatic environment which adversely affects aquatic organisms including bacteria, algae, fish, etc [92]. Similarly, the respiratory system and nervous systems are also the targets of the toxicity of NPs due to inhalation of the particulate matter in pollution or metal exposed areas like mining and metal industries [93, 94]. Another important intracellular effect of excessive use of NP leads to protein binding which may lead to their unfolding, fibrillation, aggregation, thiol crosslinking, and loss of functionality [95, 96]. Despite the rapid progress in the field of nanobiotechnology and the use of NPs in biologically important areas, the potential health hazards due to prolonged exposures to NPs must be taken care of and the toxicities also should be assessed, so that the NPs exert more good effects than bad.

1.3 Scope and motivation of the thesis

As discussed in the above sections, the last few decades have seen immense research in all areas of nanotechnology. Their applications in the biological field can be numerous, like drug delivery, vaccine formulation and delivery, adjuvants, antimicrobials, cancer therapeutics, etc. However, the excess use of NPs also poses a high risk of the toxicity associated with it. More specifically, the interaction of NPs with proteins in the body can have critical effects on their structure and function. Another issue which has very recently been surfaced is the formation of endogenous metal NPs, by the accumulation of metals in the body of people living in highly polluted areas. These endogenous NPs are being linked to high risk of diseases by interacting with intracellular proteins in their periphery. However, studies on the impact of NPs on proteins and the related toxicities are still at a very nascent stage.

Thus, the objective of the thesis is to study the effects of metal nanoparticle interface on different model proteins taken from different structural hierarchies, like:

1. The conformational changes in a small model IDP, i.e. Islet Amyloid Polypeptide (IAPP) in presence of
    a. Heparin fragments (*in-silico* study)
    b. Zinc Oxide nanoparticles (ZnONP) with negative surface potentials.
2. The conformational changes in a relatively longer IDP, i.e. α-synuclein, in presence of ZnONP.
3. The effect of ZnONP on the conformation of a model globular protein, i.e. insulin.

4. The conformational change in a tetrameric protein, i.e. Concanavalin A, in presence of
    a. Denaturants (Guanidine hydrochloride (GdnHCl), pH, Sodium dodecyl sulphate (SDS))
    b. ZnONP

First objective of the thesis will shed light on interfacial potential effect on the interaction pattern between protein and the interface, and consequences of the interaction on the IDP peptide, like IAPP which is a highly amyloidogenic peptide in nature. Whereas the second objective explores the effect of ZnONP negative surface potential on the conformational dynamics of α-synuclein into amyloid fibrils, which *in vivo* misfolds to cause PD. Additionally, the third objective looks into the nanoparticle interface effect on the conformational dynamics of a small globular protein, insulin, into amyloid fibrillation. The protein is known to enhance the proliferation of pancreatic β-cells to regulate the blood glucose level. These cells are also known to have highest concentration of zinc ions, helping the protein and cell with the regulation. The last objective of the thesis evaluated the nanoparticle interface effects on conformational dynamics of a quaternary protein, ConA, which presented a very rigid structure against different denaturants. The protein corona onto nanoparticle interface is mainly a result of interfacial properties of the nanoparticle and protein surface, which in turn defines the affinity of different protein surfaces for nanoparticle interface. Moreover, the affinity determines the extent of conformational rearrangement that a protein will undergo upon interaction with the nanoparticle interface, hence determines further consequences upon the conformational rearrangements.

Chapter 2

Review of literature

2. Review of literature

2.1. Interaction of proteins with charged surfaces: implications for amyloidogenesis

Typically, a protein has functional groups with varying polarities on its surface, thereby facilitating it to interact with other surfaces. The Poisson-Boltzmann equation is being used to calculate the interactions and has been suggested that protein molecules are attracted by oppositely charged surfaces and repelled by similar charges [97]. There have been studies for the interaction of proteins, treating them as spheres with uniform charge around them, with other charged surfaces [98]. The presence of polyelectrolyte charges in silica particle effects on protein conformation is also studied taking lysozyme as the model protein [99]. Similarly, theoretical calculations for contributions from electrostatics and van der Waals interactions have been performed considering the protein adsorption as a uniform arrangement of charged arrays [100]. Additionally, the orientations of protein over the charged interface also play an indispensable role in the interactions and adsorption of protein onto the interface. The impact of the orientation of the model protein, cytochrome c adsorbed on self-assembled monolayers have been computationally studied and the most important orientation for the adsorption has been determined [101]. In a study, equilibrium constants for protein-surface interactions were computationally calculated for lysozyme, with an application to ion exchange chromatography [102]. However, we now know that a protein does not have a uniform charge throughout its surface because of the arrangement of amino acids with different R-groups, which also forms a basis for different techniques like ion exchange (cation/anion) and affinity (Ni-NTA, Glutathione-S-Transferase, Streptavidin) chromatographies being used [103, 104]. The region of the protein interacting with a surface may or may not have a similar charge with rest of the protein molecule. Therefore, the approximation of treating proteins as uniform charged molecules becomes kind of misleading. The charge of the interacting surface depends on the functional groups present on the protein surface, local environment, presence of other ionizable groups and pH of the solution [99, 105]. A model system was devised to study the interactions at the interface. It was assumed that the important interactions are mediated by interfacial amino acids in presence or absence of electrolytes and the free energies of adsorption was calculated. This system was further applied to model proteins lysozyme and α-lactalbumin [106].

The interaction of proteins with charged interfaces is of empirical importance in different areas of science including structural biology, food and pharmaceutical sciences. These have

wide applications for use in nanocarriers, liposomes, polymers, etc [72, 73]. In recent years there have been quite a lot of developments in this field. Nonetheless, the interaction of proteins with charged surfaces might have a far reaching impact on their conformation. Although, these studies have been performed for delineating the interaction mechanisms with artificial interfaces, it must be kept in mind that the interaction of proteins with different classes of biomolecules takes place inside biological milieu. Two of the most important surfaces presented to proteins inside the biological systems are membranes (lipids) and polyelectrolytes of extracellular matrix like GAGs. These interactions have significant effects on the protein structure. Many of them have been shown to accelerate protein misfolding by affecting interaction network governing the native structure *in vitro*. The section below reviews some of the important studies reporting the interaction of proteins with lipids and GAGs and their implications in amyloidogenesis. The extracellular proteinaceous deposits in amyloid diseases have a core consisting of the protein, as well as a variety of associated factors including metal ions, serum amyloid P component (SAP), apolipoprotein E, and collagen [55, 107], which either acted as moderator of amyloidogenesis or were native interaction partners of the protein.

2.1.1 Interaction with Membrane lipids

Similarities between all the amyloidogenic proteins include their ability to interact with lipid membranes, especially through positively charged residues [108, 109]. Interactions between amyloidogenic proteins and lipid membranes have been shown to cause membrane damage by pore formation/membrane rupture, resulting in amyloidogenesis or fibril mediated cell death [110-112]. Positively-charged amyloid-forming peptides like IAPP, in particular, have the ability to interact with negatively-charged phospholipids present in membranes. The interactions could lead to the disruption of membrane integrity. Second, the membrane as platform could facilitate formation of the amyloid critical nuclei that initiate further fibril growth [113-116]. Enhanced amyloidogenesis of IAPP has been observed in the presence of several negatively charged membrane phospholipids such as phosphatidylglycerol or phosphatidylserine [117, 118]. Lipid composition has been shown to be a major factor in the interactions of membranes with IAPP. A recent study demonstrated that anionic lipids could enhance the rate of amyloid formation and membrane permeabilization. Cholesterol plays a significant role in IAPP-membrane interactions since it controls the clearance of IAPP oligomers from the membrane sites. Additionally, depletion of membrane cholesterol *in vivo* enhances amyloid formation [119]. A two-step membrane-mediated amyloidosis pathway,

however, has been proposed regarding the assembly and progression of amyloids. The first step involves the interaction of prefibrillar species with the membranes, leading to an enhanced local concentration, and a conformational change in IAPP. This is followed by fibril growth on the membrane [119]. The growth of fibrillar species enhances membrane leakage, but neither an α-helical nor a β-sheet structure is a prerequisite for membrane leakage [120]. Lipid membranes serve as matrices for the aggregation of amyloid proteins, thereby accelerating the cytotoxicity [108]. A hypothetical model for the interaction of positively charged IAPP with negatively charged membranes has been presented in **figure 2.1.**

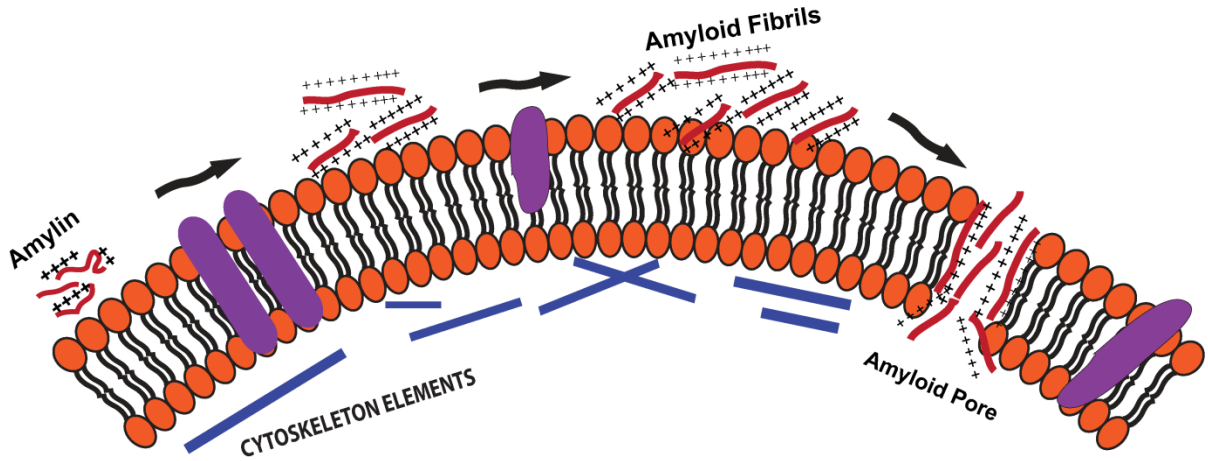

Figure 2.1. An illustration depicting the binding of positively charged IAPP to cell membrane.

2.1.2 Interaction with Glycosaminoglycans (GAGs)

GAGs are heterogeneous highly negatively-charged polymers, comprised of one of seven types of repeating disaccharide units. The disaccharide units of GAGs consist of an amino sugar (either N-acetylglucosamine or N-acetylgalactosamine), and an uronic acid derivative (glucuronic or iduronic acid). Enzymatic modifications lead to varying degrees of N- or O-linked sulfation that modulates the charge densities of GAGs. GAGs are found as either free polysaccharides or can be attached to proteins through the O-atom of a serine or the N-atom of asparagine to form proteoglycans. Proteoglycans are unbranched, typically multi-domain mosaic proteins, which have from ten to hundred GAG disaccharide monomers attached to a residue in the protein core. In some case, the molecular mass of the GAG is equal or greater than that of the protein component. Proteoglycans are ubiquitous in the extracellular matrix and on the membrane surfaces of cells, where they play key roles in cell adhesion and migration, by interacting with components of the extracellular matrix like collagen, laminin,

and fibronectin. The extracellular matrix includes polymeric surfaces like basement membranes. GAGs are involved in the pathophysiology of many diseases relating to the basement membrane like muscular dystrophy, atherosclerosis, cancer metastasis, and TIIDM [121, 122].

GAGs and proteoglycans are found integrally associated with virtually all types of amyloid deposits found *in situ*. Heparan sulfate and heparan sulfate proteoglycans (HSPGs) are most prominently associated with amyloid plaques, most likely because of the high degree of sulfation that may be required for the structural function of these proteins [107, 123]. GAGs, especially heparan sulfate, have been shown to associate with amyloid fibrils in several amyloidogenic diseases such as α-synuclein in PD [124], β-amyloid and apolipoprotein E in Alzheimer's Disease [125], β_2 microglobulin amyloid in hemodialysis-associated amyloidosis [126], and IAPP in TIIDM [122]. GAGs often enhance amyloidogenesis, by providing loci for further amyloid fibril growth/elongation, and by stabilizing the amyloids, once it is formed [127]. Moreover, the GAG heparin which is used as an anticoagulant in TIIDM patients receiving pancreas transplants could have the adverse side-effect of enhancing IAPP amyloidogenesis, thereby contributing to graft dysfunction [128].

GAGs and HSPGs have shown to enhance the rate of IAPP fibrillization *in vitro* in a manner that depends on the fraction of charged residues and their structural arrangement in polysaccharide [129-133]. In addition to mature hIAPP, GAGs have also been reported to accelerate amyloidogenesis of the incompletely processed IAPP prohormone [134, 135]. The N- and C-terminal cleavage sites of the proIAPP prohormone are rich in basic amino acids that present potential binding sites for heparin or negatively charged polymeric surfaces whereas the N-terminal 30 a.a. fragment of proIAPP binds to GAGs, and the C-terminal proIAPP fragment does not bind, localizing the GAG binding site to the N-terminus of proIAPP [134, 135]. In addition, GAGs have also been shown to accelerate the fibrillation of many other amyloidogenic proteins like Aβ-42 [136, 137], α-synuclein [124], tau (τ) [138] and gelsolin [139].

2.2. Interaction of nanoparticles with protein in physiological milieu: the concept of protein corona

The growth of nanotechnology and the increasing use of NPs have raised important issues on the fate of NPs when it enters physiological milieu. In this context, a new terminology known

as the **bio-nano interface** comes into play. When a nanoparticle is presented to the biological milieu, the myriad of interactions that take place between the NPs and the components of the system like proteins, lipids, extracellular matrix, nucleic acids, metabolites etc. results in adsorption of the components onto the interface [140]. These interactions are dependent on the physicochemical properties of the NPs like chemical composition, shape, size, effective surface charge, functionalization, curvature, and hydrophobicity or hydrophilicity [140]. The varying interactions result in varying adsorption of different biomolecules from the milieu causing further decrease in the free energy content of both nanoparticle and protein. The nature of the bio-nano interface is very dynamic as the components inside the physiological conditions keep on fluctuating depending upon the various processes taking place continuously. However, a set of interactions prevailing between the nano-bio interfaces remain primarily same. They are van der Waals interactions, electrostatic and hydrophobic interactions but must be considered differently as these interactions occur at a nanoscale level between molecular interfaces [140].

Out of these nano-bio interfaces, the interactions of nanoparticle with protein are of prime importance, first because of the high concentration of circulating proteins, and second, the subtle change in the interaction pattern may result in total change in protein interaction network governing native structure. After the NP gets coated with proteins in the biological system, a layer of different proteins is formed. This layer of adsorbed proteins on the NPs is usually referred to as **protein corona** (Figure 2.2) [140]. The size and surface charge of NPs primarily regulate the nature of protein corona. Also, the composition and properties of the corona have a direct impact on the uptake of NPs by cells [141]. The formation of the corona is dependent upon the protein structure and concentration, as well as the physicochemical properties of the NPs themselves [142]. Energetically favorable interactions that form the corona mostly include both non-covalent interactions, whereas some proteins are functionalized covalently to the surface of the nanoparticle. Protein corona is very dynamic structures where the interacting proteins keep on exchanging, according to their affinities for the NPs. This phenomenon of protein adsorption over a restricted surface at a given period is called as **Vroman Effect** and states that the composition of the corona can vary, however, the total protein content remains unchanged. It has been shown that as a nanoparticle enters the physiological environment there is rapid binding of highly abundant proteins like albumin and Immunoglobulin G, but is quickly replaced by high-affinity proteins like apolipoproteins [143, 144]. The proteins, albumin, IgG, fibrinogen, proteins of complement system, and

apolipoproteins interact strongly with NPs such as CNTs, iron oxide, liposomes and polymeric particles [140]. Complement system and IgG trigger opsonization followed by receptor-mediated phagocytosis of the complex (nanoparticle-protein corona) [145].

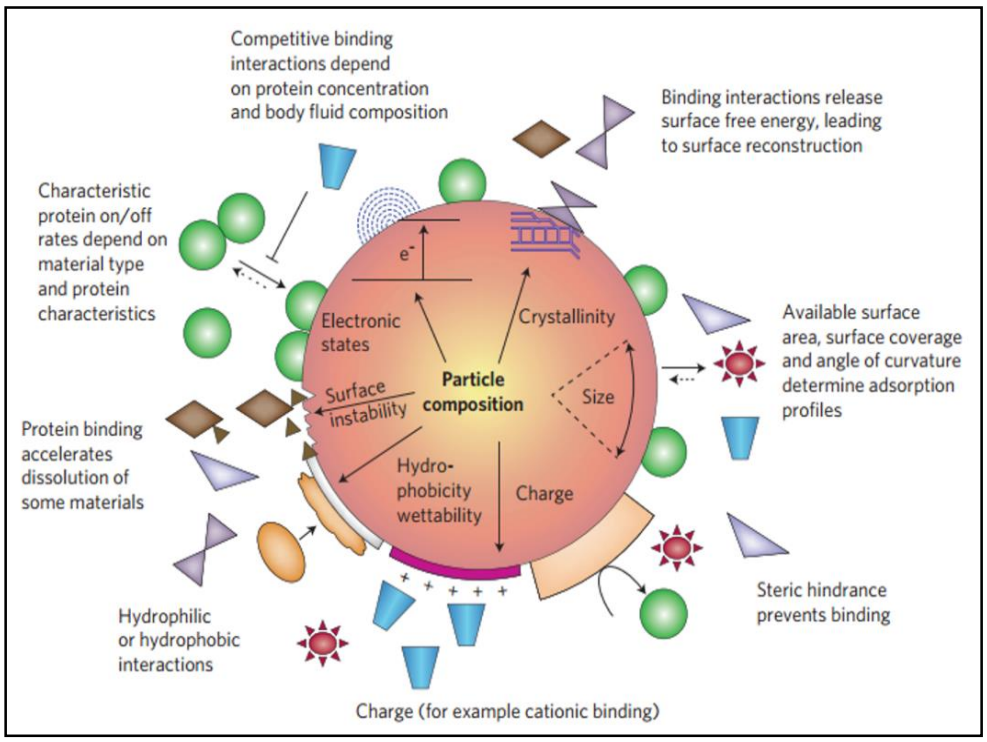

Figure 2.2. Different modes of binding and interactions between nanoparticle and protein, as soon as the particle enters biological milieu [140].

The proteins with high binding affinities which remain associated with NPs for long times form a corona called as **"hard-corona"**, whereas loosely bound proteins that desorb and adsorb back onto the surface form the **"soft-corona"** [140, 143]**.** A recent study demonstrated important differences in the corona when different types of blood preparations, i.e. whole blood, whole blood with EDTA, plasma, or serum, were presented to differently sized silica particles. It was observed that the corona formation depends on the size and composition of the biological media [146]. Inside biological systems, NPs, upon the formation of the corona, they have profound effects on the conformation and functional efficiency of corona protein. These are dependent on the properties of NPs. The interaction with proteins and the induction of conformational changes during corona formation can expose specific parts of proteins that are not normally available for interactions [147, 148]. Some of the important factors affecting protein adsorption and corona formation are discussed below:

2.2.1 Effect of size and curvature

It has been shown that the difference in the size of NPs, even with same surface functionality and composition tend to generate different protein coronas, mostly due to the curvature differences. A recent study showed that silica NPs of 9.5 nm presented approximately 4 times more surface area than NPs of 76 nm [146]. Another study observed the impact of differently sized, amidine functionalized silica NPs on the conformation of BSA and myoglobin. It was inferred from the study that although the interaction mechanism was different for both proteins, only NPs>150 nm triggered conformational rearrangements in them. Smaller NPs had negligible effects on their structure [149]. The polystyrene (PS) monodispersed NPs of 50 and 100 nm NPs were used to study the corona formation in a biological fluid, plasma. Size difference did not show many differences in the protein bound to them. However, in case of PS-NPs, differences in the charge had more impact than size [150]. Differential effects on differently sized polystyrene NPs on human carbonic anhydrase were also reported [151]. Jordi Piella and group recently studied the interaction of AuNPs of sizes 3.5 to 150 nm with cell culture media supplemented with FBS. The density of proteins adsorbed was dependent on the AuNP size and that mono or multi layers of corona were formed with increase in AuNP sizes. [152]. Similar kind of behaviour was also observed when lysozyme was presented to negatively charged silica NPs of varying [153]. Tenzer and colleagues in 2011 identified the differential adsorption of proteins on differently sized silica NPs. They showed that even a 10 nm difference in the size of NPs could affect the corona formation [154]. Thus, it would not be wrong to assume that the protein corona formed is indeed dependent on the size and surface potential of NPs presented to them. It will also be interesting to study the interaction pattern from the point of view of protein interfaces.

2.2.2 Effect of composition (functional groups and charge)

In one of the studies reported in the above section, in addition to the differently sized particles, NPs with different surface functionalities were also used for studying their impact on the protein corona. The NPs were functionalized with carboxyl modified PS, amine modified PS and bare PS NPs. Results depicted that although some proteins in the corona are common to all the different types of NPs, around 25 % proteins in the corona were unique to each NP type indicating that the proteins interact differentially depending upon the surface functionality of the NP [150]. Similarly, bare AgNPs were found to interact more strongly with BSA than detergent stabilized AgNPs by favoring an overall increase in the entropy of the system [155]. In another interesting study, four differently functionalized PS NPs,

carboxy (COOH), amino (NH_2), sulphonate (SO_3^-) and phosphonate (PO_3) were synthesized. Each PS-COOH was calculated to bind to approximately 400 protein molecules whereas other three NPs bound only half number of proteins. ITC studies indicated exothermic reaction in all the four types of NPs. All types of NPs were found to be enriched with apolipoproteins (Apo A1 and clusterin). However, selective enrichment of ApoH on PS-COOH and PS-PO_3 NPs, and ApoA2 and ApoB, on the PS-NH_2 and PS-SO_3 NPs were observed [156]. Similarly, acidic and basic groups functionalized on latex NPs showed differential binding effects on serum proteins [157]. In a particular study, it was demonstrated that over 300 different proteins formed a protein corona within 30 seconds, which however changed over the time of incubation, as some proteins desorbed off the nanoparticle interface [158].

2.2.3 Effect of metal and inorganic nanoparticles

The surfaces of NPs synthesized solely of metals have different properties than other organic and polymeric NPs, mainly because of the electron rich surface. This also gives them a propensity to interact with the components of the body fluid presented to them. These metal nanomaterials interact differently with proteins as compared to other types of NPs. The stabilization of a variety of CNTs has been performed with model proteins like albumins [159, 160]. Albumin has also been used to stabilize and prevent the agglomeration of some metal NPs [161]. The binding of proteins to metal and other inorganic NPs depend on the physicochemical properties of the NPs itself [162]. In a particular study, BSA was shown to form a hard -corona on CoCrMo alloy NPs. Following this, a strong dissolution of molybdenum (Mo) from CoCrMo alloy NPs was observed upon interaction with BSA [163]. Similarly, the binding of albumin to CNTs was shown to enhance their uptake by the scavenger receptors in RAW 264.7 cell lines [164]. Three types of extensively used metal NPs i.e. TiO_2, SiO_2, and ZnO were tested for their respective protein coronas when exposed to the human plasma. In addition to albumin, IgG, IgM, and fibrinogen were found to bind to all the NPs. IgM is known to activate the complement system and the following inflammatory response. IgA was shown to bind ZnONP only [165]. In a separate study, negative ZnO particles were shown to elicit an inflammatory response [166]. Recently AgNPs have also received a lot of attention due to their distinctive properties. In an initial study citrate and polyvinylpyrrolidone (PVP) stabilized AgNPs were shown to form stable coronas with BSA and subsequently the secondary structure of BSA was disrupted due to their binding [154]. Similar results were also reported in related studies [167, 168]. BSA-AgNP complexes are

suggested to be stabilized by electrostatic and van der Waals interactions [169, 170]. Citrate stabilized AgNP of 20 and 110 nm bound to 79 and 85 different proteins from DMEM supplemented with 10% FBS, whereas PVP-stabilized AgNP of same sizes bound to 45 and 48 different proteins only. A common subset of proteins, including albumin, apolipoproteins, keratins, fibrinogen were found to bind to both types of NPs [171]. Recently hydrophobic iron NPs (IONPs) were coated with silk fibroin protein for its enhanced biocompatibility and theranostic applications [172]. Among other metal NPs that were studies for the formation of protein corona are Au, Ag, Fe_3O_4, CoO, and CeO. All these were shown to form hard irreversible corona with the proteins in the cell culture media. The mechanism of protein adsorption and evaluation of protein corona on NPs has been represented in **figure 2.3** [173]. Likewise, in other studies, AuNPs binding to plasma proteins was investigated [174]. In a different study, variation in the corona of AuNPs after photoinduced heating was detected [175].

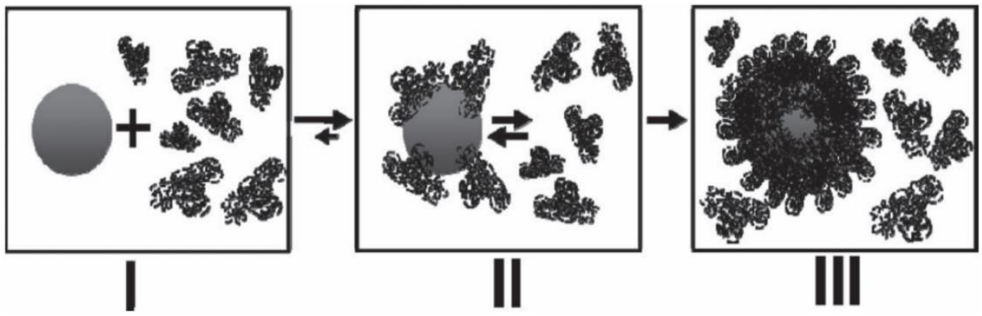

Figure 2.3. The evolution of protein corona inside biological fluids, (I) the process of adsorption starts within few minutes of exposure to working conditions, (II) this evolves to a NP coated with proteins in equilibrium with free proteins present in media and (III) finally giving rise to an irreversible protein corona, with proteins no longer in equilibrium with the free potrins present in-solution [173].

2.3 Nanoparticles in protein conformation, aggregation, and amyloidogenesis

One of the most important and often neglected aspects of protein corona formation either *in vitro* or *in vivo* is its impact on the protein conformation and function. As discussed above, binding of proteins to NPs can expose some of the sequences that would not normally be available for binding. It has now been found in numerous studies that binding of NPs can have profound effects on protein conformation. NPs provide a planar surface to the proteins, that induces perturbations in the secondary structure [176]. The conformational changes in lysozyme and ribonuclease A was reported on differently sized silica NPs in two independent

studies respectively [177, 178]. Ribonuclease A was shown to unfold on the surface of silica NPs whereas lysozyme was also reported for a significant loss of the α-helices. Similarly, albumin was also shown to undergo large structural perturbations in presence of AuNPs in a pH-dependent manner [148, 179]. In a different study, the impact of Au nanocubes and Au nanooctahedra on the conformation of lysozyme and α-chymotrypsin were studied and a significant change in the secondary structure of both the proteins were reported [180]. The interaction of metal NPs with proteins was also extended to AgNPs. A particular study showed the decrease in the helical content of bovine hemoglobin with an increase in AgNP concentrations [181]. Also, distortion of heme pockets of human hemoglobin was reported on interaction with AgNPs [182]. In addition to conformational changes in proteins, their functions were also affected by their interaction with AgNP [183-185]. Interactions of proteins and ZnONP and the subsequent conformational rearrangement in proteins used were also reported in many instances [186-189]. Apart from the metal NPs discussed above many polymeric NPs were also shown to disrupt secondary structures of the proteins adsorbed onto them [190]. Besides, disrupting secondary structures, NPs have also shown to affect aggregation of the proteins. In this regard, contrasting results have been depicted in different studies. NPs have been shown to either enhance or reduce protein aggregation. An important report reviewed that NPs can act as catalysts for protein fibrillation, **figure 2.4** [95]. The figure presented below shows how nanoparticle can act as effective templates for enhancing the fibrillation of amyloid prone proteins.

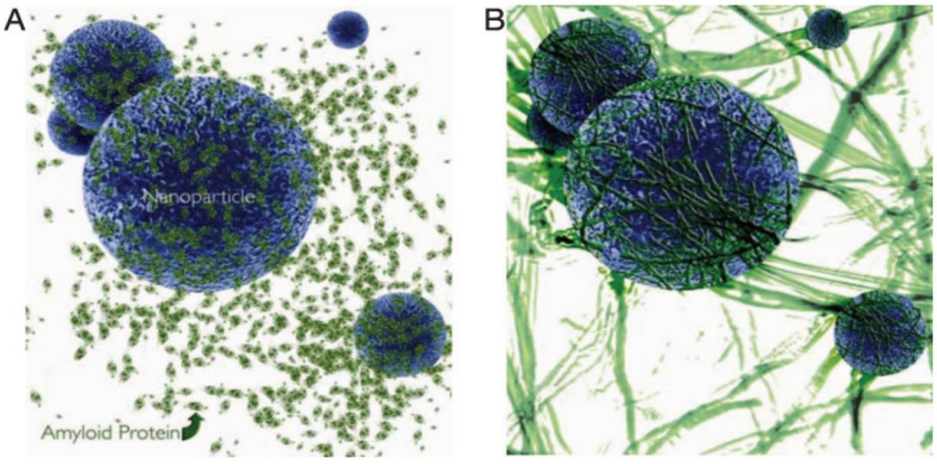

Figure 2.4. An artistic representation of NPs acting as catalysts for protein fibrillation [95].

An important study by Linse *et al.* observed the effect of different types of NPs i.e. N-isopropylacrylamide (NIPAM): N-tert-butyl acrylamide (BAM), cerium oxide particles, quantum dots (QDs), and carbon nanotubes on human β2-microglobulin. The study depicted

that there was a shortened lag phase and enhanced fibrillation of β2-microglobulin [191]. Following this, there have been several studies on the effect of NPs on protein fibrillation. TiO_2 NPs were shown to accelerate the fibrillation of α-synuclein whose aggregation plays important role in the onset of PD [192]. Enhancement of α-synuclein aggregation by AuNPs was also recently reported [193]. 20 nm AuNPs and AgNPs were shown to enhance the fibrillation of IAPP [194]. In contrast, some studies have shown that NPs can be employed as a useful strategy for preventing proteins from aggregation. A particular study demonstrated negatively charged, hydrophobic, polymeric NPs could inhibit the fibrillation of Aβ [195]. Similarly, PLGA NPs functionalized with peptides whose sequence was homologous to the central part of Aβ-42, except for some substitutions, also significantly inhibited its fibrillation [196]. Copolymeric NiPAM: BAM hydrophobic NPs of varying hydrophobicity were found to retard fibrillation of the Alzheimer's disease-associated amyloid protein Aβ [197]. In recent studies, AuNPs were shown to decrease the fibrillation of Aβ [198].

2.4 Zinc Oxide nanoparticles (ZnONP)

Zn^{2+} ion is an important trace element required for the human body. It is involved in numerous processes as co-factors of many enzymes or as a structural component of many physiologically important proteins [199]. The daily recommended dose of Zn^{2+} in healthy adult males and females are 11 mg and 9 mg respectively [200]. However, the discovery that higher exposure or dosage of metal ions can lead to the formation of NPs inside the body systems [94, 201] have led to serious concerns on the effects of excessive dose or usage of metals in our day to day life. On the contrary, nanostructures of Zn^{2+} have a variety of applications due to their unique properties. ZnONPs can be synthesized in varying shapes and sizes and can form interesting structures like rods, needles, helices, tubes, shells, sheets, flowers and snowflakes, reviewed in [86]. ZnONPs have excellent semiconducting and piezoelectric properties. It is wide band gap energy of 3.37 eV and a high bond energy 60 meV which is responsible for its near UV emission [202]. Its property to absorb UV radiation has been employed in sunscreens and has been approved by the food and drug administration (FDA) [203]. In addition to this ZnONP are being used in a variety of other fields. Since ZnONPs exhibit efficient emission at near UV and blue range, it has been used for bio-imaging. Taking the lead of their intrinsic fluorescence, the localization of ZnONP in human skin cells was analyzed *in vitro* and *in vivo* [204]. In a different study, folic acid conjugated and micelle encapsulated ZnONP were used for imaging purposes, without inducing

cytotoxicity [205]. Similarly, when fluorescent dye encapsulating SiO_2 NPs were coated with ZnO/Au nanocomposites, they internalized to endosomes and cytosol and were employed for the imaging of *E. coli* [206]. These were also shown to selectively neutralize leukemic T cells, sparing the normal immune cells. This property was attributed to the dissolution of ZnONP on the surface of cancer cells [207]. ZnONPs are also being used as efficient drug delivery vehicles in many instances [208] and also in photodynamic therapy (PDT), which is an emerging technique in the non-invasive treatment of cancer [208, 209]. The mechanism of cell death by this method is proposed to be the generation of ROS like hydrogen peroxide, superoxide and hydroxyl radicals upon irradiation with a suitable wavelength of light [210]. Additionally, in one study, ZnONP were used as gene delivery vehicles and pEGFPN1 DNA was delivered to A375 human melanoma cells [211]. ZnONP has been used as successful biosensors upon conjugation with different enzymes like glucose oxidase for glucose detection [212]. The applications of ZnONP have been summarized in **figure 2.5** below. Thus, it becomes necessary to study the effect of ZnONP on protein structures as they are being used for such varied purposes and repeated administrations.

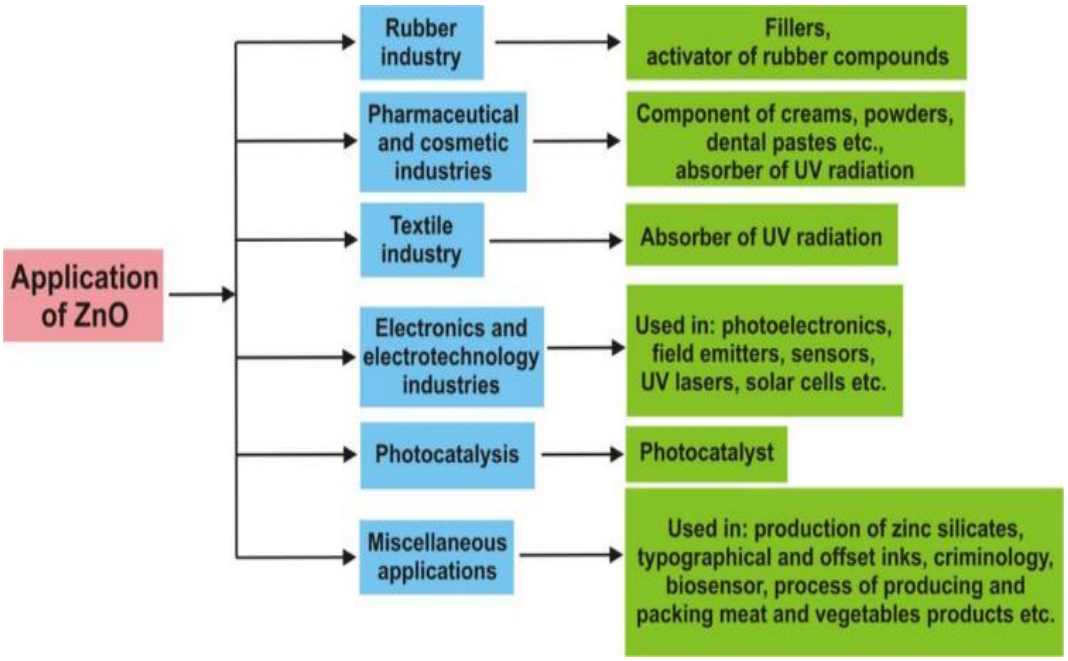

Figure 2.5. Scheme showing various applications of ZnONP across different fields [213].

Chapter 3

The conformational changes in a small model IDP, Islet Amyloid Polypeptide

3. The conformational changes in a small model IDP, Islet Amyloid Polypeptide

3.1 Introduction

TIIDM is one of the most prevailing diseases of modern society, with presently 382 million people affected worldwide [214]. IAPP or amylin, was first described as forming a hyaline in the pancreatic parenchymal cells of a diabetic patient by Eugene Opie in 1901 [215]. Since then, IAPP has been associated with the progression of type 2 diabetes disease [216, 217]. In 1986 and 1987, two groups purified IAPP from human insulinoma and human islet amyloid, respectively [37, 217]. IAPP is a 37-residue peptide, serving as an endocrine hormone, co-synthesized and co-secreted with insulin by the pancreatic β-cells. Although IAPP has long been associated with diabetes and is known to form amyloid deposits in type II diabetes [215], the precise mechanisms of IAPP involvement in β-cell death and diabetes remain uncertain [218]. In the secretory granules of the β-cells, IAPP is primarily located in the halo region, while insulin is stored in microcrystalline clusters of its hexameric form in the dense core [219]. This microcrystalline form of insulin probably has a role in protecting the highly amyloidogenic IAPP peptide from fibrillation [220]. It serves as an important hormone in glucose homeostasis, insulin secretion and gastric emptying [221]. TIIDM is fundamentally characterized by high blood sugar levels and insulin resistance. In prediabetic and diabetic conditions, there is an increased pressure on β-cells to secrete more insulin and, in turn, IAPP. Enhanced IAPP secretion results in the higher local concentration of mature and/or partially processed IAPP, which upon exceeding the critical concentration form amyloid fibrils in the extracellular matrix [222]. Since partially processed and fully processed IAPP has N-terminal positively charged residues, it is anticipated that extracellular negatively charged polymeric surfaces provide a platform for initiation of fibrillation in patients with prediabetic conditions [134], which has been discussed in the previous chapter. Amyloids formed in TIIDM contain IAPP as their chief component, and somewhere down the line have a strong correlation with degenerating pancreatic β-cell mass [223]. Studies have also revealed that in the proteome of pancreatic β-cells, IAPP is the most amyloidogenic peptide having a high *in vitro* toxic propensity toward β-cells, resulting in their degeneration [221]. Extracellular proteinaceous deposits in patients suffering from amyloid diseases including TIIDM have a protein component that encompasses the core of the amyloid. As discussed, the core is also associated with other cellular moieties like

GAGs, SAP component, apolipoprotein E, etc. Amyloids of IAPP are mostly shown to co-localize with insulin [224], zinc [225], membrane lipids [109] and GAGs [134].

This chapter deals with the interaction of IAPP with two negative surfaces i.e. GAGs and negatively charged ZnONP respectively. In the first part of the chapter, we performed *in silico* interactions between IAPP and heparin. IAPP was docked to heparin fragments of increasing lengths and the complexes were simulated for 10 ns to check their stability and further implications in TIIDM. The second part of the chapter deals with the interaction of IAPP with negatively charged ZnONP interface, wherein different concentrations of ZnONP were incubated with IAPP and subsequent effects were analyzed. Additionally, MD simulations were also performed on IAPP-ZnONP complexes to further analyse the conformational changes in IAPP upon ZNONP binding.

3.2 Effect of negatively charged heparin oligomers on the conformation of the model peptide IAPP*: in-silico study*

3.2.1 Introduction

As discussed in the previous chapter, GAGs are polymers of repeating disaccharide units, one is an amino sugar, either D-glucosamine or galactosamine, and another one is uronic acid derivative, glucuronic or iduronic acid [121]. Along with collagen, GAGs are the principal components of ECM contributing to stability and communication between cells and of them HSPGs are most prominently implicated in the amyloid plaques containing GAGs. Some early studies on docking of heparin to proteins have been quite successful in determining heparin binding sites on protein and the key amino acid residues involved in interaction [226, 227]. Hence, this is also true with heparin, which is intricately involved in IAPP amyloidogenesis causing TIIDM [132, 228]. Heparin is suggested to have a helical structure with polymeric negative charges along the axis [229], which can aid in IAPP fibrillation by binding to positively charged SRE flanking residues. 20^{th}-29^{th} residues of IAPP have been proposed to be its amyloid core or the SRE [230]. Also, histidine residue at 18^{th} position has shown to play a major role in the amyloidogenesis of IAPP depending upon the pH of its environment [231]. The published study has shown that heparin fragments, possibly because of charge density and helical nature, moderate the IAPP fibrillation, where shorter fragment delayed the fibrillation and longer fragment enhanced the fibrillation kinetics [132]. Although, there have been many studies supporting the interaction of IAPP with heparin, an explicit structure of the same has not been delineated. In the present study, we docked IAPP with different heparin fragments or heparin with different "degree of polymerization (dp)". Further, the stability of the complex formed has been studied by molecular dynamics (MD) simulations. The study indicated the strength and positions of heparin fragments binding to the key amino acid residues of IAPP. Our study helps in understanding the dependence of IAPP fibrillation on heparin/heparin fragments *in-vivo*.

3.2.2 Methods

3.2.2.1 Structure acquisition of IAPP and heparin

In the absence of an accurate monomeric structure of IAPP, its structure was acquired by homology modelling using the SWISS-MODEL server [232]. The server models the protein based on the input sequence provided and its homology with previously determined structures in the RCSB Brookhaven Protein Data Bank (PDB) [233]. Initially, sequence

alignments were done using BLASTp, and the three-dimensional coordinates of templates were obtained from PDB. IAPP was then modelled from its potential template.

The resulting models of the protein monomers were viewed in Swiss-PDB Viewer, and global energy minimization was performed using GROMOS96 43B1 force-field. Following energy minimization, quality of generated models was analyzed using the Structure Analysis and Verification Server [234, 235], SAVES (http://services.mbi.ucla.edu/SAVES/). The PROCHECK module of the SAVES server allows assessing the stereochemical quality of a modelled protein on the basis of Ramachandran plot [235]. The quality of the models was further assessed by ERRAT module, which analyses structures on the basis of non-covalent interactions between different types of atoms [234]. The PROVE (PROtein Volume Evaluation) plot was subsequently generated for all the models. This module calculates the volumes of atoms in macromolecules treating the atoms like hard spheres thereby generating a statistical z-score deviation for a model [236].

The chemical structures of heparin were obtained from PubChem database. Heparin disaccharide, heparin trisaccharide and heparin pentasaccharide having CID 46936350, 70696233 and 5282448, respectively were used for the study [237]. Structure of heptaheparin was extracted from antithrombin-anhydrothrombin-heparin ternary complex, 1SR5 (PDB ID) with ligand code NT1[238], and the structure of dodecaheparin was taken from PDB having PDB ID 1HPN [239]. For the ease of representation and understanding, we named heparin disaccharide, heparin trisaccharide, heparin pentasaccharide, heptaheparin and dodecaheparin as dp2, dp3, dp5, dp7, and dp12, respectively. Structures of the different heparin oligomer used in the docking calculations are represented in **figure 3.1**. It is quite evident that with an increase in the degree of polymerization (dp) there is an increase in a number of negative charges on the heparin molecules.

3.2.2.2 Molecular docking

Molecular docking is used to predict the best binding orientations of a ligand to receptor molecule (mostly proteins). The binding energy of a protein binding to a particular ligand provides information on affinity, complementarity, and stability of the protein-ligand complex [240].

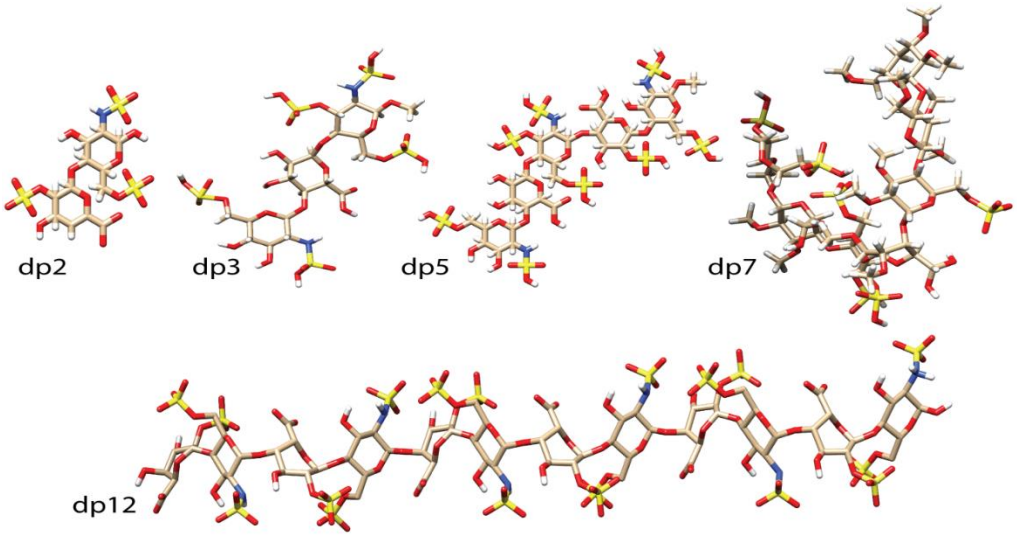

Figure 3.1. Representative structures of the ligands (heparin fragments) used in docking.

We have used Hex 8.0.0 Cuda for molecular docking. Hex is a fast Fourier transform (FFT)-based protein docking tool. It uses spherical polar Fourier (SPF) correlations to accelerate the calculations and uses Gaussian density representation of protein shape for docking calculations. The receptor and ligand to be docked are required in the .pdb format [241]. Before setting up the docking control, the receptor (IAPP) was prepared by the dockprep module of Chimera [242], which includes removal of solvent molecules, addition of hydrogen atoms and the addition of incomplete side chains. Chimera uses Amber force field parameters for energy minimization of standard residues [243]. The energy minimization for ligands was done using an online server called PRODRG [244]. The docking program in hex was activated for 100 conformations, and the conformation with the lowest energy was considered as the most stable and favorable complex. The images of the docked complex for all dockings were viewed by PyMOL [245].

The key interacting amino acid residues and the type of interaction were analyzed by ligplot^{+} v 1.4.5. Ligplot^{+} is an interactive computer program which generates the schematic 2-D image of the docked protein-ligand complexes interactions from 3D coordinates (residues denoted by red colored arc show the hydrophobic residues, and blue dotted lines show hydrogen bonds and their corresponding bond lengths) [246]. In addition to hydrogen bonds, electrostatic and salt bridge linkage in each complex of IAPP and heparin was analyzed by discovery studio 4.5 visualizer [247].

3.2.2.3 Molecular dynamics (MD) simulations and analysis

To understand the structural stability and compactness of the docked complexes, MD simulations of IAPP and IAPP-heparin complexes were carried out in GROMACS (v 4.5.5) [248], using gromos96 43A1 force-field. The force-field parameters of the heparin molecules were obtained from PRODRG server [244]. Each simulation system was solvated with three-point simple point charge (SPC 216) water model, in separate cubic boxes with dimensions 1.2 nm and subsequently neutralized by adding Cl^- ions. The whole system was then relaxed with 50,000 steps of the steepest descent energy minimization. The energy minimized models were subjected for dual step position restrained equilibrium. The first round of equilibration involved an NVT (constant temperature) simulation by applying the velocity-rescaling thermostat to stabilize the temperature at 300 K for 1 ns. The second equilibration phase was conducted under an isothermal-isobaric (NPT) ensemble to stabilize the system at constant pressure (1.0 bar) for 1 ns. In the isothermal-isobaric ensemble, amount of substance (N), pressure (P) and temperature (T) are conserved. The equilibrated systems of IAPP and heparin complexes were subjected to unbiased MD simulation for 10 ns each. The coordinates of all the systems were saved at every 0.002 ns and used for further studies. During simulation, all bonds were constrained using a LINear Constraint Solver (LINCS) algorithm [249], whereas the electrostatic interactions were calculated by particle mesh Ewald (PME) algorithm [250]. Upon simulations, the trajectory analysis was performed using the tools available with GROMACS suite. System stability parameters including root mean square deviation (RMSD), potential energy, residue wise root mean square fluctuations (RMSFs), the radius of gyration (Rg) and hydrogen bond were analysed from the resulting trajectories. The resulting trajectories were plotted using xm-grace. During the simulations, the average structures of the complex were also extracted in the form of .pdb file formats from time points where the RMSD values were stable by the inbuilt command of GROMACS, *g_covar* and were viewed in PyMOL [245].

3.2.3 Results

3.2.3.1 Homology model generation and quality validation

Although, IAPP is classified as an intrinsically disordered peptide, there are reports where IAPP has shown to adopt a helical conformation in presence of an interacting polymeric interface like membrane. Thus, in absence of an accurate 3D-structure, we modelled the structure of IAPP based on the structures already available in PDB. Sequence alignments using pBLAST resulted in a total of eight templates with 97-100% sequence similarities.

Following this, three potential models of IAPP were generated by SWISS-MODEL, model 1, 2 and 3. Template for the model1 was the structure of IAPP or Amylin fused to Maltose Binding Protein (PDB ID:3g7v) [251], template for the model2 was the solution structure of IAPP in presence of SDS micelles (PDB ID:2l86) [252], and the template for model3 was 3D NMR structure of rat Islet Amyloid Polypeptide in DPC micelles (PDB ID:2kj7) [253]. All the models generated were predominantly helical. For all the models, energy minimization was performed by SWISS PDB Viewer, and the minimum energy obtained were -1068.010 KJ/mol, -1291.660 KJ/mol and -829.847 KJ/mol for model1, model2, and model3, respectively. Following homology modelling, quality of generated models was validated using PROCHECK program, which calculates the percentage of residues in the allowed regions of Ramachandran plot and were found to be 69.6%, 84.8% and 69.7% for models 1, 2 and 3, respectively. Subsequently, the z-score mean and z-score rms for models 1, 2 and 3 were generated by PROtein Volume Evaluation (PROVE) plot, which was 0.62 and 0.678, 0.112 and 2.004, 1.584 and 1.656 respectively, indicating the overall quality of the models. ERRAT analyzes model quality on the basis of the statistics of non-bonded interactions between nitrogen (N), carbon (C) and oxygen (O) atoms. The recommended ERRAT value for a good quality model is greater than 50, and higher scores indicate better quality [234]. In the ERRAT module, the overall quality score for models 1, 2 and 3 was 75.00, 57.15 and 95.83 respectively **(Figure A1-4)**. Although the quality score of model 2 was low in the ERRAT, based upon the other model parameters like energy and Ramachandran plot **(Figure 3.2)**, it was selected for further docking studies. Furthermore, the electrostatic properties of this model were determined using H^{++} server, which is an automated system that computes pKa values of ionizable groups in macromolecules. Net charge at pH 7 and pI value for model 2 were calculated to be +3 and 10.1 respectively **(Figure A5)** [254]. The various parameters of the model quality assessment have been summarized in **table 3.1**. The structure of model 2 is depicted in **figure 3.3. Figure 3.3A** shows the secondary structure characteristics along with their functional groups, while **figure 3.3B** shows the structure according to its hydrophobicity surface. Models 1 and 3, and their respective Ramachandran plots have been provided in the supplementary data **(table A1)**. The low ERRAT score for model 2 could be because of the fact that IAPP is a very short peptide and an IDP, whereas ERRAT is generally used for statistical analysis of non-bonded atomic interaction in crystal structure of a protein. IDPs are known to have a highly flexible structure and lack the hydrophobic core [32]. This attribute of our model was further confirmed by analysing its average flexibility by an online tool from

http://web.expasy.org/protscale **(Figure A6)** [255]. It was found that IAPP is a highly flexible peptide, especially the C-terminus.

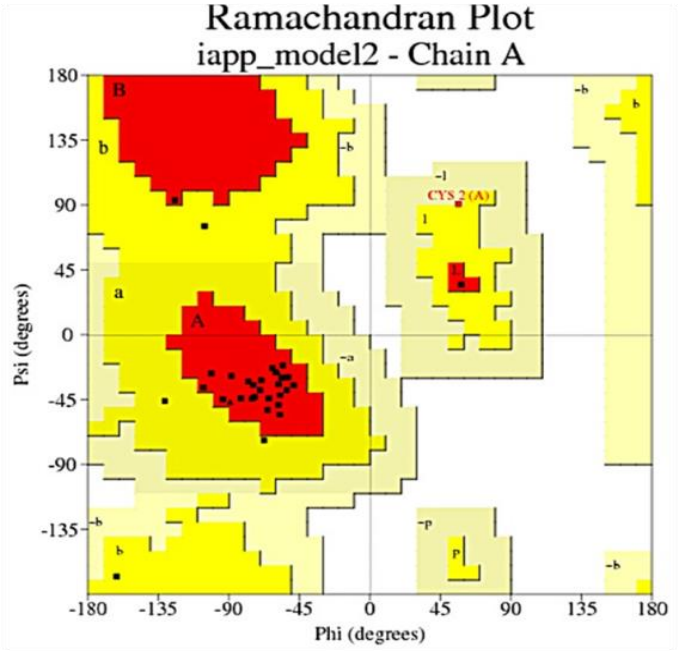

Figure 3.2. Ramachandran plot of the generated model2 for IAPP. The model represented 84.8% of residues in the most favored regions.

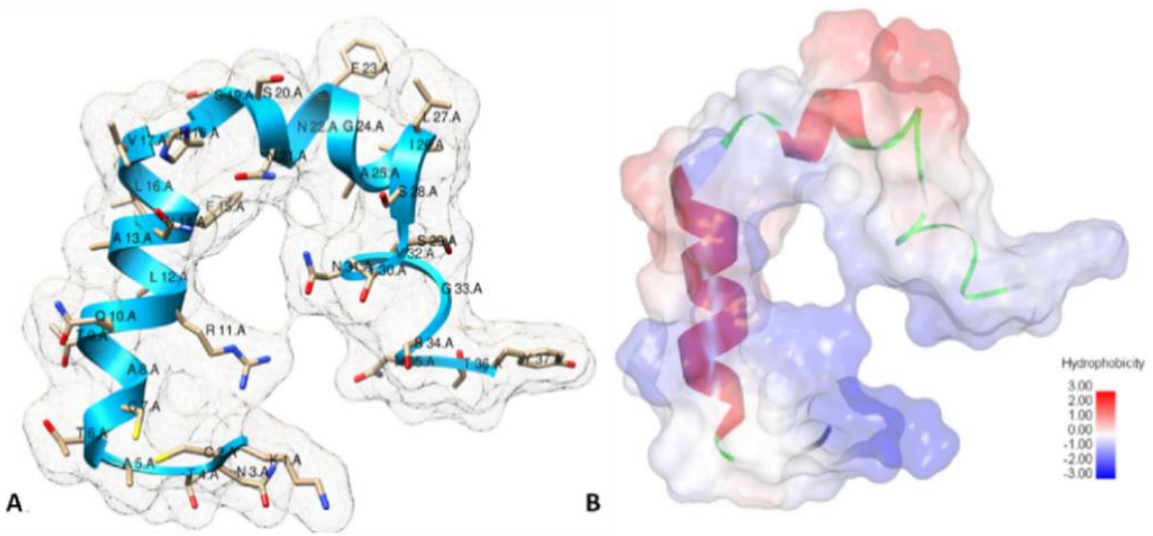

Figure 3.3. (A) Structure of the IAPP model2 generated after modelling taking 2L86 as the template which was used for docking experiments, and (B) model showed the hydrophobic surfaces, red colour showed most hydrophobic surfaces whereas blue colour represented most hydrophilic surfaces.

Table-3.1 Comparison of model validation scores of the three models generated by SWISS-MODEL.

Models	Minimum Energy (KJ/mol)	Residues in the most favoured regions in Ramachandran plot (%)	Z-score mean	Z-score rms	ERRAT score
Model1	-1068.010	69.6	0.62	2	75.00
Model2	-1291.660	84.8	0.67	1.51	57.15
Model3	-829.847	69.7	0.11	1.65	95.83

3.2.3.2 Stability and conformation of the generated models (MD simulations)

Due to limited high resolution crystal structure of IAPP, application of MD simulations plays an important role in understanding the stability and flexibility of modelled structure. To further analyse the stability of generated models, all the models were subjected to MD simulations in the GROMACS v 4.5.5 suite for 10 ns in explicit water. The system was first energy minimized, followed by NPT and NVT equilibration of 0.1 ns for each model. The dynamic stability of IAPP over the simulation of 10 ns was analysed by RMSD, RMSF and Rg. As evident from the **figure 3.4A**, the RMSD in model2 was found to be least. Although some deviations took place during the course of simulation, their value was still less than 1 and the molecule was considered fairly stable over the other two models.

RMSF plot further indicated **(figure 3.4B)** that model2 was the least fluctuating model of all three models. The N-terminus region of this model was the most fluctuating region, especially Lys1, followed by the C-terminus Tyr37. Hence, the higher stability of model2 over model 1 and 3 further makes it the most preferred model for docking with heparin.

Figure 3.4C shows a representative of IAPP structures of the chosen model in the beginning (0 ns), intermediate (2-5 ns) and end (8-10 ns) of the MD simulations. The overall structure can be depicted as U-shape, where, two helices are separated by a small turn. The N-terminus from the 1^{st} to 7^{th} residue is shown to form a loop. Further residues from 8^{th} to 17^{th} conform into a α-helical structure, followed by a small turn comprising of His18 and Ser19. The second helix is fashioned from 20^{th} to 27^{th} residue and the last loop comprises of Ser29 to Tyr37. As evident from the figure, it is anticipated that although there are slight fluctuations in IAPP conformation throughout the simulation, the overall structural integrity remains intact. This further supports the RMSF values that the amino acids conforming to

the α-helical structure are more stable and fluctuate less in comparison to the ones in the loop region.

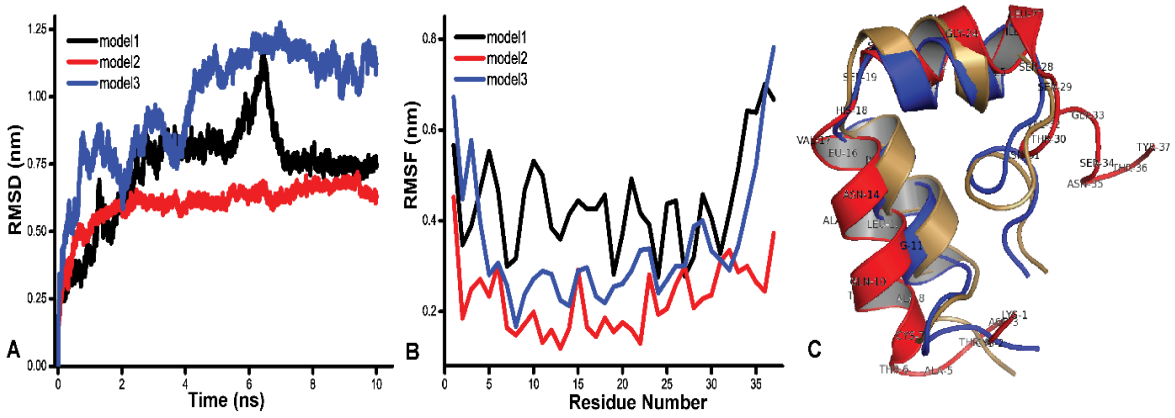

Figure 3.4. (A) Root mean square deviations (RMSD), (B) residue wise root mean square fluctuations (RMSF) of models 1, 2 and 3, and (C) superposed structures of the chosen model during the simulation.

3.2.3.3 IAPP and heparin interactions: Molecular Docking and Simulation

The docking of IAPP with different oligomers of heparin showed some intriguing results. We observed that heparin fragments of different length and charges could have varying binding affinities for IAPP. In addition, they also govern the conformation of IAPP and the stability of the complex. In the section below, we have described the interaction profiles of IAPP and each of the heparin oligomer used through molecular docking followed by their subsequent stability and conformational parameters after MD simulations.

3.2.3.3.1 The interaction of IAPP with dp2 and stability of the complex

Figure 3.5A shows the docked complex of IAPP and dp2. The binding energy to form the complex was observed to be -235.13 kcal/mol. Non-covalent interactions mostly hydrogen bonds, electrostatic interaction and hydrophobic contacts play important roles in stabilizing ligand on the peptide surface. The dominant interaction taking place between IAPP and dp2 is hydrogen bonding involving Lys1, Arg11, and Ser34 (**Figure 3.5D, table-3.2**). Intensive hydrogen bonding in lysine and arginine are brought about by the H-bond donors in cationic ammonium (NH_3^+) and guanidinium (NHC $(NH_2)_2^+$) ions respectively, whereas in serine it is by H-atoms of hydroxyl (OH) groups where serine acted as H-bond acceptor. In the ligand, the functional groups participating in H-bonding are predominantly hydroxyl groups (OH) and sulphate groups (SO_3^{2-}) of the pyranose ring in heparin. The bond lengths are relatively

longer as compared to conventional hydrogen bond (H-bond) (approximately 3Å), thus the interactions are weaker compared to those in conventional H-bonded complexes (Jeffrey 1997). Additionally, Lys1 and Arg11 also formed electrostatic interactions with negatively charged sulphate groups in heparin.

Further, the stability of IAPP-dp2 complex was studied by MD simulations. The RMSD values depicted that initially, the deviation in the complex was less, but at around 5 ns there were fluctuations in the structure, which further got stabilized till 10 ns (**Figure 3.5, table 2**). In case of RMSF (**Figure 3.5H, table 3.2**) it was observed that, although the mean fluctuation did not change much, some fluctuations at Asn34 and Asn35 increased, whereas at Phe15 decreased. As stated above, it is evident from the ligplot analysis that both, Asn34 and Asn35, showed some hydrophobic character within the complex.

The Rg which shows the compactness of a structure did not show significant change throughout the course of simulation as evident in **figure 3.5I**. The *g_hbond* command is used to find out the number of H-bonds between two residues or between protein and ligand in each frame of simulation. In the supplementary **figure A10**, it is observed that the number of H-bonds in the beginning of the simulations were higher as compared to end of the simulation. The intermediate structure between 1-4.5 ns **(Figure 3.5B)** and the structure of the complex towards the end of the simulations **(Figure 3.5C)** showed fascinating results. In the intermediate state, there is a complete dislocation of dp2 from the initial site of binding and new H-bonds are formed between dp2 and Gly24, and dp2 and Ala24 **(Figure 3.5E)**. Moreover, at the end of the simulations, it is seen that the ligand completely falls off the IAPP, and there is no further interaction **(Figure 3.5F)**, indicating an overall poor binding affinity of dp2 for IAPP. Moreover, the salt bridge formed initially also diminishes, further supporting the fact that IAPP-dp2 complex is indeed weak. When the conformation of only IAPP in all the three stages is compared, it is observed that there is a remarkable difference between them. The helical structure is getting distorted, and the loop initially formed by His18 and Ser19 are getting extended to Phe23. Additionally, the residues 29-31 initially which were found to conform into a loop, halfway during the simulations, are also shown to convert into a helical form.

Table 3.2. Comparison of the key residues involved in different types of interactions with different heparin oligomers.

Heparin fragments	Binding Energy (in kcal/mol)	Amino acid residues in H-bond (before MD simulations)	Amino acid residues in H-bond (during MD simulations)	Amino acid residues in H-bond (end of MD simulations)
dp2	-235.13	Lys1, Arg11, Ser34	Gly24, Ala25	None
dp3	-316.11	Arg11.Asn31	Cys7,Gln10, Asn21	Asn31
dp5	-337.24	Lys1,Arg11,Asn31	None	Thr36
dp7	-365.85	Lys1,Arg11,Asn35	None	None
dp12	-516.7	Asn3,Ala8,Thr9,Asn35	Thr4,Thr9,Asn35,Thr36	Thr4,Thr9

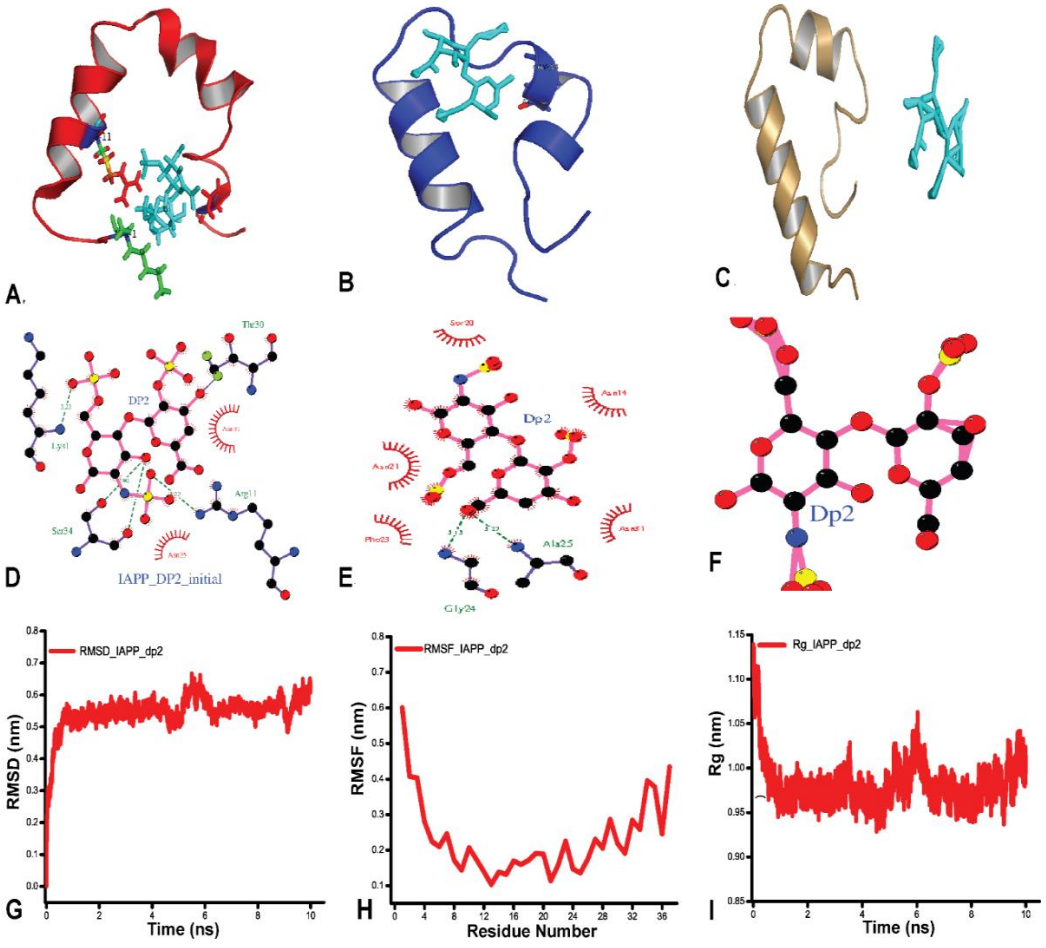

Figure 3.5. Binding of IAPP with dp2 (A) at beginning of the simulations, i.e. the docked complex, (B) & (C) structures of the docked complexes at halfway and at end of the simulations respectively, (D), (E) & (F) ligplot analysis showing the interacting amino acids

in the respective docked complexes, at beginning, middle and end of the simulations, (G), (H) & (I) RMSD, RMSF and Rg plots for the IAPP-dp2 complex.

3.2.3.3.2 The interaction of IAPP with heparin dp3 and stability of complex

The structure of the docked complex of IAPP and dp3, as shown in **figure 3.6A**, depicts the key amino acid residues involved in the interaction. The total binding energy of the complex was observed to be -316.11 kcal/mol. Residues involved in establishing hydrogen bonding are Arg11 and Asn31 **(Figure 3.6D, table 2)**, with an average bond length of around 3Å. The guanidium group of arginine (NHC $(NH_2)_2^+$) and amide group ($CO\text{-}NH_2$) in asparagine served as potent H-donors. The -OH and $-SO_3^{2-}$ functional groups of iduronic acid present in heparin, served as H-acceptor. Like in dp2, Arg11 also formed electrostatic interactions with the accessible functional groups of dp3.

During the course of simulations, it was observed that IAPP-dp3 complex was dynamic, and there were fluctuations in the orientations as depicted in **figure 3.6B**. Interacting amino acid residues also changed with the time course of MD simulations. At an intermediate stage, it is seen that the H-bonds earlier in the docked complex were broken, and a new set of H-bonds were formed involving Cys7, Gln10 and Asn21 residues of IAPP (**Figure 3.6E, table 3.2, A2**). However, H-bond lengths are relatively longer, in this case, indicating weaker binding. Towards the end of simulations, it is observed that dp3 further shifts its position and only a single H-bond formed between dp3 and Asn31 (**Figure 3.6F, table 2**) with a bond length 2.87 Å unlike dp2. The RMSD plot showed that there is a steady rise from 0.4 to 0.8 nm along the course of simulations, i.e. increasing fluctuations in the IAPP backbone (**Figure 3.6G**).

The RMSF plot (**Figure 3.6H**) indicated that there is a significant amount of fluctuations in most of the IAPP amino acid residues. Maximum fluctuations were observed at the C- and N- terminus followed by His18. His18 is present in the loop formed between the helices in the modelled structure. As it can be seen that the whole structure is undergoing a conformational change during simulation, the higher RMSF values were higher owing to the fluctuations. The change in Rg (**Figure 3.6I**) indicated that the peptide in order to adopt a compact structure expelled dp3 from its binding site. **Figure A10** shows the fluctuations in H-bond inferred that the complex is indeed dynamic. However, it is hard to explain the presence of certain H-bond in spite of the ligand being rejected by IAPP.

3.2.3.3.3 The interaction and stability of IAPP with dp5 dp3 and stability of complex

The binding energy of the docked complex of IAPP and dp5 was found to be -337.24 kcal/mol. The structure of the docked complex is depicted in **figure 3.7A**. The interacting amino acid residues are depicted in **figure 3.7D**, table 2. H-bonds are formed by Lys1, Arg11, and Asn31, whereas Lys1 and Arg11 also interact electrostatically with dp5. Initially, it is observed that the complex forms three H-bonds, but with the course of simulation it is seen that the intermediate structure (1-3 ns, **figure 3.7B**) is very unstable, and dp5 completely moves out of IAPP. Hence, we could not analyze the interacting partners for the same by ligplot. However, the complex showed significant stability after 5 ns of simulation. Although dp5 is interacting with Thr36 (**Figure 3.7C and E, table 3.2**) through H-bonding, it is relatively very far from the initial binding site, implying instability in the structure.

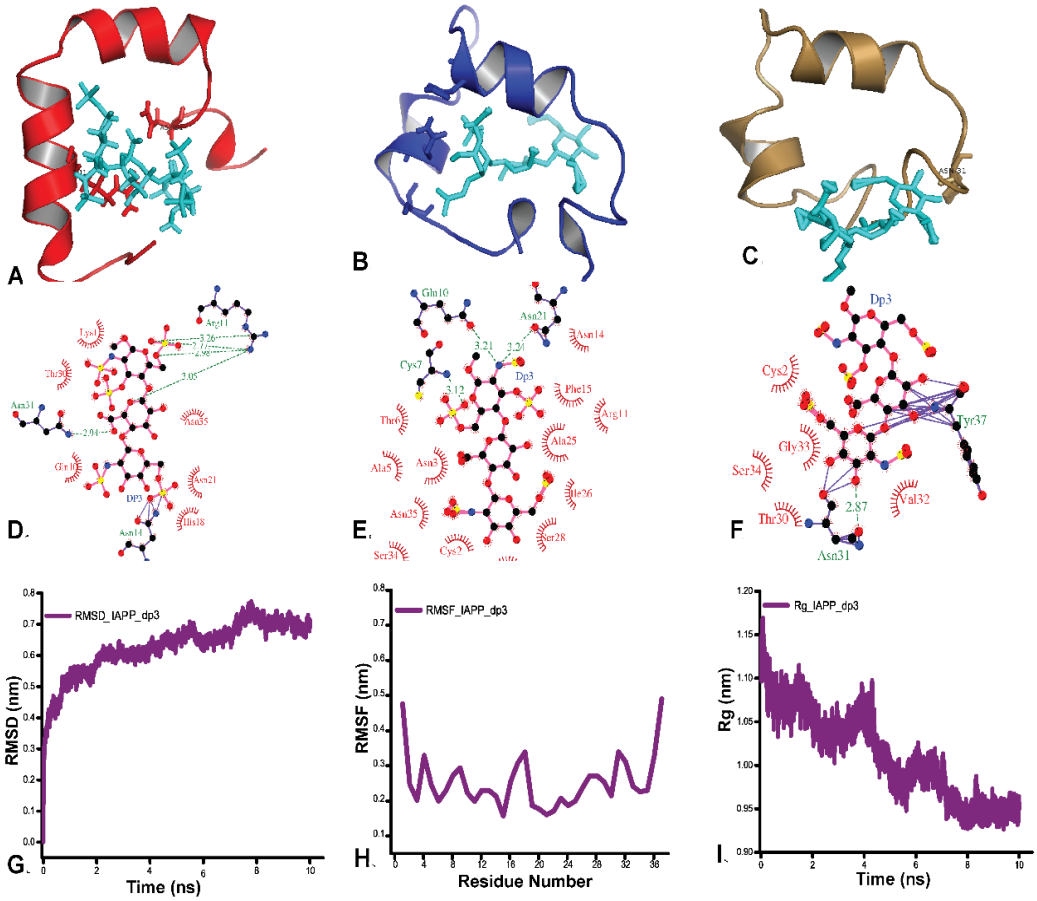

Figure 3.6. Binding of IAPP with dp3 (A) at beginning of the simulations, i.e. the docked complex, (B) & (C) structure of the docked complexes at halfway and at end of the simulations respectively, (D), (E) & (F) ligplot analysis showing the interacting amino acids in the respective docked complexes, at beginning, middle and end of the simulations, (G) (H) & (I) RMSD, RMSF and Rg plots of the IAPP-dp3 complex.

This trend is also seen in various trajectory analyses. The RMSD (**Figure 3.7F**) plot shows a lot of fluctuations till half of the time evolution during simulations, which stabilizes after that to a value 0.6 nm. The RMSF plot **(Figure 3.7G)** indicated that the N-terminus fluctuates much more than the other amino acids in the peptide. Unlike the dp2 and dp3, the C-terminus is fairly stable. This could probably be due to the interaction of dp5 with Thr36. Rg values also indicate a similar trend **(Figure 3.7H)**, as the RMSD, initially as the structure is much more dynamic and fluctuating. Hence, the structure is not compact. Although dp5 is expelled out from the complex, IAPP tries to be stable attaining a compact structure as seen towards the end of the simulation. The number of the H-bond pattern **(Figure A10)**, throughout the course of the simulation, shows an average value of 4.88 further indicating a complex wherein the binding propensity of the dp5 towards IAPP is very less.

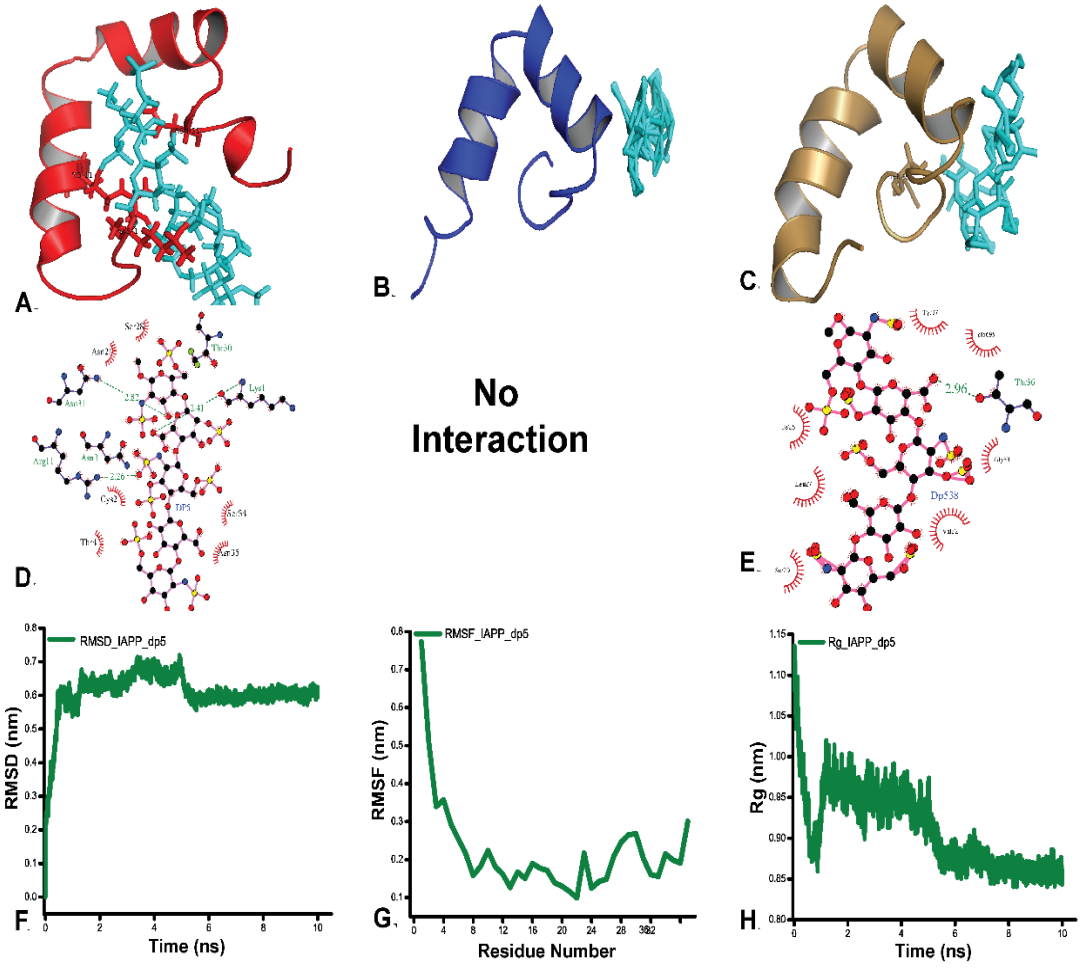

Figure 3.7. Binding of IAPP with dp5 (A) at beginning of the simulations, i.e. the docked complex, (B) & (C) structure of the docked complexes at halfway and at end of the simulations respectively, (D) & (E) ligplot analysis showing the interacting amino acids in

the respective docked complexes, at beginning, middle and end of the simulations, (F), (G) & (H) RMSD, RMSF and Rg plots of the IAPP-dp5 complex.

3.2.3.3.4 The interaction and stability of IAPP with dp7 dp3 and stability of complex

It was observed that dp7 docked quite well with IAPP. The binding energy of the best docked complex as depicted in **figure 3.8A** obtained was found to be -365.85 kcal/mol. Furthermore, as evident in the **figure 3.8D, table 3.2** and **table A2**, functional groups present in Lys1, Cys2, Asn3, Arg11 and Asn35 established crucial hydrogen bonds with electronegative groups present in iduronic acids of heparin. Lys1 and Arg11 were also involved in electrostatic interactions. Midway through the simulations (5-6 ns), the average structure was extracted and visualized. It is observed that dp7 remains in close proximity with IAPP, and the amino acids involved H-bonding with heparin were Asn21 and Asn35 (**Figure 3.8B and E, table 3.2**, and **table A2**). Likewise, when the structure of the complex towards the end of simulations was extracted, it was observed that dp7 continued to remain in close proximity with Thr30 and Asn31 forming H-bonds (**table A2**).

The RMSD plot (**Figure 3.8G**) shows that the deviations in the IAPP-dp7 complex was very less, thus the complex is relatively stable. The average value of RMSD was around 0.8 nm. The previous RMSF values of IAPP complexed with smaller heparin fragments suggest that, as the structure tends to be stable, the fluctuations within the individual amino acids must decrease. In **figure 3.8H**, we observed a fluctuation at N-terminus indicating a comparatively stable complex. However, fluctuations at C-terminus were found to be higher than N-terminus, which could be due to the absence of stabilizing interactions between the ligand and receptor. The Rg (**Figure 3.8I**) is fluctuating during the course of simulations, with an average value of 1.00 nm. The change in Rg can be attributed to the dynamic nature of dp7 within the complex. Finally, as the complex is very dynamic during time evolution of simulation, the no. of the H- bond pattern **(Figure A10)** also varies throughout. Most fluctuations in the H-bond pattern are at the initial and final steps, which are observed to stabilize midway of MD simulations.

3.2.3.3.5 The interaction and stability of IAPP with dp12 dp3 and stability of complex

Docking of IAPP with a longer heparin fragment, dp12 resulted in the lowest binding energy i.e. -516.7 kcal/mol suggesting a more stable complex (**Figure 3.9A**). This stability could be due to more number of negative charges in dp12. However, in contrast to what one would expect, we found that interactions were concentrated near the N- and C-terminus only. Key amino acid residues involved in hydrogen bonding were Asn3, Ala5, Thr6, Thr9,

Arg11, and Asn35 (**Figure 3.9D**, **table 3.2** and **table A2**). Additionally, Arg11 also formed electrostatic interactions. Interestingly, the interaction across the full-length IAPP was dramatically reduced. The intermediate structure (3.5 ns) depicted in figure **3.9B** was shown to almost retain the initial complex.

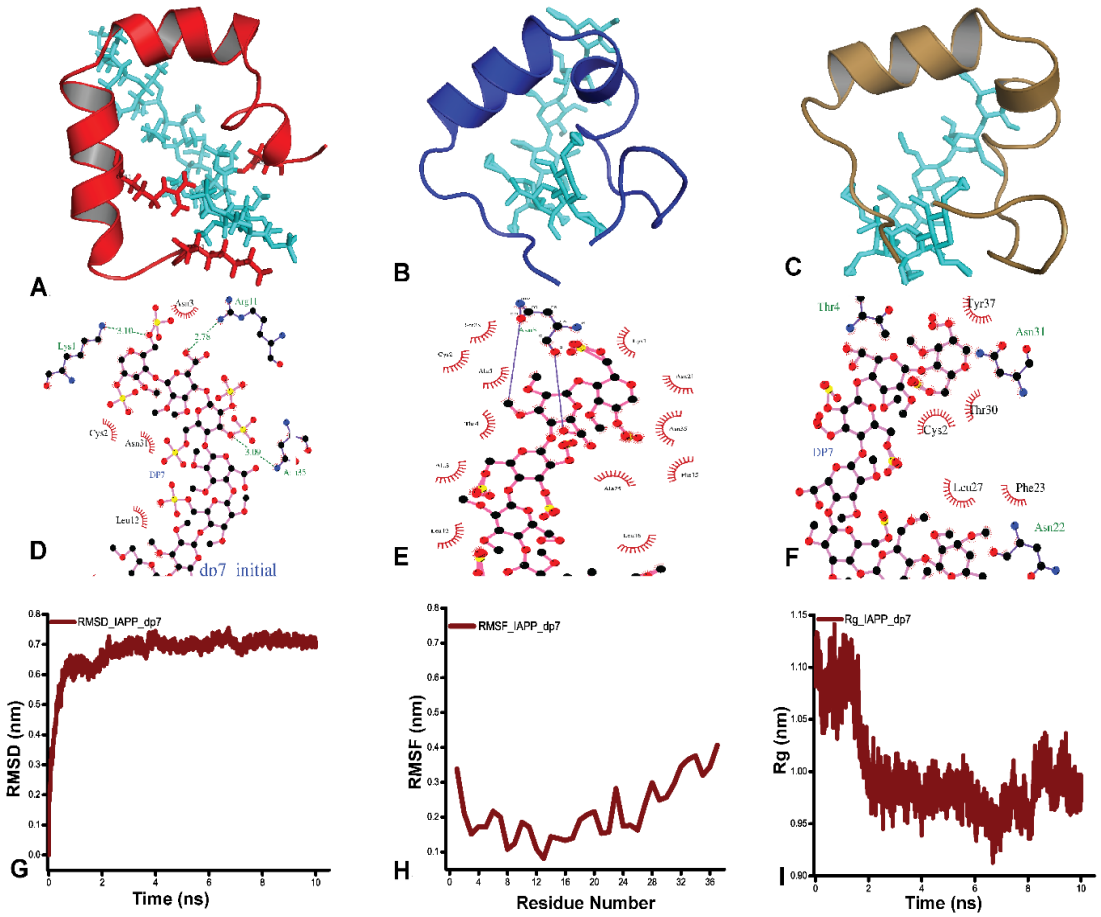

Figure 3.8. Binding of IAPP with dp7 (A) at beginning of the simulations, i.e. the docked complex, (B) & (C) structure of the docked complexes at halfway and at end of the simulations respectively, (D), (E) & (F) ligplot analysis showing the interacting amino acids in the respective docked complexes, at beginning, middle and end of the simulations, (G), (H) & (I) RMSD, RMSF and Rg plots of the IAPP-dp7 complex.

However, the number of amino acids participating in H-bonding dramatically increased and the amino acids involved were Asn3, Ala5, Ala8, Thr9, Gln10, Arg11, Val32, Gly33, Ser29, Asn35, Thr36 and Tyr37 (**Figure 3.9E, table 3.2** and **table A2**). Moreover, the average structure towards the end of the simulation also showed insignificant change with respect to the original structure. H-bond is also retained by Asn3, Cys7, Ala8, Thr9, Arg11, Val32 and As35 (**Figure 3.9C and F, table 3.2** and **table A2**). Furthermore, it is also observed that in

all the above representations, IAPP retains its secondary structure. Thus, we infer that the complex IAPP with dp12 is more stable as compared to the complexes formed with smaller heparin fragments.

RMSD (**Figure 3.9G**) values showed that throughout the course of simulations, the deviation is very less, and the RMSD values are as low as 0.4 nm. This is the lowest RMSD values of all complexes in this study, including that of only IAPP. This further indicates that IAPP-dp12 complex is highly stable than the other complexes. The RMSF values depicted in **figure 3.9H** are also as low as 0.2 for all amino acid residues including N-terminus, suggesting a very stable complex. A higher RMSF value of C-terminus, 0.5 nm, is attributed to the broken H-bond between C-terminal residues and interacting dp12, allowing the terminus to fluctuate. The average Rg **(Figure 3.9I)** value of the complex is 1.01 nm, and as anticipated is higher than other complexes because of the relatively longer dp12 structure. Similarly, the number of H-bonds in the IAPP-dp12 complex is maximum as compared to the other complexes **(Figure A10)** mostly, owing to its longer length and more number of atoms capable of forming H-bonds.

In all the above docking studies, we observed that as the length of the oligomer increased, the interaction was stronger as witnessed by their respective binding energies **(table 3.2)**. Non-covalent interactions (hydrogen bonding, salt bridge, electrostatic interaction and hydrophobic contacts) between IAPP and heparin form the basis of interactions in the complex. Chief contributors in the interactions were lysine and arginine, the functional groups of which remain ionized at physiological pH [6]. Another important residue involved in the interaction of IAPP with heparin was asparagine. There are six Asn in IAPP at 3^{rd}, 14^{th}, 21^{st}, 22^{nd}, 31^{st} and 35^{th} positions. In our studies, we found that at least any one of the asparagines was involved in forming crucial H-bonds with heparin in each complex. The functional group in asparagine is ionized, thus can actively participate in hydrogen bonding [6]. Besides hydrogen bonding, it is also evident from the ligplot analysis that both, polar and non-polar residues are present in hydrophobic contacts. To determine the hydrophobicity scale of amino acids in IAPP and their subsequent accessible surface area (ASA) **(Figure A6)**, we used the ProtScale server from ExPASy, (http://web.expasy.org/protscale) [256, 257]. The Kyte-Doolittle method is a widely applied scale for delineating the hydrophobic character of a protein. Regions with values > 0 are hydrophobic in character. In our case also it is observed that a substantial fraction of amino acids lies on the > 0 scale, depicting a

hydrophobic nature of the peptide. The hydrophobic character of amino acids is mostly imparted due to the presence of methylene groups and/or benzene rings. A study showed that although lysine is highly polar, it has the largest hydrophobic accessible surface area in folded proteins [258]. Hence, in addition to the hydrophobic amino acid residues, the polar amino acids might also contribute to some hydrophobic character when present within a protein.

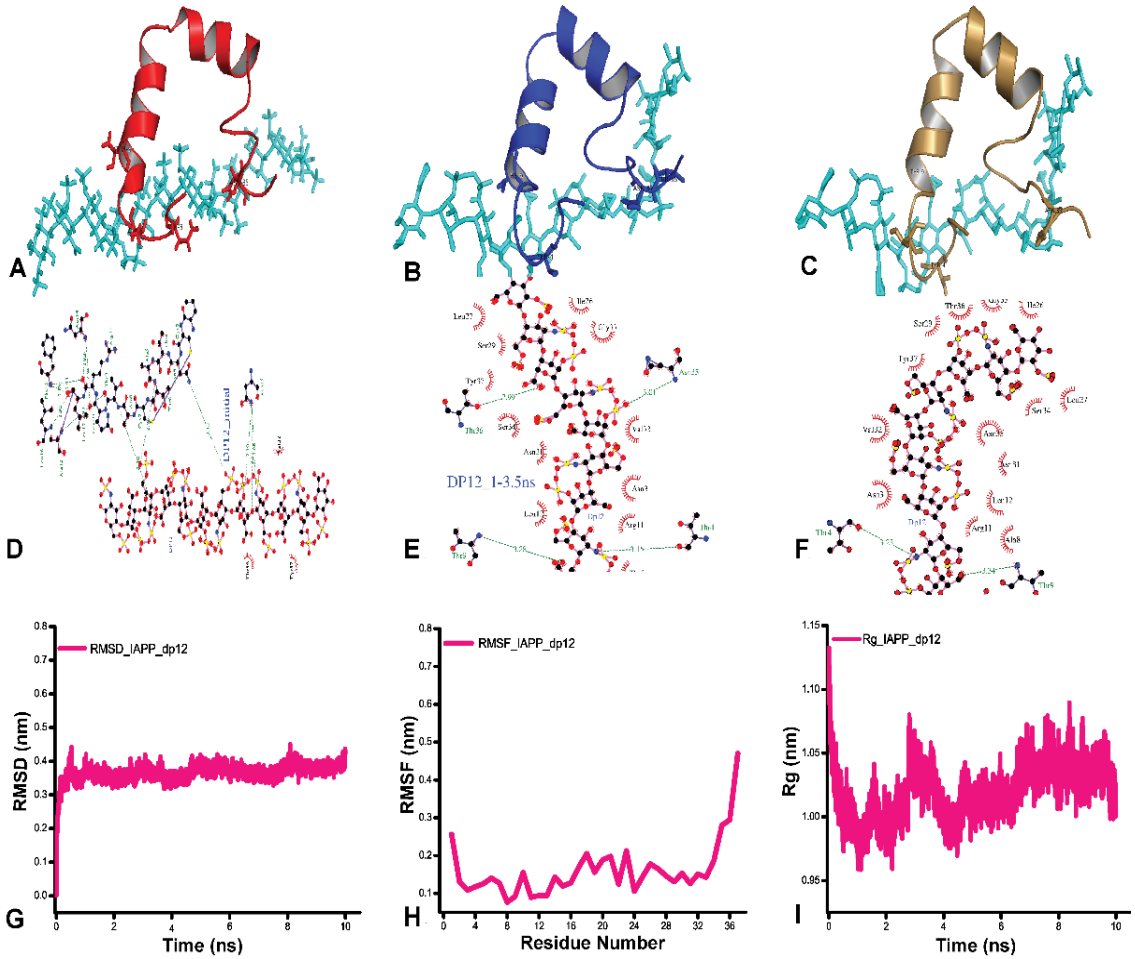

Figure 3.9. Binding of IAPP with dp12 (A) at beginning of the simulations, i.e. the docked complex, (B) & (C) structure of the docked complexes at halfway and at end of the simulations respectively, (D), (E) & (F) ligplot analysis showing the interacting amino acids in the respective docked complexes, at beginning, middle and end of the simulations, (G), (H) & (I) RMSD, RMSF and Rg plots of the IAPP-dp12 complex.

3.2.4 Discussion

Molecular docking provides an inevitable tool for studying interactions between proteins and ligands, which in turn gives an idea about binding regions in protein and the kind of interaction between the interacting partners. Additionally, docking studies with heparin

oligosaccharides and proteins can also offer vital information on the interaction pattern between them. There have already been some studies involving the docking of heparin with proteins [227, 259, 260]. The interaction of heparin and heparan sulfate with proteins plays important roles in many physiological processes like homeostasis, cell adhesion, anticoagulation etc.

Likewise, the interaction of heparin with amyloidogenic proteins has shown to enhance the amyloidogenic propensity of these proteins. This also holds true for IAPP, fibrillation of which is an important factor in pancreatic β-cell degeneration in TIIDM. Studies have revealed that IAPP interacts with heparin during its fibrillation [132, 228]. Heparin has a helical structure and is believed to project its sulfo and carboxyl groups in a precise orientation. Clusters of sulfate groups and carboxyl groups are placed at regular intervals on either side of the helical axis to bring about specific interactions with proteins. It is also suggested that conformational flexibility of iduronic acid residue within heparin is responsible for its wide range of interactions with proteins. Highest heparin binding propensity is shown by basic amino acids like lysine and arginine [261]. Other amino acids involved in H-bonding with heparin are serine, asparagine, and glutamine [262]. The most prominent type of interactions between heparin and a protein is electrostatic interaction. Positively charged basic amino acids on proteins form ion pairs with negatively charged sulfo and carboxyl groups of heparin chain. Moreover, in some cases, there is a significant contribution through hydrogen bonding as well. Numerous studies have shown that the most crucial interactions and effects of heparin with its binding protein partners are exerted when it is in highly polymeric and sulfated states [262]. Concurrent with previous findings with proteins that have well-defined structures, we also found that in IAPP, arginine, lysine, and asparagine dominated its interaction with heparin fragments. Interestingly longer heparin fragment like dp12 formed a stable complex with IAPP, where the functional groups of heparin interacted with the amino acid residues of IAPP N- and C-terminus. The SRE is thus available for self-assembly with other IAPP monomers. Conversely, for the lower length of heparin fragments, IAPP residues which interacted with the functional group of heparin are scattered throughout the peptide. The binding pocket possibly imposes steric hindrance on IAPP self-assemble into fibrils, hence lengthening the lag time of fibrillation. The average structures in each of the docking simulations suggest that there is a considerable change in the secondary structure of IAPP on its interaction with heparin. Some of the helical structures in IAPP are shown to re-arrange themselves into loops on interaction with heparin.

Additionally, it is also evident that the affinity of IAPP for smaller heparin molecules like dp2, dp3, and dp5 is likely to be less as observed during the course of simulations; the ligand tried to move out of the complex. High fluctuations in the values of RMSD and RMSF are also observed with small heparin molecules. In case of dp7, which can be assumed to be a molecule of intermediate length, it is seen that the ligand did not fall off the IAPP molecule, although with the course of simulation the H-bonds number reduced significantly. Interestingly, in case of dp12, it is seen that the structure of the docked complex was the most stable, and retained its structure throughout the course of simulations. The IAPP-dp12 complex also had the lowest RMSD and RMSF values of all the complexes. The stability of all the complexes expressed in terms of RMSD and RMSF is represented in **Figure 3.10**. On comparing RMSD values of complexes, **figure 3.10A**, it is clearly evident that deviations are lowest in the IAPP-dp12 complex. Likewise, the compiled RMSF (**figure 3.10B**) values of all the complexes also point towards maximum stability of IAPP-dp12 complex. We therefore contemplated that longer the heparin fragment better is the binding with IAPP. Previous studies have shown that IAPP fibrils with longer heparin fragments (dp20) highly cytotoxic to MIN6 cell lines. However, smaller heparin fragments (dp2) were shown to rescue cell viability and provide protection against cell death. The role of dp2 in providing protection against cellular cytotoxicity is intriguing and needs further investigation. Additionally, NMR studies depicted that the binding of heparin with IAPP does not depend on the length of heparin fragments but on the concentration of negative charges. However, enhancement of IAPP fibrillation was dependent on the length of heparin fragment. Physical interactions between IAPP and heparin was confirmed by analysing FRET pairing between ThT bound IAPP and fluorescein labelled heparin (FH) [132].

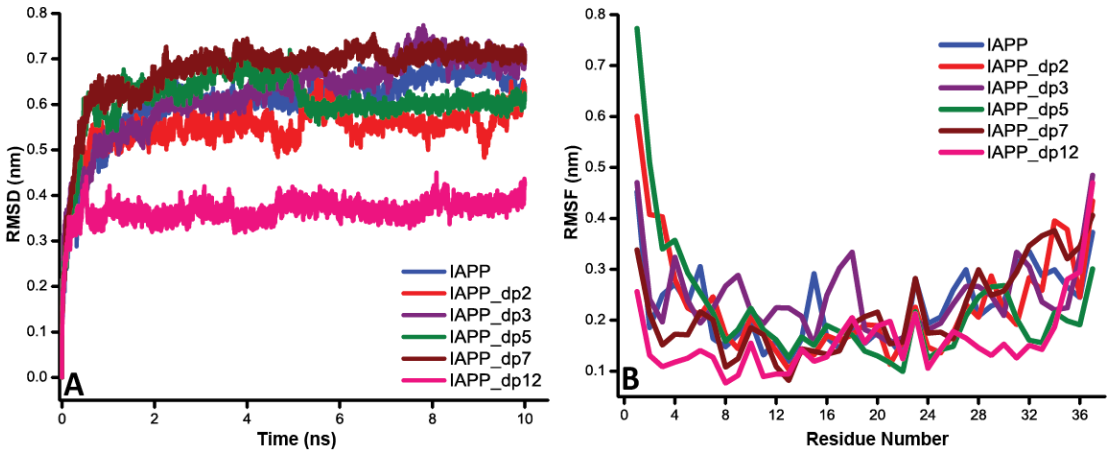

Figure 3.10. Combined plots of (A) root mean square deviations (RMSD), (B) residue wise root mean square fluctuations (RMSF) of all the studied complexes.

Till date three models for IAPP fibrils have been proposed. First by Tycko *et al* based on solid-state NMR [263], second by Kajava *et al* called as the serpentine model [264], and the third by Eisenberg *et al* called as the steric zipper model [265]. In all the models, IAPP monomers are shown to stack on top of one another; perpendicular to the fibril elongation axis, to form cross β-sheet structure. In the serpentine assembly, H-bonds involved in stacking include Asn22, Asn31, Asn35, Ser19 and Tyr37. Another interesting study proposed that IAPP could form triangular structures by winding around a hydrophobic core. In these structures, asparagine residues, Asn21, Asn31 and Asn35 established crucial contacts between the layers [266]. Very recently Eisenberg and co-workers have identified four new fibril-forming structures within the IAPP sequence, all of which exclude its N- and C-terminus [267]. Hence, in total, six amino acid stretches within IAPP have been identified which have the potential to form steric zippers. They are the sequences between 13-18, 16-21, 21-27, 22-28, 23-29 and 28-33 [267] . The IAPP-dp12 complex in our docking simulations also revealed that the amino acids excluding its N- and C-terminus remain unoccupied. We then wanted to know if this stretch of amino acid could adopt a particular secondary structure. For this, we employed a secondary structure prediction server, GOR V [268] **(Figure A11)**. It was predicted that the sequence stretch from 11^{th}-31^{st} residue was rich in extended sheet conformation, which further support the fact that these residues have high propensity of transforming into antiparallel β-sheets, hallmark of amyloids. Moreover, in our previous study, it was shown that longer heparin fragments could be potentially cytotoxic. Consistent with this, the docking results indicate that heparin acts as a platform in IAPP amyloidogenesis, and can provide a template for the growth of IAPP fibrils on its interface. Hence, based on the interaction profile of IAPP with heparin fragments of different lengths, we have put forward two hypothetical models for their interaction with IAPP **(Figure 3.11)**. It indicates that the binding of IAPP with dp2 is very dynamic and somewhat unstable. The IAPP bound dp2 and free dp2 are exchanged during their interaction with IAPP in the bulk media. This holds concurrent with our simulation data that shows the falling off of dp2 from IAPP at the end of simulations. Conversely, the model in **figure 3.11** indicates that the flanking N- and C-terminus of IAPP interact with long heparin chains (dp12). This provides a platform for fibril growth. As the other IAPP regions come in the vicinity of this platform, their SRE interact with each other. This leads to the extension of fibrils. Our study is a small step towards understanding how molecular crowding exerted by negatively charged polymeric surfaces affect amyloidogenesis of small peptides.

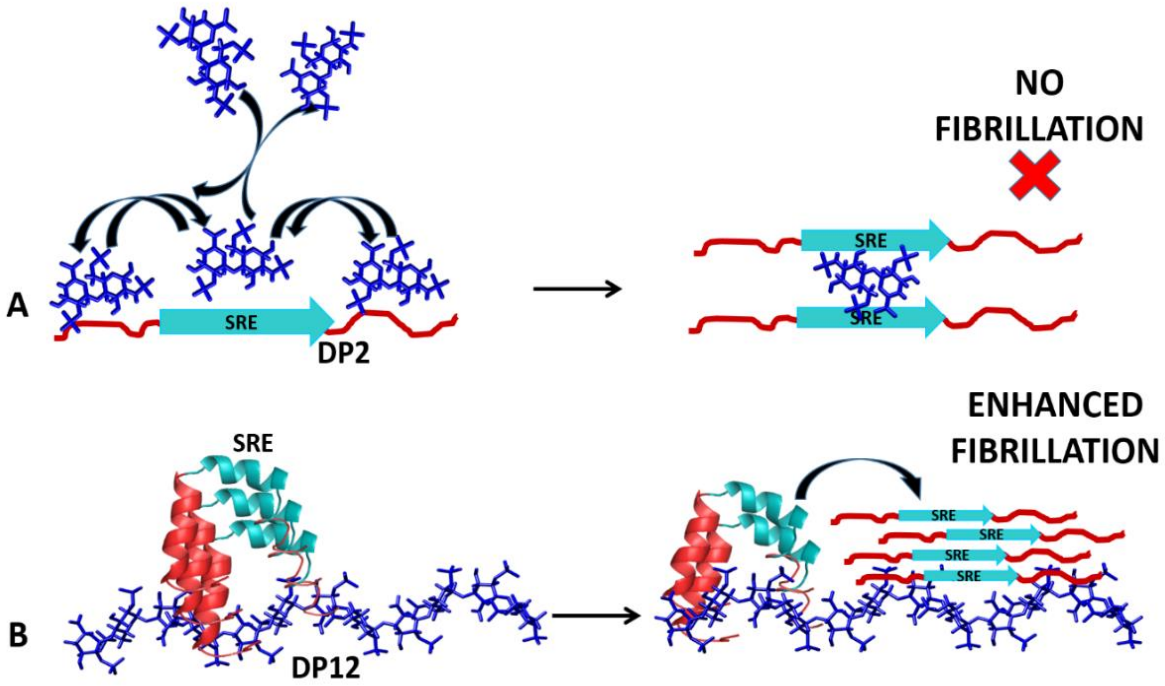

Figure 3.11. Hypothetical models representing the interaction dynamics of (A) small heparin fragment (dp2) and (B) long heparin fragment (dp12) with IAPP.

3.3 Effect of negatively charged surface on the conformation of the model peptide IAPP in presence of Zinc Oxide nanoparticles

3.3.1 Introduction

Many recent studies have looked into the effects of NPs on the amyloidogenic propensity of proteins, which has been reviewed in previous chapters [95, 191]. In case of IAPP, varying trends in their interactions with NPs have been observed. In one study, three types of Au complexes, each containing a different nitrogen-containing aromatic ligand were reported to inhibit IAPP fibrillation by stabilizing monomers [269]. In a second study, citrate and branched polyethyleneimine coated silver NPs, were also shown to inhibit IAPP aggregation but polyethylene glycol and phosphorylcholine grafted iron oxide NPs did not show any significant effect on IAPP fibrillation [270]. Likewise, *N*-isopropylacrylamide: *N-tert*-butyl acrylamide (NiPAM: BAM) co-polymeric NPs [271] and an OH-Terminated PAMAM Dendrimer [272] were shown to inhibit fibrillation of the $IAPP_{20-29}$. Finally, carbon nanotubes and graphene oxide NPs showed promising inhibitory effects on IAPP fibrillation *in-vitro* and in molecular dynamics simulations [273, 274]. Conversely, the interactions of Ag and AuNPs with the amyloid IAPP20-29 SRE fragment were shown to enhance its fibrillation. It was suggested that peptide coated NPs acted as seeds, enhancing fibrillation [194]. The present study describes the synthesis of ZnONP with negative surface potential and its effect on the amyloidogenic propensity of IAPP.

3.3.2 Materials and methods

3.3.2.1 Materials

IAPP (CAS Number,122384-88-7), ThT, Hexafluoroisopropanol (HFIP), sodium dihydrogen phosphate (NaH_2PO_4) and di-sodium hydrogen phosphate (Na_2HPO_4) were purchased from Sigma. Carbon coated copper grids and uranyl acetate alternative stain were obtained from Ted Pella, USA. Alamar blue and FBS were purchased from Life Technologies, USA. Dulbecco's Modified Eagle's Medium (DMEM), trypsin and penstrep were obtained from Himedia, India. MIN-6 cell lines were procured from National Centre for Cell Science (NCCS, Pune, India).

3.3.2.2 Synthesis of Zinc Oxide nanoparticles (ZnONPs)

Synthesis of ZnONP was carried out by using a previously reported protocol based on aqueous synthesis method with slight modifications [275]. Briefly, 500 mL solution of 0.2

M Zn acetate precursor in ultrapure water was prepared and vigorously stirred for 15 min at 60°C, 500 mL of a 0.5 M NaOH solution (aq.) was also heated separately at 60°C. Following this, the two solutions were quickly mixed and allowed to stand for additional one hour at 60°C. After this, the solution was cooled to room temperature and the NPs were allowed to precipitate. The precipitated NPs were then and cleaned by repeated rounds of centrifugation and ultracentrifugation. Finally, the nanoparticle solution was dried at 80°C and ground by mortar and pestle and dried again at 60°C and stored in an airtight bottle until further use.

3.3.2.3 Characterization of ZnONPs

The SPR properties of the ZnONPs were analyzed using a UV-Vis spectrophotometer (Cary 100, Agilent Technology, Singapore). The hydrodynamic size and zeta potential were measured by zeta analyzer (Malvern Zetasizer, Nano ZS90, Netherland). The morphology of the synthesized NPs was analyzed by transmission electron microscopy (TEM), (FEI Tecnai TF30 G2 supertwin, Netherland). Likewise, the EDS profile was performed on TEM with EDS by Bruker, Germany and high angle annular dark field scanning transmission electron microscopy (HAADF-STEM) mapping and X-Ray diffraction pattern was also performed on TEM, with STEM by Fischione. The crystalline nature of the synthesized ZnONPs was determined by X-ray diffractometer (D8, Advance, Bruker) using CU-Kα 16 radiation over 2θ range of 20 to 80°. Subsequently, the bond level vibrations were studied by ATR-FTIR spectroscope (Alpha ATR-FTIR, Bruker, Germany).

3.3.2.4 Buffer and stock solution preparation

Phosphate buffer of pH 7.4 was prepared and filtered through 0.45 μm membrane filter. The stock solution of ThT dye (1 mM) was also prepared in phosphate buffer (pH 7.4). NPs and buffers were prepared in deionized water (18 MΩ). A stock solution of IAPP was prepared in HFIP, aliquoted and stored at -20 °C until further use. During sample preparation, the stock solution in HFIP was diluted to 5 μM IAPP in phosphate buffer (pH 7.4) and the resultant concentration of HFIP in the solution was 2%.

3.3.2.5 Thioflavin T assay

Stock solution of ZnONP was sonicated in an ultrasonic water bath for 15-20 mins. Increasing concentration of ZnONP was added to 10 mM phosphate buffer (pH 7.4) and 20 μM of ThT in a fibrillation reaction volume of 200 μL each. IAPP stock solution was

sonicated on ice for 5 mins. At last, IAPP stock solution was added to attain 5 μM in each well except control negative reactions. All the reactions were prepared in triplicates. Fibrillation reaction was set up in a 96-well clear, flat bottom plate at 25°C in shaking conditions in a Synergy H1 multimode plate-reader (Biotek, USA). ThT dye was excited at 440 nm and emission readings were collected every 5 mins at 490 nm for 8 hrs.

3.3.2.6 Circular Dichroism (CD) polarimetry

CD spectroscopic measurements were performed in far UV range (190-260 nm), for 5 μM intact or in combination with ZnONP in a 2 mm cuvette in a JASCO- J1500 CD spectropolarimeter purged with N_2 gas, and equipped with a Jasco Peltier-type temperature controller system. Experiments were performed at 25°C. Far UV spectra of IAPP at different ZnONP concentrations were performed at 0, 4 and 24 hrs. To further see time-dependent spectral changes, IAPP alone and containing 32 μg/mL ZnONP were collected for 120 mins for each reactions and the change in secondary structure analyzed.

3.3.2.7 Transmission Electron microscopy

For TEM, IAPP and IAPP with 32 μg/mL ZnONP were incubated for 8 hrs. For sample preparation, these were sonicated in a bath sonicator for 5 minutes. In a 20 μl of each sample, 2 μL of 2% uranyl acetate, was added and was incubated for 10 mins. The sample was then dropped onto carbon coated copper grids (Ted Pella Inc., USA) and allowed to be absorbed for 10 minutes, followed by washing with sterile deionized water. TEM imaging was performed on TEM-TECNAI T F 30 G2 Super Twin by FEI. Samples containing IAPP with ZnONP were also analyzed under HAADF-STEM mode of FEI Tecnai TF30 G2 super twin TEM to check for the elemental composition of the complex.

3.3.2.8 Molecular Dynamics Simulations

The structure of IAPP is taken from the SDS complex as in the previous section [252]. Zinc Oxide Nanoparticle (ZnONP) structure have been prepared with Virtual Nanolab (VNL) Atomistix Toolkit version 2016.3 software (www.quantumwise.com)[276]. Spherical ZnONP was constructed using the Wulff Constructor feature of VNL. ZnONP has face-centered cubic (FCC) unit cell with unit cell edge length of 4.63Å. The cluster radius of the ZnO NP is 20Å, accounting to a total of 3064 atoms in the construct. Partial charges of +2 and -2 were assigned to Zn and O atoms of ZnONP, respectively.

The IAPP and ZnONP conjugate has been prepared with chimera software [242]. The minimum distance between ZnONP and the protein is approximately 4Å with IAPP in all the orientations. The transformed coordinates have been used for subsequent molecular dynamics simulations.

Molecular dynamics simulations have been carried out with Gromacs (Groningen Machine for Chemical Simulations) 5.1.4 package [277] using Gromos 54A7 force field [278]. Five set of simulations were carried out i.e. IAPP, ZnONP and IAPP-ZnONP conjugate in three orientations. System size varies from 25000 atoms in case of protein and ZnONP alone systems to approximately 80000 atoms in insulin-ZnONP conjugate systems. 4 Na^+ ions are added to neutralize both the protein system and the protein with ZnONP system.

The systems were solvated with SPC216 water model that extends to 1.0 nm cubic box respectively from the molecule to the edge of the box. Periodic boundary conditions were applied in all directions. The LINCS algorithm was used to constrain all the bonds. Energy minimization was performed with the steepest descent algorithm at a tolerance of 1000 kJ mol^{-1} nm^{-1}. Energy-minimized systems were equilibrated for 1 nanosecond (ns) at NVT (constant number of particles, volume and temperature) and 10 ns at NPT (constant number of particles, pressure and temperature). A temperature of 300 K and a pressure of 1 bar were maintained by applying a velocity-rescale thermostat and Parrinello–Rahman barostat. Final production runs were carried out with the equilibrated structures for 100 ns each for all the three systems with a time step of 2fs. Structural coordinates for every 10 picosecond (ps) were saved and the subsequent analyses like RMSD, RMSF and average distance were done with the tools available in the GROMACS package.

3.3.2.9 Alamar Blue assay

Cytotoxicity of IAPP in presence and absence of ZnONP (freshly prepared mixtures and amyloids) were performed against mouse insulinoma MIN6 cell line by Alamar blue assay. Cells were seeded to a density of 20,000/100 μL well in a transparent clear-bottom 96-well plate containing DMEM medium with 15% FBS, 25 mM glucose, 2 mM L-glutamine, 500 mM sodium pyruvate, 55 μM β-mercaptoethanol, 1000 units/mL penicillin, and 100 g/mL streptomycin. After 24 h of incubation at 37 °C, in a humidified incubator with 5% CO_2 inflow, the culture medium was removed and replaced with fresh medium containing IAPP and IAPP-ZnONP conjugates (both fresh mixtures and conjugates incubated for 48 hrs at 25°C). The cells were incubated for another 24 hrs followed by the addition of 10% (v/v)

Alamar Blue. Fluorescence, due to the reduction of the Alamar Blue dye by viable cells for 3 hrs, was measured using excitation and emission wavelengths of 544 and 590 nm, respectively in synergy H1 multimode plate reader.

3.3.3 Results

3.3.3.1 Characterization of ZnONP

The presence of synthesized ZnONP was initially monitored by the localised SPR in UV-Visible spectroscopy. SPR is a characteristic property of metal NPs, which is usually probed by UV-Vis spectroscopy. **Figure 3.12A** depicts the UV-visible spectrum of the ZnONP at 369 nm suggesting highly crystal NPs with small size and high band gap energy. A similar observation was also observed for ZnONP synthesized by other groups [279] and our group as well [83]. The band gap energy (E_{bg}) was calculated by the formula 1240/λ (eV), where E_{bg} and λ are band gap energy and wavelength respectively. The band gap energy (E_{bg}) of the synthesized ZnONP was found to be 3.36 eV, is in accordance with its theoretical E_{bg} and also supported by previous reports [83, 280].

Next, we determined the crystalline nature of ZnONP by X-ray Diffraction (XRD). Peaks at different 2θ values 37, 40, 42, 56, 66 and 74 corresponding to different indices 100, 002, 101, 102, 110, 103 were observed (**Figure 3.12B**). The indices indexed to the hexagonal wurtzite structure of bulk ZnO lattice parameters, conforming to standard data; reference number JCPDS 76–0704. Similar results were also obtained when ZnONP was synthesized using other methods [281, 282]. The crystal size was calculated from the Scherrer equation.

$$d = k\lambda/\beta\cos\theta \qquad \textbf{Equation 1,}$$

Where d is the crystal size in nm, k is a shape factor equal to 0.89, λ is the X-ray wavelength (0.154178 nm), θ is the Bragg's angle and β is the full width at half-maximum (FWHM) of the peak (in radians). The particle size calculated from the above equation was found to be 19.86 nm.

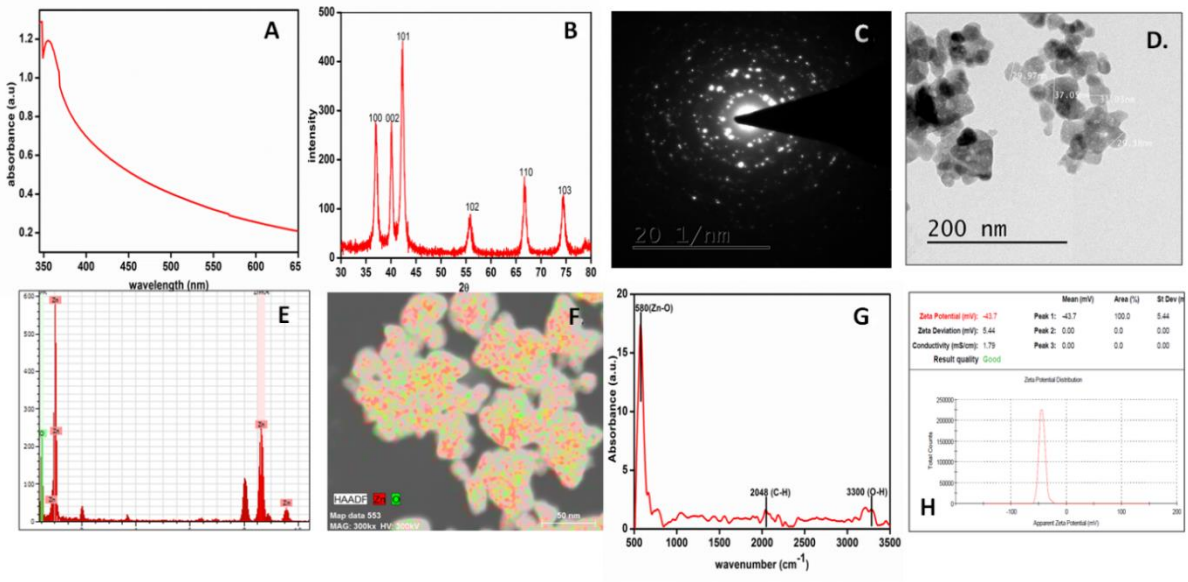

Figure 3.12. Characterization of ZnONP. (A) UV-Visible spectrum, (B) X-Ray diffraction spectrum, (C) SAED pattern, (D) TEM micrograph, (E) EDS spectrum, (F) HAADF map, (G) FT-IR spectrum and (H) zeta potentials of the fabricated ZnONP.

Likewise, the selected-area electron diffraction (SAED) pattern **(Figure 3.12C)** shows bright rings, confirming the polycrystalline nature and preferential orientation of the nanocrystals. The size and morphological characteristics of the synthesized ZnONPs were further studied by TEM. **Figure 3.12D** shows that the ZnONPs are mostly spherical in nature those tend to self-assemble and form complexes rather than single ones. The average size of the particles was found be between 20-30 nm. From the STEM and dark field, imaging it might be inferred that the synthesized NPs may also be porous in nature. The elemental composition of the NPs was further determined by Energy-dispersive X-ray spectroscopy (EDS) analysis, **(Figure 3.12E)** show the presence of zinc and oxygen depicting the purity and homogeneity of the synthesized NPs. Furthermore, HAADF-STEM shows the positions of zinc and oxygen mapped in a particular representative area from the TEM grid **(Figure 3.12F)**. The composition and bond level vibrations were then studied using Attenuated Total Reflection-Fourier Transform Infrared (ATR-FT-IR) spectroscopy. The absorption peaks below 800 cm^{-1} provide important information about internal metal-oxygen bond vibration. The most prominent peak **(Figure 3.12G)** was observed at 580 cm^{-1}, indicating the presence of Zn–O bond level vibrations [283]. Additionally, other small peaks around 2048 and 3400 cm-1 were observed which are specific for C-H and O-H respectively [284]. Zeta potential is a measure of the electrostatic potential near the surface of a particle, used to characterize electrochemical equilibrium between interfaces. The zeta potential of

the synthesized ZnONPs was measured and found that the zeta potential varied when measured in a different medium **(Figure 3.12H)**. The zeta potential, when dissolved in MilliQ water was found to be -23.0 mV, but when it was dissolved in phosphate buffer (pH 7.4), zeta potential reduced to -43.7 mV. Similar results on the dependence of zeta potential of ZnONP in different pH has also been reported by Degen *et al.* [285]. All our studies were done in phosphate buffer, so for future references, the effective zeta potential of the synthesized ZnONP was considered to be highly negative.

3.3.3.2 Fibrillation kinetics: Thioflavin T assay

ThT dye binding assay is a classical technique used for the detection of amyloid fibrils. In principle, the fluorescence emission of ThT dye in an aqueous medium is very low. However, when it binds to proteins fibrils, it intercalates into the fibril core to have 10-500-fold higher ThT fluorescence intensity at 482 nm [286]. We performed ThT assay of IAPP in presence of varying concentration of ZnONP (both in phosphate buffer pH 7.4) till 2 hrs after which saturation was achieved. Before starting the reactions all the samples were sonicated on ice to disaggregate any pre-existing fibrils from the solution. **Figure 3.13A** depicts ThT spectra of IAPP with increasing ZnONP concentration. An exponential curve with a diminished lag phase is obtained in all the samples [132]. It is evident that the fibrillation rate of IAPP is very high in presence of the particle interface. Like nucleated fibrillation, the interface enhanced the fibrillation by directly entering IAPP self assembly into exponential growth phase, as soon as the data collection is initiated. Fluorescence intensity spectra after completion of the assay are high for IAPP, suggesting high fibrillation propensity **(Figure 3.13B)**. In contrast, in the presence of ZnONP, there is a gradual reduction in the fluorescence and the minimum fluorescence is observed in IAPP fibrillation reaction incubated with 32 µg/mL of ZnONP. A reduction of almost 50% intensity in the presence of 32 µg/mL ZnONP was observed, implying a significant reduction in IAPP fibrillation on its interaction with ZnONP interface (**Figure 3.13A**).

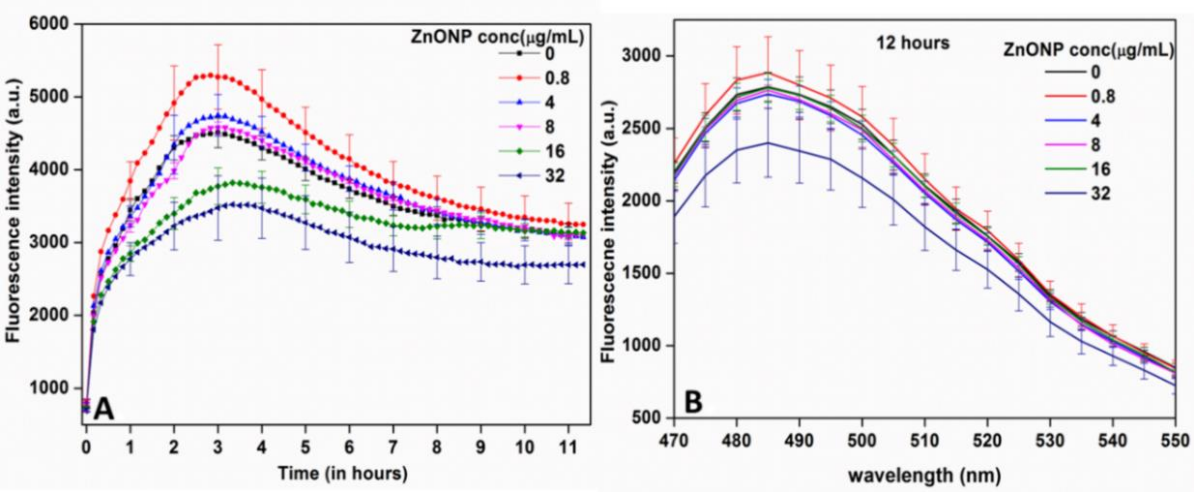

Figure 3.13. Thioflavin T dye binding to IAPP fibrils formed in absence and presence of ZnONP. (A) Thioflavin T assay of IAPP fibrillation in presence of increasing concentrations of ZnONP, and (B) fluorescence emission spectra of ThT dye after 12 hrs of IAPP incubation with increasing ZnONP concentrations.

3.3.3.3 Secondary structural transitions: CD spectroscopy

Following ThT assay, the structural transitions in IAPP alone and with different ZnONP were assessed by CD polarimetry at 0 hrs, 4 hrs and 24 hrs. **Figure 3.14** shows the CD spectra of IAPP with different ZnONP concentration. Intact IAPP shows a major minimum at 200 nm indicating its random coil structure. Presence of a slight shoulder at 219 nm is mostly because of the presence of a low percentage of HFIP, 2%; HFIP is known to induce α-helical properties in proteins [287]. Presence of ZnONP significantly reduces the ellipticity in all cases, but the negative peaks at 209 and 218 nm mostly indicated the presence of α-helical characteristics in them [288]. After 4 hrs of incubation of the samples **(figure 3.14B)**, the spectra were again collected. IAPP alone (black) shows a shift from 200 nm to 220 nm, indicating a major structural transition indicating the presence of β-sheet rich structures specific for amyloids as also shown in many previous studies [287, 289]**.** IAPP in presence of ZnONP also showed negative peaks around 220 nm, but with a much reduced ellipticity in each, implying that there could be some intermediate structures or other type of aggregates, but not characteristic β-rich amyloid fibers. Similar spectra has also been obtained while studying the inhibition of IAPP amyloids in previous studies [290, 291]. Likewise, after 24 hrs **(figure 3.14C)**, the spectrum of IAPP alone remained almost similar to the one at 4 hrs, with negative ellipticity at 224 nm, but with a much reduced ellipticity implying the formation of insoluble fibres, which could not be sampled by the CD

instrument, or formation of insoluble aggregates**.** In others reaction mixtures containing ZnONP, there was also a significant reduction in the ellipticity owing the presence of insoluble aggregates.There was an absence of characteristic secondary structural signatures**,** which further suggests the formation of other types of aggregates or turns, in presence of ZnONP.

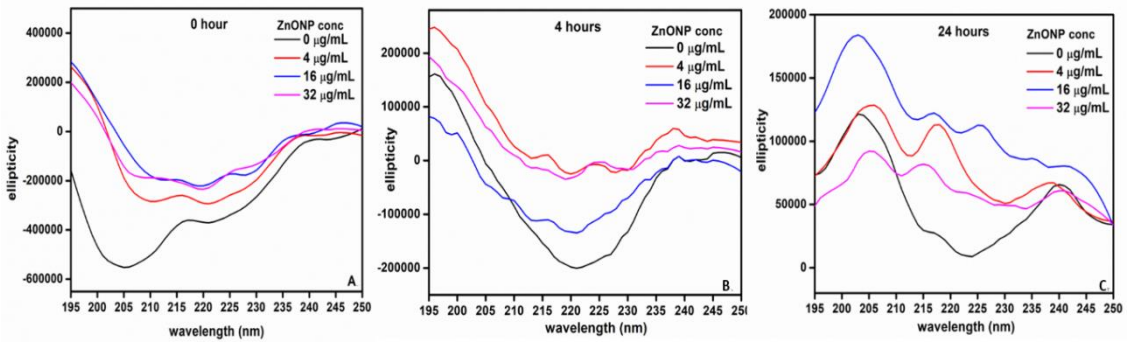

Figure 3.14. Time-dependent CD spectra of IAPP with increasing concentration of ZnONP at (A) 0 hr, (B) 4 hrs and (C) 24 hrs.

To further analyze the major structural changes with respect to time, we followed time-dependent changes in IAPP alone and IAPP with the highest concentration of ZnONP used (32 µg/mL) for 120 minutes. **Figure 3.15A** depicts the changes in IAPP alone. IAPP retains its random coil conformation predominantly till 30 minutes after which there was a pronounced red shift indicating a structural rearrangement of the maximum population. At 45 minutes, a major minimum was observed at 219 nm with a slight shoulder at 205 nm, depicting a population of peptides rich in amyloid specific β-rich structures [292]. As time proceeded, the shape of the spectra at different ZnONP concentrations remained same, with a slight reduction in the ellipticity. Visual examination of the samples revealed the presence of very minute insoluble fibers. When time-dependent CD spectra of IAPP in presence of 32 µg/mL ZnONP was performed **(Figure 3.15B)**, it was observed that IAPP attains a α-helix-rich conformation, with a major minimum around 205 nm and a slight shoulder at 220 nm till about 90 minutes, after which, a predominant structural transitions into β-sheets with minima around 220nm is observed. Data suggests that in IAPP alone the fibrillation transitions into β-sheet rich, amyloid specific structures quite fast, as compared to IAPP supplemented with ZnONP. With ZnONP, α-helical rich conformers maintained their structure till a longer time, suggesting a protective role of ZnONP in IAPP fibrillation. Reduction in the ellipticity also indicates the formation of insoluble aggregates, which

deposit at bottom of the cuvettes. Additionally, in both cases, positive band around 195 nm strengthens the presence of some degree of α-helical segments in solution. Ellipticity values at 209 nm (corresponding to α-helices) and ellipticity values at 218 nm (corresponding to β-sheets) [289] at each time point is shown in the inset of the respective figures, which also suggests that IAPP alone contains more β-sheet content than α-helix at any time point, compared to IAPP supplemented with 32 µg/mL ZnONP which has almost equal share of both the secondary structures.

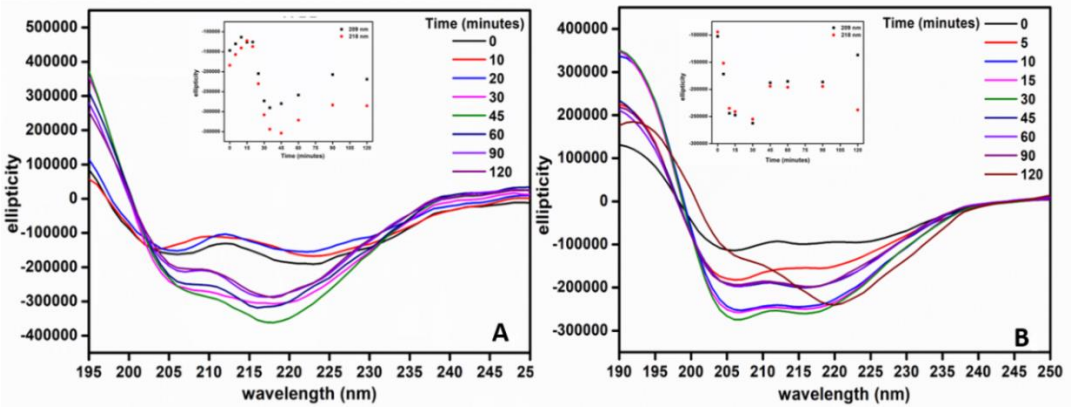

Figure 3.15. Evolution of far-UV CD spectra with time for (A) IAPP alone and (B) IAPP in presence of 32 µg/mL ZnONP. The inset in each graph shows the ellipticity value at 209 nm and 218 nm specific for α-helix and β-sheet, respectively.

3.3.3.4 Morphology of the fibres: Transmission electron microscopy

TEM is routinely used to characterize the morphology of amyloid fibrils. **Figure 3.16** shows the TEM image of fibrils formed by IAPP alone. IAPP forms fibrillary structures, evident in all the previous studies [132, 291]. A mixture of short and long fibrils has been observed, which further interact to form complex mesh-like structures observed in the micrograph. Likewise, the morphology of structures formed in the presence ZnONP was also observed **(Figure 3.17). Figure 3.17A** shows HAADF mapping of sample, which indicate the presence of IAPP with ZnONP. HAADF-STEM is used for elemental mapping in samples [293]. The figure depicts the close presence of zinc (magenta), with other elements present in proteins like nitrogen andsulfur suggesting interactions between IAPP and ZnONP.

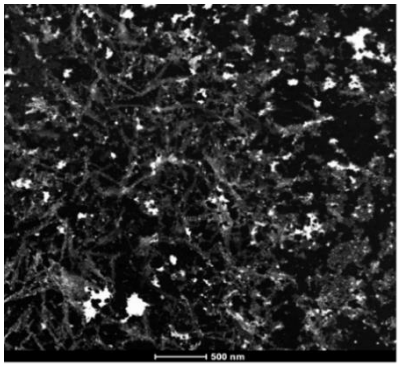

Figure 3.16. TEM micrograph of IAPP alone after 8 hrs of incubation at 25°C.

The **figure 3.17B** shows small circular aggregates of IAPP which further indicates the reduction of fibrillation of IAPP by 32 µg/mL ZnONP, as evident in ThT dye binding assay. This suggests that IAPP in presence of ZnONP forms predominantly small aggregates other than long fibrils. However, very few sparsely placed fibrils were observed in presence of ZnONP as shown in **figure 3.17C**. An explanation for the presence of small aggregates with ZnONP IAPP forms contains β-sheet rich and/or α-helical intermediates, as seen in CD, which do not interact and form long fibrils.

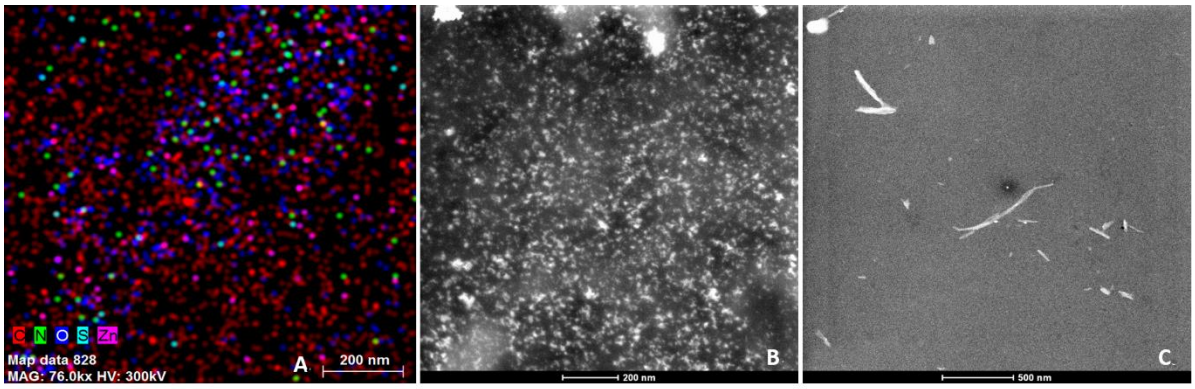

Figure 3.17. TEM micrograph of IAPP in presence of ZnONP. (A) HAADF-STEM mapping of IAPP with 32 µg/mL ZnONP. TEM micrographs of IAPP incubated with 32 µg/mL ZnONP for 8 hrs at (B) 200 nm and (C) 500 nm scale resolutions, respectively.

3.3.3.5 Molecular dynamics Simulations

MD simulations of IAPP with ZnONP were carried out with three different orientations of IAPP molecule on ZnONP surface as shown in the **figure 3.18 (A-C)** The first orientation has the N and C termini of IAPP facing the ZnONP, the second orientation has the loop region oriented towards the ZnONP, while in the third orientation, the SRE region of IAPP is oriented towards the NP. After 100 ns of simulations with each of the orientation,

snapshots collected at every 25 ns, revealed interesting changes in the IAPP conformation. In the first orientation **(Figure 3.19 A-E)** the N-terminus stays intact on the NP surface, whereas the C-terminus is highly fluctuating, which indicates that high affinity and interaction of positively charged N-terminus.

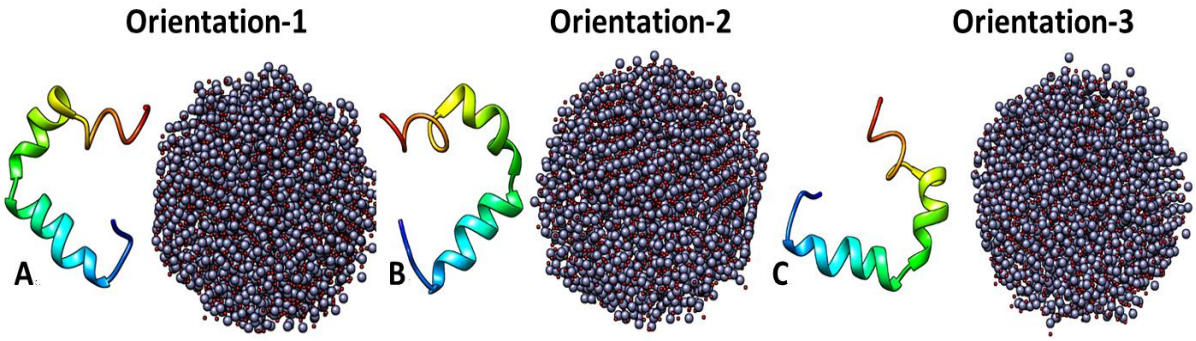

Figure 3.18. Three different orientations of IAPP at ZnONP interface, which served as initial complexes of MD simulations, (A) N- and C-terminus facing the NP, (B) loop region facing the NP and (C) SRE region facing the NP.

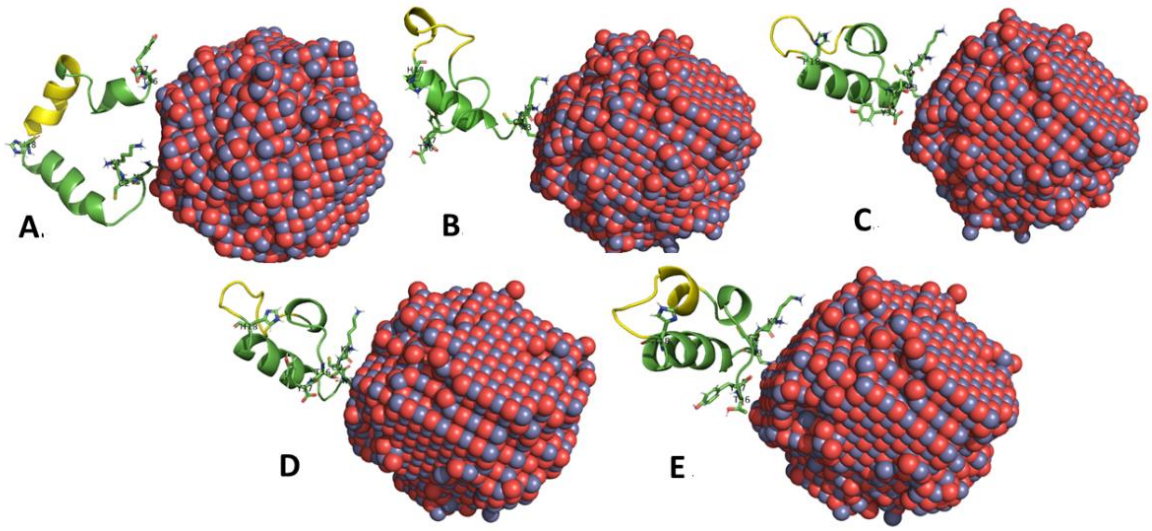

Figure 3.19. Snapshots of the MD simulations of IAPP-ZnONP complexes in orientation-1 at 0 ns (A), 25 ns (B), 50 ns (C), 75 ns (D) and 100 ns (E) of simulation, respectively. SRE region (SSNNFGAIL) is presented in yellow, and side chain of residues 1, 2, 18, 36 and 37 are shown as sticks.

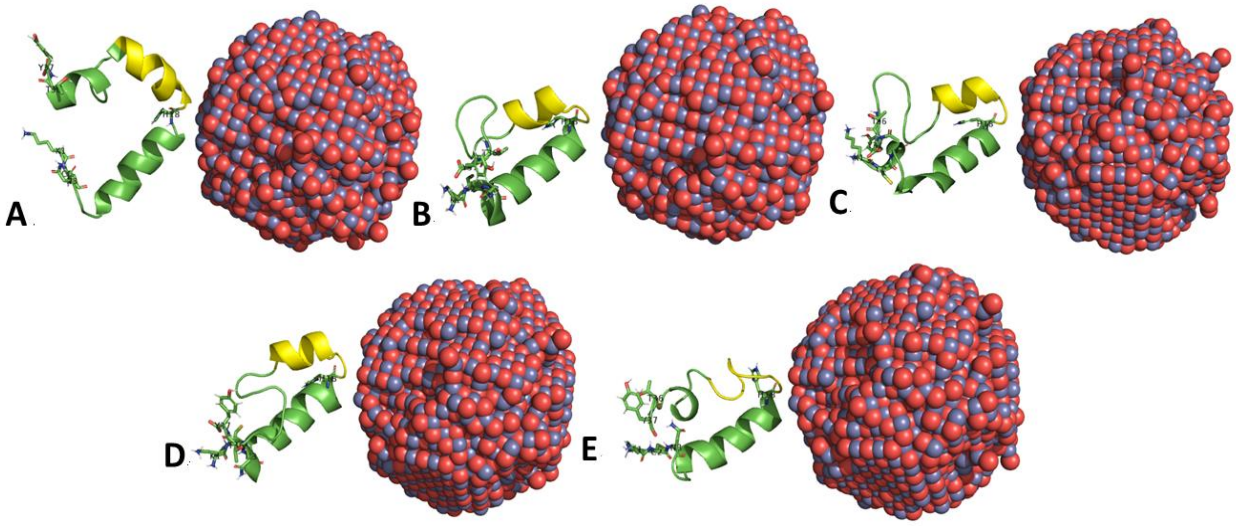

Figure 3.20. Snapshots of the MD simulations of IAPP-ZnONP complexes in orientation-2 at 0 ns (A), 25 ns (B), 50 ns (C), 75 ns (D) and 100 ns (E) of simulation, respectively. SRE region (SSNNFGAIL) is presented in yellow, and side chain of residues 1, 2, 18, 36 and 37 are shown as sticks.

In the orientation-2 **(figure 3.20 A-E),** however, it is observed that there are significant changes in the first helix encompassing the N-terminus too. The helix opens into a random coil conformation at end of the simulation (100 ns). Interestingly, when the SRE region is placed at the NP interface, i.e. in orientation-3, striking conformational changes are observed (see **figure 3.21** A-E below). Huge fluctuations are seen in the snapshots, from the beginning till the end. The structure twists around and gets extended, forming more of a disordered structure towards the end of the simulations. It is worth noting that in the second orientation, the loop region containing the His-18 is directly interacting with the ZnONP, but is free in the other two orientations. Several studies, have suggested a direct role of the charge and orientation of His-18 in IAPP fibrillation. We propose that as in the orientation-2, His-18 is not free and is sterically hindered, therefore, fibrillation is suppressed. However, in the orientation 1 and 3, as His-18 is free for interaction with other IAPP monomers, thus facilitating fibrillation. At any given time, there is a mixed population of IAPP-ZnONP complexes with IAPP in different orientations on the ZnONP interface and the dominant population decides the fate of reaction and whether or not fibrillation takes place. Altogether, we propose that it is the orientation of IAPP which binds to the ZnONP, determines its amyloidogenic propensity.

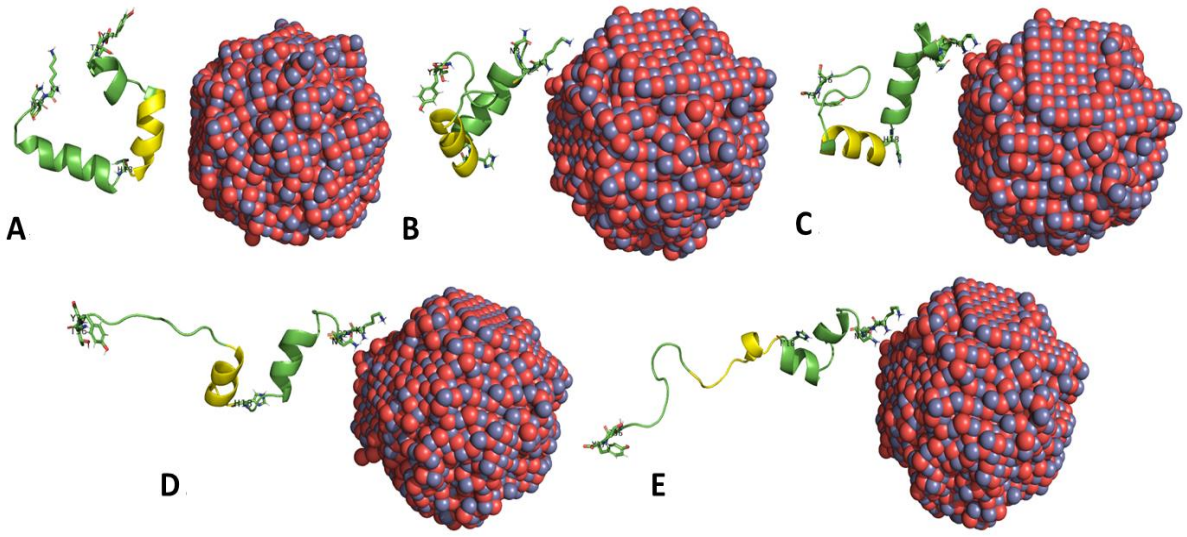

Figure 3.21. Snapshots of the MD simulations of IAPP-ZnONP complexes in orientation-3 at 0 ns (A), 25 ns (B), 50 ns (C), 75 ns (D) and 100 ns (E) of simulation, respectively. SRE region (SSNNFGAIL) is presented in yellow, and Residues 1, 2, 18, 36 and 37 are shown as sticks.

Additionally, we also analysed the various trajectories during the simulation runs. RMSD provides the information about the structural change in IAPP in presence and absence of ZnO NP with three different orientations (orientation 1, 2 and 3) respectively. Only IAPP (**Figure 3.22A**) showed initial fluctuations till 30 ns of simulation time. It stabilizes after 30 ns and maintains its stability till the end of 100ns time. In the case of IAPP in presence of ZnONP, a large deviation has been observed for IAPP with orientation 1 compared to the control simulation. Meanwhile IAPP with orientation 2 showed a similar trend with that of the control system. In the case of IAPP with orientation three, however, the IAPP showed a similar trend of fluctuation with that of control until 58ns. After 58ns of time, the second helix (residue 20-29) starts to elongate and moves away from the NP surface. Thus we can observe a sudden sharp peak around 58ns to 60ns after which it stabilizes till the end of the simulation. Similarly, RMSF analyses have also been performed. The RMSF plot shows that the residue stretch from 20 to 29 have higher fluctuation in case of IAPP - ZnONP conjugate (orientation 1, **Figure 3.22B**). IAPP in orientation 2 showed similar trend to that of the control system. In case of orientation 3, the RMSF of the residues are higher compared to all the other complexes, most probably because of the stretching of the peptide in this orientation as described above. Further, to understand the interactions between ZnONP and IAPP in different orientations, distance analyses were performed. From the plot **(Figure 3.22C)** it can be inferred that the second helix in orientation 1 was initially at a distance of 2.4nm

approximately from the ZnO NP which fluctuated till 50ns of simulation time. It attempts to stabilize after that time and remains at a distance of around 1.7 nm to that of NP. In the case of orientation 2, the selected helix remains at a distance of approximately 1.75nm throughout the simulation time, whereas in orientation 3, as the second helix stretches out and initiates to move away from the NP, a sharp peak in the distance plot can be observed for the event around 40ns time. It then stabilizes after 90ns of simulation time.

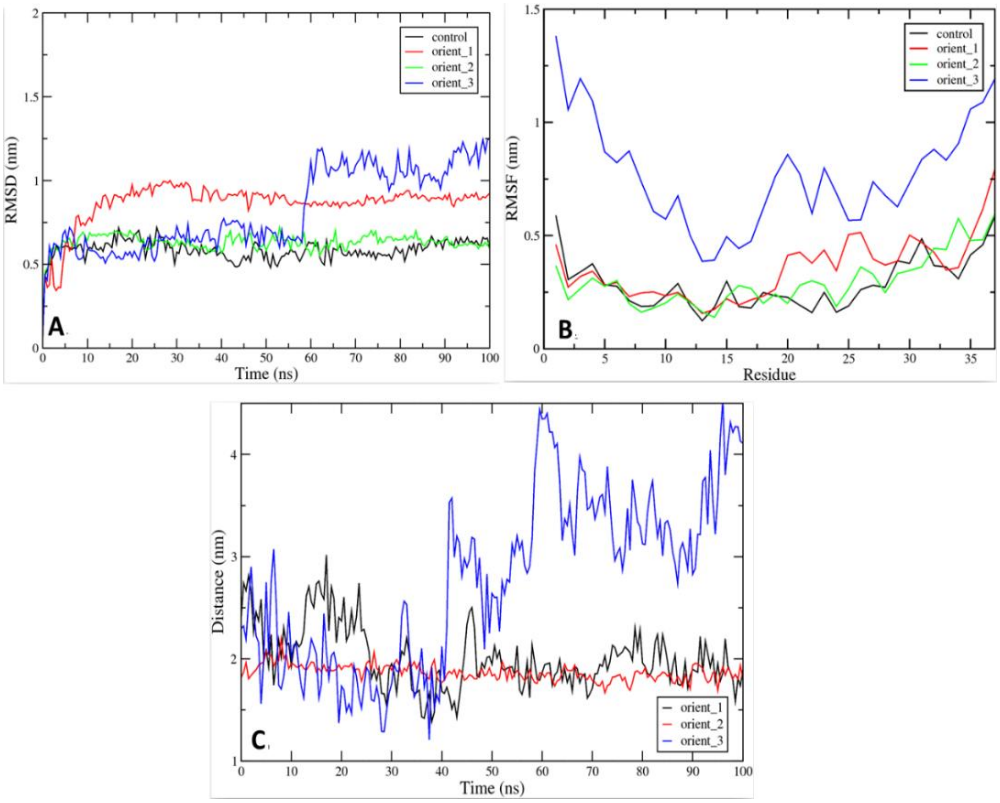

Figure 3.22. Trajectory analyses of MD simulations of IAPP-ZnONP complexes. (A) RMSD, (B) RMSF (control is shown in black, and the orientation 1, 2 and 3 are shown in red, green and blue respectively) and (C) distance plots for orientation 1, 2 and 3 (black, red and blue, respectively) from the ZnONP.

3.3.3.6 Cytotoxicity of IAPP fibrils: Alamar blue assay

Alamar blue assay results showed that when MIN6 cell lines were treated with fresh mixtures of IAPP alone and IAPP with increasing ZnONP concentrations, there was a significant reduction in the number of cells. Only ZnONP was not toxic to the cells **(Figure 3.23A).** More than 60% of the cells died depicting, for freshly added ZnONP, could not interact with IAPP. Hence could not reduce amyloid fibril-mediated cytotoxicity **(Figure 3.23B).** Therefore, the cell death by IAPP is independent of the ZnONP concentration used in the study. However, when IAPP was incubated with ZnONP previously allowing the interactions to take place, IAPP alone and IAPP with a low concentration of ZnONP did not

reduce the cell death. In contrast, IAPP incubated with 16 and 32 µg/mL of significantly reduced the cell death, and the percentage of viable cells remained at par to the control cells, further indicating a protective role of ZnONP in IAPP amyloid-mediated cell death **(Figure 3.23C).**

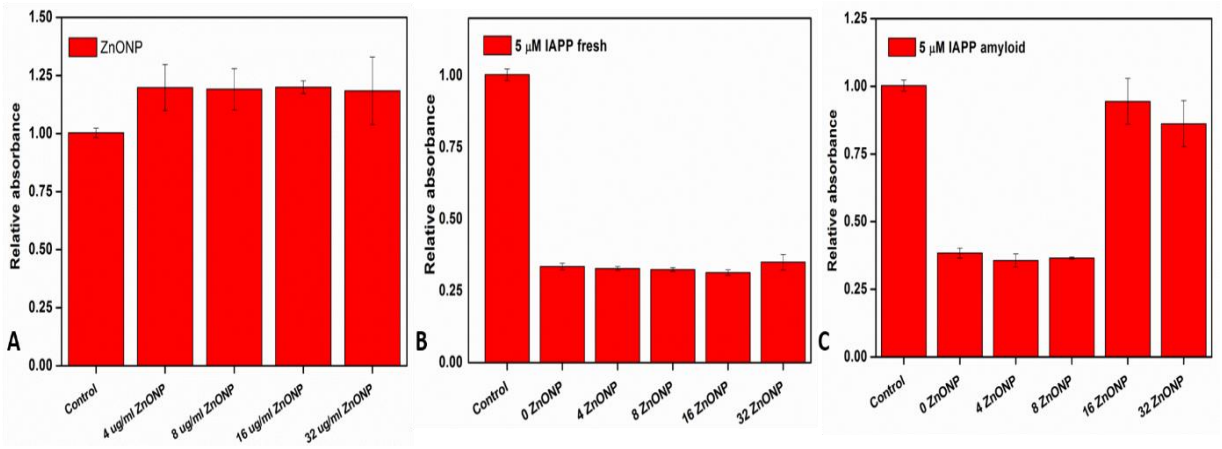

Figure 3.23. Alamar Blue assay for MIN6 cell viability on treatment with (A) only ZnONP, (B) fresh solution of IAPP-ZnONP and (C) amyloids of IAPP fabricated in presence of ZnONP.

3.3.4 Discussion

IAPP is one of the most amyloidogenic peptide known [221]. The fibrillation of IAPP has been studied in many different conditions by different groups for quite a long time now. IAPP as such exists as a random coil [109]. It shows transition into a somewhat molten globule-like conformation with exposed hydrophobic patches in presence of 4.25 M GdnHCl and 45°C before aggregation [289] and follows characteristic seeded aggregation kinetics [289, 294]. The fibrillation of IAPP involves the conversion from random coil state to β-sheet as demonstrated by CD and NMR studies [291, 295]. The fibrillation of IAPP is enhanced in presence of negatively charged biomacromolecules like heparin and negatively charged membranes, etc. [109, 132]. Rat IAPP (rIAPP) proves to be informative for studying intermediate conformations relating to human IAPP (hIAPP) as it forms the intermediate structures, similar to human IAPP, but does not form fibrils. In this context, it was shown that a considerable amount of α-helical content is present in the rIAPP, which might provide a link that formation of hIAPP fibrils are also preceded by a α-helix rich transient states [296]. Presence of α-helical intermediates for other amyloidogenic proteins including hIAPP is proposed [297, 298]. More recently, the presence of transient β-sheet intermediate has also been reported [295]. Aggregation prone sequences in IAPP's primary structure include amino acids 1-8, 8-20, 20-29 and 30-37 [299-301]. Of these, the sequence

from 20-29 is most widely studied and that mutations in these regions can significantly reduce self-assembly and fibrillation [302, 303]. With this knowledge, the search for successful inhibitors of IAPP fibrillation began. Inhibitors of IAPP fibrillation mostly comprise of peptide based inhibitors or small molecules inhibitors [304-306]. It was shown that a double methylated full-length analog of IAPP could block IAPP fibrillation at even nanomolar concentrations. Similarly, a methylated hexapeptide of the fibrillogenic core (22-27) of IAPP also inhibited fibrillation and apoptotic β-cell death [306]. Similar approaches of employing peptide and peptide based inhibitors have a useful strategy since then [307]. Apart from peptide based inhibitors, recently NPs have been extensively researched for their ability to inhibit IAPP fibrillation. Inhibition of IAPP fibrillation has been demonstrated by polymeric NPs (NiPAM: BAM) [271], polyethyleneimine-coated AgNPs, OH-Terminated PAMAM Dendrimer and grapheme oxide NPs. Inhibition of fibrillation of other amyloidogenic proteins by NPs have also been demonstrated in different studies [197, 308].

In the present study, ZnONP possessing an overall negative charge suppresses the fibrillation of IAPP, as confirmed by ThT dye binding assay. Secondary structural characteristics of IAPP-ZnONP complexes were probed by CD polarimetry. It was evident that the conversion of IAPP from random coil to amyloid fibrils involved a substantial amount of helical intermediates. After 4 and 24 hrs of incubation, samples in presence of ZnONP did not show any characteristics of amyloid specific β-sheet. The reduction of ellipticity in presence of ZnONP strongly suggests the interaction of IAPP with ZnONP. HAADF-TEM micrographs also supported the interaction of IAPP with ZnONP. Also, IAPP alone formed a dense network of fibrils, but in presence of ZnONP, very few fibrils were observed. Rather, small, rounded structures populated in presence of ZnONP as observed in the TEM. The interaction between IAPP and ZnONP is dependent on their charges. IAPP is positively charged at physiological pH and with the ZnONP being negative (-43 mV), electrostatic interactions could be quite possible between the two entities. Our studies support a recently proposed hypothesis that in order to form amyloids, peptide-peptide interactions must dominate compared to peptide-nanoparticle interaction [309]. In this context, the role of His18 in IAPP fibrillation has been already studied in detail, whereionized form of His18 at low pH prevents fibrillation rather than its uncharged form at neutral pH [231]. Here, in our case, the strong interaction between oppositely charged IAPP and ZnONP, dominates. MD simulations data suggested the importance of orientations in peptide-nanoparticle binding. Although all the three studied orientations studied, showed

fluctuations, these fluctuations were minimum in the case of 2nd orientation where His-18 continually remained interacting with the NP interface even at the end of 100 ns of simulations. Additionally, the point of interfacial interaction is in atomic proximity of the IAPP SRE region, indicating possibility of sterically-hindered ZnONP-mediated inhibition of IAPP fibrillation. In the case of orientation 1 and 3 huge fluctuations in the secondary structures were observed, which were even more prominent in case of the 3rd orientation where the whole IAPP structure gets opened up and extended away from the ZnONP. Thus it can be inferred that the interfacial interaction in 2nd orientation might reduce fibrillation by sterically hindering the self-assembly of SRE. Whereas in orientation 1 and 3 where due to relatively higher fluctuations, the SRE regions are exposed, that will not allow the hindrance, hence the peptide will self-assemble without any significant inhibitions. Thus, at a given point of time where IAPP and ZnONP exist in a solution, the orientation of IAPP which interacts with ZnONP and the population of the dominating complexes determine the IAPP's propensity to fibrillate. The protective role of ZnONP was also deduced from the cytotoxicity assay. Amyloids fabricated in presence of ZnONP, had a protective effect on MIN6 cell lines at 16 and 32 μg/mL ZnONP. Additionally, zinc, which is found in mill molar concentrations in pancreas, could significantly inhibit IAPP fibrillation *in vitro,* that also supports our finding. The interaction of ZnONP with IAPP might form other forms of aggregates incapable of forming typical fibrils. The presence of off-pathway intermediates has been involved in inhibition of IAPP fibrillation in a recent study [271]. ZnONP are usually non-toxic at low concentrations and have also been approved by the FDA, which might support its uses in therapeutics targeted against protein misfolding. Altogether, the study demonstrates the importance of interaction, orientation and concentration of ZnONP and IAPP in the fibrillation process of IAPP.

Chapter 4

Zinc oxide nanoparticle reduces α-synuclein fibrillation by stabilizing off-pathway intermediates

4. Zinc oxide nanoparticle reduces α-synuclein fibrillation by stabilizing off-pathway intermediates

4.1 Introduction

α-synuclein is a 140 amino acid long protein, abundantly found in the presynaptic areas of neurons [310]. It has been shown to be involved in the etiology of PD. PD is characterized by gradual loss of dopaminergic neurons from the substantia nigra of brain [36]. The hallmark of the disease is presence of proteinaceous lesions called lewy bodies, which stained positive for α-synuclein. Thereby, it was concluded that α-synuclein is present in substantial amount in the lewy bodies [311, 312]. Several evidences and studies have now confirmed that aggregation of α-synuclein is a critical step in progression of PD. The presence of α-synuclein was demonstrated in both soluble and membrane associated fractions of brain [313]. The aggregation of α-synuclein is speculated as a major cause of death of dopaminergic neurons [313]. Although the exact functions of this protein remain elusive, possible functions like involvement in vesicular transport and trafficking, fatty acid binding, prevention of lipid peroxidation and neuronal survival have been suggested [314].

α-synuclein is an IDPs in physiological conditions, *in vitro.* The protein is essentially divided into three regions. The N-terminus 1-60 amino acids, contains four 11 amino acid imperfect repeats, mainly consisting of a conserved hexameric motif (KTKEGV) [315]. The central region comprises of amino acids 61-95 that contains the aggregation prone non-amyloid-□ component (NAC), and the C-terminal region from 96-140 amino acids is highly rich in acidic residues and proline **(Figure 4.1)** [316]. The three highly conserved tyrosine residues are also located within C-terminus region [315]. The sequence of α-synuclein is also peculiar due to the fact that it is devoid of tryptophan and cysteine. The native disordered nature of α-synuclein is attributed to the low hydrophobicity and high negative charge density in the sequence [317]. The far-UV circular dichroism spectrum showed a random coil specific minimum around 196 nm, whereas in FT-IR spectrum the peak dominated by amide bond vibration at random coil structure (1650 cm^{-1}) [318-320]. The sedimentation, gel-filtration, dynamic light scattering, and small angle X-ray scattering results also well corresponded to the natively disordered conformation [320]. Additionally, several disorder prediction tools like PONDR VL3, VSL2 and IUPred also predicted it as completely disordered protein **(Figure 4.1)** [321, 322]. Being a IDPs α-synuclein is very dynamic, hence, the concept of protein chameleon was proposed for this protein. α-synuclein is suggested to conform into a number of different ensembles depending on its environment. At low pH, high temperature,

low concentration of organic solvents, TMAO and metal ions, α-synuclein is known to adopt to a pre-molten globule state [320, 323, 324]. In the presence of membranes, the N-terminus mostly attains an α-helical conformation, however, the acidic C-terminus remains in an unstructured form [325, 326]. In addition to these, α-synuclein has shown to adopt many other conformations including dimers and oligomers. These oligomers can be spherical, annular, ring shaped or protofibrils. Although, most of these oligomers are soluble, stable and non-toxic, some of them have been involved in forming the protofibrillar species during the early stages of fibrillation [327-329].

The aggregation of α-synuclein has been observed with two distinct morphologies, amorphous aggregates and ordered aggregation, also known as fibrillation. IDPs amyloid form fibrils by undergoing conformational transition from random coil to β-sheet rich structures. α-synuclein fibrils are formed by protofibrils arranged in parallel, with amino acid side chains exposed to the outside of the β-sheets [330]. These amino acid side chains interdigitate giving rise to higher order structures called steric zipper [330]. The fibrillation follows a characteristic conserved pathway, wherein the monomers attain a pre-molten globule state. The fibrillation occurs via a nucleation dependent manner which is initiated by the formation of a metastable nucleus, essentially composed of oligomeric intermediates. Moreover, the fibrillation of α-synuclein is influenced by many factors like pH, temperature, salt concentration, organic solvents, metal ions, GAGs and the concentration of monomeric α-synuclein itself [51, 320, 331].

The aggregation of α-synuclein in PD is often linked to the death of neuronal cells. However, the exact causative species or conformers of α-synuclein remain elusive. Previous studies have shown that amyloid aggregates can permeate cell membranes. α-Synuclein oligomers have also been shown to bind lipid membranes, and disrupt membrane bilayers, resulting into pore formation [332-334]. Generation of ROS has also been proposed as one of the important mechanisms in α-synuclein fibrillation-mediated cytotoxicity [335]. To combat α-synuclein-mediated amyloidosis, the inhibition of α-synuclein fibrillation employing different small molecules likes EGCG, baicalein, curcumin, etc. have been suggested [336-338].

Zinc is an important element for the human body involved as a cofactor for many enzymes especially in the central nervous system [339]. Some studies have demonstrated zinc to enhance the fibrillation of α-synuclein, and others have reported high concentration of zinc in Parkinsonian brains, compared to their normal counterparts [320, 340]. Recently, the effects of various nanoparticle formulations on the aggregation of α-synuclein have also been demonstrated as NPs may act as artificial chaperones to help prevent amyloidogenesis. In this

context, conflicting results have been put forward. Very recently, two independent groups showed α-synuclein fibrillation enhancing effect of Au nanoparticle and silica NPs [193, 341]. In a different study, NPs were shown to promote fibrillation of β2-microglobulin by providing a platform for the protein fibrillation [191]. Present study explores the effects of increasing ZnONP interface on α-synuclein conformation and fibrillation. To this end, the interaction of α-synuclein with ZnONP interface has been analysed, followed by ThT assay and TEM to see the effect of interface on the protein fibrillation.

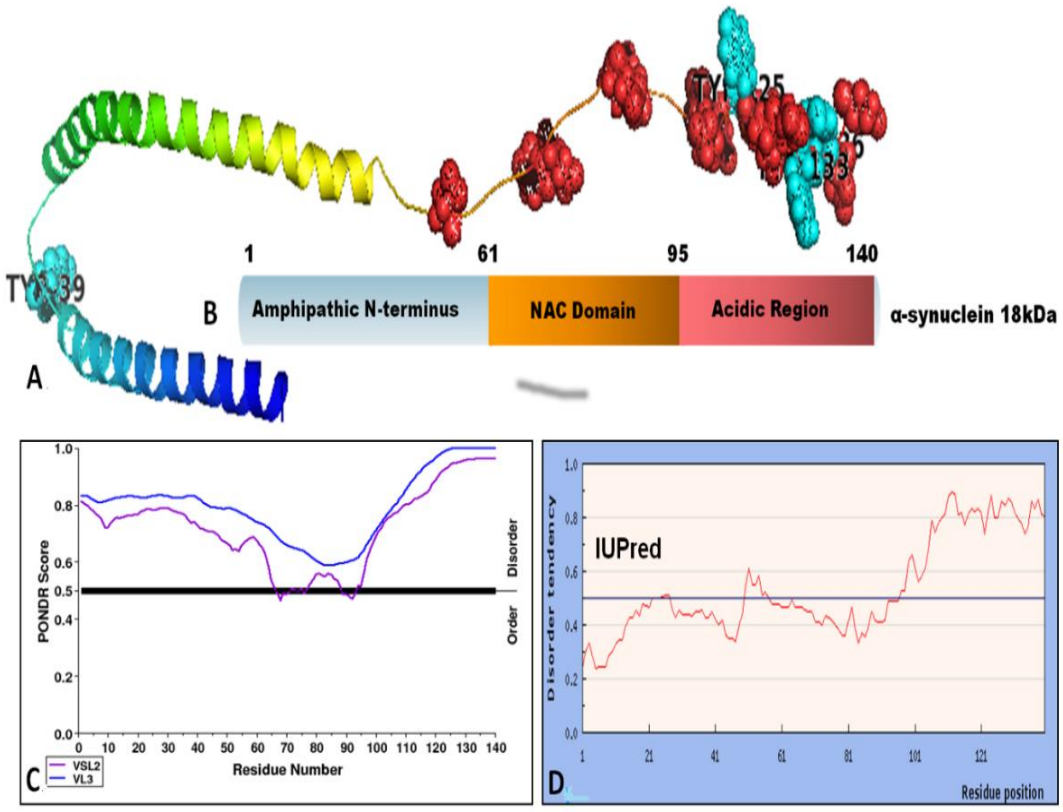

Figure 4.1. Structure and disorder prediction of α-synuclein. (A) Structure of α-synuclein in presence of SDS micelles (PDB ID: 1XQ8), acidic residues at the C-terminus are marked in red whereas tyrosines are represented in cyan. (B) Representation of the different domains of α-synuclein. Disorder predictions for α-synuclein sequence by (C) PONDR and (D) IUPred, respectively.

4.2 Materials and Methods

4.2.1 Materials

Plasmid encoding α-synuclein was purchased from Addgene. Phenylmethanesulfonyl fluoride (PMSF) and ampicillin were purchased from sigma. Hydrochloric acid (HCl), sodium hydroxide (NaOH), Sodium chloride (NaCl) were obtained from Merck. LB broth,

Isopropyl thio-β-D-galactoside (IPTG) and ammonium sulfate ($(NH_4)_2SO_4$) and Tris were procured from Himedia laboratories. Other chemicals and buffers were procured and used the same way as described in chapter-3.

4.2.2 Expression and purification of α-synuclein

α-synuclein was expressed in *E. coli* $BL21DE_3$ cells containing pET-28a plasmid encoding SNCA gene following a previously established protocol with slight modifications [342]. A 50 ml starter culture of $BL21DE_3$ harboring pET28a was inoculated in 600 ml LB media, with 100 μg/ml ampicillin. When its absorbance at 600 nm reached 0.6, the expression was induced with 1 mM IPTG for 5 hrs at 37 °C. Following this, the cells were harvested by centrifugation at 7500 rpm, 20 minutes. The pellet was dislodged in 20 mM Tris, 5 mM EDTA and 1 mM PMSF (pH 8.0) and lysed by ultrasonication on ice for 30 secs interval, 80 % amplitude for 30 minutes. The non-α-synuclein proteins were removed by heat treatment at 90 °C for 10 minutes, followed by centrifugation at 14000 rpm for 30 minutes. After this, α-synuclein was allowed to precipitate by the addition of $(NH_4)_2SO_4$ to 50 % saturation at 4 °C for 6-8 hrs followed by centrifugation at 14000 rpm. The pellet obtained was suspended in 20 mM Tris, 1 mM EDTA (pH 8) and dialyzed in 2 liters of the same buffer overnight. Following this, the lysate was allowed to bind to Q-sepharose and then eluted with increasing NaCl concentrations (100-500 mM) [343]. The eluents were checked for the desired protein on 13 % SDS-PAGE **(Figure A11)**. Fractions containing pure fractions were dialyzed to remove salts and lyophilized and stored at -20 °C until further use.

4.2.3 ZnONP synthesis and characterization

ZnONP was synthesized and characterized as described in chapter 3, section 3.3.2.2, and used as such for further studies.

4.2.4 Preparation of ZnONP- α-synuclein conjugates

The preparation of ZnONP- α-synuclein conjugates was performed by mixing 10 μM of α-synuclein with requisite amounts of ZnONP (0, 0.8, 4, 8, 16 and 32 μg/mL) in a total of 1.5 ml in phosphate buffer and incubated at 25 °C for 10-12 hrs to ensure equilibrium. Following this, the conjugates were characterized by SPR peaks by UV-Visible spectroscopy from 200-600 nm and the presence of elements in the conjugates was performed by HADDF-STEM in an FEI Tecnai TF30 G2 supertwin TEM. Furthermore, the zeta potential of the conjugates was measured by incubating the highest concentration of ZnONP i.e. 32 μg/mL with increasing concentrations of α-synuclein (0-10 μM). The reaction mixture was incubated for

10-12 hrs before measuring the zeta-potential at 25 °C by zeta analyzer (Malvern Zetasizer, Nano ZS90, Netherland).

4.2.5 *In-silico analysis* of α-synculein and ZnO interaction

In order to analyse the interaction between α-synuclein and ZnO, we further performed blind docking studies using Autodock 4.2 [344]. α-synuclein (PDB: 1XQ8) was taken as the receptor and ZnO molecule as the ligand. The grid box was prepared as such to accommodate the whole structure of receptor in it. Protein was prepared by adding Kollman charges and merging non-polar hydrogen atoms. Ligand was applying Gasteiger charges and merging non-polar hydrogen atoms. After docking, 5 clusters were generated depending upon the binding energy. Best pose of each cluster was viewed in PyMOL [245] and the interactions were analysed by Ligplot [246].

4.2.6 Isothermal Titration Calorimetry (ITC)

Isothermal titration calorimetry was performed on a microcal iTC 200 instrument (GE healthcare). α-synuclein was titrated into the cell containing 32 μg/mL (16.3 pM) of ZnONP. 20 injections of 2 μL each were added to the ZnONP solution. The spacing between two consecutive injections was 120 seconds and the mixing speed was 200 rpm. Two concentrations of α-synuclein i.e. 10 μM and 25 μM were used in two separate experiments respectively. The parameters and the plot were then fitted by using the software provided with the instrument (origin 8).

4.2.7 Time-resolved fluorescence

Fluorescence lifetimes measurements of the α-synuclein samples with and without ZnONP were performed on an IBH 5000F Nano LED equipment (Horiba Jobin Yvon, Edison, NJ in the time-correlated single photon counting (TCSPC) mode. 10 μM of α-synuclein was used in each case with increasing ZnONP concentrations as mentioned above. In the absence of tryptophan, tyrosine was excited at 276 nm and the emissions were recorded at 309 nm. A slit width of 16 nm was used for each experiment. In order to minimize the signal to noise ratio, 10000 photon counts were collected for 100 ns. The data obtained was in terms of channel number, where each channel step corresponds to $2.683843*10^{-11}$ sec/channel. Thus, the x-axis from 0 to 1480 channels (time) corresponded to 0 to 40 ns of time window. The data points, in final representation, were presented in terms of time in nanosecond (ns) on x-axis and total photon counts on y-axis of the graph. Data were fitted to tri-exponential decay curves with low χ^2 values. Subsequently, the average fluorescence lifetime was calculated and plotted by the following equation.

$$\tau_{avg} = \frac{(\alpha_1 \tau_1^2 + \alpha_2 \tau_2^2 + \alpha_3 \tau_3^2)}{(\alpha_1 \tau_1 + \alpha_2 \tau_2 + \alpha_3 \tau_3)} \qquad \textbf{Equation 1}$$

4.2.8 Intrinsic fluorescence

Intrinsic fluorescence spectra of tyrosine residues within α-synuclein were measured in presence of different ZnONP concentrations at three time intervals i.e. 0 hour, 24 hrs and 48 hrs. This experiment was performed on an LS-55 Perkin Elmer spectrofluorimeter in a 10 mm cuvette, with a slit width of 5 nm each for excitation and emission filters and scan speed 100 nm/min. The emission spectra were recorded between 300-400 nm with an excitation wavelength of 276 nm and each spectrum was an average of three accumulations.

4.2.9 Thioflavin T assay

The stock solutions of ThT, ZnONP and α-synuclein were prepared in 10 mM phosphate buffer (pH 7.4). 50 μM of α-synuclein was used for fibrillation assay and final ThT concentration was 75 μM. The final reaction volume was 200 μl and was performed in triplicates. The samples were incubated for 48 hrs at shaking conditions before setting up fibrillationreaction the multimode plate reader. The fibrillation was set-up in a 96-well clear, flat bottom plate at 25°C in shaking conditions in a Synergy H1 multimode plate-reader (Biotek, USA). ThT was excited at 440 nm and the emission was recorded every 20 minutes at 490 nm for 72 hrs. Lag times were obtained from the value at *x* axis at the intersection of lag phase baseline slope and the slope of the steepest part of the exponential phase. Rate of fibrillation was calculated by fitting the early exponential part of the growth curve to the exponential function $y = a + b * exp(-kx)$ in Origin Pro [132]

4.2.10 Circular Dichroism polarimetry

CD polarimetry measurements were performed in the far UV range (190-260 nm), with 10 μM α-synuclein with or without the presence of varying concentration of ZnONP in 1 mm cuvette in a JASCO- J1500 CD spectropolarimeter purged with N_2 gas, and equipped with a Jasco Peltier-type temperature controller system. Experiments were performed at 25°C and three time points (0, 24 and 48 hrs) to analyze the conformational changes in α-synuclein in the presence of ZnONP with time. Each spectra obtained was an average of three accumulations.

4.2.11 Transmission Electron Microscopy

α-synuclein was incubated with 32 μg/ml of ZnONP for 72 hrs. For TEM, only α-synuclein, incubated for 48 hrs (control) and α-synuclein with ZnONP were sonicated in a bath sonicator for 5 minutes. 20 μl of sample was mixed with 2 μL of 2% uranyl acetate alternative stain and was incubated for 10 minutes. The sample was then dropped onto carbon coated copper grids (Ted Pella Inc., USA) and allowed to be absorbed for 10 minutes, followed by washing with sterile MilliQ water. TEM imaging was performed on TEM-TECNAI T F 30 G2 Super Twin by FEI.

4.2.12 Cell culture and Alamar Blue assay

Cytotoxicity of α-synuclein amyloids and α-synuclein-ZnONP complexes was measured against imr32 neuroblastoma and monocytic THP-1 cell line through the Alamar Blue assay. Cells were seeded to a density of 10,000/100 μL well in a transparent clear-bottom 96-well plate containing MEM medium with 10% fetal bovine serum, 1000 units/mL penicillin, and 100 g/mL streptomycin for imr32 cells and 25,000/100 μL containing 1640 RPMI for THP-1 cells. After 24 h of incubation at 37 °C, in a humidified incubator with 5% CO_2 inflow, the spent medium was removed and replaced with fresh medium containing α-synuclein and α-synuclein-ZnONP conjugates (both fresh mixtures and conjugates incubated for 5 days at 25°C, shaking). The cells were incubated for another 24 hrs followed by the addition of fresh media containing 10% (v/v) Alamar Blue. Fluorescence was measured using excitation and emission wavelengths of 544 and 590 nm, respectively in synergy H1 multimode plate reader.

4.3 Results

4.3.1 Characterization of the adsorption of α-synuclein over ZnONP

The adsorption and binding of α-synulcein to ZnONP was initially studied by UV-Visible spectroscopy, HAADF-STEM mapping and zeta potential analysis. UV-Visible spectroscopy has been used to characterize the interaction between proteins and NPs in many previous studies [186, 345]. **Figure 4.2A** depicts the absorption spectra of 10 μM α-synuclein with increasing ZnONP concentration. The SPR peak of ZnONP is not detectable due to very low concentration. However, the peaks specific for the tyrosine residues in α-synuclein clearly indicate an increase in absorption maxima of α-synuclein with increase in the ZnONP concentration. In presence of 32 μg/mL ZnONP, the complex precipitation is anticipated to decrease the absorbance intensity at 263 nm. Here since the concentration of α-synuclein is kept constant, increase in the absorption could be due to the increased exposure of tyrosine

residues upon conjugation and/or increased effective local concentration of protein upon adsorption at the interface. In addition to this, the UV-Visible spectrum for α-synuclein with 32 μg/mL ZnONP was also accompanied by a significant bathochromic shift from 255 to 260 nm and peak broadening, further suggesting a conformational rearrangement of α-synuclein in presence of ZnONP. As α-synuclein is an IDP, an increase in interaction of amino acids flanking tyrosine or tyrosine itself with the negative potential ZnONP interface is likely a plausible explanation for the increase in absorption with increasing ZnONP interface. Other than this, a previous study has also linked this kind of behaviour with the formation of a ground state complex between the protein and nanoparticle [345]. HAADF-STEM mapping, provides a powerful and reliable method for mapping elements in a sample [293]. We incubated α-synuclein with 32 μg/mL of ZnONP for 12 hrs before mapping. The image **(figure 4.2B)** shows zinc in red colour, which is in atomic proximity of other elements generally present in protein like nitrogen, oxygen and sulfur. The observation indicated the interactions prevailing between ZnONP and the protein.

For zeta potential analysis, 32 μg/mL ZnONP was incubated with increasing concentrations of α-synuclein (0-10 μM). Deionized water was taken as a control in order to ensure that phosphate ions from the buffer do not affect the neutralization. **Figure 4.2C** showed the changes in zeta potential in both deionized water and phosphate buffer. In both the mediums, there is a gradual decrease in the zeta potential values with an increase in α-synuclein concentration. α-synuclein has a net negative charge at physiological pH, and the nanoparticle interface has negative potential. Hence, if the protein is interacting with the interface, as observed, the protein polar interface must be interacting with the nanoparticle negative interface with exposed negatively charged C-terminus flanking from the nanoparticle surface, resulting in higher negative surface potential with increase in α-synuclein monomers adsorbing onto the nanoparticle interface. As observed in neutralization study, the interface potential eventually becomes more negative, and saturates when the adsorption attains equilibrium. However, the N-terminus is rich in lysine residues which form a part of the consensus sequence (KTKEGV), and could be responsible for establishing strong electrostatic interactions between α-synuclein and ZnONP. Thus, the observation suggested while positive and polar amino acids bestow strong electrostatic interactions with nanoparticle interface, thereby provides a suitable binding platform between the two entities, negatively charged residues provide stability to the overall conjugates. In addition to electrostatic interactions, other interactions that prevail between the nano-protein interface,

like salt linkages, van der Waals interaction and hydrophobic interaction, also play important roles in the surface properties and stability of the conjugates.

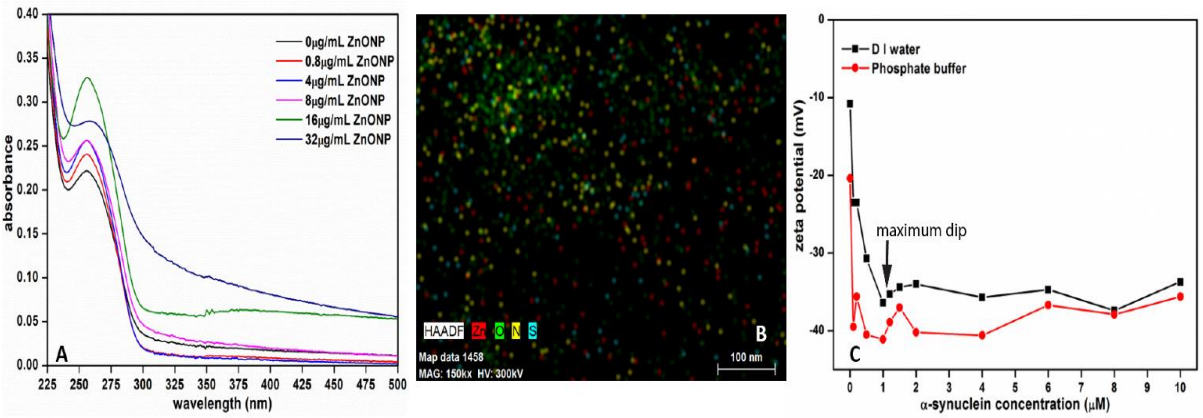

Figure 4.2. Characterization of α-synuclein adsorption onto ZnONP interface. (A) UV-Visible spectroscopy, (B) HAADF mapping and (C) zeta potential analysis showing the maximum dip in surface potential in presence of 1 to 2 µM α-synuclein.

4.3.2 *In-silico* analysis of α-synuclein-ZnO binding

Keeping in the mind the affinity of α-synuclein for ZnONP, docking between them were performed. *In-silico* analysis of α-synuclein-ZnO interaction by autodock revealed 5 clusters/probable binding sites of ZnO within α-synuclein with different binding energies. The binding energies for these clusters ranged between -1.59 and -1.82 Kcal/mol represented in **figure 4.3A and table-4.1**. Different clusters of ZnO are shown to be distributed all through α-synuclein and especially amino acids from 1-3, 39-44, 98-100 and 115-117 are shown to be in very close proximity of ZnO. Interacting amino acids were analysed by ligplot and are Met1, Asp2, Met5, Tyr39, Val40, Lys43, Lys 97, Asp98, Gln99, Leu100 and Met116 **(Figure 4.3B-F)**. Lys97-Leu100 are close to the SRE region of α-synuclein, suggesting an involvement of SRE during interaction with ZnO.

Table 4.1. Binding energies of different clusters generated during α-synuclein-ZnO interactions.

Cluster Rank	Mean binding energy
1	-1.82 Kcal/mol
2	-1.75 Kcal/mol
3	-1.70 Kcal/mol
4	-1.66 Kcal/mol
5	-1.59 Kcal/mol

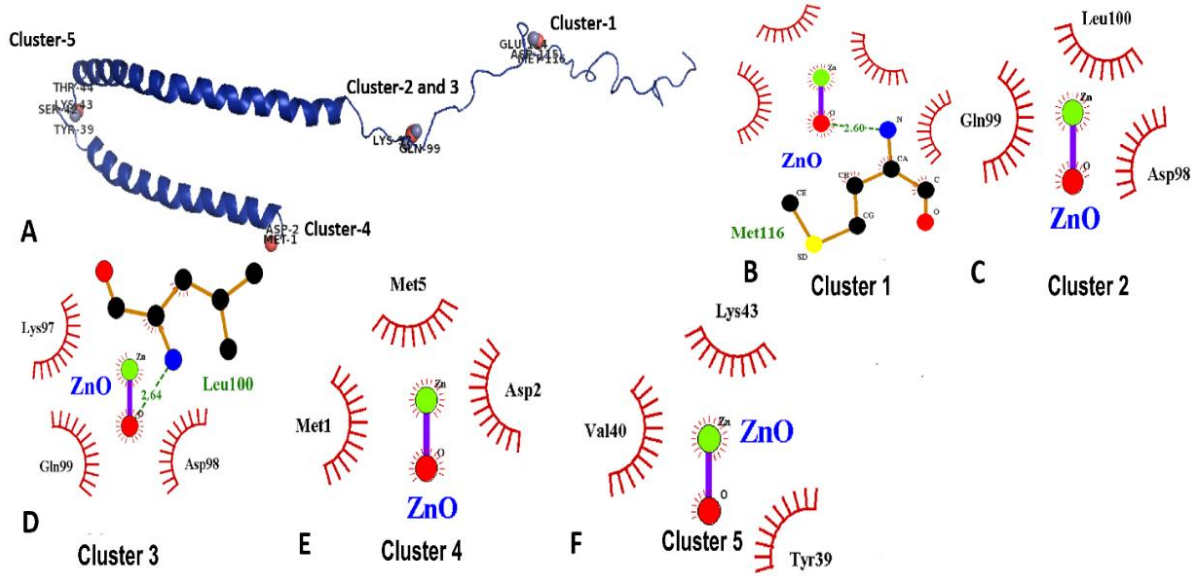

Figure 4.3. *In-silico* analysis of α-synuclein binding with zinc oxide (ZnO) molecule. (A) α-synuclein (IXQ8) showing different clusters of ZnO binding, and (B-F) ligplot analysis of the best five docked clusters, cluster 1 to cluster 5.

4.3.3 Isothermal titration calorimetry

Isothermal titration calorimetry is a technique to analyze the thermodynamic of binding/interaction between two molecules [346, 347]. Some of the previous studies have extensively used ITC for characterization of interactions between ZnONP with model proteins like lysozyme and lactalbumin [187], ToxR protein [188] and bovine serum albumin [186]. In our study 32 μg/mL ZnONP was titrated with 10 and 25 μM α-synuclein in two different experiments, respectively. As shown in figure 4, the upper panel showed the heat evolution for each injection of titrant (α-synuclein), while the bottom panels show the heat flow per mole of the titrant versus protein: NP ratios. In figure 4.4, negative heat evolutions in the thermograms imply the binding as an exothermic process. Also the decrease in the heat changes with each injection indicates a slow saturation of the interaction. In case of 10 μM α-synuclein, the heat evolved is around 1300 Kcal/mol, although saturation is not attained. However, with 25 μM the heat change is around 1000 Kcal/mol that becomes constant towards the end of the titration suggesting saturation of the binding sites. Hence, the data indicate that the nanoparticle interface saturates with 2 μM of α-synuclein. This is also concurrent with the ζ-potential neutralisation results, where the neutralisation reached a saturation point 1-2 μM of α-synuclein. The data for 10 μM α-synuclein fits to a single binding site scheme, whereas for 25 μM, the data was fitted in a three site sequential model,

depicting cooperativity in the binding. Enthalpy (ΔH) and entropy (ΔS) values for 10 μM α-synuclein were found to be $-1.13*10^{11}$ KCal/mol and $-3.78*10^{8}$ KCal/mol/deg, respectively. In case of 25 μM, the values of entropy for the first site was found negative, while for the other two sites were positive (Table 4.2). The values for both 10 and 25 μM α-synuclein suggest that the interactions between α-synuclein and ZnONP are enthalpically driven for the 1st binding site, whereas in 25 μM α-synuclein, the binding is entropically driven for 2nd and 3rd binding sites. Results depict that the most dominant interactions between the two species are electrostatic, van der Waals forces and hydrogen bonding for 10 μM and 1st binding site of 25 μM, whereas an additional hydrophobic interaction play important contribution for 2nd and 3rd binding sites for 25 μM α-synuclein [348]. It is, thus, important to note that the positively charged lysine residues in the consensus N-terminal must play important roles in the interaction between the two entities as discussed in the previous section. Also the fact that α-synuclein is an IDP, which makes it dynamic and conformationally less restricted for interacting with the NPs, in comparison to other globular proteins that have well defined structures. Interestingly, the binding constant and free energy is also shown to increase with more α-synuclein titrated onto ZnONP interface, which might be indicative of high affinity of α-synuclein for ZnONP.

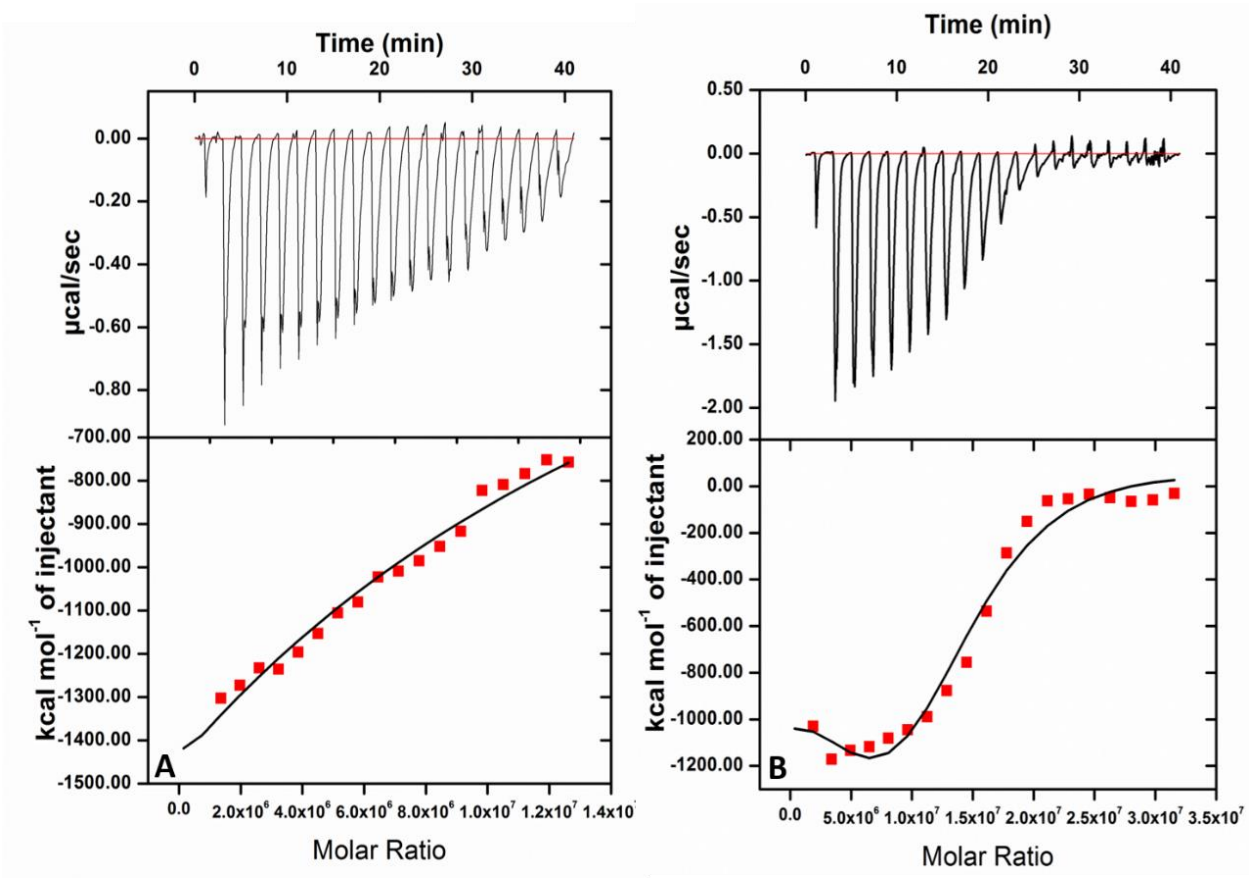

Figure 4.4. Isotherms depicting the interaction between α-synuclein and ZnONP, when 32 μg/ml ZnONP was titrated with (A) 10 μM and (B) 25 μM α-synuclein at 25 °C.

Table 4.2. Thermodynamic parameters, like enthalpy change, entropy change and free energy change of binding as observed from the ITC experiments.

α-synuclein concentration	**Stoichiometry (N)**	**Enthalphy (ΔH), Cal/mol**	**Entropy (ΔS), Cal/mol/deg**	**Binding constant (K), M^{-1}**	**Free energy change (ΔG), Cal/mol**
10 μM	1	-1.13×10^{14}	-3.87×10^{11}	77600	-6643.45077
25 μM	1 (1st site)	-1.08×10^{19}	-3.63×10^{16}	2	-408.9845624
25 μM	2 (2nd site)	5.51×10^{18}	1.85×10^{16}	71300	-6593.491434
25 μM	3 (3rd site)	5.33×10^{18}	1.79×10^{16}	1.64×10^{12}	-16595.29827

4.3.4 Time-resolved fluorescence

Time-resolved fluorescence measurements provide an important tool for studying the population distribution of a fluorophore in a particular excited state and the microenvironment around it [349]. We performed time-resolved fluorescence measurements on 10 μM α-synuclein with increasing ZnONP concentration. **Figures 4.5A and B** show the fluorescence lifetime decay spectra and the average τ respectively. The data were fitted to tri-exponential decay profiles and reveals an increase the average τ value up to 16 μg/mL ZnONP followed by an insignificant change at 32 μg/mL. The increase in the fluorescence lifetime with an increase in the ZnONP concentration confirms the absence of α-synuclein fluorescence quenching by ZnONP. An increase in the fluorescence lifetimes **(table 4.3**) are also attributed to the formation of either a stable complex between α-synuclein and ZnONP or the adsorption of α-synuclein over ZnONP and that the newly formed species spends more time in the excited state owing to its higher stability. Most of the previous studies have either shown either no change or static quenching of fluorescence in NPs in lactalbumin and bovine serum albumin respectively [187, 345]. This deduction is also in line with our discussions in the above sections.

Table 4.3. Fluorescence life times (τ) parameters of α-synuclein-tyrosine in presence of different concentrations of ZnONP.

ZnONP concentration	α1	τ1	α2	τ2	α3	τ3	**Avg. τ**
0	32.69	0.45	35.41	1.33	11.9	3.67	2.176138
0.8	29.95	0.41	57.72	1.27	12.33	3.55	1.959872
4	27.21	0.4	58.76	1.26	14.03	3.5	2.010858
8	25.2	0.35	55.96	1.22	18.83	3.8	2.410324
16	14.46	0.17	33.77	1.72	52.77	3.84	3.337831
32	16.33	0.13	34.72	1.89	48.94	3.99	3.434904

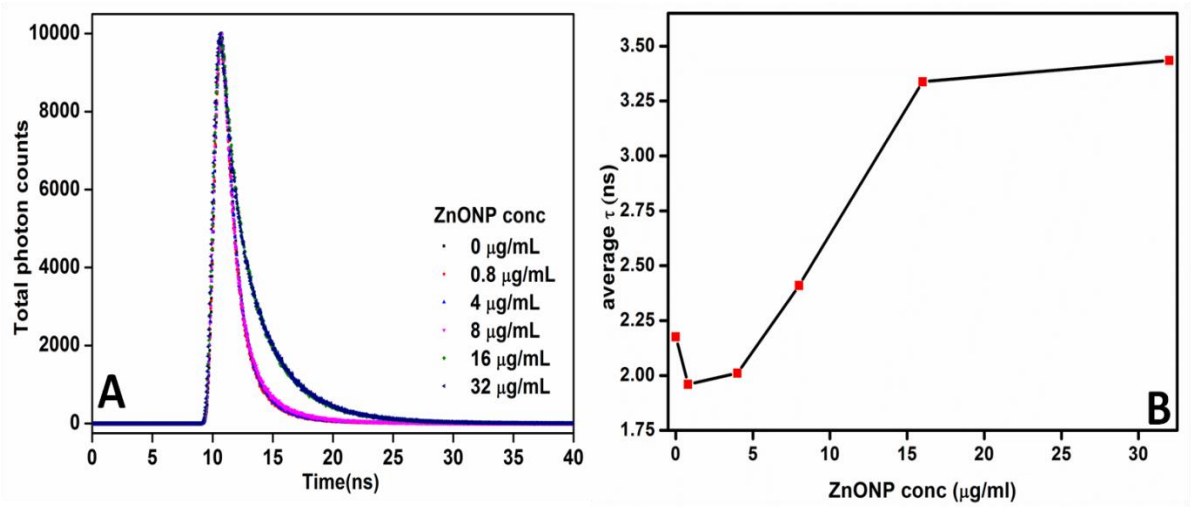

Figure 4.5. (A) Time resolved fluorescence of α-synuclein-tyrosine in presence of different concentrations of ZnONP interface, and (B) observed average τ value at each concentration of ZnONP.

4.3.5 Thioflavin T assay

ThT assay is one of the most important assays for assessing the formation of amyloids, as it is specific for binding to fibrils, sparing other forms of aggregates. We studied the amyloid fibrillation of 50 μM α-synuclein in presence of varying concentrations of ZnONP by ThT binding assay at 25 °C **(Figure 4.6A)**. The kinetics shows that the lag phase of 50 μM α-synuclein alone is around 70-72 hrs consistent with the previous reports [323, 350]. The lag phase is followed by an exponential phase that attains saturation at 108 hrs. In others, containing ZnONP the lag phase remained almost unchanged but the fluorescence intensity was significantly reduced compared to α-synuclein alone. Since the lag phase remains unaltered, it is clear that ZnONP do not affect the nucleation step, but the elongation phase is

altered. Results suggested that the growth rate (K), **figure 4.6B** of α-synuclein is highest compared to the ones in presence of ZnONP. However, as the reaction proceeds, α-synuclein monomers self-assemble to form fibrils. Whereas in presence of ZnONP interface, α-synuclein molecules interact favourably with interface to form stable complexes, hence the solution is left with relatively very less monomers. Initially due to molecular crowding the growth rate of samples containing ZnONP is very high, which is then followed by the formation of stable complexes between α-synuclein and ZnONP [331]. These complexes then get preferentially excluded from the solution, and do not form typical fibrils. The adsorption of α-synuclein onto the surface of ZnONP may divert the fibrillation process to other forms of aggregates. Therefore, the reduction in ThT fluorescence in presence ZnONP indicates the inhibition of α-synuclein fibrillation by ZnONP. Similarly, the reduction in ThT fluorescence of α-synuclein in presence of different phenolic small molecules has been directly linked to their property to inhibit fibril formation [337, 351-353]. Conversely, a study recently reported the enhancement of α-synuclein fibrillation in presence of Au NPs which was dependent on size of the studied NPs [193].

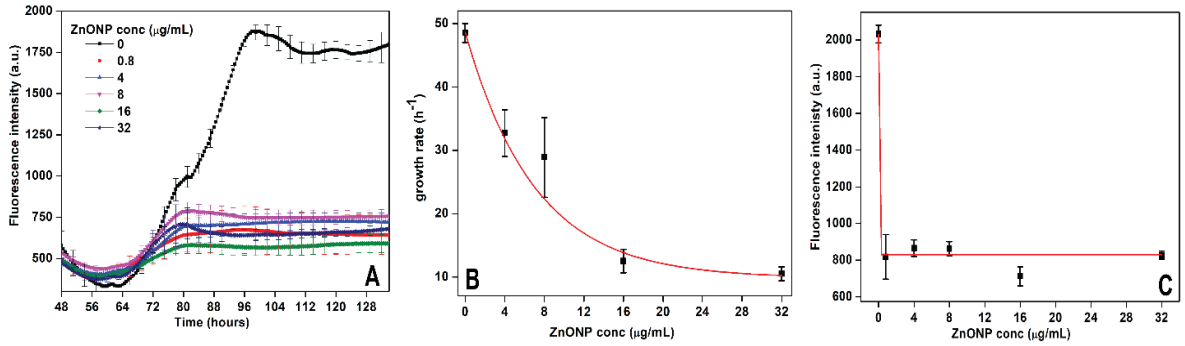

Figure 4.6. ThT dye binding assay for 50 μM α-synuclein fibrillation in presence of increasing ZnONP concentrations. (A) ThT was excited at 440 nm and emission was collected at 490 nm for a period of 48-130 hrs, (B) change in fibrillation growth rate and (C) change in maximum fluorescence intensity at plateau of α-synuclein fibrillation with increasing concentrations of ZnONP.

4.3.6 Changes in the microenvironment: Intrinsic fluorescence

Intrinsic tyrosine fluorescence of α-synuclein in presence of increasing ZnONP concentration were then measured at 0, 24 and 48 hrs, shown in **figure 4.7**. As α-synuclein is devoid of tryptophan, we probed the changes by following tyrosine fluorescence. Intrinsic fluorescence changes in amyloid proteins upon fibrillation or interaction with the probe, hence it is used to characterize the presence of early aggregates [354]. At 0 hr **(figure 4.7A)**, the fluorescence

emission maxima is at 309 nm, specific for the tyrosine residues. There is a little decrease in the fluorescence intensity of the samples containing ZnONP implying that, initially neither there is quenching of fluorescence nor any significant structural perturbations in α-synuclein. Significant changes in the tyrosine fluorescence may also be absent as α-synuclein is a random coil. In general, presence of NPs has been reported to quench the tryptophan fluorescence in proteins [186, 345]. After 24 hrs **(figure 4.7B)**, there is a concentration dependent decrease in the fluorescence intensity at 309 nm for 0-8 μg/mL of ZnONP, whereas in 16 and 32 μg/mL ZnONP there is a pronounced bathochromic shift in the emission maximum from 309 nm to 314 nm, accompanied with the decrease in fluorescence. This red shift suggested changes in the microenvironment of tyrosine and structural perturbations, upon interaction of α-synuclein with the ZnONP surface. Moreover, the shift is also due to hydrogen bonding of acidic amino acids to the tyrosine hydroxide, related to basicity of the acceptor as explained in a previous study [355]. After 48 hrs **(figure 4.7C)** of incubation, no significant changes were observed in the spectra of samples containing 0, 0.8 and 4 μg/mL of ZnONP. However, α-synuclein with 8, 16 and 32 μg/mL of ZnONP showed a pronounced increase in the fluorescence intensity accompanied by a relatively stronger bathochromic shift to 335 nm. This peak at 335 nm is specific for the presence of tyrosinate ions in proteins. It is usually centred around 330-350 nm, and characterized by an hyperchromic shift in the fluorescence intensity [356]. The appearance of tyrosinate peak has been suggested to originate from an excited state tyrosine proton transfer from the phenolic hydroxyl to other proton acceptors present in atomic vicinity [356]. We, however, did not observe the presence of dityrosine till 48 hrs. Souza *et al* have reported the presence of dityrosine linkages in stable α-synuclein oligomers in the lewy bodies [329]. Our data suggested that high ZnONP concentration induces the formation of stable oligomers which interact with ZnONP, and get arrested in this particular conformation, making it unavailable to form full fibrils. This could be a plausible explanation for the low fluorescence intensity in the ThT binding assay. Also, as it is seen that none of the tyrosine residues are present in the amyloidogenic core of α-synuclein, it is clear that these tyrosine residues are involved in other non-native type of interactions with ZnONP interface, thereby stabilizing the oligomeric forms.

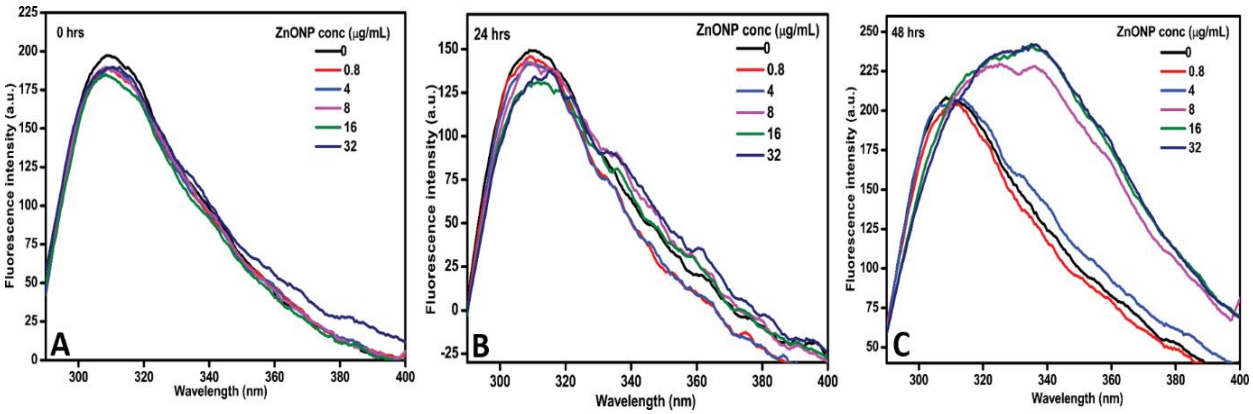

Figure 4.7. Changes in the intrinsic fluorescence spectra of 10 µM α-synuclein in presence of varying ZnONP concentrations at (A) 0 hrs, (B) 24 hrs and (C) 48 hrs of incubation. Tyrosine was excited at 276 nm and emission spectra were collected from 295 to 400 nm.

4.3.7 Changes in the secondary structure: Circular Dichroism (CD)

Figure 4.8 shows changes in the secondary structure of α-synuclein in presence of increasing concentration of ZnONP interface, at 0 hr, 24 hrs and 48 hrs, respectively. Consistent with previous studies, α-synuclein was found to be an unstructured, random coil with a minimum around 198-200 nm [357]. Initially, **(figure 4.8A)**, we observed that intact α-synuclein has an ellipiticty at 198 nm, with amplitude of -25 millidegrees. As the concentration of ZnONP is increased, there is an increase in the ellipticity; the one with the highest ZnONP (32 µg/mL) had an ellipticity -48 millidegrees. This indicates that in presence of ZnONP the natively disordered α-synuclein adsorbed onto the surface of ZnONP. It is conformationally restricted for adopting changes in its structure. As more ZnONP is available, there is an enhanced local concentration of α-synuclein, thereby an increased ellipticity is observed. After 24 hrs **(figure 4.8B)** of incubation, the spectra remained almost same, with insignificant changes in the ellipticity compared to 0 hr. However, at 48 hrs **(figure 4.8C)**, some significant changes were observed. It was observed that the ellipticity of only α-synuclein remained same accompanied by a slight red shift whereas in samples containing ZnONP, there was a pronounced decrease in the ellipticity in a concentration dependent manner, and the one with 32 µg/mL almost reduced to -3 millidgrees, compared to -48 millidegrees at 0 hr. The reduced ellipticity and visual examination of the samples revealed formation of amorphous aggregates with ZnONP that sediment to the bottom of tubes, further indicating that the complex formed on adsorption of α-synuclein, as some of the forms of α-synuclein intermediates are sticky in nature[358]. The formation of flocs of α-synuclein with poly(allylamine hydrochloride)

coated AuNP has been reported earlier [359] and the formation of these flocs have been linked to the formation of reversible aggregates, preceding fibrillation [360].

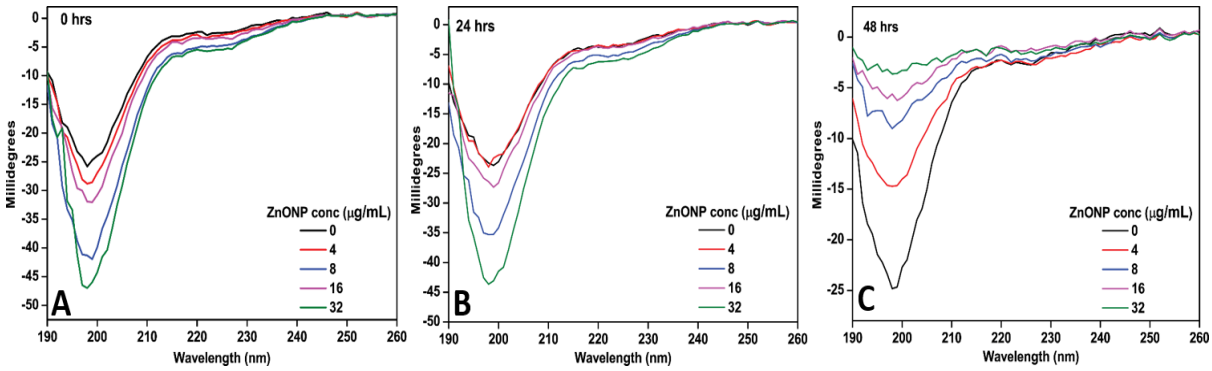

Figure 4.8. Changes in far-UV CD spectra of 10 µM α-synuclein recorded from 190-260 nm in presence of varying ZnONP concentrations at (A) 0 hrs, (B) 24 hrs and (C) 48 hrs of incubation.

4.3.8 Transmission Electron Microscopy (TEM)

Based on the above results and to further gain insights into the structure and morphology of the aggregates formed, we performed TEM on α-synuclein and α-synuclein with 32 µg/ml ZnONP. Figure 4.3.2.4 shows the fibrils formed by α-synuclein in the absence of ZnONP. The fibrils are linear about 5-7 nm thick and around 25-30 nm in length after 48 hrs of incubation **(Figure 4.9A).** These fibrillary structures are also reported in previous studies [324]. In the presence of 32 µg/mL ZnONP also **(Figure 4.9B and C)**, the aggregation of α-synuclein over ZnONP is evident. However, typical independent fibrillar structures are not observed. α-synuclein is seen to be adsorbed on ZnONPs **(Figure 4.9B)** surface and forming very small prefibrillar aggregates that are brought together in a mesh like structure through interactions with the ZnONP surface. Thus, we assume, while ZnONP acts as a platform for the adsorption of α-synuclein, α-synuclein molecules interact with each other and the ZnONP giving rise to large aggregates that may form flocs. Here, the concept of molecular crowding comes into play, as how presence of ZnONP may affect the α-synuclein's property to form typical long fibrillar structures [331, 361].

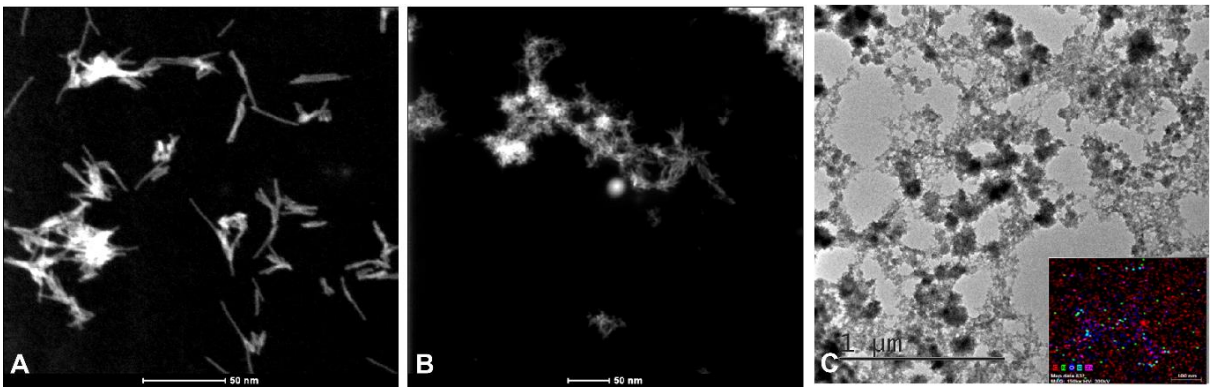

Figure 4.9. TEM micrograph of (A) α-synuclein incubated for 48 hours, (B) α-synuclein with 32 µg/mL ZnONP showing the morphology of the aggregates, and (C) α-synuclein incubated in presence of 32 µg/mL ZnONP at relatively lower resolution. α-synuclein is shown to form mesh like structures in presence of ZnONP, where ZnONP is seen as dark/black spots.

4.3.9 Alamar Blue assay

Alamar Blue assay uses a resazurin dye to probe the metabolic status of cell. Effectively viable eukaryotic cells maintain a reducing environment, while non-viable cells produce an oxidizing environment within themselves. The resazurin dye, being a cell permeable weakly fluorescent dye, gets irreversibly reduce by intracellular metabolic reductants like NADPH/NADH that are engaged with electron transport chain and other metabolic processes in viable cells into a relatively highly fluorescent resorufin dye. Hence, the dye has often been used to probe cytotoxic potential of an additive on viable cell [210]. Interestingly, considering nature of the assay, ZnONP (0-32 µg/mL) and α-synuclein in absence and presence of the particle interface showed a varying effect on viability of IMR32 and THP-1 cells **(Figure 4.10 and 4.11)**. The results showed that ZnONP causes significant IMR32 cell death (by 25 %, **Figure 4.10A**) at highest concentration (32 µg/mL) only. Whereas, lower ZnONP concentrations had insignificant effect on the cell viability. On the other hand, THP-1 cell viability consistently decreased with increase in ZnONP interface fraction in culture, with LD_{50} at 16 µg/mL. A recent study has also shown that largeer cells promote more NP uptake than small cells due to more available membrane surface for cell adhesion, while uptake volume per unit area of membrane is smaller than in small cells [362]. Additionally, when freshly incubated α-synuclein in absence and presence of varying concentrations of ZnONP were added to IMR32 cell culture, the cell viability significantly decreased by ~ 25 % **(Figure 4.10B)**. Although, the lower concentrations of interface (< 32 µg/mL) had insignificant effect on α-synuclein mediated cell death, which reduced the cell viability by ~ 25 %. However, 5 days incubated samples, by when the α-synuclein-ZnONP samples

flocculated, showed insignificant effect on α-synuclein-mediated cell death that reduced the cell viability by ~ 20 %, even in presence of the highest interface concentration **(Figure 4.10C)**. The observation indicated that the observed loss of cell viability is triggered by free α-synuclein fibrillation intermediate(s), which forms during the lag phase of fibrillation kinetics. The lag phase remains constant in both the kinetics, *i.e.* in absence and presence of the interface **(Figure 4.6A)**. Additionally, it has been shown that oligomers or fibrillation intermediates are relatively more cytotoxic than mature fibrils [363].

On the contrary, THP-1 cell, which was relatively more sensitive to ZnONP treatment, showed more viability or more reductive intracellular environment on treatment with fresh α-synuclein. Hence, when the cells were treated with increasing concentrations of ZnONP interface, insignificant change in viability is observed at lower concentrations, *i.e.* < 16 μg/mL, compared to untreated cells. The observation indicated that fresh α-synuclein reduces the ZnONP-mediated THP-1 cell death. However, like in IMR32 cells, 5 days incubated α-synuclein sample, *i.e.* α-synuclein amyloid, reduced THP-1 cell viability by ~ 20 %. The activation of THP-1 cells and subsequent inflammatory responses by soluble forms of α-synuclein have also been reported in another study [364]. Furthermore, the cell viability increased as ZnONP fraction in the 5 days incubated protein sample is increased, *i.e.* the flocculated α-synuclein-ZnONP samples did not show the fibrillation-mediated cell death. In fact, at highest flocculation, i.e. in presence of 32 μg/mL of ZnONP in 5 days incubated samples, the cell viability enhanced. The data, altogether, indicated that α-synuclein, which enhances THP-1 cell viability in monomeric form and causes cell death on fibrillation, retains the cell compatibility nature in ZnONP-mediated flocculated forms.

It has been reported that cell undergoing fibrillation-mediated death indicates enhanced-ROS level [335]. Following this, when the level of reactive oxygen species was studied, the data closely corroborated with Alamar Blue reduction assay. In case of IMR32, ROS levels were enhanced by 20 % for treated cells. Whereas, in THP-1 cells, the level of ROS in presence of ZnONP interface in 5 days incubated protein samples were relatively very less compared to α-synuclein amyloid treated cells and significantly higher than the untreated cells. The ROS levels in differently treated THP-1 cell corroborate with previous finding [364], indicating that as the α-synuclein monomer fractions more in floccs the ROS level reduces compare to the α-synuclein amyloid population treated cells. Thus, the data, altogether, indicate that

ZnONP interaction with α-synuclein causes flocculation of the complex, thus trapping the protein monomers in non-amyloidogenic forms.

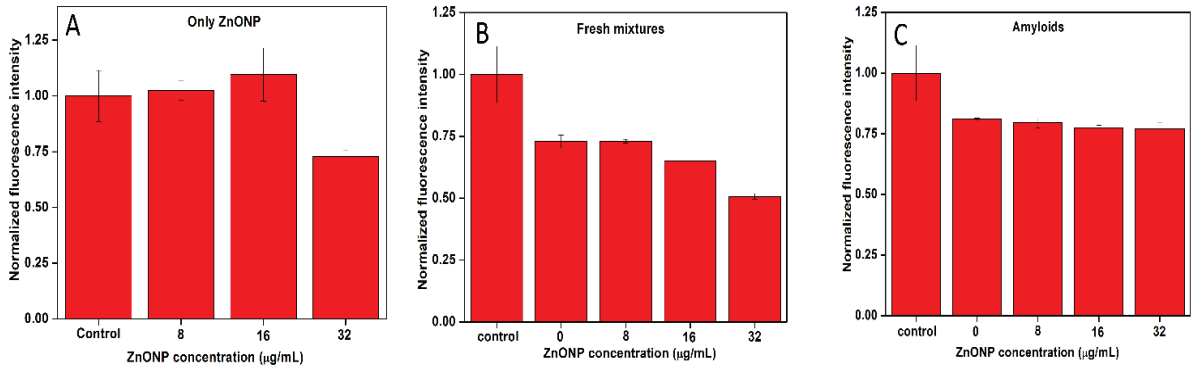

Figure 4.10. Alamar Blue assay for IMR32 neuroblastoma cell viability after treatment with (A) only ZnONP (0-32 μg/mL ZnONP), (B) fresh mixtures of α-synuclein with 0 to 32 μg/mL of ZnONP and (C) 7 days incubated α-synuclein-ZnONP complexes with varying ZnONP fraction.

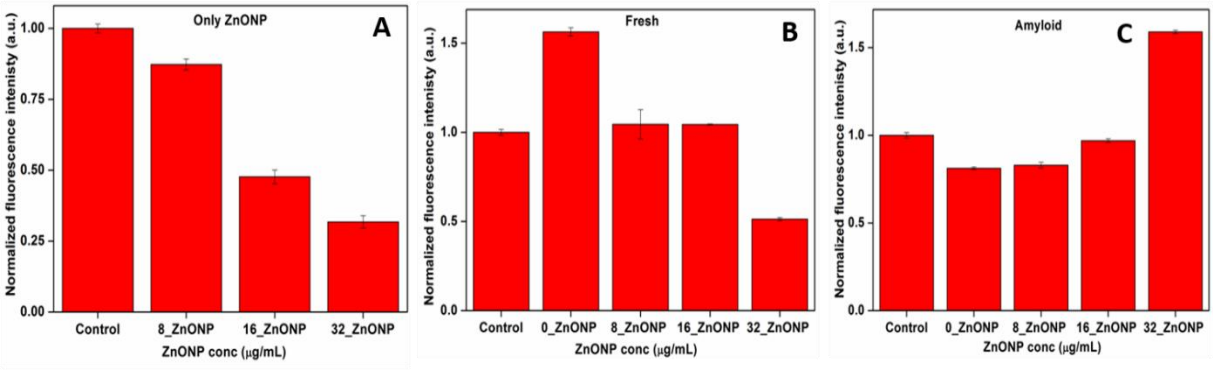

Figure 4.11. Alamar blue assay for THP-1 monocytic cell viability after treatment with (A) only ZnONP (0-32 μg/mL ZnONP), (B) fresh mixtures α-synuclein with 0 to 32 μg/mL of ZnONP and (C) 7 days incubated α-synuclein-ZnONP complexes with varying ZnONP fraction.

4.4 Discussion

Nanoparticles have found their far reaching applications in the field of biology and medicine. Some nanoparticles have shown promising results in specifically targeting cancer cells, chemical sensing and waste water treatment [365]. ZnONP has been specifically used in sunscreens, drug delivery, biomedical and biosensing applications. The most important features of ZnONP, making it suitable for biological uses, are its low toxicity and better biodegradability [86, 366, 367]. However, the use and efficacy of nanoparticles is being highly debated in lieu of its ability to cause aggregation of many proteins *in vitro* [95, 191].

Once inside a biological medium, a nanoparticle interacts with variety of proteins to form a corona. The interaction, thereby, affects protein structure [95]. In present investigation, we used negatively charged ZnONP to study its effects on α-synuclein fibrillation, a natively disordered protein. To this end, non-cytotoxic concentrations of ZnONP, as observed in different studies [368, 369], were taken to study its effect on α-synuclein conformation. Interaction between the interfaces indicated that protein has moderate affinity with the particle interface. However, at higher protein concentration, protein affinity enhances, which is likely because of stronger protein-protein interactions. α-synuclein has shown to attain sticky conformation in presence of certain interacting partners [358], which resulted in relatively higher exothermic binding at higher protein concentration. The conclusion was further supported by thermodynamic parameters extracted from ITC data fitting, which also indicated the nature of interaction. As indicated in Table 2, the second and third sequential bindings were enthalpy as well as entropy driven binding, as both were following favourable changes. Hence, the initial binding reduced conformational entropy, whereas the second and third sequential bindings enhanced the entropy. As observed from α-synuclein docking with Zn-O molecule and the change in tyrosine fluorescence life time and quantum yield with ZnONP concentration and time further indicated the protein-tyrosine residue involvement in the interaction. Interestingly, the tyrosine residue after 48 hrs of incubation ionizes to tyrosinate form possibly to form favourable stable interaction with other protein monomer or the particle interface. Coincidently, the time frame of tyrosine ionization and flocculation does not rule out the favourable interactions, involving tyrosine residues, between α-synuclein-ZnONP complexes resulting in flocculation. These flocculates are generally characterized as prefibrillar aggregates [360]. However, the ThT assay indicated that the flocculates are relatively non-fibrillating population within the studied time frame, i.e. up to 132 hrs, in studied conditions. TEM micrographs also indicated the mesh-like flocculates in the protein samples incubated with highest ZnONP fraction for 5 days. Whereas, the protein only samples showed fine amyloid-like structures in the micrographs. Thus, the data indicated that the enhanced conformational entropy on interaction with the nanoparticle interface and sticky nature of the protein are anticipated to kinetically trap α-synuclein in stable non-amyloidogenic structure in the form of flocculates (as described in Figure 4.12).

The intermediate(s) of fibrillation process is known to cause ROS-mediated cytotoxicity [335]. Neuroblast cell treatment with α-synuclein monomers and fibrils reduced the cell viability, as also reported in previous studies [193]. Additionally, α-synuclein monomers and

amyloid effect on reductive property of circulatory cell like THP-1 were established. THP-1 cells exposed to α-synuclein have shown to produce the factors that affected neuronal cell viability [364, 370]. Hence, when the activated monocytic cell (THP-1) treated with α-synuclein monomers showed enhanced resazurin reductive property, whereas reductive property decreased when treated with the protein amyloid. Interestingly, as flocculation happen at highest concentration of ZnONP interface, the incubated sample also enhanced the reductive property of THP-1 cells, i.e. the floccs affected THP-1 cells like the protein monomers did. The observation is indicating that either the protein present in floccs are acting as the monomer or the protein monomers are desorbing from floccs and positively affecting the cell reductive property. Nevertheless, enhanced ROS level was observed in the amyloid treated cells. Whereas, cells treated with floccs showed either enhanced cell viability in case of THP-1 cells or reduced ZnONP-mediated cell death. Taken together, the study suggested that the fibrillation is governed by physico-chemical properties of both the interacting interfaces, i.e. protein and nanoparticle interfaces, which predominantly determines the fate of the complex.

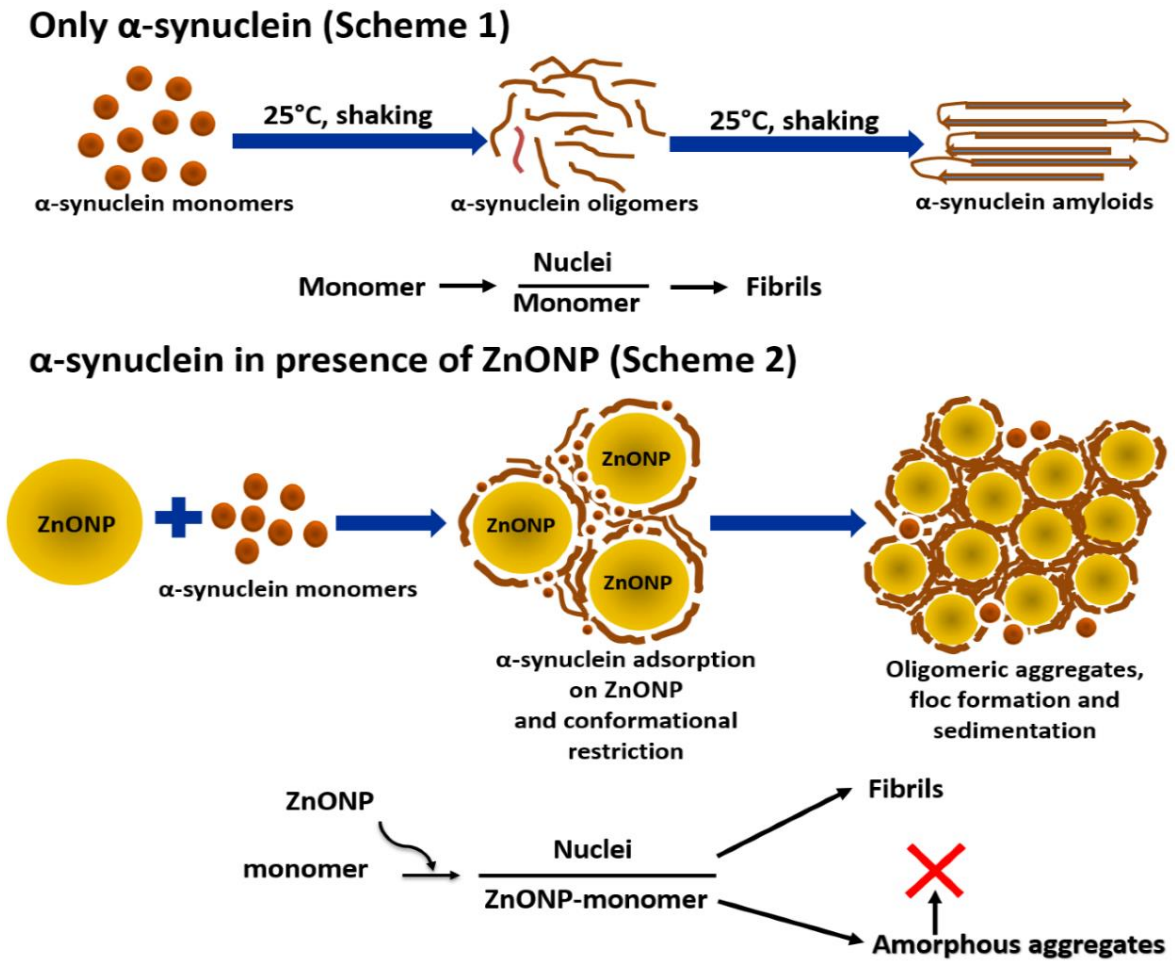

Figure 4.12. Graphical representation of the proposed ZnONP-mediated inhibition of α-synuclein fibrillation.

Chapter 5

Insulin adsorption onto zinc oxide nanoparticle mediates conformational rearrangement into amyloid-prone structure with an enhanced cytotoxic propensity

5. Insulin adsorption onto zinc oxide nanoparticle mediates conformational rearrangement into amyloid-prone structure with an enhanced cytotoxic propensity

5.1 Introduction

Injection localized amyloidosis is one of the 30 major disorders characterized as protein misfolding diseases [371]. Additionally, insulin amyloid deposits have also been observed in patients with type II diabetes mellitus [372], normal aging [373] and subcutaneous insulin infusions [374]. The subcutaneous insulin infusion resulting into amyloid deposit occurs when full-length insulin molecules assemble into amyloid fibril at the site of frequent injections, in patients suffering from Type I diabetes mellitus [374]. The insulin amyloid fibril formation is preceded by amorphous insulin aggregate that formed because of interactions between non-native insulin conformations [375]. Insulin is composed of 21 amino acids long A-chain and 30 amino acids long B-chain. Both chains are connected by 2 disulfide bridges, A7-B7 and A20-B19, with an additional intrachain disulfide bridge between A6-A11 in A-chain [376]. Secondary structure analysis of insulin shows that the A-chain is composed of two α-helices separated by a β-turn, whereas B-chain is composed of an α-helix, one β-turn, and one β-strand [376] **(Figure 5.1)**. The structure, normally, exists as a zinc ion coordinated hexamer complex at physiological pH. Each hexamer complex is composed of three dimers and two to four zinc ions. Zinc free insulin exists as dimers at low concentrations over a pH range of 2-8, and as tetramers at higher concentrations [377]. The amyloidosis of insulin depends on several factors like insulin concentration, temperature, agitation, pH, ionic strength, seeding and presence of additives like urea, sucrose, 1-anilinonaphthalene-8-sulfonic acid (ANS), trimethylamine *N*-oxide dihydrate (TMAO) etc. [378, 379]. It is recently demonstrated that both nucleation and fibrillation reactions are governed by non-covalent interactions, especially hydrophobic and electrostatic interactions, in insulin fibrillation [378, 379]. It is, further, shown that the initiation of insulin fibrillation is triggered by its monomeric state that undergoes a partially unfolded state, prone to fibrillation [380, 381]. Thus, it has been anticipated that, in certain conditions, the dissociation of hexameric insulin complex into its monomeric state is a rate-limiting step for insulin fibrillation. The conversion from hexamer to monomer, principally, results in exposure of hydrophobic residues those are normally buried in the native hexamer [381-383]. Insulin exists as a monomer at low pH, and most of the studies involving insulin fibrillation have been performed at low pH, < pH 2 [384-386]. The insulin fibrillation is one of the major

problems in commercial isolation and purification process, where the purification method involves exposure of insulin to acidic medium pH 1-3. However, most of the insulin fibrillation *in vivo* occurs at physiological pH, pH 7.4. Recently, there has been a report that studied the insulin fibrillation at physiological pH [387]. Notably, at physiological pH, insulin fibrillation is concentration dependent, and the amyloids formed have different morphology and cytotoxic propensity compared to the amyloid forms at low pH and/or heating [379, 387].

Apart from insulin amyloidosis, Alzheimer's disease (AD) caused by Aβ-42 misfolding, tops the list of protein misfolding diseases [388]. A recent study has shown the presence of endogenous nanoscale magnetite NPs in brain tissue sections of AD patients. Subsequently, it was proposed that endogenous magnetite NPs could be formed by the accumulation of airborne magnetite particulate matter in the brain [94]. Some NPs are small enough to access most parts of the body, including brain [389]. In a particular study, it has been suggested that titanium oxide NPs (TiONPs) up to 200 nm can have direct entry to the brain through axons of the olfactory nerves [390]. Likewise, ZnONP with positive surface potential passively diffuses through the reconstituted cell membrane [391]. Inside a biological system, NPs interact with different components of cells including lipid-rich membranes, nucleic acids, and proteins, establishing a nano-bio interface [392]. In this context, Prof. Dawson and group has shown a plethora of proteins bind to NPs when the nanoparticle is introduced into blood plasma [150]. Additionally, a significant change in conformation of a protein is observed upon interaction with NP. The change is mostly due to the physicochemical properties of both the interacting surfaces [95]. Studies have shown that changes triggered in presence of a nanoparticle surface, acting as a template for protein nucleation, catalyze protein fibrillation for many model proteins [95, 191]. Conversely, some studies reported that NPs can also inhibit protein fibrillation [393, 394]. We hypothesize, here, that nanoparticle-mediated protein fibrillation mainly depends on interaction at the interfaces, which defines the binding thermodynamics and accordingly triggers the conformational rearrangement in the protein. For the protein, where self-recognition element (SRE) becomes solvent exposed upon the conformational rearrangement, the interaction accelerates the fibrillation. On the other hand, for the protein where SRE is further buried into the inaccessible core upon conformational rearrangement, the interaction results in inhibition of the fibrillation. The present investigation addresses the hypothesis using insulin as a model protein and ZnONP interface as a model nanoparticle system.

As described in previous chapters in details, Zinc oxide NPs (ZnONPs) have potent antibacterial, depending upon the strength of interfacial interaction, which is mostly related to the generation of ROS [210]. However, the cytotoxicity of ZnONP is contentious. A particular study has also reported nanosized ZnONP to be nontoxic to cells [395]. Due to the increased usage of the NP and exposure to metal ions, there are chances that the presence of abruptly high concentrations of Zn^{2+} in the body form ZnONP inside the biological system [94]. This chapter explores effects of negatively charged ZnONP on insulin conformation, amyloidosis and amyloid-dependent cytotoxicity at physiological pH.

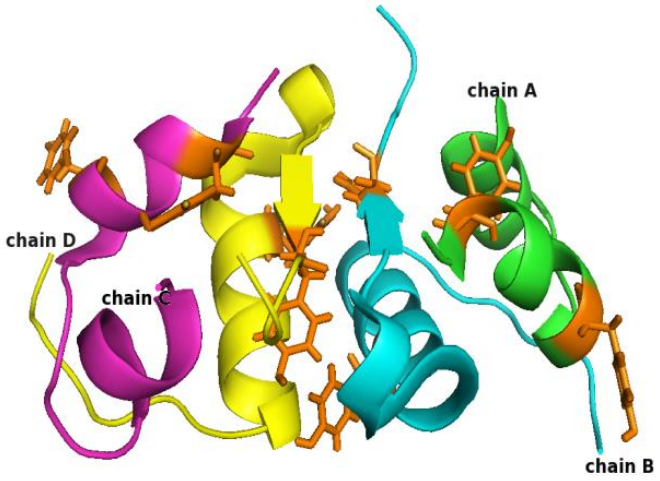

Figure 5.1. Structure of dimeric bovine insulin, extracted from PDB: 4M4L. Tyrosine residues are represented in sticks in orange colour.

5.2 Materials and Methods

5.2.1 Materials

Bovine insulin was purchased from sigma. Hydrochloric acid (HCl), and sodium hydroxide (NaOH) were obtained from Merck. All other chemicals and solutions were procured and prepared as described in the previous chapters.

5.2.2 Preparation and characterization of ZnONP and insulin-ZnONPs conjugates

ZnONP were synthesized and characterized as described in chapter 3 and were used as such in this study without any further modification. For the preparation of insulin-ZnONPs conjugates, same protocol as chapter 4.

5.2.3 Isothermal Titration Calorimetry

The thermodynamic features of the interaction between insulin and ZnONP were studied using isothermal titration calorimetry, ITC was performed on Microcal iTC 200 (GE healthcare) as described in previous chapter, 10 μM, 25 μM and 50 μM of insulin were used.

5.2.4 Time resolved fluorescence

Fluorescence lifetimes of insulin with and without ZnONPs were calculated from time-resolved fluorescence intensity decays using IBH 5000F Nano LED equipment (Horiba Jobin Yvon, Edison, NJ in the time-correlated single photon counting (TCSPC) mode using the same protocol as described in the previous chapter, section 4.2.7.

5.2.5 Molecular Dynamics (MD) Simulations

The structure of the bovine insulin protein has been retrieved from RCSB PDB (PDB ID: 4M4L) [233]. Zinc Oxide Nanoparticle (ZnO NP) structure have been prepared with Virtual Nanolab (VNL) Atomistix Toolkit version 2016.3 software (www.quantumwise.com) [276]. The insulin and ZnONP conjugate has been prepared with chimera [242]. All the other parameters and procedures were kept same as described in chapter 3.

5.2.6 Thioflavin T assay

Stock solutions of both insulin and ZnONP were sonicated in an ultrasonic water bath before setting up the fibrillization reactions. Increasing concentration of ZnONP was mixed with insulin (10 μM) in 10 mM phosphate buffer (pH 7.4) and 20 μM of ThT in a final reaction volume of 200 μl each and other parameters were kept same as in previous chapters. Fibrillation reaction was initiated by shaking. Lag times and rate of fibrillation were also calculated as described in the previous chapter.

5.2.7 Congo red (CR) Assay

This assay was performed using a previously established protocol with slight modifications [396]. 250 μM CR stock solution was prepared by dissolving CR in 90 % 10 mM phosphate buffer (pH 7.4) and 10 % ethanol. The solution was mixed thoroughly and filtered through 0.45 μm cut-off membrane filter. The final concentration of CR was then determined spectrophotometrically by measuring the absorbance at 495 nm with molar absorptivity coefficient (ε) = 6.26×10^4 $M^{-1}cm^{-1}$. 10 μM insulin was incubated alone or with increasing concentration of ZnONP, and Congo red solution was added to the fibrillation reaction to a final concentration of 5 μM, and incubated with agitation. Absorbance of CR alone, insulin with CR and insulin-ZnONP with CR was recorded from 300 nm to 700 nm at 0, 48 and 72 hrs. After 72 hrs, the samples were centrifuged and the pellet obtained were washed twice with deionised water. After the wash, pellets were re-suspended in MilliQ water and placed on glass slides for image acquisition with green filters using Olympus IX71 microscope fluorescence microscope.

5.2.8 Intrinsic fluorescence assay

The intrinsic fluorescent property of tyrosine residues in insulin was exploited in these experiments. The reaction mixture was prepared with 10 μM insulin and the requisite concentration ZnONP in 10 mM phosphate buffer (pH 7.4) at 25°C and the intrinsic fluorescence was measured at three different time points 0, 24 and 48 hrs as described in the previous chapter.

5.2.9 Circular Dichroism (CD) polarimetry

CD spectroscopic measurements were performed in far UV range (190-260 nm), for 10 μM insulin with or without the presence of ZnONP in 1 mm cuvette in a JASCO- J1500 CD spectropolarimeter at 25°C and three time points (0, 24 and 48 hrs). The data were deconvulated using CDNN software [397].

5.2.10 Transmission Electron Microscopy

Insulin was incubated with 32 μg/mL of ZnONP for 48 hrs and the same process as for IAPP and α-synuclein was followed.

5.2.11 Alamar Blue assay

Cytotoxicity of insulin amyloids and insulin-ZnONP complexes was measured in mouse insulinoma MIN6 cell line through alamar blue assay in same procedure as previously described for IAPP.

5.2.12 Cellular uptake assay

Insulin was tagged with FITC by following a standardized protocol with slight modifications [398]. 1 mg/mL FITC in DMSO was added to 2 mg/mL bovine insulin solution, and stirred continuously for 8 hrs in dark. The resulting solution was then passed through sephadex G-100, and absorbance of the elutes were measured using UV-Visible spectroscopy. Elutes containing a suitable ratio of insulin:FITC (1:0.5) were determined, and used for further experiments **(Figure A14)**. Insulin-FITC was incubated with requisite concentrations of ZnONP, and agitated for 48 hrs for the conjugation and insulin fibrillation. After 48 hrs, the samples were centrifuged, and the pellets obtained were washed twice with deionised water and re-suspended in minimal amount of MilliQ water. MIN6 and THP-1 cells were seeded in 12-well plates. After 24 hrs of incubation, both the cells were treated with insulin-FITC and insulin-FITC-ZnONP conjugates for 6 hrs. Following the treatment, the cells were harvested using centrifuge, and the cells were washed thrice with PBS. They were then counterstained with DAPI for 5 mins, and were washed thrice to remove any background. Fluorescence microscopy was then performed on the cells using Olympus IX71 fluorescence microscope.

5.3 Results

5.3.1 Interaction between insulin and ZnONP

5.3.1.1 Characterization of ZnONP-insulin complex

Figure 5.2A shows the absorption spectrum of insulin with varying concentrations of ZnONP. As shown in the fig, insulin with low ZnONP (0, 0.8, 4, and 8μg/mL) concentrations have insignificant ZnONP-specific SPR peak intensity and protein absorption peaks. In presence of 16 and 32 μg/mL ZnONP interface, ZnONP-specific SPR peak is absent, but protein-tyrosine specific peak at 276 nm is observed. only has either increased the effective local concentration of the protein-tyrosine or the adsorption leading into protein conformational rearrangement into enhanced number of photon exposed protein-tyrosine residues. Hence, in both the conditions, the absorbance at 276 nm is likely to cross lower detection limit of the instrument at higher interface concentration, despite of constant protein concentration in the complexes. Similar observation has been observed when protein has high affinity interaction with nanoparticle [345]. Additionally, a red shift and peak broadening in case of insulin containing 32 μg/mL ZnONP is observed compared to insulin only solution. This further confirms the varying local chemical environment of protein tyrosine resulting from adsorption of insulin onto ZnONP interface. The data is also consistent with previous studies [399]. To further analyse the adsorption of insulin molecules onto ZnONP interface, the ζ potential of 32 μg/mL ZnONP with increasing concentration of insulin (0 to 40 μM) both in both the medium were observed. In both the conditions, data indicated neutralization of ZnONP ζ-potential value with increase in insulin concentration, until a constant ζ-potential value is reached **(Figure 5.2B)**. The ζ-potential gradually neutralised from -36 mV at no insulin to around +8 mV at 40 μM insulin in 32 μg/mL ZnONP containing solution, after which the change in surface potential. Further addition of insulin to the solution had insignificant effect on ζ-potential. The progressive neutralization and screening of the potential are likely due to electrostatic interaction between the positively charged amino acid residues in the B-chain like His5, His10, Arg22 and Lys29, as previously reported, with the negative surface potential interface [400, 401]. Since the ζ-potential values neutralises to +8.34 mV indicates the conjugate fall in the index of incipient stability, the instability of the complex is likely causing the agglomeration of the complex; in order to be monodisperse entity, the ζ-potential values of any nanoparticle or nanoparticle-protein conjugate must have a magnitude higher than +/- 25 mV [402]. The elemental mapping of insulin-ZnONP complexes, as analyzed by HAADF-STEM, indicated the presence of biomolecular elements

like N and S in atomic proximity of Zn and O atoms **(Figure 5.2C)**. HAADF-STEM as shown previously, is applicable to biological samples for elemental composition analysis. Hence, the image indicated the Zn element distribution in the sample, in an atomic proximity of N and S, thereby further confirming the adsorption of insulin on ZnONP interface.

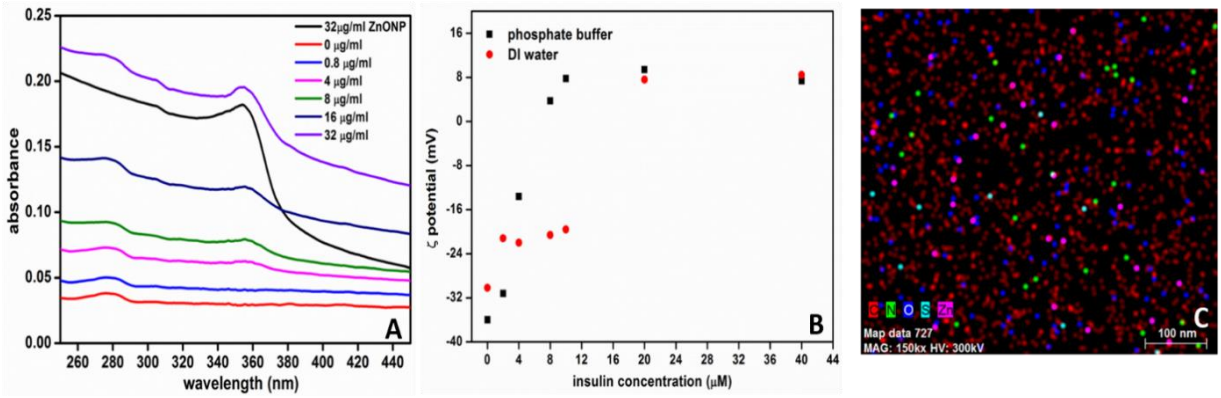

Figure 5.2. Characterization of physical adsorption of insulin onto ZnONP interface using (A) UV-Visible spectroscopy, (B) zeta potential and (C) HAADF-STEM mapping.

5.3.1.2 MD Simulations

To further gain insights into atomic level interactions between insulin and ZnONP, we performed MD simulations on intact insulin and insulin-ZnONP conjugate **(Figure 5.3)**. MD simulations on peptide and NPs have been performed in some of the previous studies reported by our group [403, 404], which revealed interesting aspects of nanoparticle protein interactions. **Figure 5.3A** showed the RMSD values of only insulin (blue) and insulin-ZnONP conjugate (red). Only insulin showed maximum deviation at 30 ns, which is followed by a stable RMSD. In case of insulin-ZnONP complexes, the deviation (0.2 – 0.5 nm) is significantly reaching a very low point from 30-60 ns, which increases sharply after 60 ns, and stabilizes near the end of simulation. Likewise, RMSF values plotted in **figure 5.3B** depicted the atom wise fluctuations in insulin (blue) and insulin-ZnONP (red) conjugates. As evident from the figure, insulin-ZnONP complexes have an overall high fluctuation compared to intact insulin. More specifically in case of insulin-ZnONP complexes, atom numbers 62 to 75 corresponding to Ala8, Ser9 and Val10 of the loop region of chain-A showed a higher fluctuation. Similarly, in Chain-B, atom numbers 206 to 267 corresponding to Phe1, Val2, Asn3, Gln4 and His5 of the loop region showed higher fluctuations. Data from both RMSD and RMSF plots depicted that there is a high degree of fluctuations in the insulin-ZnONP complex, compared to intact insulin, which is attributed to interfacial interactions resulting in conformational rearrangement/fluctuations.

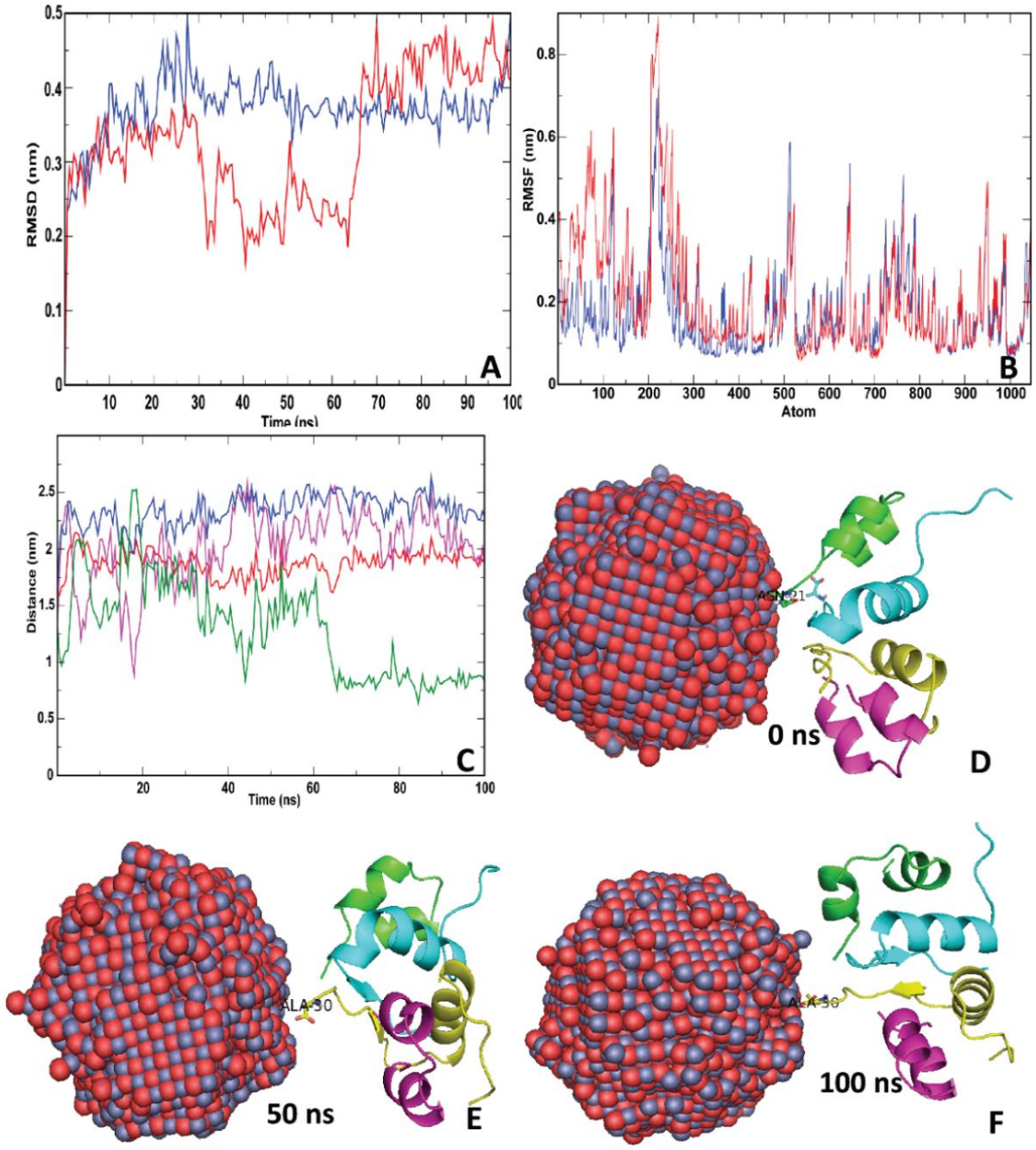

Figure 5.3. MD simulation analysis of insulin and insulin-ZnONP complexes. (A) RMSD, (B) RMSF (blue indicates only insulin and red indicates insulin-ZnONP complex), (C) average distance of chain-A (green), Chain-B (red), Chain-C (magenta) and Chain-D (blue) from ZnONP, and snapshots of insulin-ZnONP complex at 0 ns (D), 50 ns (E) and 100 ns (F).

The amino acids in the loop region generally have a relatively dynamic character compared to other secondary structures in a protein [405]. Following the fluctuations, we further analysed the average distance between the ZnONP and the amino acid residues Leu13-Asn18 of chain A & C, Leu11-Leu17 of chain B & D chains, the known self-recognition element (SRE,

amyloidogenic region) in insulin sequence in **figure 5.3D** [385]. Chain-A (green) is shown to be coming closer to the ZnONP during the course of simulations. However, chains B, C and D maintained an approximate distance of around 2 nm from ZnONP throughout the simulations **(Figure 5.3C)**. Respective snapshots of the complex at 50 and 100 ns are provided in **figure 5.3D-F**. The results depicted a favourable stable interaction between insulin and ZnONP interface.

5.3.1.3 Time resolved fluorescence

Time resolved fluorescence studies provide detailed information about the population distribution of molecular species in the excited state [349]. In the absence of tryptophan residues in insulin, the intrinsic fluorescence of tyrosine was taken advantage of in our studies.

Table 5.1. Table depicting the fluorescence lifetime of insulin-tyrosine in presence of increasing ZnONP concentrations.

ZnONP (µg/mL)	α1	τ1	α2	τ2	α3	τ3	Avg. τ
0	35.61	1.29	15.04	0.19	49.35	3.33	2.848209
0.8	44.67	1.18	28.73	0.12	26.6	3.87	2.897531
4	39.93	1.51	35.75	0.1	24.32	4.46	3.337457
8	33.75	1.66	35.58	0.09	28.66	4.62	3.678947
16	31.48	1.68	41.17	0.08	27.35	4.69	3.744648
32	31.39	1.62	42.01	0.08	26.6	4.63	3.680826

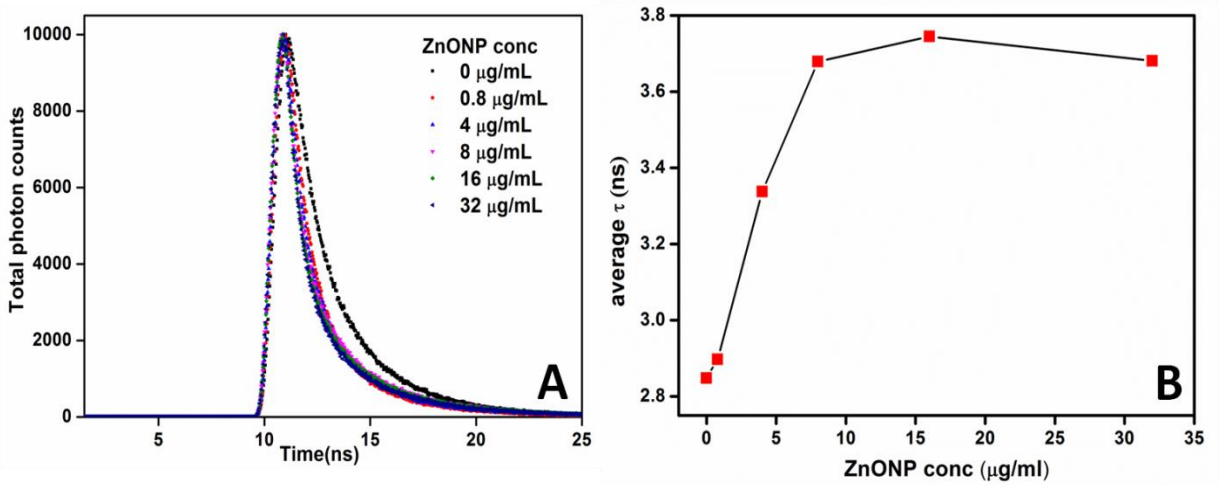

Figure 5.4. (A) Time resolved fluorescence of insulin and insulin-ZnONP complexes and (B) average life time of insulin in presence of different concentrations of ZnONP.

Samples with and without ZnONP were excited at 276 nm and fluorescence lifetimes were recorded at 309 nm. Data were fitted with three exponential decay components. Table 4.1 shows the three lifetimes values τ in each case. τ1 and τ3 have been shown to increase with the increase in concentration of ZnONP, whereas τ2 is shown to decrease in a concentration dependent manner. However, average lifetime (τ_{avg}) **(table 5.1, figure 5.4)** is shown to increase from 2.84 to 3.74 ns until 8 μg/mL of ZnONP and then attains a plateau till 32 μg/mL of ZnONP. Thus it can be inferred that there is binding between insulin and ZnONP and that insulin is getting adsorbed on the surface of ZnONP unlike quenching reported in a previous study [345]. It can also be explained that on the interaction or adsorption of insulin on ZnONP interface there is a change in the microenvironment of the tyrosine residues, which causes an increase in the fluorescence lifetime of the tyrosine residues of insulin. Moreover, it is also noteworthy that the low concentrations of ZnONP used in the study do not cause any artefacts or scattering of fluorescence of any kind. Therefore, the changes in the fluorescence lifetimes are solely attributed to the changes in conformation of insulin.

5.3.1.4 Isothermal Titration Calorimetry

To further confirm the binding of insulin to ZnONP, isothermal titration calorimetry was performed to determine the thermodynamic parameters of insulin interaction with ZnONP interface. Thermodynamic parameters like change in enthalpy (ΔH) and entropy (ΔS) indicate the predominant interactions at the protein-nanoparticle interfaces, and help to quantify the binding affinity (K_a) and stoichiometry (n). However, the quantified binding thermodynamic parameters value are approximate, since the molar concentration of ZnONP is approximate value that is based on the simulated numbers of Zn-O elements fitting into a 20 nm diameter sphere in a hexagonal wurtzite-like packing, assuming homogenous nanoparticle population in solution. Nevertheless, the binding thermodynamics gave direct experimental data on interaction pattern at the interface. In particular, we titrated ZnONP with three different insulin concentrations in the syringe, 10, 25 and 50 μM, respectively. Negative heat change of titration for all three insulin concentrations implied that the binding is an exothermic process triggered predominantly by polar interaction **(Figure 5.5A-C)**. Isotherms indicated the decrease in heat change with increase in number of injections. Interestingly, the heat evolved for 10, 25 and 50 μM insulin titration against ZnONP was ~ 130 Kcal/mole, ~ 340 Kcal/mole and 800 Kcal/mol, respectively. The heat evolved increased by 3 and 6 folds with increase in protein concentrations in syringe by 2.5 and 5 folds, respectively. The decrease in

heat of binding with each successive injection followed the trend as observed for ζ-potential neutralization study. Moreover, the saturation of ZnONP with insulin molecules was not observed in both the cases. However, the isotherms fit well into single site binding scheme with binding constants $3.5*10^4$ M^{-1}, $5.24*10^3$ M^{-1} and $3.591*10^2$ M^{-1} for 10, 25 and 50 μM insulin respectively, indicating very weak non-specific binding. The decreasing binding constant with increase in insulin concentration in injection indicates that multiple layer of insulin adsorbs onto the interface; soft corona has lower binding constant than hard corona [406]. Additionally, the negative enthalpy change suggested favourable non-covalent interactions like electrostatic, hydrogen bonding and van der Waals interactions. Conversely, unfavourable negative entropy change signifies the presence of hydrophobic effect, indicating relatively constrained conformational entropy of insulin upon binding to ZnONP interface [186, 187]. Taken together, the ITC data suggested that insulin has a concentration dependent affinity for ZnONP interface, which has predominantly enthalpy contribution than the entropy contribution.

The interactions take place between hydroxyl groups present on the surface of NPs and the polar residues of insulin those are already exposed and/or get exposed upon conformational rearrangement following initial contact with the interface, like tyrosine as indicated by time-resolved fluorescence study.

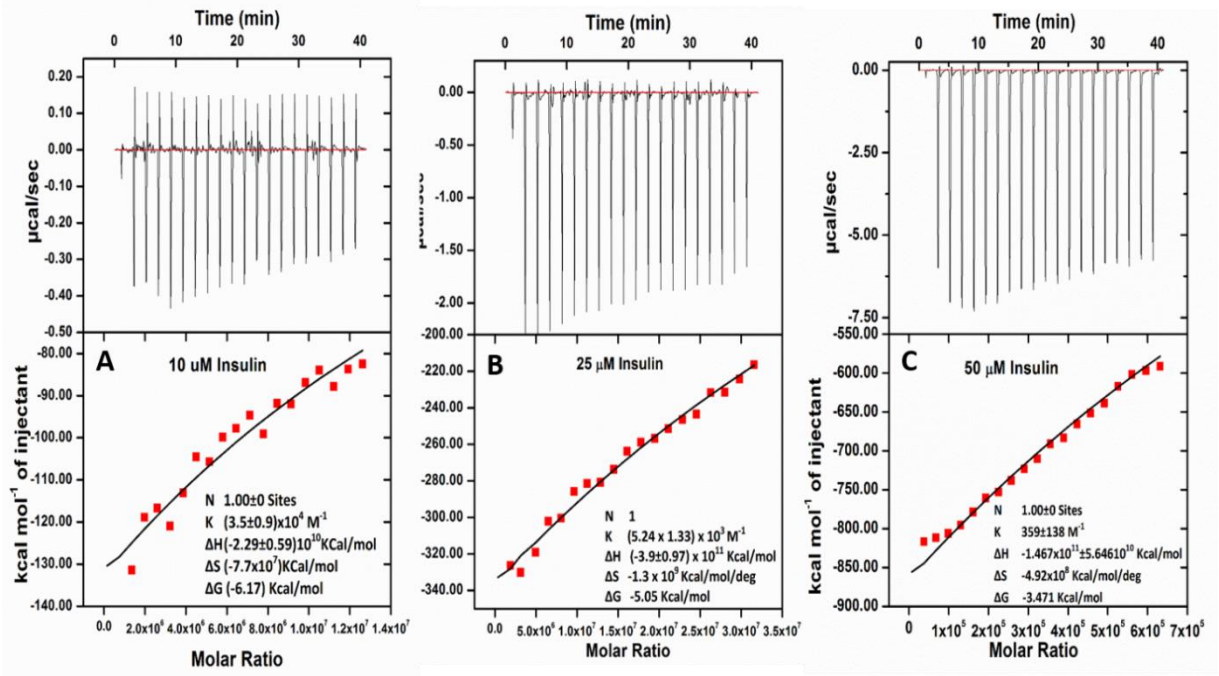

Figure 5.5. Isotherms of 32 μg/mL ZnONP titration with (A) 10 μM, (B) 25 μM and (C) 50 μM insulin at 25 °C. The upper panel depicts the raw titration, whereas the lower panel

depicts change in heat of titration against their respective molar ratios after subtraction of change in heat of buffer titration with protein.

5.3.2 Effect of ZnONP on conformation and fibrillization of insulin

5.3.2.1 Amyloid fibril formation: Thioflavin T assay and Congo red assay

ThT dye is an amyloid specific due, which has been widely used for tracking the fibrillation kinetics *in vitro* [286]. In principle, the fluorescence emission of ThT dye in an aqueous medium is very low. However, upon binding to protein amyloid fibrils, fluorescence intensity of ThT dye increases many folds following excitation at 440 nm. Thus, the assay is used to track insulin fibrillation kinetics in presence of varying concentrations of ZnONP (both in 10 mM phosphate buffer, pH 7.4). The fibrillation kinetics in presence of low ZnONP concentrations followed typical fibrillation kinetics, consisting of an initial lag phase, followed by an elongation phase and equilibrium phase. As shown in **figure 5.6A**, a dose dependent increase in the fibrillation is observed with increase in the interface concentration from 0 to 32 μg/mL. Intact insulin did not fibrillate in first 40 hrs, depicting relatively longer lag phase. The one with the shortest lag phase was in presence of highest studied ZnONP concentration, i.e. 32 μg/mL. However, presence of the interface enhanced elongation rate compared to the absence of interface in a concentration dependent manner **(Figure 5.6AandB)**. The data referred that ZnONP interface enhanced the rate of elongation and lowers the lag phase of insulin fibrillation kinetics in a concentration dependent manner. Studies have shown that the insulin fibrillation, at physiological pH, highly depends upon concentration of the protein monomer; low concentrations of insulin (2.5 - 10 μM) fibrillates faster than the higher concentrations (> 10 μM) [379]. Additionally, the fibrils, formed at physiological pH, morphologically differ from the fibrils formed at acidic pH [387]. However, fibrillation of insulin at low pH and high temperature has relatively faster kinetics with discrete fibrils than the one fibrillated at physiological pH. The differences observed in fibrillation at lower and physiological pH are likely due to the resulting fibrils have differently solvent exposed flanking residues determining properties of the fibrils [407]. Likewise, the aggregate formed in presence of the interface were discrete amyloid-like fibrils than the aggregate formed in absence of the interface.

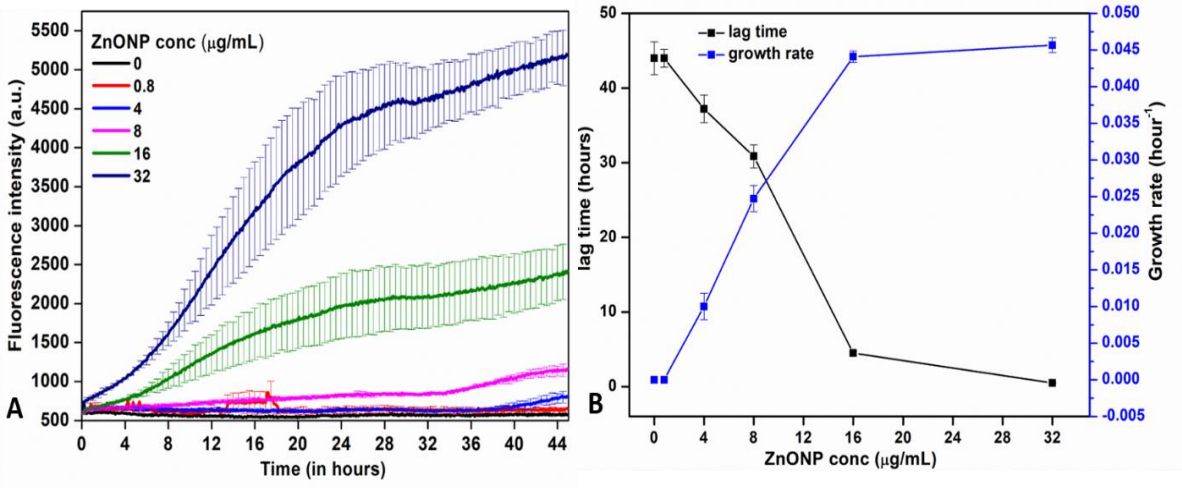

Figure 5.6. (A) Thioflavin T dye binding assay of insulin in the presence of different concentration of ZnONP and (B) lag times and their respective growth rates of insulin fibrillation at different ZnONP concentrations.

To further confirm the fibrillation, Congo Red absorption assay for insulin alone and insulin containing 32 μg/mL ZnONP interface solutions at 0, 48 and 72 hrs of incubations was conducted. Congo red dye has been previously used in several studies for the detection of amyloids using UV-Visible spectroscopy and fluorescence microscopy [396]. **Figure 5.7A** showed insulin alone has a low intensity absorbance spectrum for the dye, without any change in the intensity or shift in peak-maxima with time. On the other hand, insulin with 32 μg/mL **(figure 5.7B)** has around four-folds higher absorbance from start of the fibrillation reaction, i.e. at time point 0 hr, which is accompanied by a further rise in fluorescence and a red shift in peak-maxima in 48 and 72 hrs incubated samples. The increase in intensity with red-shift in absorption maxima of the dye indicated insulin fibrillation in presence of the interface. Additionally, when these samples were imaged under a fluorescent microscope, similar results were observed. Insulin alone showed very low fluorescent body, while one with ZnONP interface showed numerous and larger fluorescent body, depicting enhanced fibrillation of insulin in presence of ZnONP interface. The fibrils, formed at physiological pH, morphologically differ from the fibrils formed at acidic pH [387]. However, fibrillation of insulin at low pH and high temperature has relatively faster kinetics with discrete amyloid-like fibrils than the one fibrillated at physiological pH. The differences observed in fibrillation at lower and physiological pH are likely due to the resulting fibrils have differently solvent exposed flanking residues contributing to the fibril properties [407]. Likewise, the aggregate formed in presence of the interface were discrete amyloid-like fibrils than the aggregate formed in absence of the interface.

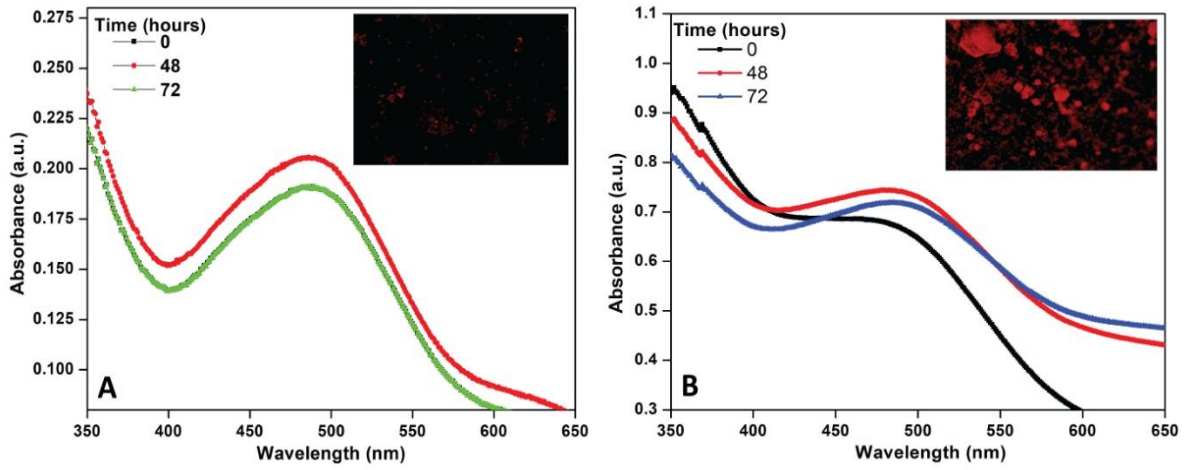

Figure 5.7. Congo Red assay of (A) insulin alone and (B) insulin incubated with 32 μg/mL ZnONP by recording absorbance from 350-650 nm at 0, 48 and 72 hrs, respectivley. The figure insets show the corresponding fluoroscent micrograph of respective samples.

5.3.2.2 Secondary structure of the fibrils formed: CD polarimetry

The secondary structure of insulin in presence of ZnONP was further assessed by CD polarimetry at 0 hr, i.e., just upon mixing of insulin and ZnONP, 24 hrs and 48 hrs of incubations at 25 °C. **Figure 5.8A** depicted that insulin is predominantly an α-helical protein in its native state, which is consistent with previous studies [375, 378, 379]. As the concentration of ZnONP is increased, ellipticity decreased in a concentration dependent manner, which suggested decrease in the helical containing population fraction. However, there is no significant change in the peak positions, further indicating that a major part of the secondary structure is being retained until 32 μg/mL of ZnONP interface in solution. After 24 hrs of incubation, it was observed that insulin without ZnONP, still contained mainly α-helix, i.e. a major minimum at 209 nm and a shoulder at 222 nm. Insulin containing different ZnONP concentrations showed diminishing α-helix characteristic, as there is a significant decrease in the ellipticity **(Figure 5.8B).** However, typical β-sheet, which is a signature of amyloid fibrils, could not be detected. Similarly, after 48 hrs of incubation for all the samples, including the ones without ZnONP, a significant reduction in the α-helix is observed **(Figure 5.8C)**. The trough at 209 nm decreased significantly in all the samples. Additionally, in samples with higher ZnONP interface concentrations, there is an increase in the minima at 223 nm that is anticipated because of net ellipticity signal from β-sheets present in amyloid oligomers/fibrils and from α-helix in the protein monomeric fraction. The CD data, on deconvolution using CDNN software (Fig. 4C), further supported an increase in total β-sheet

content **(Figure A12)**, which rationalises the increasing minima at 223 nm with time in presence of the interface.

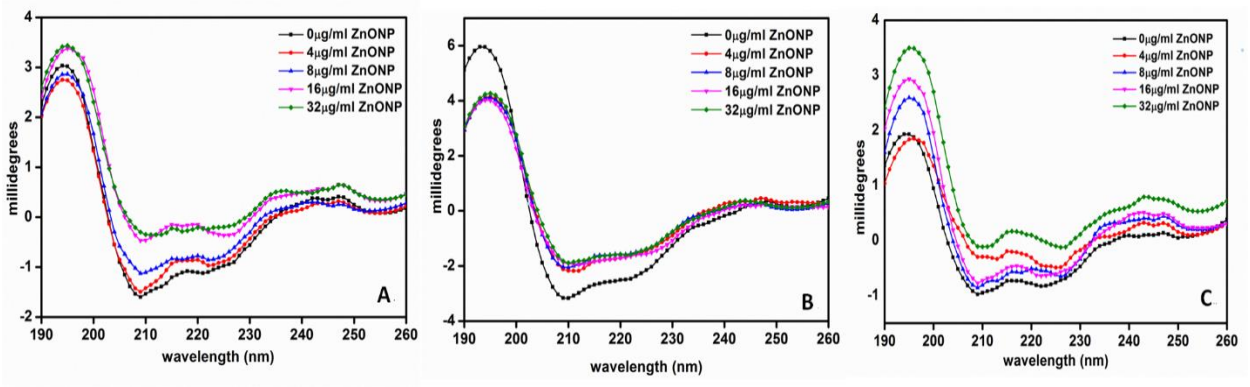

Figure 5.8. Far-UV Circular Dichroism spectra depicting changes in the secondary structures of insulin in presence of ZnONP after (A) 0 hr, (B) 24 hrs and (C) 48 hrs of incubation.

5.3.2.3 Microenvironment and conformation of insulin in presence of ZnONP: Intrinsic fluorescence

For steady-state fluorescence, the auto-fluorescence of tyrosine to study the conformational changes in insulin in presence of ZnONP at 0 hr, 24 hrs and 48 hrs of incubations was observed. Firstly, the decrease in intrinsic fluorescence with increase in concentration of ZnONP interface indicated change in microenvironment of insulin-tyrosine in a dose dependent manner **(Figure 5.9A)**. The emission peak was centred at 308 nm for all the concentrations, a specific emission peak for tyrosine with excitation at 276 nm. In each monomer of insulin, only Tyr14 of chain A is solvent exposed. The other residues, i.e. Tyr19 in chain A, Tyr16 and Tyr26 in chain B, remain buried in the insulin structure. The most plausible explanation for decrease in tyrosine fluorescence with respect to increase in ZnONP concentrations can be the exposure of tyrosine residues to the polar environment. The decrease in the intrinsic fluorescence (fluorescence quenching) was further extrapolated using Stern-Volmer plot for possible nanoparticle-mediated fluorescence quenching **(Figure A12)**. The quenching constant (K_{sv}) was 3.80 x 10^{19} $M^{-1}s^{-1}$, which falls in the range of static quenching suggesting insulin-tyrosine forms either stable non-fluorescent complexes with ZnONP interface or multilayered adsorption of the protein onto the interface results in decreased number of the fluorophore. The later reason is more rational, since insignificant tyrosine quenching, either dynamic or static, was found for free tyrosine molecule in presence of ZnONP interface for the studied concentrations **(Figure A13)**. The intrinsic fluorescence quenching has also been observed for other protein interactions with ZnONP interface [187,

345]. Thus, the observation indicated that the interface induces conformational rearrangement in insulin.

A fall in fluorescence intensity of insulin-tyrosine is observed after 24 hrs of incubation **(Figure 5.9B)**. The trend remains same as observed in CD data, i.e. decrease in the fluorescence intensity with increase in ZnONP concentration. Interestingly after 48 hrs of incubation **(Figure 5.9C)**, the insulin-tyrosine peak around 308 nm for insulin only and insulin containing 0.8 μg/mL ZnONP shifted to 335 nm, which indicated tyrosinate formation. The tyrosinate has higher quantum yield than tyrosine. Hence, the bathochromic shift is accompanied by hyperchromic shift, as shown in our data. Other samples with higher ZnONP (4, 8, 16 and 32 μg/mL) also showed a red shift in the emission maxima upto 313-316 nm. The increase in peak intensity showed a concentration dependent change, which is likely because of interaction of the tyrosine residues with ZnONP. A red shift in emission spectra of aromatic amino acid residues with fluorophore property is generally observed on exposure to polar solvent [408]. Thus, the red shift, here, is partly due to disruption of insulin tertiary structure resulting into solvent exposed tyrosine residues.

Tyrosine side chain, in itself, is partly hydrophobic and only Tyr19 of the four residues remains exposed in native protein. Hence, the hyperchromic shift accompanied by bathochromic shift indicated that the other tyrosine residues are also exposed upon the interface-mediated conformational rearrangement in insulin. Interestingly, a study has shown that there is an enhanced exposure of non-polar side chains including Tyr26 of the B-chain during insulin fibrillation [382]. The appearance of the new peak at 335 nm is likely due to the tyrosinate formation, since its emission peak is generally centred around 330-350 nm. Tyrosinate emission in proteins has been suggested to originate from an intramolecular excited state proton transfer from the phenolic hydroxyl of tyrosine to proton acceptors [356]. From the data, it can be inferred that in insulin only and insulin with 0.8 μg/mL ZnONP solutions tyrosine residues ionize to form tyrosinate on incubation for 48 hrs. An increase in the interface concentration might also provide efficient template for adsorption of insulin monomers. Therefore, at an enhanced interface concentration, tyrosine residues from maximum insulin molecules are interacting with ZnONP interface. Thus, the major insulin fraction is sterically hindered for deprotonation or hindered from detection. It has also been suggested that the shielding of hydrophobic domains is one of the main driving forces for insulin fibrillation [375].

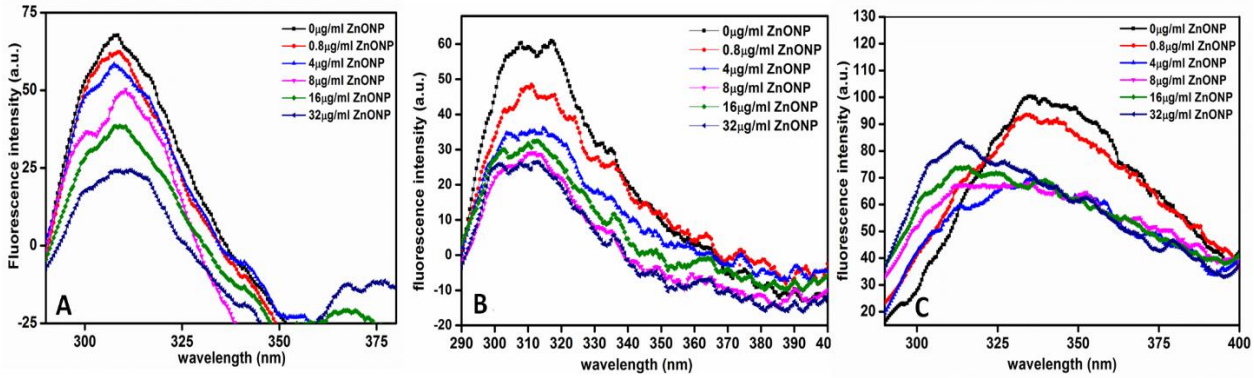

Figure 5.9. Change in the intrinsic insulin-tyrosine fluorescence in presence of ZnONP at (A) 0 hr, (B) 24 hrs and (C) 48 hrs of incubation.

5.3.2.4 Morphology of the fibrils formed: Transmission Electron Microscopy

The morphological features of the aggregates formed by insulin in presence of ZnONP were analysed by TEM. The micrographs showed that intact (without ZnONP) insulin, after 48 hrs of incubation, formed aggregates. However, it can be inferred that insulin alone does not form amyloids as more amorphous structures are present than the typical fibrils **(Figure 5.10A)**. On the other hand, increasing concentration of ZnONP allows the growth of fibrils (mixture of short and long fibrils). The growth of fibrils witnesses a slight decrease in α-helical and increase in antiparallel β-sheets content in insulin as observed from CD measurements. The thin fibers are around 2.5 nm in width and 50-60 nm in length, mostly unbranched in nature **(Figure 5.10B)**, as reported in literature [379]. These small amyloid-prone structures are often believed to be more cytotoxic, rather than the amorphous ones, since amyloid fibrils interact with membrane, and physically disrupt cell membrane [409].

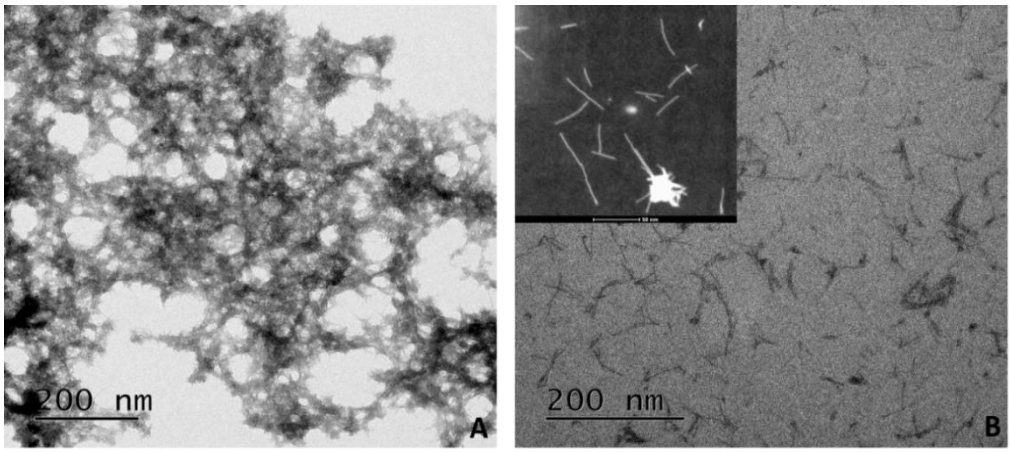

Figure 5.10. TEM micrographs of (A) only insulin and (B) insulin incubated with 32 μg/mL ZnONP. The inset shows a higher resolution image of the fibrils formed in presence of 32 μg/mL ZnONP.

5.3.3 Cytotoxic propensities of insulin-ZnONP conjugates: Alamar Blue assay

The cytotoxic potentials of the synthesized ZnONP, fresh insulin-ZnONP conjugates, and insulin-ZnONP amyloids (fresh complexes incubated for 48 hrs prior to cell treatment) were performed against MIN6 pancreatic cell line. The main component of Alamar blue dye is resazurin, which is known to reduce to highly fluorescent resorufin and dihydroresorufin dyes by active cells [410]. In the **figure 5.11Ai**, it is evident that the concentrations of ZnONP (0 - 32 μg/mL) are non-toxic to cells, rather the cells proliferation increased insignificantly ($p < 0.05$) in presence of ZnONP. This could imply that the studied ZnONP concentrations are nontoxic to pancreatic cells, partly because of the importance of zinc ions to the pancreatic cells. The total zinc ion concentration is highest in pancreas, and may have roles in paracrine signalling in pancreas for β-cell viability [411]. It has been demonstrated that ZnONP dissolute into Zn^{2+} ions that positively affects the growth of pancreatic cells [412], whereas ZnONP may cause ROS-mediated cell death at higher concentrations [413]. Thus, observing no cell death for the studied ZnONP concentrations indicate that the observed cytotoxicity in further experiments must depend only on cytotoxic propensity of the amyloid-like fibrils.

Thereafter, the MIN6 cells were treated with fresh insulin-ZnONP complexes. The **figure 5.11Aii** depicted normalized fluorescence intensities of cells treated with 10 μM insulin with increasing concentration of ZnONP (0-32 μg/mL). The fluorescence intensities of the treated cells were at par with the control cells, suggesting that fresh mixtures of insulin-ZnONP complexes are non-cytotoxic; rather the mixtures of insulin and ZnONP have positive effect on MIN6 cell viability because of their importance in a pancreatic cell proliferation. Thus, the mixtures synergistically enhanced the cell proliferation.

Following the cell treatment with fresh complexes, we further treated MIN6 cells with insulin amyloid fibrils formed in absence and presence of varying ZnONP concentrations. In the **figure 5.11Aiii**, the cell treated with insulin-aggregate formed upon the incubation in absence of ZnONP showed significantly higher fluorescence intensity than the control, depicting enhanced MIN6 cell proliferation in presence of insulin. However, in presence of insulin-

aggregate formed in presence of ZnONP, it is seen that the amyloid formed with increasing ZnONP interface concentration are significantly more toxic ($p < 0.05$). The amyloid formed in presence of highest concentration of ZnONP interface, 32 μg/mL, caused 40% of the cell death compared to control. However, the effective percentage of cell death must be higher than that observed, since the residual insulin monomer that did not precipitate in fibrillation must be enhancing the cell proliferation. Hence, the observed cell death is the net outcome of antagonistic effect of insulin amyloid and monomers present in the solution. Nevertheless, the data indicates that amyloids of insulin-ZnONP complexes are relatively more toxic to cell. Conversely, fresh mixtures of the same failed to cause significant cytotoxicity to MIN6 cell; rather they enhanced the cell proliferation. Hence, the amyloids, once formed by the mixtures of two entities, are relatively more toxic to the cell.

Following this, the uptake of insulin and insulin-ZnONP conjugate was studied on MIN6 cell lines **(Figure 5.11 B and C)**. Both insulin and insulin-ZnONP complex showed an efficient uptake into the cells, indicating that insulin facilitates entry of the NPs into the cells. Since MIN6 is host cell for insulin secretion, to rule out the possibility of cell specific internalisation, a similar set of experiments were executed on THP-1 cell lines **(Figure 5.12 B-D)**. Like in MIN6 cell, an efficient uptake of insulin and insulin-ZnONP conjugates were observed, implying insulin facilitates the uptake of ZnONP and that, as both MIN6 and THP1 cells have receptors for insulin, the uptake of these conjugates are presumably by the process of receptor mediated endocytosis in addition to other known mechanism for the nanoparticle. The observation also rationalises the enhanced MIN6 and THP-1 cells proliferation in presence of fresh insulin, as depicted in the Alamar blue assays **(Figure 5.11A.ii and 5.12Ai)** [414, 415]. In a recent study, insulin capped mesoporous silica nanoparticles showed an enhanced endocytosis efficiency than uncapped ones in RIN5F cell lines [416]. The effect of these fresh and fibrils from conjugate solutions were then further studied for morphology of MIN6 cells. Results of this study are quite concurrent with the Alamar blue assay. Fresh mixtures of insulin alone, insulin-ZnONP and ZnONP only were not cytotoxic, as intact cell morphology was observed **(Figure 5.11D.i-iv)**. In contrast, cell morphology upon treatment with aggregated insulin (amorphous) and insulin-ZnONP amyloid (amyloid) showed deformed membrane leading to morphologically damaged cells, though extensive damage cells were observed in medium treated with amyloid fibrils formed in presence of ZnONP interface **(Figure 5.11D.v-vi)** [417].

Hence, the data, altogether, indicated that the presence of ZnONP interface results in insulin adsorption onto the interface. The interfacial adsorption becomes more prominent with the conformational rearrangement into an amyloid-prone structure on increasing the interface concentration. Since the rearrangement produces amyloid-prone structure, the interface acts as loci for onset of insulin fibrillation by providing amyloid nuclei. Additionally, considering the binding affinity for the interface, nuclei detaching to bulk solution and enhancing insulin fibrillation in solution cannot be ruled out. Nonetheless, the interface presence shortens the lag phase and enhances the elongation rate to produce relatively more cytotoxic amyloid fibrils.

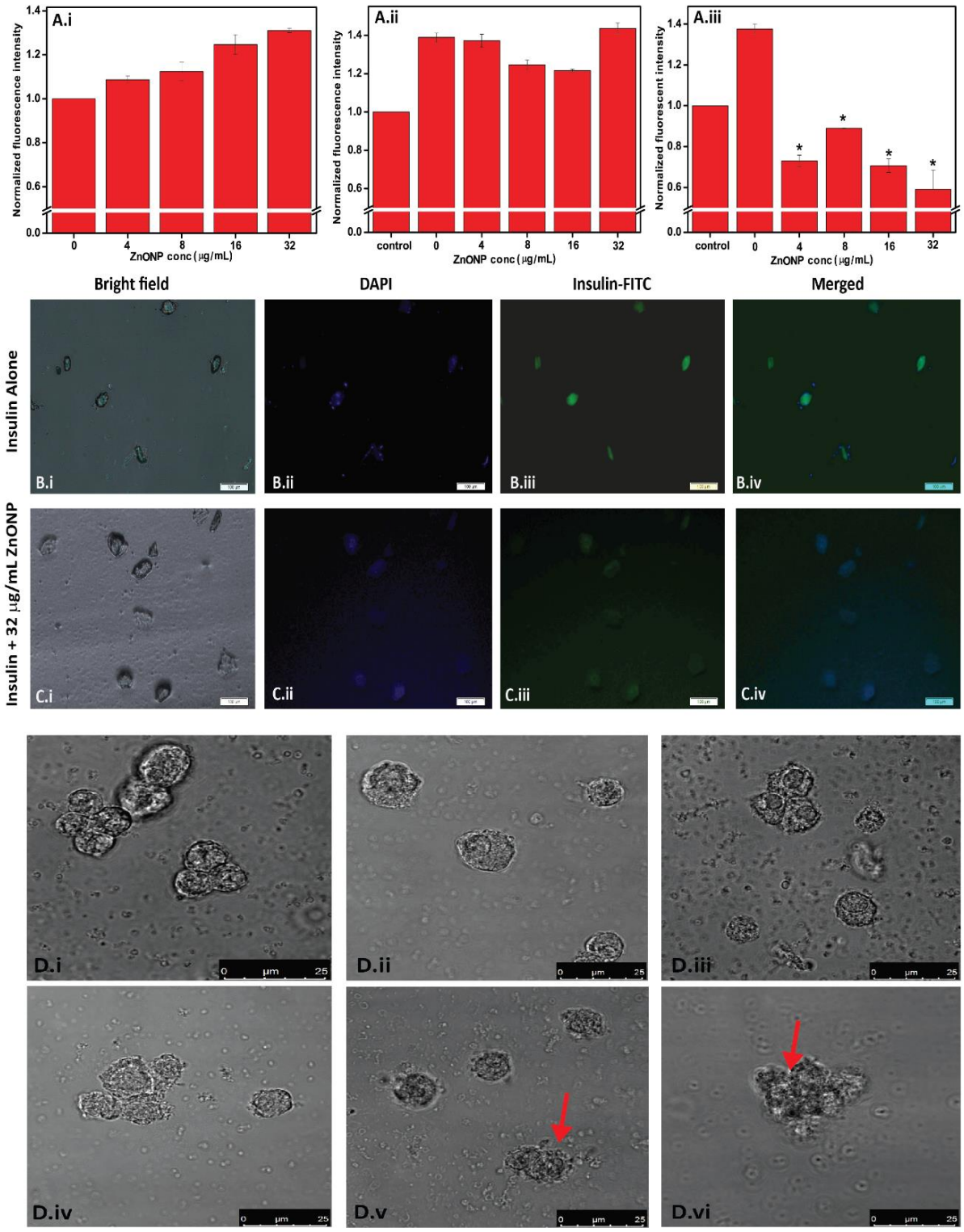

Figure 5.11. Cytotoxicity and internalization of insulin and insulin-ZnONP conujugate to MIN6 cell. (A) Alamar blue fluorescence assay for cell viability after treatment with (A.i) ZnONP only, (A.ii) fresh mixtures of insulin and ZnONP, and (A.iii) insulin amyloids formed in presence of ZnONP interfaces. Data represented were taken from independent triplicate reactions with significance value, $p < 0.05$. (B) Fluorescence micrographs to show

internalization of FITC-tagged insulin alone, (B.i) bright field image, (B.ii) image representing nucleus stained by DAPI (blue), (B.iii) FITC-tagged insulin and (B.iv) merged images (scale bars represent 100 μm). (C) Fluorescence micrographs to show internalization of FITC-tagged insulin with 32 μg/mL ZnONP, (C.i) bright field image, (C.ii) nucleus stained by DAPI (blue), (C.iii) FITC-tagged insulin and (C.iv) merged image (scale bars represent 100 μm). (D) Bright field micrographs of MIN6 cells after different treatments. (D.i) non-treated cells, (D.ii) fresh insulin only treated cells, (D.iii) ZnONP only treated cells, (D.iv) fresh mixture of insulin and ZnONP treated cells, (D.v) 48 hrs incubated aggregated insulin treated cells, and (D.vi) amyloid insulin formed in presence of ZnONP interface treated cells (scale bars represent 25 μm).

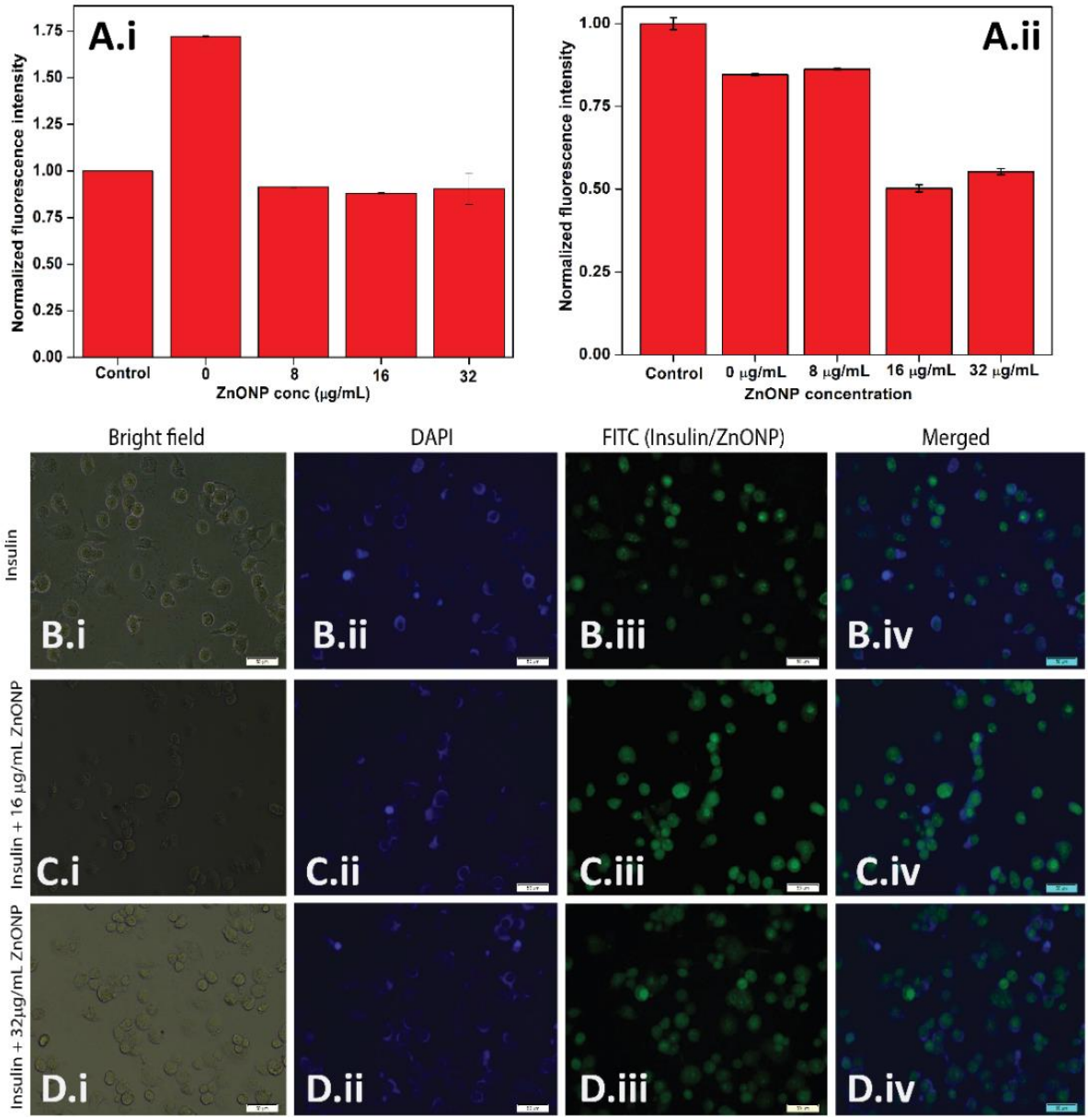

Figure 5.12. Cytotoxicity and uptake of insulin and ZnONP in THP-1 cells. (A) Alamar blue assay for THP-1 cell viability after treatment with fresh mixtures of insulin and ZnONP (Ai), and amyloids of insulin formed in absence and presence of ZnONP interfaces (Aii). (B) Cellular uptake of only insulin by THP-1 cells, bright field image (B.i), image representing nucleus stained by DAPI (blue) (B.ii), image representing FITC tagged insulin (B.iii) and merged images (B.iv). (C) Cellular uptake of FITC tagged insulin with 16 μg/mL ZnONP by THP-1 cells, bright field image (C.i), image representing nucleus stained by DAPI (blue) (C.ii), image representing FITC tagged insulin-adsorbed onto ZnONP interface (C.iii) and merged images (C.iv). (D) Cellular uptake of FITC tagged insulin adsorbed onto 32 μg/mL ZnONP by THP-1 cells, bright field image (D.i), image representing nucleus stained by DAPI (blue) (D.ii), image represent FITC tagged insulin-adsorbed onto ZnONP interface (D.iii) and merged images (D.iv) (all scale bars represent 50 μm).

5.4 Discussion

Fibrillation of insulin has long been an issue since the time of its commercial manufacture and storage. While it has been demonstrated that the monomeric insulin is highly prone to fibrillation, the exact causes and mechanisms are not known. Most of the studies have focussed on the fibrillation of monomeric insulin at pH 1.6-2, [385, 386]. In the present investigation, we demonstrated the fibrillation of bovine insulin at physiological pH in presence of varying ZnONP concentrations. Recent works, depicting the impact of NPs on conformation of proteins, have shown the changes in protein structure upon interaction with nanoparticle interfaces, and its consequence on protein function, have been reviewed in chapter 2. Interestingly, a study has shown that transferrin-functionalized NPs lose their targeting capabilities when placed in a biological environment [185]. In this context, the effects of nanoparticle on fibrillization propensity of different amyloidogenic proteins have also been studied. In many cases like β2-microglobulin, α-synuclein and IAPP, metal NPs have shown to enhance the amyloidogenic propensities of these proteins [191, 193, 194].

However, some studies have shown that functionalized NPs have the capacity to arrest or inhibit amyloidosis *in vitro*. In contrast, Se/Ru NPs can inhibit metal-induced aggregation of Aβ-40 [418]. Similarly, Au complexes [269] showed inhibition of IAPP fibrillation. In case of insulin, tryptophan and tyrosine coated AuNPs have shown the potential to inhibit the proteins fibrillation [419]. In our case, we found that ZnONP nanoparticle enhances insulin fibrillation. ThT dye binding showed diminishing lag phase with 16 μg/mL and 32 μg/ mL of ZnONP. The SPR peaks and ITC data indicated adsorption of insulin molecules over the

ZnONP interface, predominantly through hydrogen bonding. The net charge, -4, on insulin dimer is calculated by ADT tools **(Figure A16)** [344]. MD simulation results also indicated that non-covalent interactions between insulin residues and ZnONP interface resulted in increased local concentration of insulin, which onsets the fibrillation by either providing platform or triggering conformational rearrangement into amyloid-prone structure or both. Similar observations were recorded in previous studies reporting with different proteins [191]. After 48 hrs of incubation with ZnONP, there is increase in the β-sheet content with traces of α-helix [382]. Besides agitation, no structural or physical stress (low pH and high temperature) were given. In absence of agitation, the transformation from native structure to typical cross β-sheets is likely delayed. It has been shown that agitation is important factor for insulin fibrillation at physiological pH [379]. Insulin fibrillation at physiological pH *in vitro* is also characterized by a reverse dependence on peptide concentration, i.e. the fibrillation is faster at low insulin concentration in contrast to fibrillation at low pH. Thus, the low concentration used in our study favours insignificant fibrillation in studied conditions, whereas the fibrillation enhanced in presence of ZnONP. Additionally, it further suggested that the mechanisms by which insulin fibrillates at low pH and physiological pH are entirely different. At low pH and low insulin concentration the fibrillation of insulin is less, as the histidine (at B5 and B10 positions) residues are ionized, thus the repulsion prevents self-assembly of monomers into fibrils. However, at physiological pH, the imidazole groups are uncharged. Hence, no electrostatic repulsion leads to relatively more fibrillation [379]. In our case, the fibrillation of insulin is enhanced in presence of ZnONP interface with negative surface potential. It can be explained by considering two points, first as the insulin concentration is very less, insulin oligomerization into hexamers is not significant. Second, there are structural perturbation(s) on interaction with ZnONP interface, as evident from the CD and intrinsic fluorescence experiments. The interaction of insulin molecules with ZnONP interface led to conformational changes in insulin with higher propensity to fibrillate. Additionally, as concluded from the ITC and fluorescence results, multi-layered insulin adsorption onto interface with accompanied conformational rearrangement into amyloidogenic conformation lead to shorten lag phase, the phase in fibrillation process known for nuclei accumulation. Hence, as the interface concentration increased, more platforms were available to shorten time for more nuclei formation. Thus, the conditions shorten lag phase and enhances insulin fibrillation. Considering lower free energy change of the adsorption than the change for fibrillation process, the nuclei is anticipated to fall-off into bulk medium to recruit insulin monomers towards fibril maturation, i.e. elongation phase.

However, growth of nuclei into mature fibrils, while attached to the interface, is also anticipated. A generally accepted mechanism of insulin fibrillation also suggested a similar mechanism involving the dissociation of hexamers into monomers for fibrillation [382, 420]. This monomer undergoes a structural transition, which makes it prone for fibrillation. It has also been reported that under certain amyloidogenic conditions insulin, while fibrillating, retains native-like topology [382]. Our results suggest that NPs can have enormous impacts on protein structure and conformation. The impacts depend on the physico-chemical properties of both the protein and nanoparticle interfaces. The nanoparticle with different surfaces can enhance or reduce the fibrillation. The surface of NPs could efficiently be modified with different molecules or peptides, and their effects on proteins can be assessed. Based on our results, a hypothetical scheme of ZnONP interface behaviour as loci for insulin adsorption and fibrillation has been presented in **figure 5.13**. The figure stipulates that the initial nanoparticle-protein binding results in conformational rearrangement in protein to an amyloid-prone structure, which act as a nucleus either at the interface or in bulk solution upon desorption from the interface for insulin fibrillation with enhanced cytotoxic propensity.

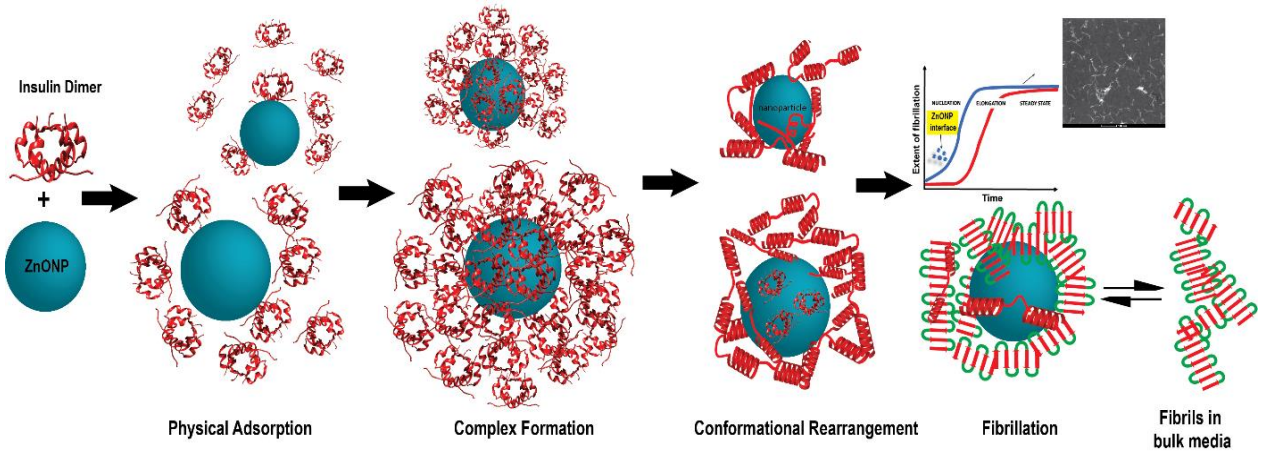

Figure 5.13. A hypothetical model representing ZnONP interface-mediated enhanced insulin fibrillation upon adsorption onto the interface.

Chapter 6

The conformational changes in a tetrameric protein, i.e. Concanavalin A

6. The conformational changes in a tetrameric protein, i.e. Concanavalin A

6.1 Introduction

Lectins are a family of carbohydrate binding, all-β sheet proteins mostly existing in multimeric forms. Monomeric subunits are mostly similar in structure with huge variations in the respective quaternary structures. Therefore, lectins present an interesting model for studying conformational states in proteins because of their conserved secondary and tertiary structures. Studying multimeric proteins will provide important insights into the impact of inter- and intra- molecular interactions on stability of the proteins. ConA is a plant lectin predominantly extracted from *Canavalia ensiformis* (jack bean). Each monomer is composed of 237 amino acids with an approximate molecular weight of 26 kDa. In physiological conditions, the protein exists as a tetramer [421]. It is an all-β protein, containing three β sheets in the form of jelly roll motif [422]. First 6-stranded back sheet, second 7-stranded front sheet and a 5-stranded smaller sheet that forms a roof between the two large sheets and holds them together [10], sterically hindering two hydrophobic cores from exposure to hydrophilic environment **(Figure 6.1)**. These β-sheets are connected by several turns of varying sizes [423]. The first hydrophobic core is present between the front and back sheet and the second is present between the front sheet and a loop, conserved for carbohydrate binding [424]. Two identical dimers have been shown to associate with the centre of their back sheets forming a tetramer [10]. It has high specificity for sugars like glucose and mannose, and one binding site each for transition metals, typically Ca^{2+} and Mn^{2+}. Demetallization of ConA results in the loss of carbohydrate binding. The amino acid residues involved in interaction with Mn^{2+} and Ca^{2+} are Glu8, Tyr12, Asn14, Asp19, and His24. The sugar-binding pocket of ConA is surrounded by Asn14, Asp16, Asp208, Tyr12, Tyr100, Leu99 and Arg228. The number of tryptophan residues in a protein is very crucial as far as the biophysical studies are concerned because they act as reporters of microenvironment of the protein, thereby giving an idea about the protein conformation. Each subunit of ConA has four tryptophan residues, (Trp40/88/109/182). In monomeric ConA, Trp40/109 remain buried and present close to the residues involved in Ca^{2+} binding, while Trp88/182 remain exposed. Consequently, Trp88/182 residues of each of the subunits are part of the monomer-monomer interface in dimer **(Figure 6.1)**. Thus, in the native ConA tetramer, none of the Trp residues are accessible [421, 425]. The stability of oligomeric proteins like ConA greatly depends on their subunit interactions. Intersubunit interactions and higher subunit buried surface area

contribute to a higher stability in comparison to monomeric proteins which rely solely on intrasubunit interactions for their stability. The impact of subunit interactions on the stability of lectins have been studied in many lectins including ConA [426, 427]. A particular study compared solvent denaturation studies on ConA and winged bean acidic agglutinin (WBA) to determine how intersubunit interactions affect stability. It showed that as ConA and WBA have different oligomerization patterns and intersubunit interactions, ConA was more stable than WBA [426]. In contrast, when the stability of ConA with soybean agglutinin (SBA) was compared, it depicted that SBA was more stable as compared to ConA as ConA forms a total of six salt bridges per dimer in contrast to ten salt bridges in SBA imparting it a greater stability [427]. ConA has been used in isolation of plasma membrane proteins [428]. It has several biological functions like induction of autophagy in cancer cells [429] and agglutination of various cell types, affinity purification of polysaccharides and glycoproteins of biological importance [430, 431]. There are also some previous reports towards the folding and unfolding of ConA. However, the precise pathways into the conformational behavior of ConA in presence of different chaotropes remain yet to be elucidated. The first part of this chapter deals with the studying the conformation of ConA in presence of three chaotropes and their varying concentrations (pH, SDS, and GdnHCl). The second part of the chapter involved studying the interaction and adsorption of ConA over ZnONP interface and the subsequent structural perturbations.

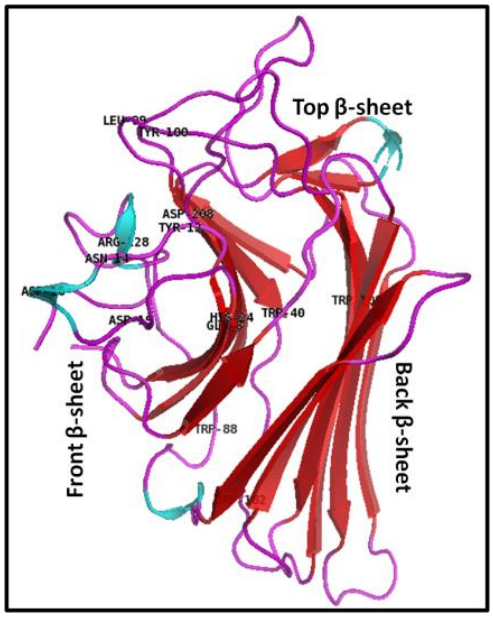

Figure 6.1. Jelly roll motif represented in monomeric ConA, depicting front, top and back β-sheets arrangement.

6.2 To study the conformation of tetrameric model protein concanavalin A in the presence of denaturants

6.2.1 Introduction

The three-dimensional structure of any native protein is determined by "thermodynamic principle", which means that amino acid sequence and environmental physicochemical parameters determine the three-dimensional structure of the protein [432]. Studying the conformation of a protein at various conditions provides useful insights for determining its stability and biological activity of the protein. Additionally, the protein conformational changes can help in identifying optimal conditions to preserve functionality, stability and broaden the range of applications [433]. The balance between activity and stability is, therefore, necessary.

Conformational studies of proteins are usually done in presence of various physical and chemical parameters. For unfolding studies, chaotropes like GdnHCl and urea are routinely used [434]. GdnHCl is believed to be an ideal chemical denaturant for protein unfolding reaction. Interaction of GdnHCl occurs to both folded and unfolded states of proteins, but its binding affinity and the number of binding sites for each of the states is different. The precise mechanism is however not understood properly [435]. On the contrary, reports relating to the denaturation of ConA by detergents have been few. Ionic detergents can denature proteins by binding strongly to oppositely charge and hydrophobic side chains at millimolar concentrations. The all α-helical proteins are sensitive towards SDS denaturation, but all β-sheet proteins are suggested to be more resistant to the denaturation by SDS [436]. Not only does chemical environment of a protein, but the physical environment like the extremes of temperature and pressure can induce conformational changes in the protein. Heat denaturation is believed to interfere with some important intra-molecular interactions in a globular protein [437]. Similarly, change in pH can also have profound effects on stability and activity of a protein.

6.2.2 Materials and Methods

6.2.2.1 Materials

Jack bean (*Canavalia ensiformis*) seeds were a gift from Dr. Sujit Kumar Bhutia, Department of Life Science, N.I.T Rourkela, Odisha, India. Sephadex-G-100, Guanidine hydrochloride (GdnHCl), Sodium Dodecyl Sulfate (SDS), and 8-anilino-1-naphthalene sulfonic acid (ANS) were obtained from Sigma (USA). All the other reagents used were of analytical grade. All

the buffers and solutions were prepared in MilliQ water, and they were filtered through 0.45 µm syringe filter before spectrophotometric measurements. Molar concentration of ANS was determined spectrophotometrically using the extinction coefficient of 7800 $M^{-1}cm^{-1}$ at 372 nm [438]. All the experiments were performed in 10 mM phosphate buffer (pH-7.4), 25 ˚C unless otherwise stated.

6.2.2.2 Protein Purification

Native ConA was purified using the protocol of Goldstein and Agarwal with slight modifications [439]. In brief, 10 % w/v jackbean powder (washed, dried and ground powder) was prepared in 10 mM phosphate buffer and stirred overnight at 4°C. Next morning the mixture was centrifuged at 7000 rpm, and the supernatant was used for a series of ammonium sulfate precipitation (30% to 90% cut-off). The pellet obtained after each precipitation was dissolved in a lower volume of phosphate buffer, and dialyzed against phosphate buffer to remove salts. The dialyzed solution was solubilized in phosphate buffer, and centrifuged at 7000 rpm, 30 mins at 4 °C. The clear supernatant obtained was further purified using Sephadex-G-100 as an affinity matrix, and eluted with 0.2 M glucose. The eluted samples were again dialyzed to remove glucose. The purity of the protein was confirmed by sodium dodecyl sulfate-polyacrylamide gel electrophoresis (SDS-PAGE) and native PAGE. The concentration of ConA was determined spectrophotometrically by Bradford assay (Bradford 1976). Pure fractions were lyophilized and stored at 4 °C, until further use. Protein stock solution was prepared in filtered and degassed 10 mM phosphate buffer.

6.2.2.3 Spectroscopic measurements

Absorption spectra were recorded on a UV–Visible spectrophotometer (Agilent Technologies, Cary100, Singapore) in a quartz cuvette. Additionally, FT-IR spectrometer also serves as a useful tool for qualitative analysis of secondary structures in proteins [440]. The IR spectra of the native protein were recorded on ATR-FTIR spectrometer, Bruker, Germany, in a range of 500-2000 cm^{-1} with a resolution of 2 cm^{-1}, and the data was further processed from the region 1580-1710 cm^{-1} specific for amide I peak in proteins [440]. Intrinsic fluorescence is usually a function of the tryptophan residues in proteins [441]. Intrinsic fluorescence measurements were performed for a 2 µM ConA using LS-55 Perkin Elmer spectrofluorimeter in a 10 mm cuvette, with a slit width of 5 nm each for excitation and emission filters with a scan speed 100 nm/min. The emission spectra were recorded between 300-400 nm with an excitation wavelength of 280 nm. Circular Dichroism (CD)

spectroscopic measurements were performed in the far UV range (190-260 nm), taking 10 µM of ConA in 1 mm cuvette using JASCO- J1500 CD spectropolarimeter purged with N_2 gas, and equipped with a Jasco Peltier-type temperature controller system. All the data were an average of three accumulations and were expressed in millidegrees

6.2.2.4 ANS Binding

Extrinsic fluorescence dyes also play important roles in studying protein conformations [46]. The surface hydrophobicity changes in a protein can be probed by ANS. It is an extensively utilized fluorescent probe for the characterization of hydrophobic patches in proteins. It has also been used to study conformational changes and molten globule structures formed upon protein unfolding [442]. The principle is based on the fact that on binding with proteins there is a blue shift of fluorescence emission maxima and increases in fluorescence intensity and lifetime, attributed to the hydrophobicity of a binding site and the restricted mobility of ANS within the given site [443]. ANS binding experiments were performed using a Synergy H1 multimode plate-reader (Biotek, USA). ANS was excited at 388 nm and the emission spectra were recorded from 420 nm to 580 nm with a 5 nm step size at 25 °C. For each set of experiments with or without the denaturant, the protein and ANS concentrations used were 5 and 100 µM, respectively.

6.2.2.5 Protein denaturation

For pH-dependent and chemical denaturation, intrinsic tryptophan fluorescence, extrinsic ANS fluorescence, and CD spectra were recorded. Stock solutions of the chemical denaturants, GdnHCl and SDS, were prepared in 10 mM phosphate buffer pH 7.4 and filtered through 0.45 µm membrane filter. Buffers of different pH ranging from 2 to 11 were prepared with either the acidic or the basic component of phosphate buffer in combination with HCl or NaOH depending upon required pH of the studied condition. For each denaturation experiment, a known amount of phosphate buffer was mixed with a fixed volume of the protein stock solution and varying amounts of the concentrated denaturant (both in phosphate buffer) to make a final volume of 0.5 mL. The mixture was then incubated at 25 °C for 4-6 hrs to ensure that the equilibrium was achieved. For extrinsic fluorescence experiments, ANS was added to a final concentration of 100 µM and incubated for 30 mins for ANS binding.

6.2.3 Results

6.2.3.1 Native ConA

Denaturing PAGE showed a single band at 28 kDa, corresponding to the weight of its monomeric subunit. Native PAGE also yielded a major band on the gel further confirming to the purity of the protein **(Figure A17)**. Secondary structural features of native Con A were further confirmed by FT-IR and CD spectra. Purified ConA showed an unusual spectrum having a trough at 222 ± 2 nm and a positive peak at 195 nm, a blueprint CD signal for lectin like proteins **(Figure 6.2A)** [444, 445]. The crystal structure of ConA is predominantly β-sheet. Additionally, the FT-IR spectrum of native ConA showed a major peak at 1636 cm^{-1} corresponding to native β-sheets in proteins **(Figure 6.2B)**. Other important peaks were also observed at 1658 and 1696 cm^{-1}, corresponding to turns which account for a considerable part of ConA structure, mainly connecting the stranded sheets to each other [109, 446].

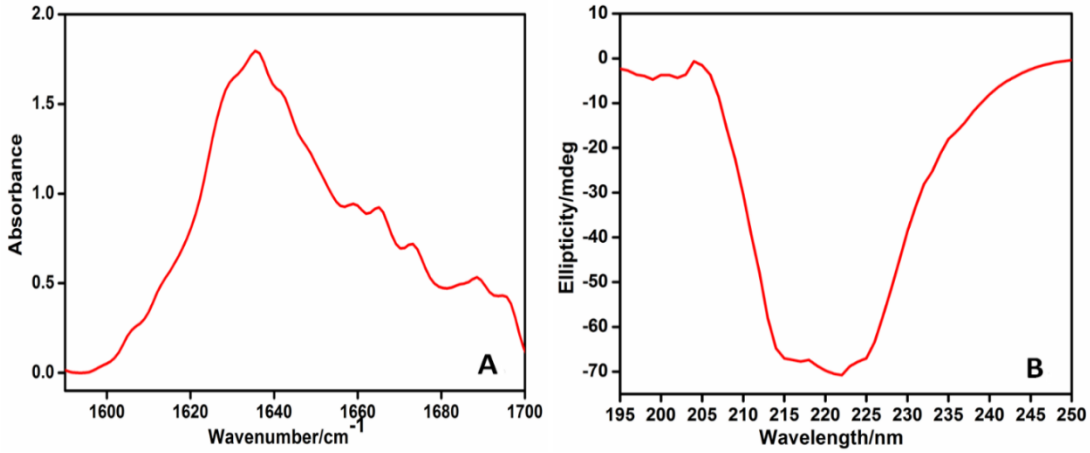

Figure 6.2. Characterization of native ConA. (A) FT-IR spectrum of 10 µM purified ConA showing a major peak at 1636 cm^{-1} and (B) far UV-CD spectrum of 10 µM native ConA in 10 mM phosphate buffer showing ellipticity (mdeg) at 223 nm, a characteristic lectin-like ellipticity spectrum.

6.2.3.2 pH-induced conformational changes

We employed CD to determine the structural changes in ConA at different pH. Native ConA shows a characteristic peak at 223 nm at pH 6 and 7. ConA exists in a dimeric form at pH 6 and as a tetramer at pH 7 [447]. In both the cases, it is seen that the prevalent structure, jelly roll motif, retained with an insignificant change in the position of the peaks. A single negative peak is at 223 nm for both, only differing in amplitude. At pH 2 there is a slight shift to lower wavelength (221 nm) which also accounts for jelly roll motif in proteins. This is consistent with a of the previous study [447]. At lower pH (< pH 4), ConA is shown to be demetallized. This can lead to exposure of amino acids involved in interaction with metal

ions and cause slight perturbations in the overall structure. However, the secondary structures remain undisturbed [448]. At higher pH of 9 and 11, a significant shift towards lower wavelength was seen with a pronounced increase in amplitude. Major negative peaks at 216 and 209 nm were observed indicating the presence of α-helical structures **(Figure 6.3A)**. It was shown earlier that at pH between 8-9 ConA undergoes an irreversible conformational transition [445]. Moreover, it was also shown that at a pH of 8.9 ConA formed amorphous aggregates [449]. This suggests that at pH > 8, key conformational changes in the secondary structure of ConA lead to the formation of some atypical, but relatively stable, conformation.

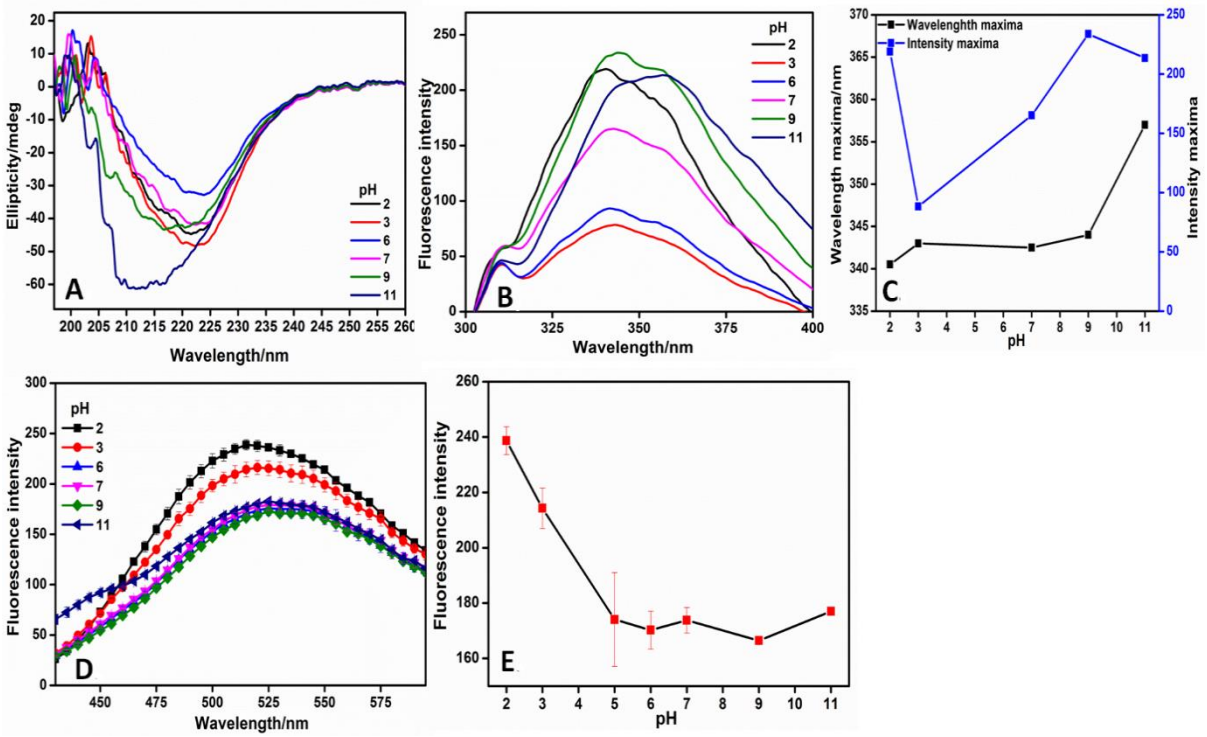

Figure 6.3. Effect of pH on ConA. (A) ConA far–UV CD spectra expressed in milli degree ellipticity for ConA in different pH conditions. (B) Fluorescence emission spectra of ConA tryptophan from 300 - 400 nm at 280 nm excitation with change in pH. (C) tryptophan fluorescence emission maxima and intensity are plotted against change in pH conditions. (D) ANS fluorescence upon binding to ConA in different pH conditions are observed from 420-580 nm with excitation at 388 nm. (E) change in ConA bound ANS fluorescence intensity at varying pH values (2, 3, 6, 7, 9 and 11) are plotted. Each data represented are an average of three scans with scan speed of 100 nm/min for both CD and fluorescence measurements.

Intrinsic fluorescence studies provide an inevitable tool for studying conformational dynamics in proteins. The tryptophan residues in protein act as an intrinsic fluorophore which

can give the idea about polarity of microenvironment surrounding the indole ring of tryptophan [450]. Native ConA at pH 7 shows emission intensity maxima at 338 nm (λ_{max}), whereas at pH 6, the dimer shows no change λ_{max} at 341 nm. Likewise, for pH 2 and 3, the λ_{max} was at 341 nm. However, there was a significant increase in intensity at pH 2, which could be due to demetallization of the dimer leading to the formation of relatively compact state with exposed Trp88/182. At alkaline pH 9 and 11, the emission maxima red shifted to 345 and 358 nm respectively **(Figure 6.3B and C),** which is accounted for the denaturation of ConA and exposure of the fluorophore into the polar environment. Tryptophan emission maximum and intensity are shown to be influenced by the polarity of its micro-environment, hydrogen bonding and other non-covalent interactions. The study indicated a red shift in increasing polarity of the tryptophan micro-environment [451].

To study the changes in the surface hydrophobicity of ConA, hydrophobic patch binding extrinsic fluorescence probe, ANS, was used. Native ConA at pH 7 showed a major peak around 525 nm, revealing a less accessible hydrophobic core and more compact structure of ConA. At pH 2 it is seen that there is a characteristic blue shift from 525 nm to 515 nm in the λ_{max}, accompanied by an enhancement of fluorescence intensity **(Figure 6.3D and E)**. A plausible explanation for the observation could be that the demetallization of ConA at low pH resulting in an enhanced exposure of protein hydrophobic regions leading to increased number of ANS binding, hence the ANS quantum yield. Additionally, the presence of dimeric states at low pH suggests relatively more exposed hydrophobic patches than in the tetrameric form. At high pH (9 and 11), no significant changes in the ANS fluorescence spectra were seen, though a huge conformational change was observed in the CD spectra. This could be explained by the fact that, at extreme basic pH 9 and 11, ConA adopts a conformational state, which is significantly different from its native form with the hydrophobic patches buried in the rearranged structure. Thus, the data altogether indicated that ConA is fairly stable within the range of 3-8, while denaturation is evident at extreme basic pH, i.e. 9 to 11. We thus hypothesize that at high pH ConA may adopt either α-helical conformation or other disordered intermediates, which can ultimately lead to aggregation [449].

6.2.3.3 SDS induced conformational changes

SDS is an amphiphile, which has long been known to induce conformational changes in protein at concentration of about 10 mM [452]. SDS induced perturbations in ConA structure

were studied by following tryptophan and ANS fluorescence in absence and presence of varying SDS concentration whereas, the change in secondary structure, in presence of varying SDS concentration, was studied using CD polarimeter. The change in ellipticity with increase in SDS concentration was attributed to relatively higher ordered protein structures. In CD experiments, initially with an increase in SDS concentration upto 1 mM very small shift towards higher wavelength and increase in the ellipticity is observed **(Figure 6.4A)**. The change depicts the SDS binding to ConA and insignificant changes in the secondary structure. This general increase in the ellipticity on SDS binding to proteins is also reported in other studies as well [453]. However, above 2 mM SDS, a shift towards lower wavelength was observed. These ellipticity maxima shifted from 222 nm to 208 nm and further to 206 nm at 5 mM and 10 mM SDS, respectively **(Figure 6.4A)**. This shift is also accompanied by more than a two-fold increase in amplitude of the ellipticity at 208 nm, indicating introduction of α-helical content in ConA. The critical micelle concentration (CMC) of SDS in 10 mM phosphate buffer is 4.61 ± 0.01 mM [454], implying that below the CMC, SDS leads to minute changes in the overall conformation of ConA. However, the secondary structure is disrupted when SDS concentration higher than its CMC is used. SDS concentration higher than 2 mM is required to bring about the disruption of the protein structure. The SDS mediated unfolding of proteins thus shows presence of not only unordered states but also significant amounts of α-helical intermediates. The process of SDS mediated denaturation, where protein rearrange into predominantly all-α protein, is called as reconstructive denaturation [455]. Tryptophan fluorescence showed an increase in the fluorescence intensity with increasing SDS concentration, with maximum change at 10 mM depicting a change in the microenvironment of tryptophan residues. However, the emission maxima of tryptophan showed insignificant shift with increase in SDS concentration. The increase in quantum yield of tryptophan residues in ConA, on introducing SDS in microenvironment, indicated that either the ConA structure is getting compact on conformational rearrangement or exposed tryptophan residues, Trp88/182 in native conformation, are buried in hydrophobic environment of SDS micelle.

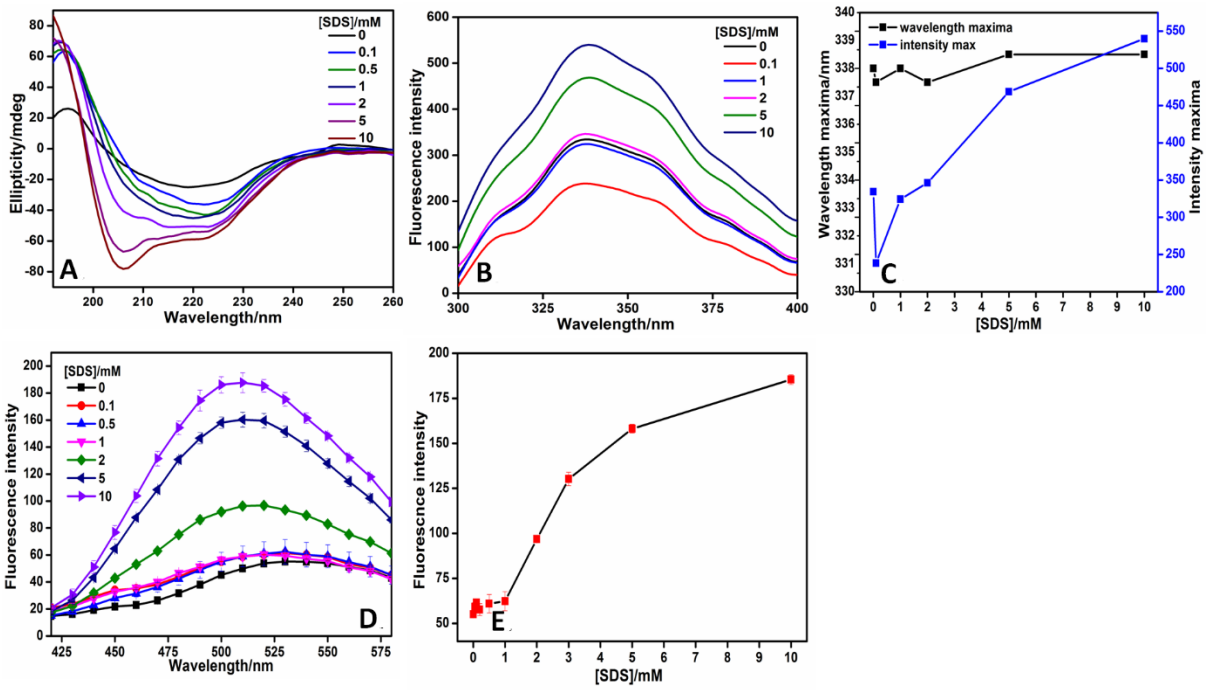

Figure 6.4. Effect of SDS on ConA. (A) Far–UV CD spectrum for ConA expressed in milli degree ellipticity with change in SDS concentrations. (B) ConA fluorescence emission spectra for tryptophan from 300 - 400 nm with excitation at 280 nm in different SDS concentrations. (C) the tryptophan emission maxima and intensity are plotted against SDS concentrations. (D) ConA bound ANS fluorescence emission spectra are plotted from 420 – 580 nm with excitation at 388 nm in different SDS concentrations. (E) emission maxima are plotted against SDS concentrations. Each data represented are an average of three scans with scan speed of 100 nm/min for both CD and fluorescence measurements.

At micellar levels of SDS, the microenvironment around tryptophan is getting more nonpolar, and therefore, although no red shift during is observed, there is increase in the quantum yield **(Figure 6.4B and C).** In both the cases, the orientational and vibrational entropies tryptophan indole ring will be restricted, resulting into enhanced quantum yield [456]. When the ANS fluorescence of the SDS-ConA complexes was measured, it appeared that till 1 mM of SDS, there was a negligible change in the fluorescence maxima depicting the inaccessible hydrophobic surface of ConA. Concurrent with the CD spectroscopy study, it was seen that at 2 mM SDS, there is a two-fold increase in ANS quantum yield. The increase was accompanied by a large shift from 530 nm to 515 nm. At 5 and 10 mM, the emission maxima showed further shift to 508 nm with an increase in the fluorescence intensity. Both rise in fluorescence and the blue shift indicate the disruption of protein structure at high SDS concentration and presence of partially folded intermediates, molten globule like structures,

for which ANS has high affinity **(Figure 6.4 D & E)**. This increase in fluorescence intensity can be rationalized to ANS binding to the hydrophobic patch in ConA. Molten globule structures are rich in secondary structures lacking important tertiary contacts. In case of ConA, interestingly a switch from the native jelly-roll motif to the all-α conformation is seen in presence of SDS, which is quite evident from CD spectroscopy. However, the fact that ANS could be trapped in the hydrophobic interior of SDS micelles should not be ignored [457]. The mechanism of SDS mediated protein denaturation have been contradicting. Some studies have shown that the main driving force is electrostatic interactions between the negatively charged SDS with the positively charged residues in proteins [453]. However a different theory states that at sub-CMC concentrations, SDS monomers bind to proteins by predominantly hydrophobic interactions causing unfolding of the tertiary structure. Whereas, at concentrations higher than CMC, the micelles nucleate on the hydrophobic patches of the protein chain causing the micellar structure to expand [457]. The expansion of micellar structures lead to non-covalent interaction perturbations among the unfunctional groups of amino acids side chains, which mainly intricate into the micellar structure. Thereby, the perturbed interaction result in an expanded and weakened structure, resembling a molten globule. A particular study indicated the effect of micelle shape and ionic concentration on protein structure [458].

6.2.3.4 Guanidine hydrochloride induced conformational changes

Varying concentration of GdnHCl from 0 M to 4 M was used to analyze the denaturation and conformational changes in ConA. The far Ultra-Violet (UV) CD spectrum of native ConA showed a major trough at 222 nm. There was a significant reduction in the ellipticity from 0 M to 4 M GdnHCl, which indicate the loss of secondary structures. At 1 M GdnHCl concentration, the major trough is at 222 nm with a shoulder at 210 nm, mostly accounting for the lectins with some degree of unfolding. In presence of 2 M GdnHCl, a trough is observed at 217 nm mostly accounting for native β-sheet in proteins. Additionally, another peak at 212 nm is also observed, similar to the one in case of 1M GdnHCl that can be due to a typical β-sheet structure. We thus propose the presence of intermediate monomeric structures of ConA from 1-2 M GdnHCl. At 3M, there is a significant reduction in the ellipticity with a shoulder at 212 nm indicating the presence of disordered structures and loss of secondary structures [288]. Likewise, at 4 M GdnHCl, the ellipticity further reduced, resulting in significant loss of prominent CD signal suggesting complete unfolding **(Figure 6.5A)**.

Maximum change of amplitude in ellipticity was observed at 222 nm so, the extent of denaturation was expressed in terms of fraction folded (α) by evaluating the ellipticity at 222 nm at any given (i^{th}) concentration of GdnHCl, and can be calculated from the equation 1:

$$\alpha = ([\theta]_i-[\theta]_u)/ ([\theta]_f-[\theta]_u) \qquad \textbf{Equation 2}$$

Where $[\theta]_i$ is the ellipticity at any particular (i^{th}) concentration of GdnHCl, $[\theta]_u$ is the ellipticity where the protein is unfolded usually at the highest GdnHCl concentration, and $[\theta]_f$ is the ellipticity at which the protein fully folded, at the beginning of the unfolding experiment [459] and fraction denatured is (1-α).

Tryptophan fluorescence studies shows that upto 1 M GdnHCl, there is an insignificant change in fluorescence intensity as well as emission maxmia, indicating that although there could be slight perturbations in the quaternary structure of the protein, major changes do not take place keeping the environment of the tryptophan residues intact. However, increasing the GdnHCl concentration upto 4 M leads to an increase in intensity and a large stoke shift in the emission maxima from 336 nm to 358 nm accountable for exposure of tryptophans to more polar environment, which could be due to unfolding of ConA **(Figure 6.5B and C)**. The fraction of protein in the denatured state was calculated from the I_0 (fluorescence intensity without denaturant), I_{max} (Fluorescence intensity at maximum denaturant concentration) and I (fluorescence intensity at a particular denaturant concentration)

$$F_d = ([I- I_0]/ [I_{max}- I_0]) \qquad \textbf{Equation 3}$$

Both CD and fluorescence data support the presence of intermediates at low GdnHCl concentrations, which could either be structured or unstructured monomers ahead of complete unfolding **(Figure 6.5D)**. Additionally, the ANS data were also concurrent with CD and fluorescence studies. It is seen that the ANS fluorescence maxima in presence of intact ConA was at 520 nm, depicting the inaccessibility of ANS for the hydrophobic core of ConA, which shifts to 470 nm in the presence of GdnHCl. Initially, there was a rise in the fluorescence intensity up to 1 M, thereafter a significant decline in the fluorescence intensity with lowest at 2 M GdnHCl was observed. Above 2 M GdnHCl, insignificant change in the fluorescence intensity was observed **(Figure 6.5E and F)**. A rise in the fluorescence intensity suggests that the hydrophobic patches in ConA were exposed. A hydrophobic region is present between the front sheet and a loop conserved for carbohydrate binding [444]. At 1 M GdnHCl, some degree of unfolding could expose this site leading to increase in ANS binding. Thus, the increase in ANS binding resulted in the molten globule-like intermediates, whereas

low fluorescence intensities could be linked to the unfolding of the hydrophobic patches present in the protein.

Combining the results of both CD and fluorescence studies, we conclude that possibly around 1 M GdnHCl, an intermediate structure in the tetramer is formed having the characteristics of a molten globule. Following this, there could be deoligomerization of ConA leading to the persistence of monomers of ConA. High concentrations of GdnHCl, above 2 M lead to complete denaturation of ConA, all-random coil conformation. GdnHCl being an ionic chaotropic agent could provide some stability to the protein structure at low concentrations. Previously ConA was reported to undergo a three state unfolding mechanism, induced by urea and GdnHCl, i.e. tetramer follwed by structured monomers to unfolded monomer. It was shown that the free energy preference of quaternary tetrameric structure was greater than that of the tertiary monomeric structure, owing to structural stability of ConA by subunit association [460]. Low concentrations of GdnHCl can help in stabilizing the structure of a protein [435]. Our data is consistent with the presence of a stable intermediate evident in both the CD and fluorescence studies.

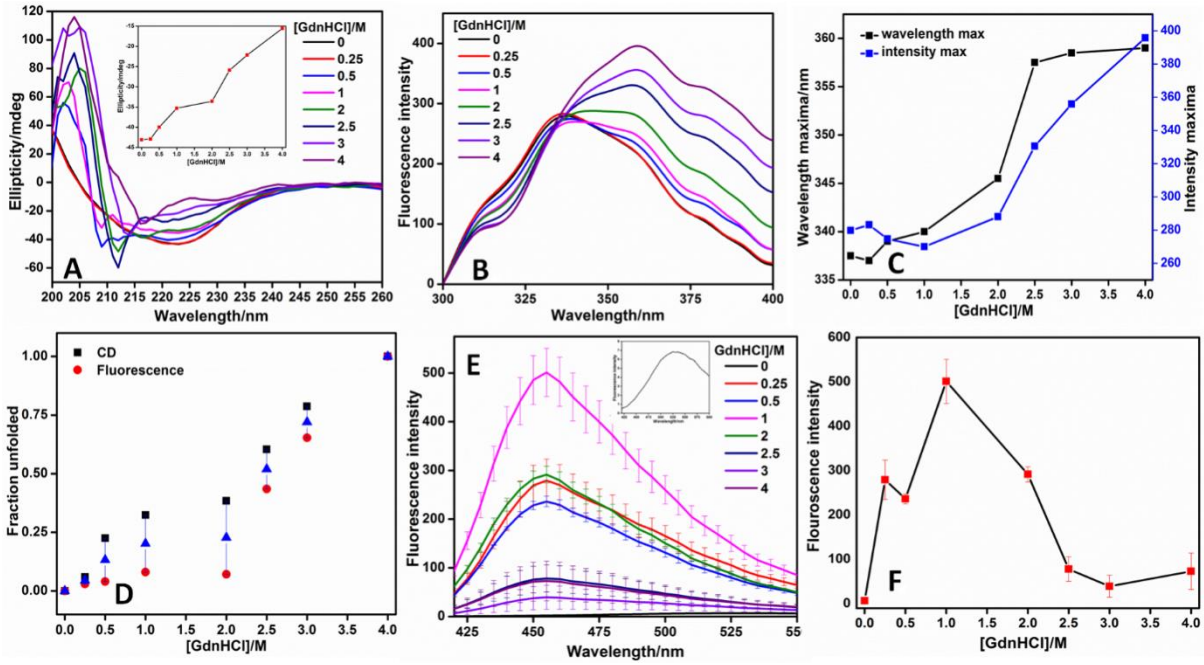

Figure 6.5. Effect of GdnHCl on ConA. (A) Far–UV CD spectrum of ConA expressed in milli degree ellipticity in absence and presence of GdnHCl, and the inset shows the change in ellipticity at 222 nm. (B) Fluorescence emission spectra of ConA tryptophan from 300 - 400 nm are plotted with excitation at 280 nm. (C) The λ_{max} and maximum fluorescence intensity are plotted against change in GdnHCl concentration. (D) Fraction of unfolded protein

calculated from CD and intrinsic fluorescence experiments are plotted against change in GdnHCl concentrations. (E) Fluorescence emission spectra of ConA following ANS binding from 420 - 580 nm with excitation at 388 nm are plotted, and the inset shows ConA bound ANS fluorescence emission spectrum without GdnHCl. (F) The change in ConA bound ANS fluorescence maxima with GdnHCl concentration are plotted. Each data represented are an average of three scans with a scan speed of 100 nm/min for both CD and fluorescence measurements.

6.2.4 Discussion

Although much has been studied about the structural features of ConA, some key features regarding its precise denaturation pathways are missing. In the present study, we aimed to study the conformational transitions in ConA under different pH, and different concentration of GdnHCl and SDS in equilibrium conditions. GdnHCl has long been used to study the unfolding reaction in proteins [435]. However, reports relating to denaturation of proteins by the ionic detergents like SDS have been comparatively few [453, 457]. We characterized the denaturation of ConA by Circular Dichroism spectroscopy, tryptophan fluorescence and ANS fluorescence. It could be inferred that there can be different denaturation pathways for a particular protein when exposed to different types of chemical and physical extremes. Deanturation can involve several different intermediates depending upon the microenvironment to which the protein is exposed. Thus, it becomes clearer that denaturation of a protein is not just a simple process of folding in reverse. Denaturation can be any mechanism that interferes with the intra and inter molecular interactions in the protein and disrupts the tertiary structure of protein. **Figure 6.6** shows a graphical abstract of the different modes of denaturation of ConA by varying GdnHCl, hydronium ion and SDS concentration respectively. The figure depicts that, GdnHCl leads to formation of monomers followed by complete unfolding of ConA. However, SDS could not unfold the protein but results in the formation of helical structures. The effect of high and low pH are different on ConA.At low pH ConA is shown to form native like molten globular structure whereas at high pH it is shown to form aggregates with a considerable fraction of helical intermediates.

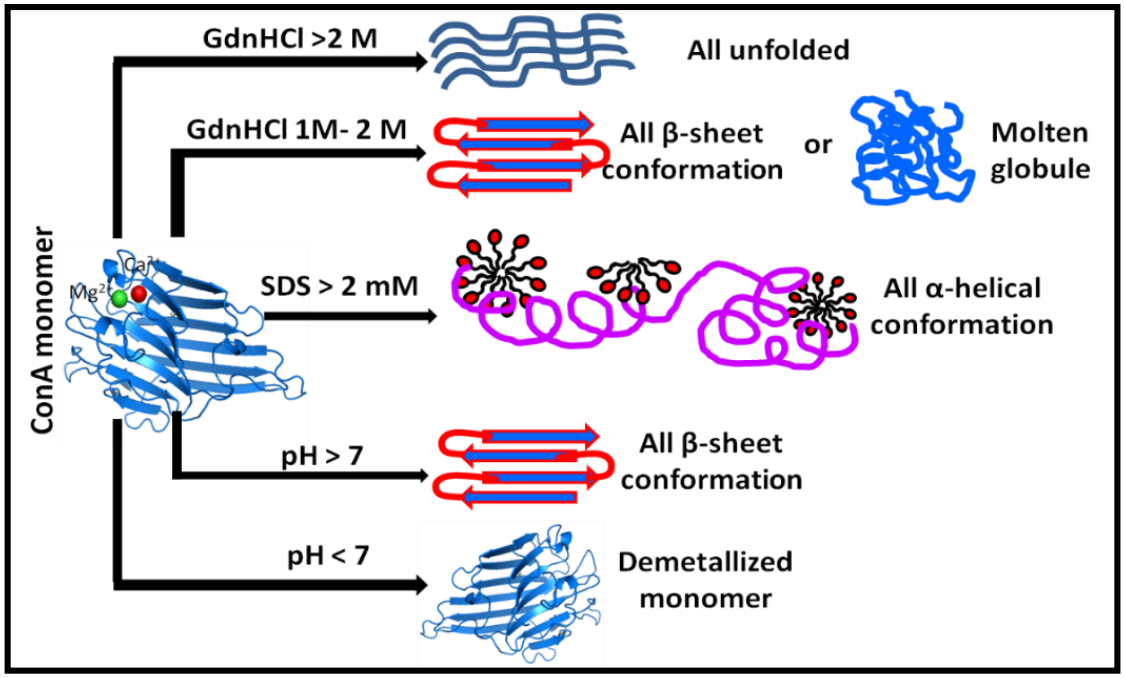

Figure 6.6. Schematic diagram depicting ConA conformational changes in different stress conditions. Guanidine hydrochloride shows complete unfolding of ConA above 2 M concentration, whereas 1–2 M GdnHCl triggers formation of the molten globule-like conformation. At basic pH, ConA adopts all β-sheet conformation, and at acidic pH it retained demetallized monomeric jelly roll motif. Additionally, in presence of > 2 mM SDS, ConA undergoes conformational rearrangement into a predominantly α-helix conformation, rather a lectin-like all β-sheet conformation at lower concentrations of SDS.

6.3. The conformational change in a tetrameric protein, i.e. Concanavalin A, in presence of ZnONP

6.3.1 Introduction

It has been speculated that in principle any protein, even with well-defined structures under appropriate destabilizing conditions can form either amorphous or amyloid aggregates. Thus, the formation of aggregates could be considered as a generic property of any protein [41]. Conformational changes and disruption of secondary structures are known to play important roles during aggregation of proteins, the main reason anticipated is the exposure of hydrophobic patches, which are normally, are buried in proteins [461-463]. Variety of external factors like temperature, pH, ionic strength, co-solutes can determine the conformational preferences of a protein to adopt amorphous or amyloid aggregates [231, 361, 464, 465]. Interestingly, ConA shares a striking structural homology with SAP, which forms the main constituent of many amyloid deposits **(Figure 6.7)** [466]. SAP is also an all β-sheet protein belonging to Concanavalin A like lectins superfamily, bears close resemblance with legume lectins and also contains a jelly-roll motif [467]. This makes ConA an interesting model to study amyloidosis in large globular proteins. Recently, there have been studies on some important aspects of ConA amyloidosis [449, 468-471]. However, detailed studies and mechanisms are still sparse. As discussed in the previous chapters, studying the effect of NPs on protein conformation is of utmost importance, thus, this study aims at studying the conformational changes in ConA in presence of ZnONP and subsequent amyloidogenic effects.

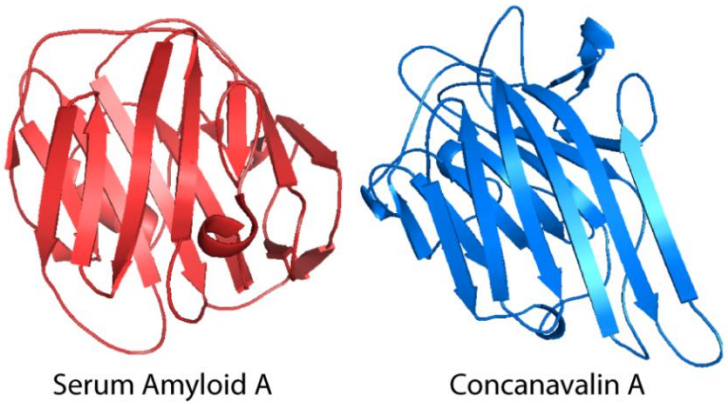

Figure 6.7. Figure showing cartoon representations of Serum Amyloid A monomer (PDB: 2A3W) and Concanavalin A monomer (PDB: 1NXD). Note the striking structural similarity between the two proteins.

6.3.2 Materials and Methods

6.3.2.1 Materials

ConA was purified as stated in the previous part of this chapter. Other chemicals and buffers were same as used in other chapters, and were used in the same way unless otherwise stated.

6.3.2.2 Synthesis and characterization of ZnONP and ConA-ZnONP complexes

ZnONPs were synthesized using the same protocol as described in **chapter 3b** and used as such without any further modification.

6.3.2.3 UV-Vis spectroscopy

5 μM ConA was incubated with increasing concentration of ZnONP (0-64 μg/mL) for 4-6 hrs. Following this, absorption spectra were collected from 200-500 nm on an Agilent UV-Vis spectrophotometer. In a different setup, ZnONP was kept constant (64 μg/mL), and the concentration of ConA was increased from 0-5 μM and the absorbance spectra were recorded. Zeta potentials of the same samples were also analysed by zeta-sizer (Malvern Zetasizer, Nano ZS90, Netherland).

6.3.2.4 Steady state fluorescence

Intrinsic fluorescence measurements were collected on an LS-55 Perkin Elmer spectrofluorimeter in a 10 mm cuvette. As mentioned above, 5 μM ConA incubated with increasing concentrations of ZnONP and the steady state fluorescence spectra was collected. Tryptophan was excited at 280 nm and emission was collected between 300-400 nm, slit width was kept 2.5 nm for both excitation and emission filters.

6.3.2.5 ANS fluorescence

ANS binding experiments of ConA-ZnONP complexes were performed using a Synergy H1 multimode plate-reader (Biotek, USA). ANS was excited at 388 nm and the emission spectra were recorded from 420 nm to 580 nm with a 5 nm step size at 25°C. The protein and ANS concentrations used were 5 and 100 μM, respectively [472]. Additionally, a time dependent study was also performed upto 24 hrs, with the same excitation wavelength and emission at 480 nm, which is the λ_{max} of ANS upon protein binding.

6.3.2.6 CD polarimetry

Far UV-CD spectra (190-260 nm) of ConA-ZnONP conjugates were collected on 2 mm cuvette in a JASCO- J1500 CD spectropolarimeter purged with N_2 gas, and equipped with a Jasco Peltier-type temperature controller system. Each spectrum obtained were an average of three accumulations. All the other parameters were kept same as with other proteins in the previous chapters.

6.3.2.7 Thioflavin T assay

Stock solutions of both ConA and ZnONP were sonicated in an ultrasonic water bath before setting up the fibrillization reactions. Increasing concentration of ZnONP was added to 5 μM ConA in 10 mM phosphate buffer (pH 7.4) and 20 μM of ThT in a fibrillation reaction volume of 200 μL each. All the samples were prepared in triplicates. Fibrillation reaction was set up in a 96-well clear, flat bottom plate at 25°C in shaking conditions (180 rpm) in a Synergy H1 multimode plate-reader (Biotek, USA). ThT dye was excited at 440 nm and emission readings were collected every 15 mins at 490 nm for a period of 0-30 hrs.

6.3.2.8 Transmission electron microscopy

ConA was incubated with 32 μg/mL of ZnONP for 24 hrs. For TEM, samples were sonicated in a bath sonicator for 5 minutes. In a 20 μl of sample, 2 μL of 2% uranyl acetate, was added and was incubated for 10 minutes. The sample was then dropped onto carbon coated copper grids (Ted Pella Inc., USA) and allowed to be absorbed for 10 minutes, followed by washing with sterile deionized water. TEM imaging was performed on TEM-TECNAI T F 30 G2 Super Twin by FEI. Elemental mapping was performed on HAADF-STEM mode.

6.3.3 Results

6.3.3.1 UV-Vis Spectroscopy

UV-visible spectroscopy is the most common method to monitor the changes in absorption spectra of NPs and the conjugated protein (Bhunia, Samanta et al. 2013) for studying interactions between them. Here in the **figure 6.8A**, as the concentration of ZnONP is increased, there is an increase in intensity of the peak centred at 354 nm, corresponding to ZnONP [473]. The increase in the intensity is due to increasing ZnONP concentration. Interestingly, there is an increase in the intensity of the peak centred at 280 nm specific for the tryptophan residues in proteins **(Figure 6.8B)**. The increase in the intensity, despite the concentration being same in all samples can be in part due to the change in microenvironment

of tryptophan residues [441]. Also, a particular study has related it to the formation of ground state complex and the complex promotes more absorption of photons in the system [345, 474, 475]. In the next set of experiments, ZnONP was kept constant and the concentration of ConA was increased from 0 to 5 μM **(Figure 6.8C)**. A slight red shift of the ZnONP SPR peak from 354 nm to 359 further confirmed the adsorption of ConA over ZnONP surface [476, 477]. The adsorption of ConA over ZnONP interface causes an increase in the diameter of ZnONP, causing a bathochromic shift in LSPR peak [477]. Moreover, the adsorption of ConA over the ZnONP was analysed by the change in zeta potential measurement of ZnONP with increasing concentration of ConA **(Figure 6.8D)**. ZnONP alone has a negative potential around -43 mV, indicating its colloidal stable in deionized water [285]. As the concentration of ConA in increased in the solution, the ζ-potential keeps on decreasing in a concentration dependent fashion, which suggests the neutralization of ZnONP surface by ConA. At 2 μM ConA, ζ-potential of the complex is about half of initial, after which a kind of saturation is achieved. This supports the previous explanation of ground complex formation between ConA and ZnONP. With a pI of 5.5-6.5, ConA is slightly negatively charged at neutral pH. Thus, when more and more ConA molecules are adsorbed over ZnONP, its surface charge is screened by ConA and ζ-potential of ConA becomes the effective ζ-potential as depicted in the **figure 6.8D.**

6.3.3.2 Stoichiometry of ConA-ZnONP binding: ITC

The thermodynamic parameters of ConA binding to ZnONP, were studied by ITC at 25 °C. The top panel of **figure 6.9** shows the raw titration profile while bottom panel shows the heat flow per mole of the titrant versus the molar ratio of protein: NP at each consecutive injection. The molar concentration of 32 μg/mL of ZnONP was calculated to be 16.3 pM. The binding event is highly exothermic in nature, as depicted by a negative energy change. The complete thermogram was fitted to a single-site binding curve. The value of binding constant (K) indicates a moderate affinity of ConA-ZnONP binding. The binding of ConA to ZnONP is enthalpically driven as indicated by the highly negative ΔH value. This further suggests that the mode of interaction between two entities is polar in nature, mostly hydrogen bonding, electrostatic interaction and Van der Waal interactions. Likewise, the highly negative value of (ΔS), points towards the absence of hydrophobic interactions. The free energy was calculated to be -7.481 Kcal/mol which suggests an overall favourable interaction between the ConA and ZnONP. The polar interactions between them is most likely attributed to the polar amino acid residues on the surface of ConA with hydroxyl groups on the surface of ZnONPs.

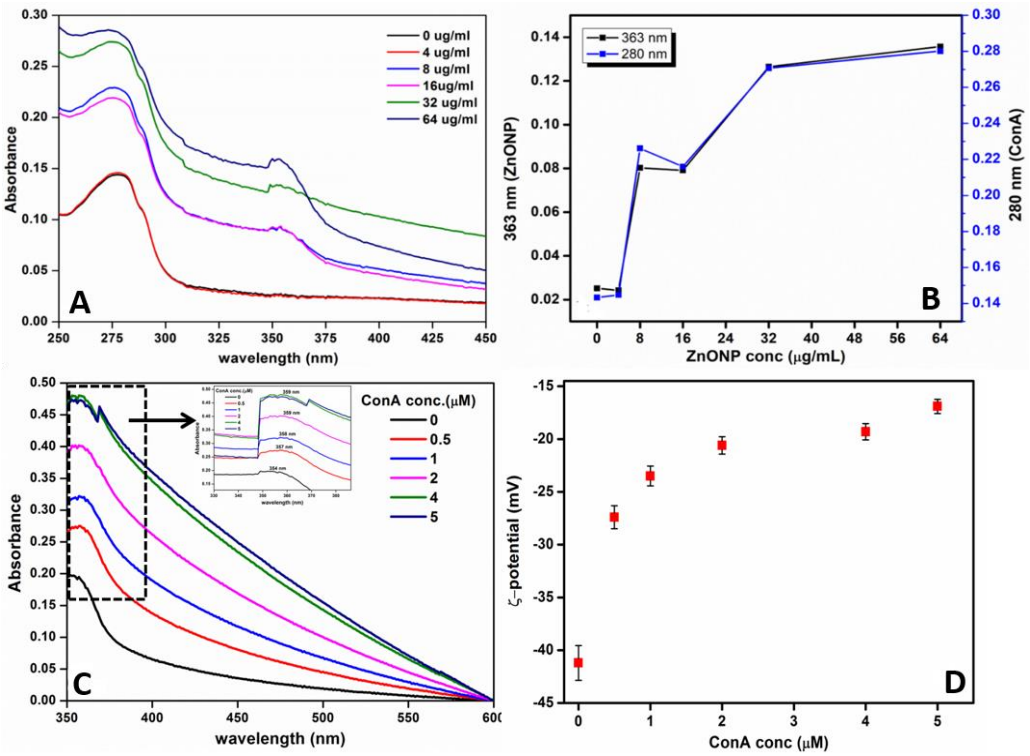

Figure 6.8. Characterization of ConA adsorption over ZnONP interface (A) UV-Vis spectra of ConA with increasing ZnONP concentration, (B) peak positions of SPR maxima (363 nm) and ConA (280 nm), (C) UV-Vis spectra of 64 µg/mL ZnONP, with increasing ConA concentration, inset shows the zoomed image showing red shift and (D) charge neutralization 64 µg/mL ZnONP, with increasing ConA concentration by zeta potential analysis.

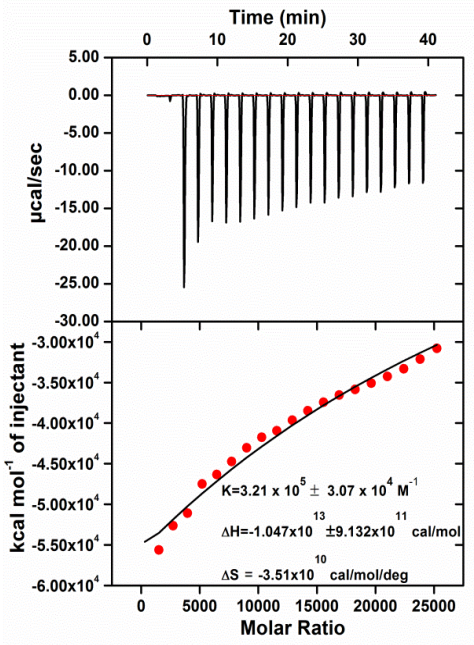

Figure 6.9. ITC isotherm for 32 µg/mL ZnONP titration with 2 µM ConA. Upper panel shows heat released per second whereas lower panel shows the heat released with increasing molar ratio of ConA.

6.3.3.3 Steady state intrinsic fluorescence

Intrinsic fluorescence of proteins from the aromatic residues present excellent probes for studying the conformational dynamics in a protein. More so, they give idea about the microenvironment of the protein [441]. This property of proteins has been employed to study the interaction of NPs with proteins in several previous studies [187, 345]. **Figure 6.10A** shows change in the fluorescence spectra with increasing ZnONP concentration. The peak is centered at 342 nm, specific for tryptophan residues. The decrease in fluorescence is due to the slight perturbations in tertiary structural changes in ConA [472]. At the highest ZnONP concentration, there is a little red shift indicating small change in the polarity around the tryptophan residues. The reduction may also be due to the quenching of fluorescence by ZnONP as reported in previous studies [345]. To decipher the type of quenching (static or dynamic), we plotted the Stern-Volmer plot **(Figure 6.10B**) using the Stern Volmer equation. The Stern Volmer plot is fitted to a straight line equation and the slope gives the Stern Volmer constant (K_{sv})

$$\mathbf{F_0/F = 1 + K_{SV}[Q] = 1 + K_q\tau_0[Q]} \qquad \textbf{Equation 4}$$

The Y-axis shows the ratio F_0/F where F_0 is fluorescence intensity maxima without the quencher, and F is the fluorescence intensity maxima at different quencher concentration (Keizer 1983). The X-axis shows the concentration of the quencher (ZnONP) in moles. Here 32 µg/mL ZnONP was calculated to be 16.3 pM. Stern Volmer constant was found to be 3 x 10^{10} M^{-1}. Fluorescence lifetime (τ_0) without quencher for biological macromolecules is usually taken as 5.78 $\times 10^{-9}$ seconds [478]. The quenching rate constant (K_q) was calculated to be 5 x 10^{18} $M^{-1}s^{-1}$. For a static quenching, the value must exceed 2 x 10^{10} M^{-1} s^{-1}, which is maximal for a diffusional or collisional quenching in biomolecules. Thus, the results suggest that the quenching is static. Static quenching involves the formation of a ground state complex between the quencher and the biomacromolecule, which is also concurrent with our UV-Vis results. Hence, it can be inferred that there is a complex formation between ConA and ZnONP, due to the adsorption of ConA molecules over ZnONP interface.

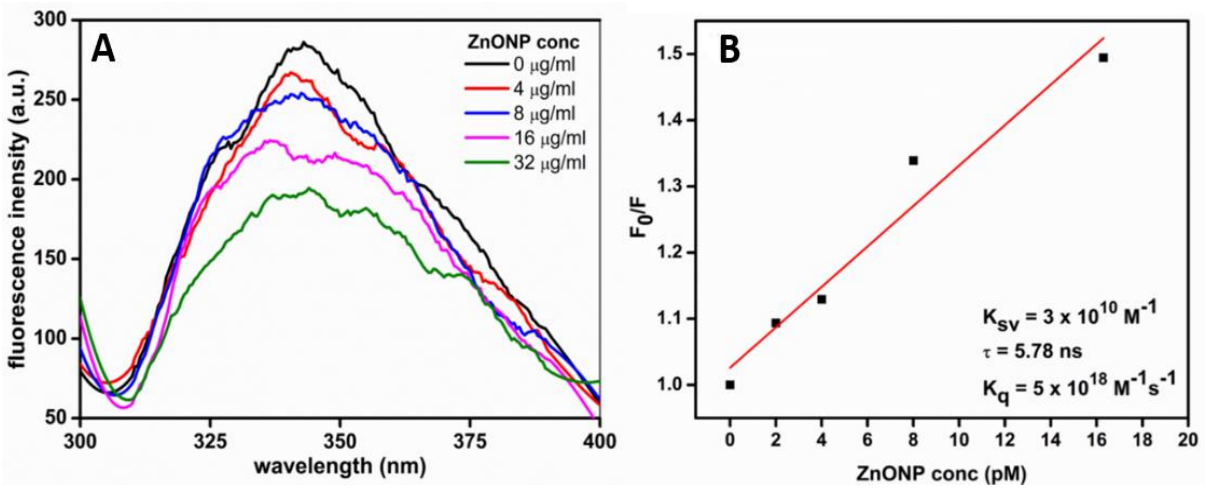

Figure 6.10. Intrinsic fluorescence of ConA in presence of varying ZnONP concentrations. (A) Fluorescence spectra of ConA in presence of ZnONP and (B) Stern-Volmer plot, as a measure of fluorescence quenching of ConA with increasing ZnONP concentrations.

6.3.3.4 ANS Fluorescence

Figure 6.11 shows the ANS fluorescence spectra of ConA with increasing concentration of ZnONP. The peak was centred at 523 nm suggesting weak binding between ANS and ConA. This is can be explained by the fact that ConA has a compact, globular structure, thus the inaccessibility of ANS to ConA [472]. With the addition of ZnONP concentration, there is an increase in the fluorescence intensity, at both 523 and 470 nm **(Figure 6.11A)**, mostly evident at the highest ZnONP (64 µg/mL). As stated above, in the presence of ZnONP, ConA forms a ground state complex with the nanoparticle. This explains the structural perturbations and exposure of hydrophobic patches in ConA upon interaction with ZnONP. Thus, from the intrinsic and ANS fluorescence results it can be inferred that the tryptophan residues (trp 40/109) that remain buried in ConA are loosened or perturbed following ZnONP addition. Additionally, the trp residues that relatively remain exposed (trp 88/182) may be interacting with ZnONP. This gives a plausible explanation for the decrease in the intrinsic fluorescence and insignificant change in ANS fluorescence in the presence of ZnONP. Furthermore, we also performed time dependent ANS fluorescence for ConA-ZnONP conjugates **(Figure 6.11B)**. It is evident that in ConA alone and low ZnONP, the change in the fluorescence is insignificant, suggesting that the hydrophobic patches in ConA remain intact and the hydrophobic patches are in accessible to the environment. Conversely, at high ZnONP concentration, there is a rise in ANS fluorescence over a period of 24 hrs. This shows ConA and ConA with low ZnONP concentrations remain stable, while at high ZnONP concentration there is a concentration dependent continual increase in the ANS fluorescence

indicating the disruption tertiary structure and increased exposure of hydrophobic patches in ConA.

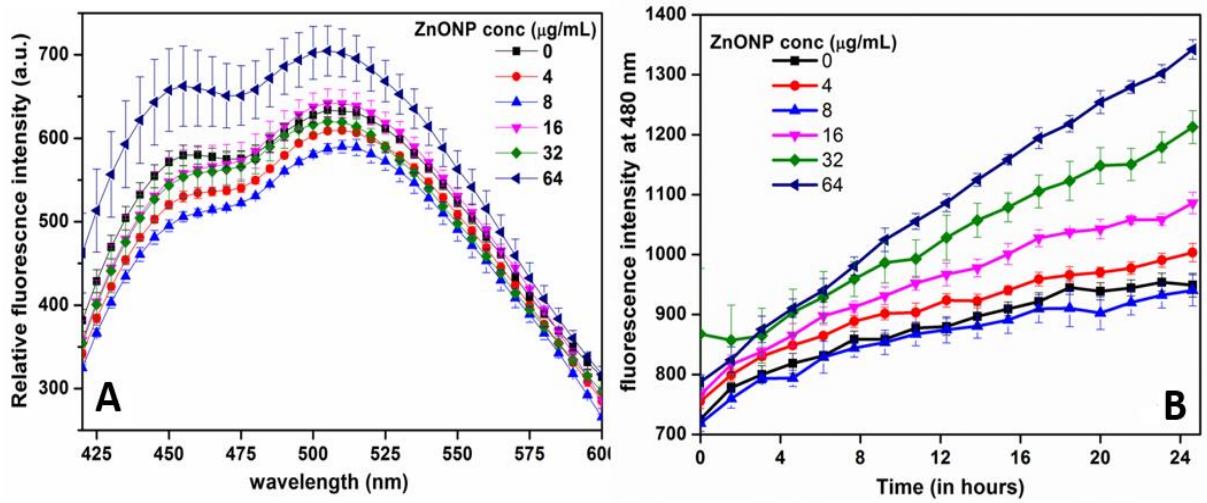

Figure 6.11. ANS dye binding to ConA in presence of varying ZnONP concentrations. (A) ANS fluorescence spectra and (B) time dependent ANS fluorescence when bound to ConA incubated with different concentrations of ZnONP interface. ANS was excited at 388 nm and emission was collected at 480 nm.

6.3.3.5 CD Polarimetry

Further, changes in the secondary structure in ConA upon binding to ZnONP were assessed by CD Polarimetry **(Figure 6.12)**. Native ConA shows a major minimum at 220 nm, specific for lectins [460, 472]. Lectins are all β-sheet proteins with major trough between 222 ± 2 nm. With increase in the ZnONP concentration, the ellipticity of ConA decreases. Very slight change in the peak position (220 to 217 nm) was observed.

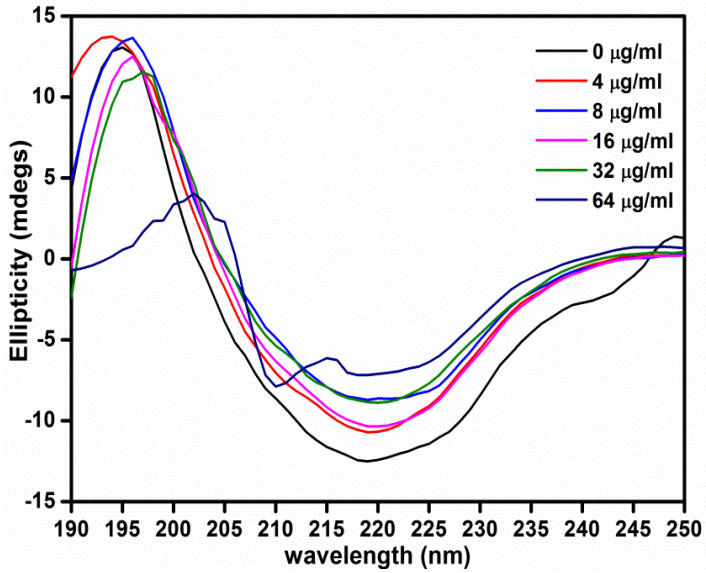

Figure 6.12. Far-UV CD spectra of ConA with increasing concentration of ZnONP.

Although, both the peak positions correspond to β-sheets, it is difficult to distinguish if they are native or amyloid β-sheets. However, a decrease in the ellipticity can be accounted for the formation of aggregates, which might be due to sedimentation of aggregates. However, it was suggested in a particular study relating ConA aggregation that shifting of the major minimum from 220 to 215 indicated conversion of native β-sheet to β-aggregates [471]. At the highest concentration of ZnONP i.e. 64 μg/mL, there is drastic change in secondary structural elements. Peaks at 209 and 216 nm indicate formation of helical elements at higher ZnONP, but loss in the positive peak suggests huge structural perturbations at this concentration, and also some degree of denaturation.

6.3.3.6 Thioflavin T assay

As from the above studies, it is evident that following adsorption of ConA over ZnONP surface, secondary structures almost remain intact, but tertiary structure is perturbed. To further study if ZnONP can cause amyloid aggregation of ConA, we performed ThT assay on ConA with increasing ZnONP concentrations. As described in detail in the previous chapters, ThT presents a classical technique to follow the formation of amyloids on a time dependent scale and ThT assay profile of ConA and ZnONP are presented in **Figure 6.13**. The fluorescence kept on increasing till 5-6 hrs after which it became constant till 30 hrs. In the presence of varying ZnONP, there is a concentration dependent increase in the fluorescence intensity. The fluorescence at highest ZnONP is almost twice of intact ConA. However, the difference between the fluorescence intensities of individual ZnONP concentrations with respect to intact ConA is insignificant. Although there is an increase the ThT intensity in both intact and ConA-ZnONP, we suppose that the affinity of ThT for β-sheet rich proteins may cause such increase in intensity. It might happen that low fluorescence intensity in case of intact ConA be due to the intercalation of ThT between its β-sheets. In case of ConA in presence of ZnONP, the protein corona formation and increased local concentration of ConA may cause enhanced ThT concentration compared to ConA alone. It has been shown earlier that ThT could bind to native acetylcholine esterase at its hydrophobic pockets [479]. This could also be true for ConA because ANS results show an increased exposure of hydrophobic patches in ConA at high ZnONP concentration. However, some studies have suggested that ThT dye does not bind to β-sheet in globular proteins as they are too short and distorted to form a ThT binding site [480, 481]. Studies of ThT binding on Peptide self-assembly mimics containing eight β-strands suggested a minimal requirement of five or more β-strands for

ThT binding [480, 482]. ConA being a tetrameric protein, with five and seven stranded β-sheets, connected by a six stranded top β-sheet in each monomer [10], therefore, the tetramer as a whole contains high number of β-sheets, which might lead to ThT binding, which might not necessarily be typical cross β-strands found in amyloids. Additionally, the solvent exposed hydrophobic patches of ConA in presence of ZnONP also supports this explanation.

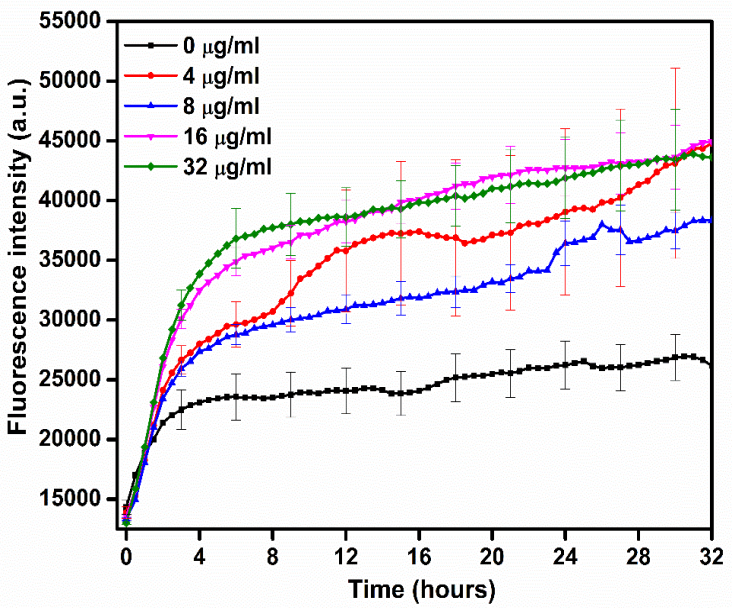

Figure 6.13. Thioflavin T dye binding assay of ConA with increasing concentration of ZnONP for 32 hrs. ThT dye fluorescence is observed at 485 nm with excitation at 440 nm.

6.3.3.7 Transmission electron microscopy

Further, to analyze whether ZnONP causes the aggregation of ConA and if yes, the morphology of the aggregates formed, we further performed TEM on ConA in presence of 32 μg/mL ZnONP. **Figure 6.14A** shows the elemental mapping of ConA-ZnONP conjugates on HAADF-STEM mode, where zinc closely co-exists with elements present in the protein i.e. sulfur, oxygen and nitrogen indicating interactions between ConA and ZnONP. In the second panel, there is a corresponding dark field image **(Figure 6.14B)** of the same. The presence of amorphous aggregates is observed, which further suggests, ZnONP might promote the aggregation of ConA, but not fibrillar aggregates corresponding to amyloids. Thus, ZnONP interface provides a platform for ConA adsorption and subsequent aggregation but salt bridges and hydrogen bonding bestow much stability on the ConA structure to prevent it from undergoing fibrillogenesis under physiological conditions.

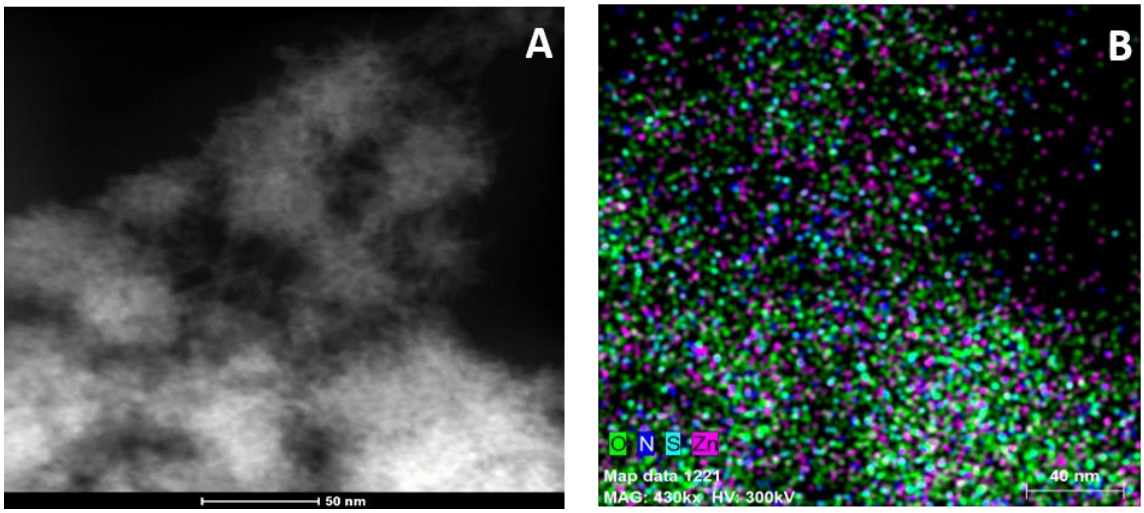

Figure 6.14. TEM micrographs of ConA-ZnONP complex. (A) TEM micrograph of ConA aggregated in presence of ZnONP and (B) corresponding HAADF-STEM map showing the elemental composition of the aggreagte.

6.3.4 Discussion

The conversion of globular proteins, which normally are stable at physiological conditions into amyloids has been a topic of investigation for quite some time now. Globular proteins like lysozyme, human superoxide dismutase 1 (SOD1), human transthyretin (TTR) have been shown to form amyloids at conditions slightly different from the physiological condition. Conditions like high temperature, low pH, presence of co-solvents and high pressure promote lead to partial unfolding and promote amyloidogenesis. In addition, specific mutations are also known to play roles in conversion a globular protein to a protein prone to form amyloids. However, recent findings suggest that partial unfolding might not be necessary for aggregation. Other transition states slightly distinct from the native state in terms of thermodynamics, but structurally similar sample out more frequently than partially unfolded states and might be primary determinants of amyloidogenesis [57]. Heat induced aggregates of ConA have been characterized. It was shown that at 45 °C, the ANS fluorescence was highest, depicting the exposure of hydrophobic patches. This was accompanied by high scattering and ThT fluorescence which further supported aggregation [483]. Following this, another group studied the pH dependence of ConA amyloidogenesis at 40°C and it was suggested that the the fibrillation of ConA was dependent on pH. At low pH <5.1 amorphous aggregates were formed, while at high pH >8.9 amyloid fibrils were formed [449]. It has been suggested that high pH triggers conformational changes in the protein, which leads to the formation of ThT binding aggregates. A concentration dependence of the amount of fibrils

was also established, which followed a non-nucleation growth mechanism [469]. At low pH (3) where ConA is demetallized and has positive charge, high temperatures are also able to induce aggregation, in a temperature and time dependent way. Role of long lived "crinkled intermediates", possessing exposed tryptophan and hydrophobic groups have also been demonstrated [471]. Additionally, the role of charges and attractive and repulsive electrostatic interactions have also shown to play important roles in the conversion of native ConA, to either dimers or long lived intermediates or amyloids and how the interplay between pH and temperature modulate the aggregation is highlighted [468].

This study suggests that on the adsorption of ConA on ZnONP surface, the overall secondary structure essentially remain unperturbed, and the access to the hydrophobic patches of ConA is not that pronounced initially, but increases with time at higher ZnONP as evident in ANS fluorescence measurements. The reduction in the tryptophan fluorescence is due to its quenching, which is a common phenomenon shown by most NPs. The CD data depicts structural changes at high ZnONP concentration, and slight blue shift in the ellipticity maxima, indicating an increase in intermolecular β-sheets [471]. Finally, the ThT assay also revealed an increase in the fluorescence intensity with respect to ZnONP concentration. Increase in ThT fluorescence might support a new theory put forward that, initial stages amyloidosis may be attained due to slight local unfolding and transient structural fluctuations, while the overall structure is being preserved. The concept of highly amyloidogenic, native like states have been put forward wherein the proteins retain native like states but still undergo amyloidosis as seen in many globular proteins like insulin, lysozyme, etc. [57]. However, TEM data show presence of amorphous type aggregates compared to individual fibrillar structures. Thus, the process of ConA adsorption over ZnONP might cause perturbations in a local region, while the overall structured being retained. These local perturbations might trigger aggregation of ConA, rich in intermolecular β-sheets, as depicted in CD and ThT assay, but the aggregates are amorphous in nature, as supported by TEM. The probability of formation of intermolecular β-sheet is high in this case as ConA itself is an all β-sheet protein and formations of multiple corona layers support the interaction between. The use of ConA for cancer therapy, alone or in combination with NPs must be therefore carefully assessed both structurally and functionally in order to be used as successful therapeutics.

Chapter 7

Summary, Conclusions and Scope of further research

7. Summary, Conclusions and Scope of further research

7.1 Summary

Proteins comprise about two thirds dry weight of a cell. Almost all proteins need to be folded in a particular conformation in order to be functional. Recently, a new class of proteins have been discovered, which are called as IDPs, which are completely or in part disordered. They are rich in charged amino acids and often lack a considerable number of hydrophobic amino acids, preventing them to form hydrophobic patches or clusters. Protein folding is an important process in biological systems and one of the most important aspects of biological self-assembly. However, in some cases, a protein can escape the normal folding process and undergo misfolding, Misfolding leads to the formation of aggregates, which can be either amorphous or amyloid. Amyloids are highly arranged crossβ-sheet structures, while amorphous aggregates are loosely arranged and lack a concrete arrangement. These aggregates have lower free energy as compared to their native forms indicating their higher stability than their native counterparts. Protein misfolding and the formation of amyloids has been linked to over 30 diseases, TIIDM, PD, AD, dialysis-related amyloidosis and injection-related amyloidosis being the important ones. The fibrils found in the in vivo, in the extracellular matrix, interact with its components like collagen, heparin etc. Heparin has been shown to interact with a variety of amyloid of different species, thereby enhancing their fibrillation propensity. Another group of entities which have recently gained much attention is NPs. NPs can be of different shapes, sizes and functionality depending on its intended use. Once a nanoparticle is inside the body, it quickly interacts with the components of the biological fluids, mostly the proteins. Initially, the adsorption and desorption of the proteins is a very dynamic process, following which a stable layer around the nanoparticle called as protein corona, is formed. Now, these NPs have been shown have far-reaching effects on the structure and conformation of proteins. In some cases, NPs have been shown to distort the structure of proteins and enhance the fibrillation process of some amyloid prone proteins. Few cases where the deposition of metal ions inside the body have led to the formation of NPs, which are toxic to the nearby cells have also been reported. On the contrary, some studies have also suggested reducing the fibrillation of some proteins using NPs. Thus, NPs can have contrasting roles depending on the type of nanoparticle itself and the interacting protein. The present study was thus designed to study the impact of negatively charged interfaces namely heparin and zinc oxide NPs on different model proteins. These model proteins belonged to different classes on the basis of their structural hierarchy.

The first model protein was Islet amyloid polypeptide (IAPP), a 37 amino acid long peptide which has been shown to misfold and form amyloids in TIIDM. To start with we studied its interaction with heparin molecules of increasing length by molecular docking followed by molecular dynamics simulations. Results indicated that the binding of IAPP to heparin was dependent on the length of the heparin oligomer used, concurrent with previously performed experimental studies by our group. Major interactions involved in complex formation were electrostatic and hydrogen bonding. As IAPP is positively charged at physiological pH and heparin is negatively charged, the presence of electrostatic interactions is quite obvious. Based on the results it was proposed that binding between IAPP and smaller heparin molecules are weaker, therefore the complex is not stable. On the other hand, interactions between IAPP and longer heparin is more stable, due to the presence of more number of negative charges. Longer heparin fragments act as a platform for the interaction of IAPP molecules and thus enhance is fibrillation. Next, biophysical studies and MD simulations were performed on the interaction of IAPP with negatively charged ZnONP. ThT assay showed a reduction of fibrillation of IAPP in presence of IAPP. TEM data also supported ThT data. Cytotoxic assay suggested that presence of ZnONP could rescue MIN6 cells from cell death. Here it could be proposed that the as IAPP is positively charged at physiological pH and ZnONP is negatively charged, there might be electrostatic interactions between then and preferential binding IAPP to ZnONP as compared to other IAPP monomers, thereby reducing the fibrillation. MD simulations results suggested that the conformation of IAPP might be dependent on its orientation at which it binds at the ZnONP interface. Among the 3 orientations tried, the second orientation showed least fluctuation. His-18 was shown to bind with ZnONP and was sterically hindered. As the charge on His-18 plays an essential part in IAPP fibrillation, its sterical hindrance affects the fibrillation. It has been therefore speculated that, orientation of IAPP that interacts with ZnONP, decides the fate, whether or not IAPP will fibrillate.

The second model protein was α-synuclein, a 140 amino acid long, IDP, which misfolds and form amyloids in PD. Interaction of α-synuclein with ZnONP. were studied using UV-Vis, TRF, zeta-potential and ITC. Results suggested favorable binding between the two species. The interactions were shown to be enthalpically driven. This binding may be due to the presence of more number of positively charged amino acids at the N-terminus. ThT and TEM assay showed a significant reduction in fibrillation. CD results and visual examination suggested the formation of floc like complexes between the two entities.

Likewise, the third model protein was insulin, which is a 51 amino acid long, globular protein, serving important functions in glucose homeostasis. It forms amyloids in diabetic patients, taking insulin injections. The study of the interaction of insulin with negatively charged ZnONP showed that the fibrillation of ZnONP was enhanced in a concentration-dependent manner, as shown by ThT assay and TEM. Insulin and ZnONP were shown to interact with each other through an enthalpically driven process, as in α-synuclein. Cytotoxicity assays showed that the amyloids fabricated in the presence of ZnONP were cytotoxic to MIN6 cells. We propose here that the adsorption of insulin molecules over ZnONP interface induces conformational rearrangement in insulin, thereby increasing its fibrillation propensity.

Finally, the last model protein was ConA. ConA is a homotetrameric protein, each monomer of about 28 kDa. ConA has a wide range of applications in cellular studies. It also shares structural similarity with SAP component and thus presents a good model for studying protein conformation and amyloids. The first part of the study aimed at studying its conformational propensities in the presence of different chaotropes. Results indicate that GdnHCl causes complete unfolding, while SDS triggers α-helices in ConA. When the conformation of ConA was studied in the presence of ZnONP, we found that the overall secondary was maintained, however perturbations in terirtary structure was observed. An increase ThT fluorescence intensity indicated the increase in β-sheet content. However, we could not link it to the increase in amyloids, as ConA is already an all β-sheet protein and multiple layers of corona on the ZnONP, could be an explanation for the increase in ThT fluorescence. TEM results suggested the presence of amorphous aggregates, rather than amyloids.

7.2 Conclusions

Thesis will have several implications for the effect of ZnONP with negative surface potential on proteins of different structural hierarchies. It suggests that the nanoparticle have differential effects on proteins with different structural hierarchies, mainly depending upon the properties of the individual proteins interacting surface, like number of side chains, functional groups, interacting surface proximity to SRE region etc. Also, the solvent and buffer conditions like pH, ionic strength and presence of co-solvents change the conformational dynamics of a protein, directly or indirectly by changing the physico-chemical properties of protein interacting surface. In IDPs, like IAPP and α-synuclein, ZnONP showed a decrease in fibrillation by binding in atomic proximity to SRE region of

respective peptides. Hence, the interface sterically inhibitied the fibrillation process. Infact, the conformational rearrangements, which happened upon adsorption onto the interface, caused the protein's solvent exposed hydrophobic patches to flocculate into amorphous-like aggregates. Additionally, the adsorption onto interface into a relatively stable complexes must be raising the activation energy threshold so high that the complexes kinetically trapped into amorphous-like aggregate rather than forming amyloid-like fibrils. Similarly with a rigid quaternary protein structure, the interface interaction resulted in amorphous-like aggregate. Interestingly, with globular proteins like insulin, the interface interaction caused conformational rearrangement into an amyloid-prone conformation with enhanced amyloid-mediated cytotoxicity. In fact, the interface acted as a platform for nuclei formation, and enhcnaed the fibrillation. Thus, the results presented in the thesis draw attention of scientific community working with nanoparticle-mediated approaches for biological applications to cross-check the interface's behaviour towards globular dynamic proteins, especially for the protein that is known to cause diseases upon misfolding. However, IDP and rigid quaternary protein have shown least perturbation of the native structures, but flocculation into amorphous-like aggregate is likely to interfere efficiency of the protein functions in organism.

7.3 Scope of future research

Our basic study with the simple ZnONP might be extended for synthesizing NPs with different surface properties by capping them with other functional groups and studying their effects on protein structures. These structural studies might be extended further to cellular and *in vivo* studies in mouse models to decipher the cellular pathways that might be getting activated or suppressed. Also, functionalized NPs might be helpful in therapies for treating misfolding diseases. NPs could be developed as effective model chaperones to assist protein folding. Cross seeding experiments using different amyloid proteins would help understand the effect of a particular protein, and the interactions involved. Additionally, basic research on NPs and protein folding might help in determining the key intermediate stages of protein folding, in turn, be helpful for understanding the protein folding process as a whole.

Appendices

APPENDIX 1-SUPPLEMENTARY TO CHAPTER 3A

Table A1. The percentage of residues in the different regions of ramchandran plot for IAPP model 1, 2 and 3.

MODELS	RESIDUES IN THE MOST FAVOURED REGIONS	RESIDUES IN ADDITIONAL FAVOURED REGIONS	RESIDUES IN GENEROUSLY ALLOWED REGIONS	RESIDUES IN DISALLOWED REGIONS
1	69.7 %	24.2 %	0%	6.1%
2	84.2 %	12.1%	3.0%	0%
3	69.7 %	30.3%	0%	0%

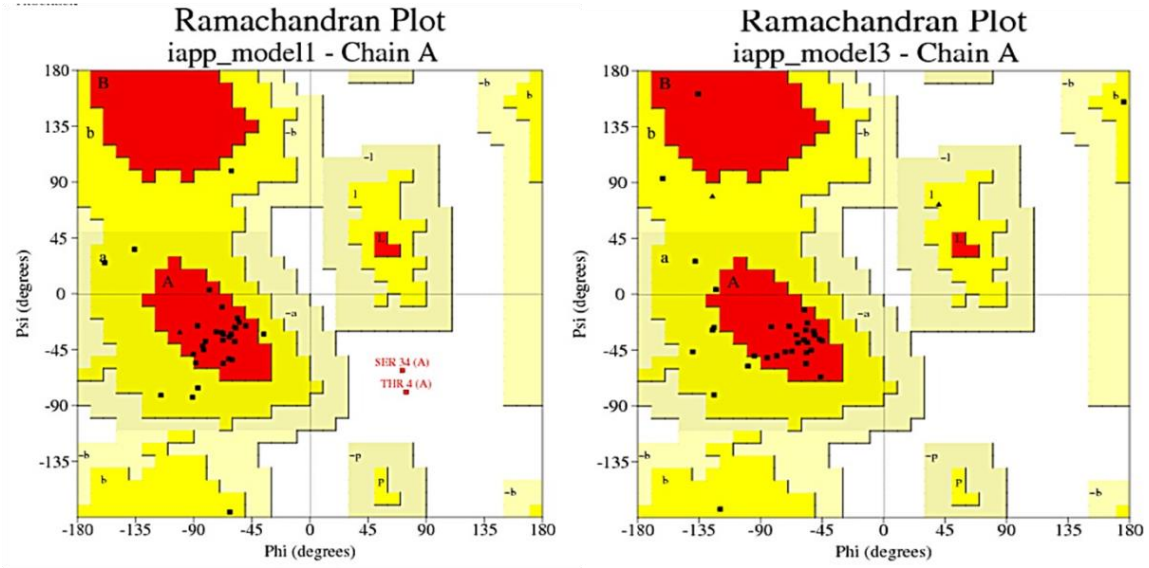

Figure A1. Ramachandran plots of IAPP model 1 and model 3.

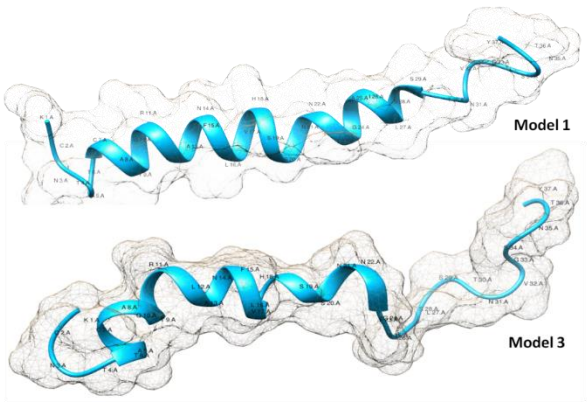

Figure A2. Structures of IAPP model 1 and 3, generated by SWISS MODEL.

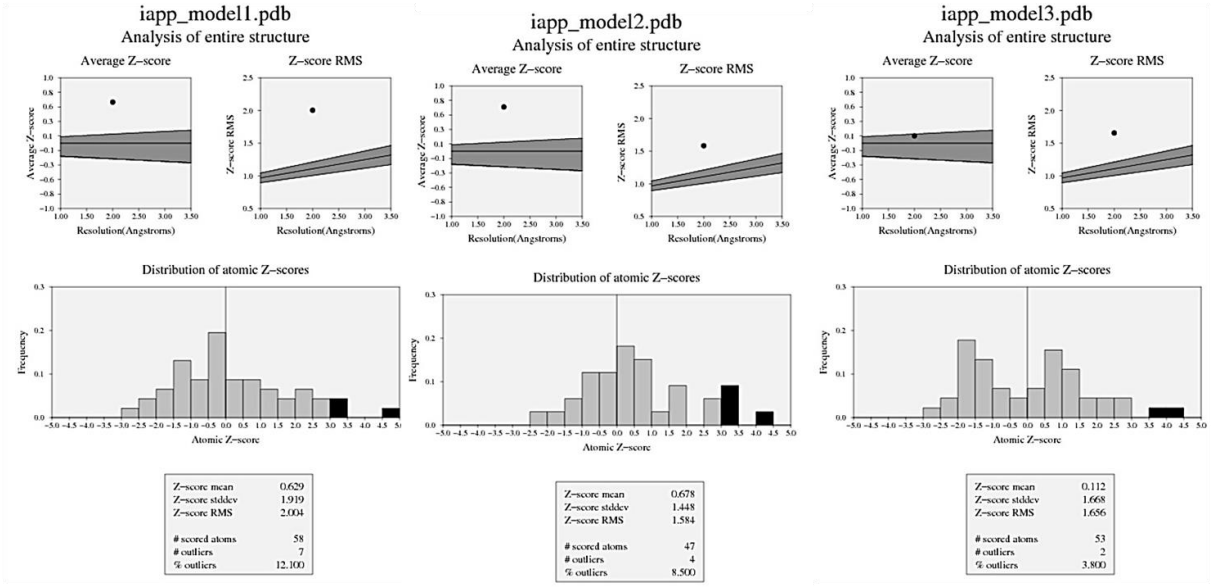

Figure A3. PROVE plot showing z-scores generated for IAPP model 1, 2 and 3.

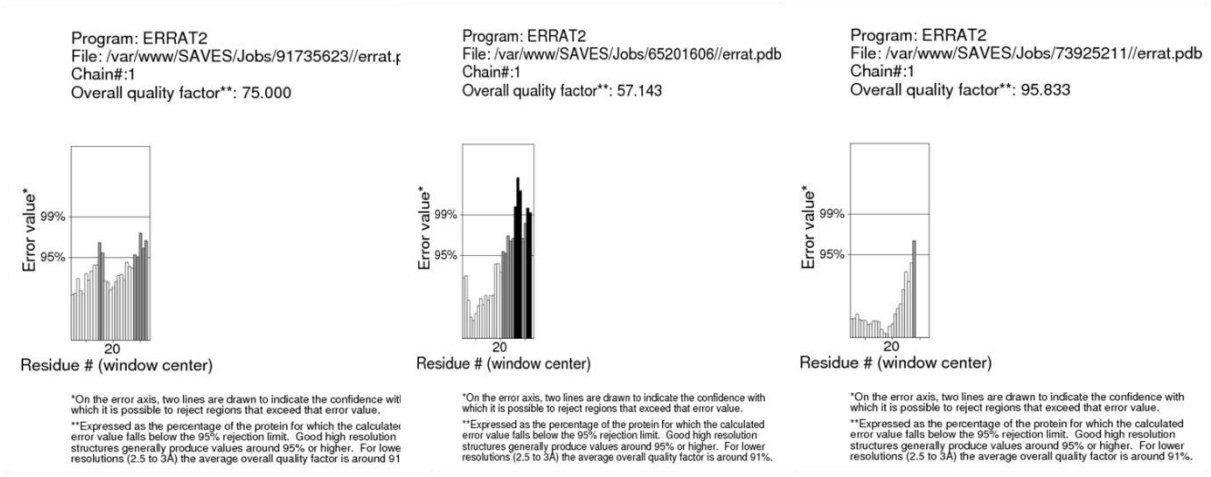

Figure A4. ERRAT scores generated for the IAPP model 1, 2 and 3.

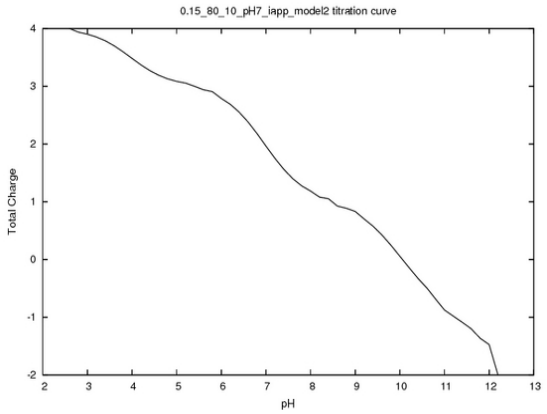

Figure A5. Total charge and the pKa value of IAPP at pH 7 calculated by H^{++} server.

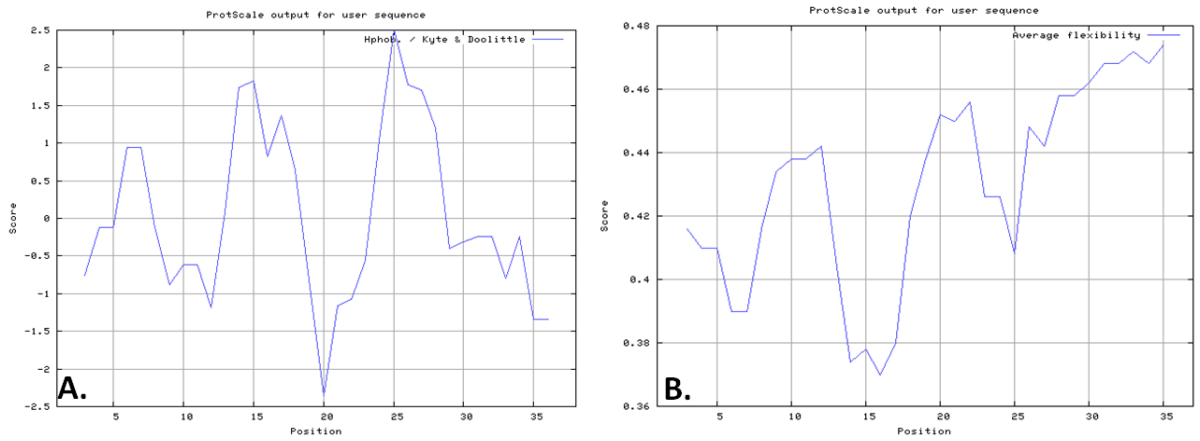

Figure A6. (A) Average hydrophobicity and (B) Residue wise average flexibility of IAPP model 2 generated by ProtScale sever.

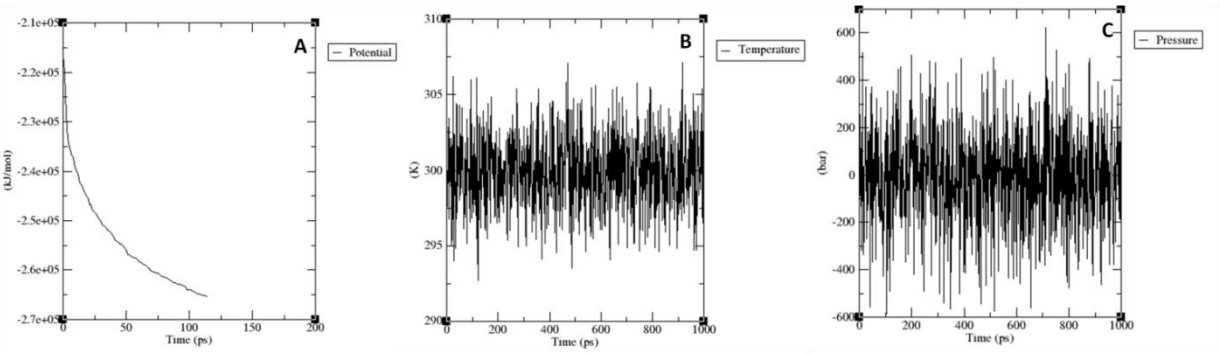

Figure A7. Time evolution of MD simulation of IAPP model2, depicting (A) potential energy, (B) Temperature and (C) Pressure.

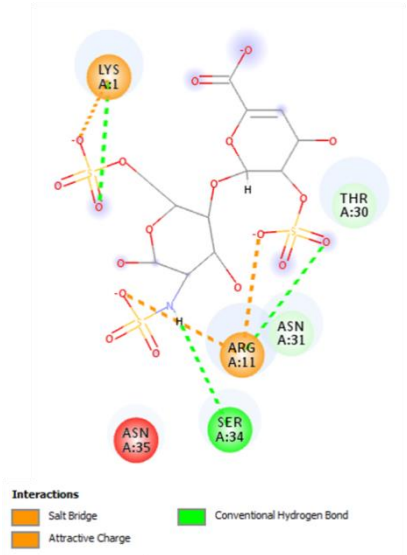

Figure A8. A representative of the salt bridge between positively charged residues of IAPP and negatively charged heparin fragments.

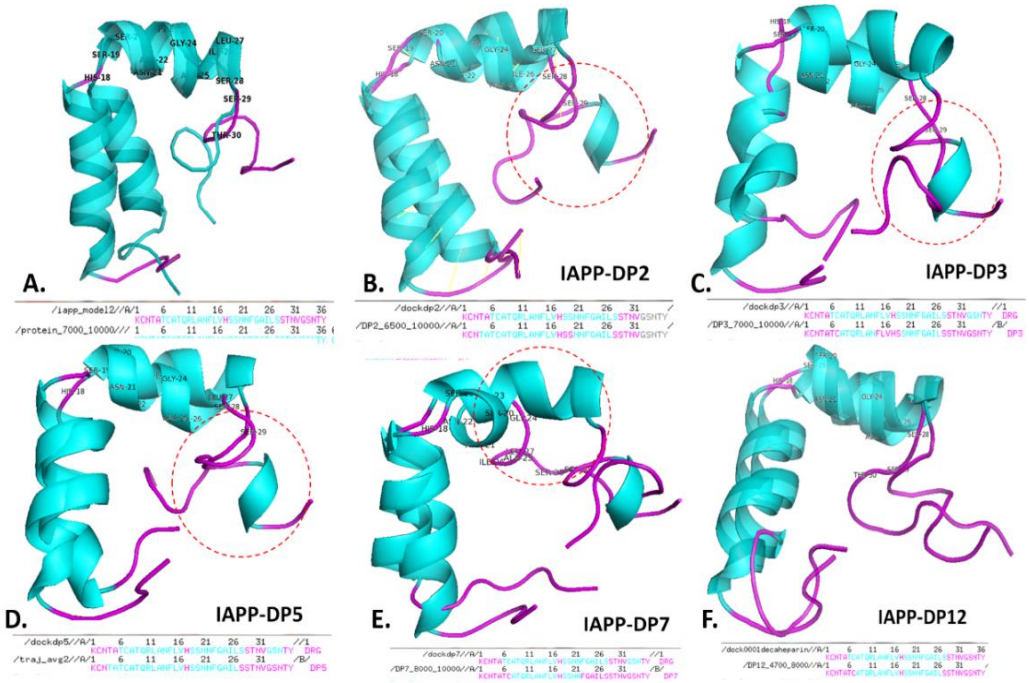

Figure A9. Superposed images of IAPP-heparin fragment complexes at beginning and end of the simulations. Cyan depicts helices and magenta depicts coils in each case, (A) only IAPP, (B) IAPP-DP2 complex, (C) IAPP-DP3 complex, (D) IAPP-DP5 complex, (E) IAPP-DP7 complex, and (F) IAPP-DP12 complex.

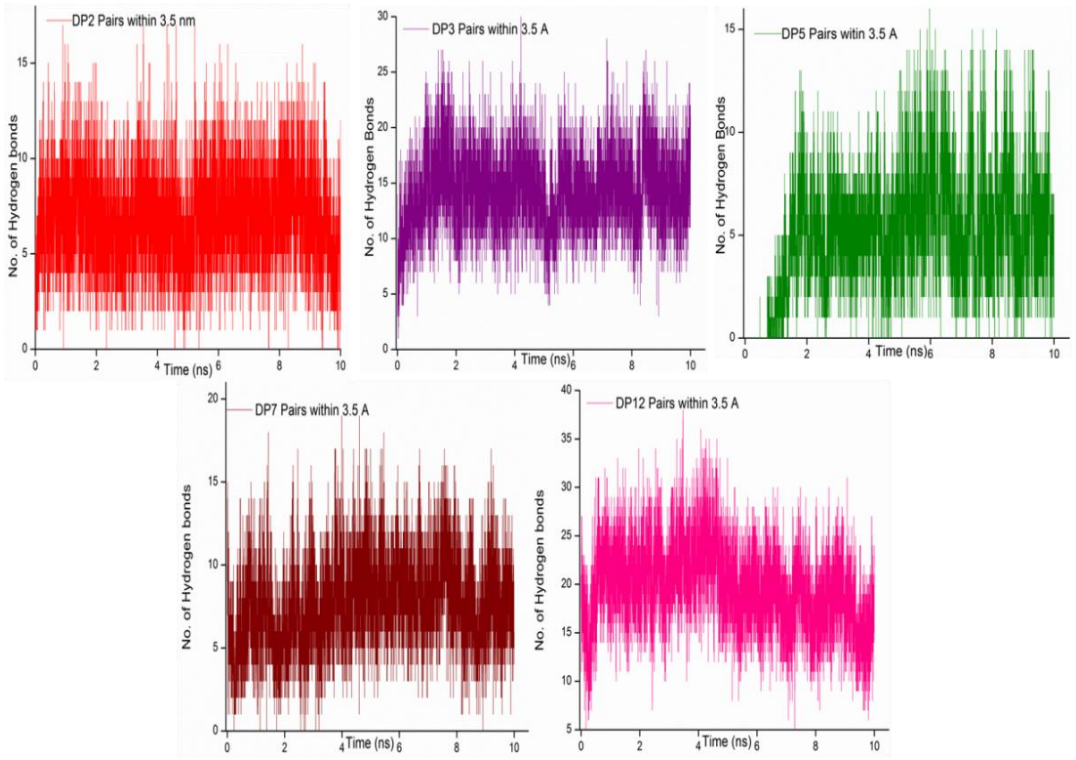

Figure A10. H-bonding fluctuations in each of the docked complex of IAPP-dp2 (red), IAPP-dp3 (purple), IAPP-dp5 (green), IAPP-dp7 (brown) and IAPP-dp12 (pink).

Table A2. Interaction details of each complex after simulation and the respective bond types, as analysed by Discovery studio visualizer.

Group Involved	Bond length	Bond category	Bond type
dp2 initial			
Arg11:H - dp2:O	2.30717	Hydrogen Bond;Electrostatic	Salt Bridge;Attractive Charge
Lys1:N - dp2:O	5.45311	Electrostatic	Attractive Charge
Lys1:H - dp2:O	2.95785	Hydrogen Bond	Conventional Hydrogen Bond
Arg11:H - dp2:O	2.46691	Hydrogen Bond	Conventional Hydrogen Bond
Ser34:H - dp2:O	2.84676	Hydrogen Bond	Conventional Hydrogen Bond
dp2:H - Thr30:O	2.79759	Hydrogen Bond	Conventional Hydrogen Bond
dp2:H - dp2:O	2.1069	Hydrogen Bond	Conventional Hydrogen Bond
Lys1:H - dp2:O	1.97084	Hydrogen Bond	Carbon Hydrogen Bond
Asn31:H - dp2:O	2.44747	Hydrogen Bond	Carbon Hydrogen Bond
dp2:H - Thr30:O	2.01208	Hydrogen Bond	Carbon Hydrogen Bond
dp2:H - Thr30:O	3.05483	Hydrogen Bond	Carbon Hydrogen Bond
dp2:H - Asn31:O	2.87324	Hydrogen Bond	Carbon Hydrogen Bond
dp2:H - Lys1:O	2.92871	Hydrogen Bond	Carbon Hydrogen Bond
dp2 intermediate			
Asn21:H - His18:N	2.74971	Hydrogen Bond	Conventional

			Hydrogen Bond
Asn21:H - dp2:O	2.7884	Hydrogen Bond	Conventional Hydrogen Bond
Phe23:HN - Asn21:O	2.53105	Hydrogen Bond	Conventional Hydrogen Bond
Gly24:HN - dp2:O	2.63736	Hydrogen Bond	Conventional Hydrogen Bond
Gly24:HN - dp2:O	2.55019	Hydrogen Bond	Conventional Hydrogen Bond
Ala25:HN - dp2:O	2.45314	Hydrogen Bond	Conventional Hydrogen Bond
Ala25:HN - dp2:O	2.51964	Hydrogen Bond	Conventional Hydrogen Bond
dp2:O- Asn21:O	3.29221	Hydrogen Bond	Conventional Hydrogen Bond
dp2:O- Asn21:O	3.20453	Hydrogen Bond	Conventional Hydrogen Bond
Asn21:CA - dp2:O	3.21177	Hydrogen Bond	Carbon Hydrogen Bond
dp2:C - Asn21:O	3.39777	Hydrogen Bond	Carbon Hydrogen Bond
dp2:O- His18	4.16158	Hydrogen Bond	Pi-Donor Hydrogen Bond
dp2 end			
none			
Group Involved	Bond length	Bond category	Bond type
dp3 initial			
Lys1:H - dp3:O	3.07468	Hydrogen Bond ;Electrostatic	Salt Bridge; Attractive Charge
Arg11:NH2 - dp3:O	4.64017	Electrostatic	Attractive Charge
Arg11:H - : dp3:O	2.47523	Hydrogen Bond	Conventional

			Hydrogen Bond
Arg11:H - : dp3:O	2.55591	Hydrogen Bond	Conventional Hydrogen Bond
Arg11:H - dp3:O	1.80656	Hydrogen Bond	Conventional Hydrogen Bond
Asn31:H - : dp3:O	2.12559	Hydrogen Bond	Conventional Hydrogen Bond
dp3:H - Lys1:O	2.87162	Hydrogen Bond	Conventional Hydrogen Bond
Lys1:H - dp3:O	2.83293	Hydrogen Bond	Carbon Hydrogen Bond
dp3:H - Thr30:O	2.82803	Hydrogen Bond	Carbon Hydrogen Bond
dp3:H - Thr30:O	2.99614	Hydrogen Bond	Carbon Hydrogen Bond
dp3:H4- Thr30:O	2.83677	Hydrogen Bond	Carbon Hydrogen Bond
dp3 intermediate			
Cys7:HN - dp3:O	2.39095	Hydrogen Bond	Conventional Hydrogen Bond
dp3:H - Gln10:O	2.86515	Hydrogen Bond	Conventional Hydrogen Bond
dp3:H - Asn21:O	2.7416	Hydrogen Bond	Conventional Hydrogen Bond
dp3:O- Ser29:O	2.99326	Hydrogen Bond	Conventional Hydrogen Bond
dp3:S - Thr30:O	3.52749	Hydrogen Bond	Conventional Hydrogen Bond
Ala25:C - dp3:O	3.58305	Hydrogen Bond	Carbon Hydrogen Bond
Ile26:C - dp3:O	3.34013	Hydrogen Bond	Carbon Hydrogen Bond

dp3:C - Ser28:O	2.76624	Hydrogen Bond	Carbon Hydrogen Bond
dp3 end			
dp3:N - Tyr37:C	5.05351	Electrostatic	Attractive Charge
dp3:N - Tyr37:C	4.94851	Electrostatic	Attractive Charge
dp3:N - Tyr37:O	5.30157	Electrostatic	Attractive Charge
dp3:N- Tyr37:O	5.29955	Electrostatic	Attractive Charge
Cys2:H - dp3:O	2.22797	Hydrogen Bond	Conventional Hydrogen Bond
Cys2:H - dp3:O	2.25204	Hydrogen Bond	Conventional Hydrogen Bond
Thr36:H - dp3:O	2.06755	Hydrogen Bond	Conventional Hydrogen Bond
Thr36:H - dp3:O	2.20496	Hydrogen Bond	Conventional Hydrogen Bond
Thr36:H- dp3:O	2.02615	Hydrogen Bond	Conventional Hydrogen Bond
Group Involved	Bond length	Bond category	Bond type
dp5 initial			
Arg11:H - dp5:O	2.74273	Hydrogen Bond; Electrostatic	Salt Bridge; Attractive Charge
Lys1:N - : dp5:O	3.02993	Electrostatic	Attractive Charge
Lys1:N - dp5:O	4.33408	Electrostatic	Attractive Charge
Arg11:NH - dp5:O	4.03132	Electrostatic	Attractive Charge
Lys1:H - dp5:O	1.83196	Hydrogen Bond	Conventional Hydrogen Bond
Asn3:H - dp5:O	3.07757	Hydrogen Bond	Conventional Hydrogen Bond
Asn3:H - dp5:O	2.75216	Hydrogen Bond	Conventional Hydrogen Bond

Asn3:H- dp5:O	3.00477	Hydrogen Bond	Conventional Hydrogen Bond
Arg11:H - dp5:O	1.36878	Hydrogen Bond	Conventional Hydrogen Bond
Asn31:H - dp5:O	2.53955	Hydrogen Bond	Conventional Hydrogen Bond
dp5:H - Thr30:O	2.37552	Hydrogen Bond	Conventional Hydrogen Bond
dp5:H - dp5:O	2.81798	Hydrogen Bond	Conventional Hydrogen Bond
Lys1:H - dp5:O	2.84971	Hydrogen Bond	Carbon Hydrogen Bond
Lys1:H- dp5:O	1.4729	Hydrogen Bond	Carbon Hydrogen Bond
Asn3:H - dp5:O	2.92943	Hydrogen Bond	Carbon Hydrogen Bond
dp5:H :Thr30:O	2.37812	Hydrogen Bond	Carbon Hydrogen Bond
dp5:H - Asn21:O	3.02502	Hydrogen Bond	Carbon Hydrogen Bond
dp5:H - Asn31:O	2.89722	Hydrogen Bond	Carbon Hydrogen Bond
dp5:H- Asn31:O	2.51513	Hydrogen Bond	Carbon Hydrogen Bond
dp5:H - Ser34:O	2.55536	Hydrogen Bond	Carbon Hydrogen Bond
dp5:H - Ser34:O	3.0361	Hydrogen Bond	Carbon Hydrogen Bond
dp5 end			
Thr36:H - dp5:O	2.41803	Hydrogen Bond	Conventional Hydrogen Bond
dp5:H - Val32:O	2.5583	Hydrogen Bond	Conventional

			Hydrogen Bond
dp5:O - Val32:O	3.0652	Hydrogen Bond	Conventional Hydrogen Bond
dp 5:C - Tyr37:O	3.29896	Hydrogen Bond	Carbon Hydrogen Bond
dp5:CCS - Tyr37:O	3.34419	Hydrogen Bond	Carbon Hydrogen Bond
Lys1:H - dp5:O	2.62451	Hydrogen Bond	Carbon Hydrogen Bond
Lys1:H - dp5:O	2.63494	Hydrogen Bond	Carbon Hydrogen Bond
Group Involved	Bond length	Bond category	Bond type
dp7 initial			
Lys1:H - dp7:O	3.02029	Hydrogen Bond; Electrostatic	Salt Bridge; Attractive Charge
Arg11:H - dp7:O	3.29785	Hydrogen Bond; Electrostatic	Salt Bridge; Attractive Charge
Arg11:NH2 - dp7:O	5.34424	Electrostatic	Attractive Charge
Lys1:H - dp7:O	2.52698	Hydrogen Bond	Conventional Hydrogen Bond
Asn3:H - dp7:O	2.75341	Hydrogen Bond	Conventional Hydrogen Bond
dp7:H - Cys2:O	2.28261	Hydrogen Bond	Carbon Hydrogen Bond
dp7:H - Asn3:O	2.64053	Hydrogen Bond	Carbon Hydrogen Bond
dp7:H - Asn35:O	3.06377	Hydrogen Bond	Carbon Hydrogen Bond
dp7:H - Asn35:O	2.68315	Hydrogen Bond	Carbon Hydrogen Bond
dp7 intermediate			

dp7:S - Asn21:O	2.85427	Hydrogen Bond	Conventional Hydrogen Bond
dp7:S - Asn35:O	3.6354	Hydrogen Bond	Conventional Hydrogen Bond
Lys1:C - dp7:O	2.38391	Hydrogen Bond	Carbon Hydrogen Bond
dp7 end			
Asn31:HN - dp7:O	2.4088	Hydrogen Bond	Conventional Hydrogen Bond
Asn31:HN - dp7:O	2.42818	Hydrogen Bond	Conventional Hydrogen Bond
Thr30:C - dp7:O	3.32379	Hydrogen Bond	Carbon Hydrogen Bond
Thr30:C - dp7:O	3.57132	Hydrogen Bond	Carbon Hydrogen Bond
Thr30:C - dp7:O	3.43319	Hydrogen Bond	Carbon Hydrogen Bond
Group Involved	Bond length	Bond category	Bond type
dp12 initial			
Arg11:NH - dp12:OS	5.07536	Electrostatic	Attractive Charge
Asn3:H - dp12:OS	2.63213	Hydrogen Bond	Conventional Hydrogen Bond
Thr6:HN - dp12:OS	1.99331	Hydrogen Bond	Conventional Hydrogen Bond
Thr9:HN - dp12:O	2.58286	Hydrogen Bond	Conventional Hydrogen Bond
Arg11:H - dp12:OS	2.89696	Hydrogen Bond	Conventional Hydrogen Bond
Arg11:H- dp12:O5	2.96022	Hydrogen Bond	Conventional Hydrogen Bond
Arg11:HH - dp12:O	2.70781	Hydrogen Bond	Conventional Hydrogen Bond

Asn35:HD22 - dp12:O2	1.64582	Hydrogen Bond	Conventional Hydrogen Bond
Asn35:HD22 - dp12:O1	1.97372	Hydrogen Bond	Conventional Hydrogen Bond
Ala5:H - dp12:OS	2.59383	Hydrogen Bond	Carbon Hydrogen Bond
Thr6:H - dp12:O	2.29751	Hydrogen Bond	Carbon Hydrogen Bond
Thr6:H - dp12:O	2.66584	Hydrogen Bond	Carbon Hydrogen Bond
Thr6:H - dp12:O	2.28153	Hydrogen Bond	Carbon Hydrogen Bond
dp12:H4- Asn3:O	2.06655	Hydrogen Bond	Carbon Hydrogen Bond
dp12:H- Asn3:O	2.05967	Hydrogen Bond	Carbon Hydrogen Bond
dp12:H - Asn35:O	1.96813	Hydrogen Bond	Carbon Hydrogen Bond
dp12 intermediate			
Asn3:H - dp12:O	2.46642	Hydrogen Bond	Conventional Hydrogen Bond
Ala5:HN - Thr4:O	2.54808	Hydrogen Bond	Conventional Hydrogen Bond
Ala8:HN - dp12:O	2.78391	Hydrogen Bond	Conventional Hydrogen Bond
Thr9:HN - dp12:O	2.52793	Hydrogen Bond	Conventional Hydrogen Bond
Gln10:HE - dp12:O	3.07799	Hydrogen Bond	Conventional Hydrogen Bond
Arg11:H - dp12:O	2.97248	Hydrogen Bond	Conventional Hydrogen Bond
Gly33:HN - dp12:O	2.98106	Hydrogen Bond	Conventional

			Hydrogen Bond
Ser34:HN - dp12:O	3.08895	Hydrogen Bond	Conventional Hydrogen Bond
Ser34:HN - dp12:O	2.88795	Hydrogen Bond	Conventional Hydrogen Bond
Asn35:HN - dp12:O	2.30451	Hydrogen Bond	Conventional Hydrogen Bond
Asn35:HN - dp12:O	2.68915	Hydrogen Bond	Conventional Hydrogen Bond
Thr36:H- dp12:O	2.39678	Hydrogen Bond	Conventional Hydrogen Bond
Tyr37:HN - dp12:OH	2.729	Hydrogen Bond	Conventional Hydrogen Bond
dp12:SH - Ser34:O	3.74187	Hydrogen Bond	Conventional Hydrogen Bond
dp12:O - Asn3:O	3.04804	Hydrogen Bond	Conventional Hydrogen Bond
dp12:H - Thr4:O	2.24195	Hydrogen Bond	Conventional Hydrogen Bond
Ser29:C - dp12:OH	3.3491	Hydrogen Bond	Carbon Hydrogen Bond
dp12:C - Leu27:O	2.82789	Hydrogen Bond	Carbon Hydrogen Bond
dp12:C - Val32:O	3.51977	Hydrogen Bond	Carbon Hydrogen Bond
dp12:C - Asn3:O	3.59907	Hydrogen Bond	Carbon Hydrogen Bond
dp12:C - Asn3:O	3.6005	Hydrogen Bond	Carbon Hydrogen Bond
dp12:C - Asn3:O	3.18256	Hydrogen Bond	Carbon Hydrogen Bond
dp12 end			

Asn3:HD - dp12:O	2.88891	Hydrogen Bond	Conventional Hydrogen Bond
Cys7:HN - dp12:O	2.71145	Hydrogen Bond	Conventional Hydrogen Bond
Ala8:HN - dp12:O	2.9175	Hydrogen Bond	Conventional Hydrogen Bond
Ala8:HN - dp12:O	2.89195	Hydrogen Bond	Conventional Hydrogen Bond
Thr9:HN - dp12:O	2.50592	Hydrogen Bond	Conventional Hydrogen Bond
Thr9:HN - dp12:O	2.51946	Hydrogen Bond	Conventional Hydrogen Bond
Arg11:H- dp12:O	2.84986	Hydrogen Bond	Conventional Hydrogen Bond
dp12:OF- Asn35:O	3.10568	Hydrogen Bond	Conventional Hydrogen Bond
dp12:O - Asn35:O	2.8306	Hydrogen Bond	Conventional Hydrogen Bond
dp12:HC- Thr4:O	2.28571	Hydrogen Bond	Conventional Hydrogen Bond
Thr9:C - dp12:O	3.45438	Hydrogen Bond	Carbon Hydrogen Bond
dp12:C - Leu27:O	3.25983	Hydrogen Bond	Carbon Hydrogen Bond
dp12:CEE - Val32:O	3.21609	Hydrogen Bond	Carbon Hydrogen Bond
dp12:C - Asn3:O	3.26881	Hydrogen Bond	Carbon Hydrogen Bond
dp12:C- Asn3:O	3.1834	Hydrogen Bond	Carbon Hydrogen Bond

Table A3. Secondary structure prediction of IAPP (11-31) predicted by GOR V.

RESIDUE NUMBER	AMINO ACID	GORV PREDICTION
11	R	C
12	L	C
13	A	E
14	N	E
15	F	E
16	L	E
17	V	E
18	H	E
19	S	C
20	S	C
21	N	C
22	N	C
23	F	C
24	G	C
25	A	E
26	I	E
27	L	E
28	S	E
29	S	C
30	T	C
31	N	C

APPENDIX 2-SUPPLEMENTARY TO CHAPTER 4

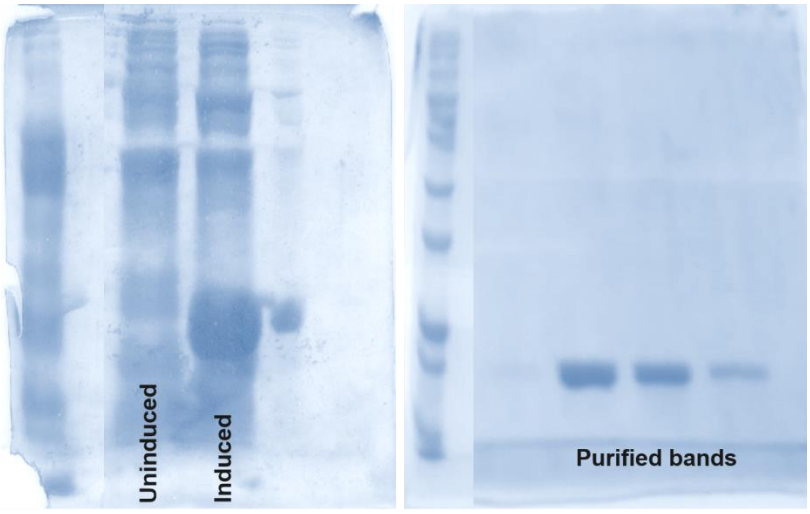

Figure A11. 13% SDS-PAGE of α-synuclein expression (left) and after purification (right).

APPENDIX 3-SUPPLEMENTARY TO CHAPTER 5

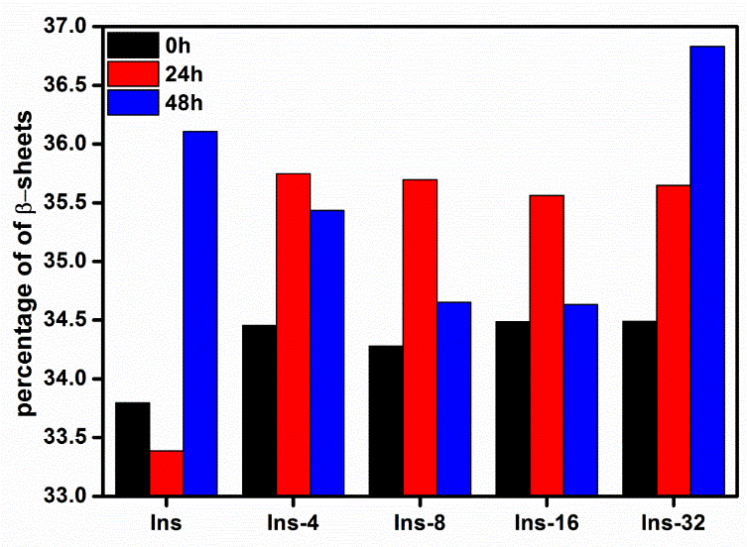

Figure A12. The percentage of β-sheets in insulin with increasing ZnONP concentrations, deconvulated using CDNN.

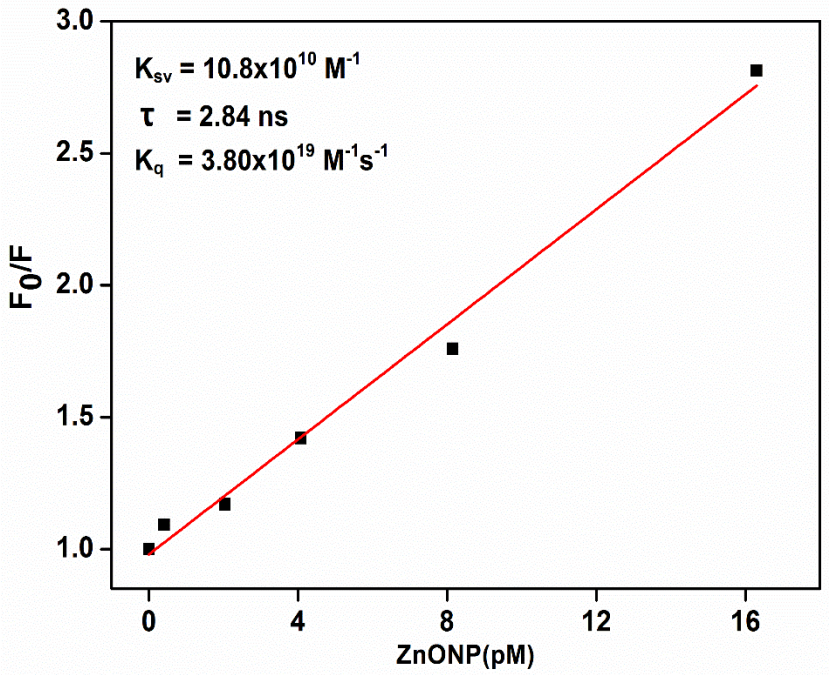

Figure A13. Stern-Volmer plot extrapolated from the insulin-tyrosine fluorescence in presence of increasing concentration of ZnONP at 0 hr.

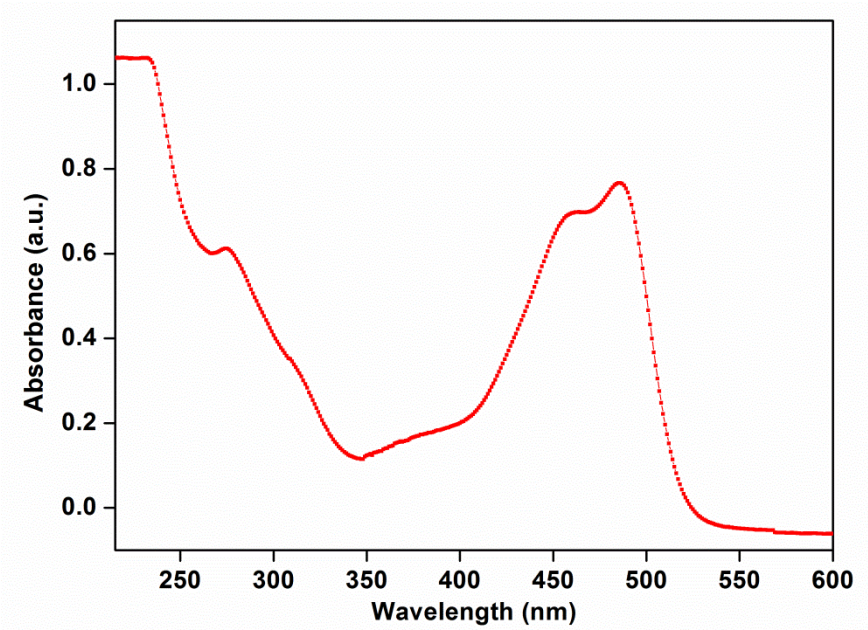

Figure A14. UV-Visible spectrum of insulin-FITC conjugate**.**

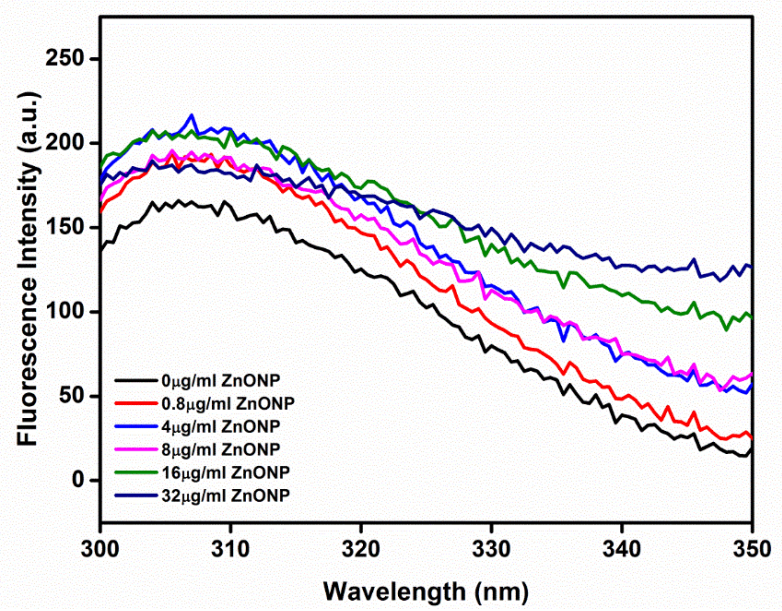

Figure A15. Fluorescence intensity of 5 μM tyrosine with increasing concentration of ZnONP, depicting that ZnONP is unable to quench tyrosine fluorescence.

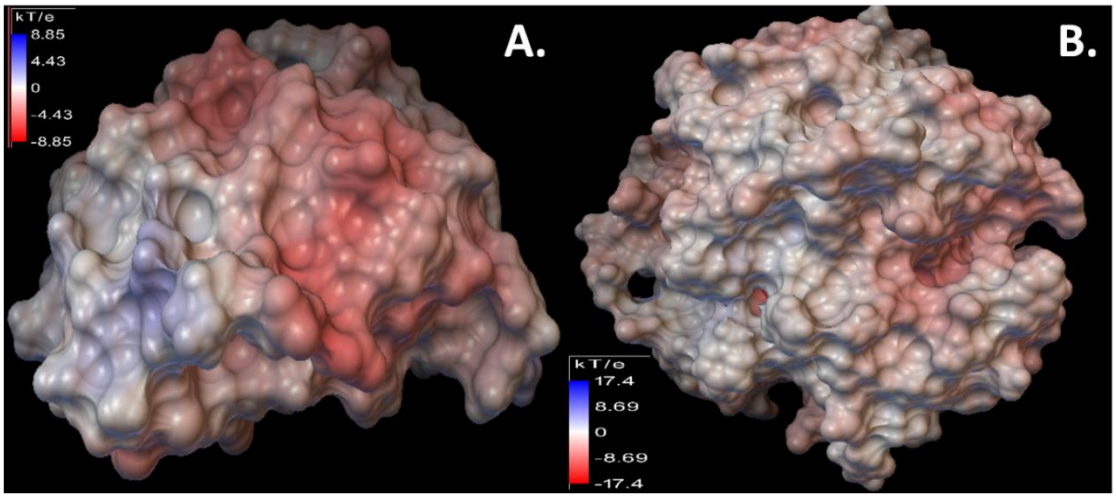

Figure A16. The net charge on insulin (A) dimer and (B) hexamer, as calculated by Autodock tools.

APPENDIX 4-SUPPLEMENTARY TO CHAPTER 6A

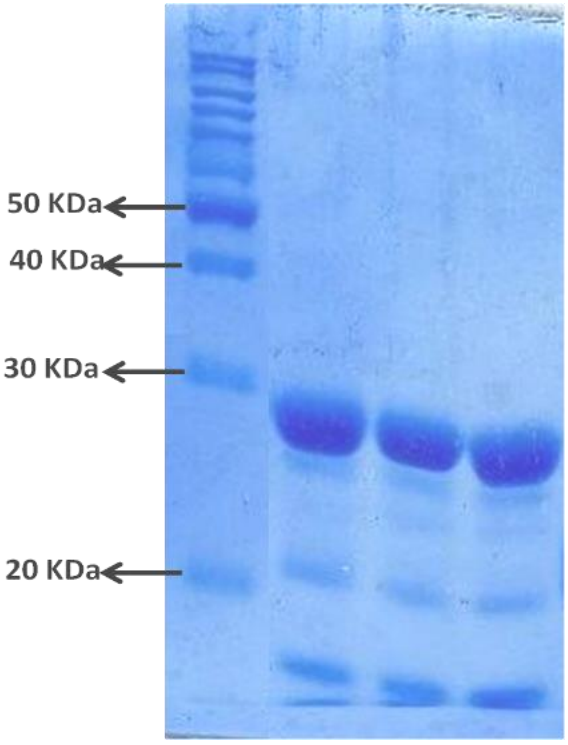

Figure A17. Purified ConA was run on 10 % SDS-PAGE in lane 2, 3, 4, and protein marker in lane 1. Protein band corresponding to ~ 28 KDa represents the ConA subunits, while lighter bands corresponding to ~ 26, 22 and 10 KDa represent post-translationally modified subunits.

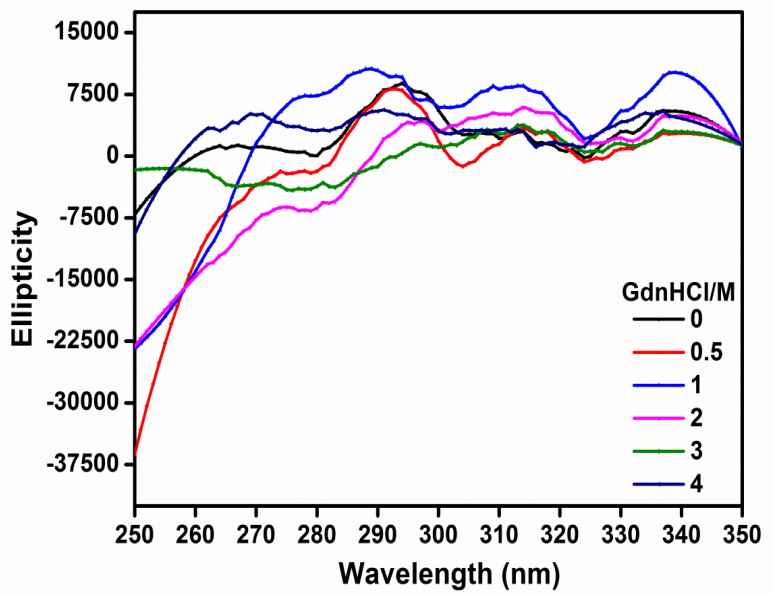

Figure A18. Near-UV CD spectra of ConA in presence of GdnHCl. The image depicts that, at 0 and 0.5 M GdnHCl, a prominent peak at 290 nm is observed which corresponds to tryptophan (trp) residues. At 1 M GdnHCl, a distorted peak for trp is seen, which further reduces in presence of 2 M GdnHCl. This can be a possible explanation for the presence of "molten globules" where, although, overall secondary structures remain intact, tertiary interactions are broken as concluded from the change in trp microenvironment. At high GdnHCl concentrations (3-4 M), there is a complete dissolution of tertiary and secondary structures. Thus, insignificant signal of trp residues in the near-UV region is observed.

References

1. Clamp, M., et al., *Distinguishing protein-coding and noncoding genes in the human genome.* Proceedings of the National Academy of Sciences, 2007. **104**(49): p. 19428-19433.
2. Kidera, A., et al., *Statistical analysis of the physical properties of the 20 naturally occurring amino acids.* Journal of Protein Chemistry, 1985. **4**(1): p. 23-55.
3. Morgan, A.A. and E. Rubenstein, *Proline: the distribution, frequency, positioning, and common functional roles of proline and polyproline sequences in the human proteome.* PloS one, 2013. **8**(1): p. e53785.
4. Dunker, A.K., et al., *Function and structure of inherently disordered proteins.* Current opinion in structural biology, 2008. **18**(6): p. 756-764.
5. Nelson, D.L., A.L. Lehninger, and M.M. Cox, *Lehninger principles of biochemistry*. 2008: Macmillan.
6. Creighton, T.E., *Proteins: structures and molecular properties*. 1993: Macmillan.
7. Ramachandran, G.t. and V. Sasisekharan, *Conformation of polypeptides and proteins.* Advances in protein chemistry, 1968. **23**: p. 283-437.
8. Kabsch, W. and C. Sander, *Dictionary of protein secondary structure: pattern recognition of hydrogen-bonded and geometrical features.* Biopolymers, 1983. **22**(12): p. 2577-2637.
9. Berndt, K.D., *Protein Secondary Structure.* Principles of Protein Structure using the Internet, Birkbeck College, University of London, 1996.
10. Brinda, K., et al., *Determinants of quaternary association in legume lectins.* Protein Science, 2004. **13**(7): p. 1735-1749.
11. Mei, G., et al., *The importance of being dimeric.* The FEBS journal, 2005. **272**(1): p. 16-27.
12. Natchiar, S.K., et al., *Structural studies on peanut lectin complexed with disaccharides involving different linkages: further insights into the structure and interactions of the lectin.* Acta Crystallographica Section D: Biological Crystallography, 2006. **62**(11): p. 1413-1421.
13. Rose, G.D., et al., *Hydrophobicity of amino acid residues in globular proteins.* Science, 1985. **229**: p. 834-839.
14. Kellis, J.T., K. Nyberg, and A.R. Fersht, *Contribution of hydrophobic interactions to protein stability.* Nature, 1988. **333**(6175): p. 784-786.
15. Strickler, S.S., et al., *Protein stability and surface electrostatics: a charged relationship.* Biochemistry, 2006. **45**(9): p. 2761-2766.
16. Gallivan, J.P. and D.A. Dougherty, *Cation-π interactions in structural biology.* Proceedings of the National Academy of Sciences, 1999. **96**(17): p. 9459-9464.
17. Crowley, P.B. and A. Golovin, *Cation–π interactions in protein–protein interfaces.* Proteins: Structure, Function, and Bioinformatics, 2005. **59**(2): p. 231-239.
18. Hogg, P.J., *Disulfide bonds as switches for protein function.* Trends in biochemical sciences, 2003. **28**(4): p. 210-214.
19. Dobson, C.M., *Protein folding and misfolding.* Nature, 2003. **426**(6968): p. 884-890.
20. Anfinsen, C.B., *Principles that govern the folding of protein chains.* Science, 1973. **181**(4096): p. 223-230.
21. Levinthal, C., *Are there pathways for protein folding?* Journal de chimie physique, 1968. **65**: p. 44-45.
22. Karplus, M., *The Levinthal paradox: yesterday and today.* Folding and design, 1997. **2**: p. S69-S75.
23. Ptitsyn, O., *Stages in the mechanism of self-organization of protein molecules.* Doklady Akademii Nauk SSSR, 1973. **210**(5): p. 1213.
24. Kim, P.S. and R.L. Baldwin, *Specific intermediates in the folding reactions of small proteins and the mechanism of protein folding.* Annual review of biochemistry, 1982. **51**(1): p. 459-489.
25. Gutin, A., V. Abkevich, and E. Shakhnovich, *Is burst hydrophobic collapse necessary for protein folding?* Biochemistry, 1995. **34**(9): p. 3066-3076.

26. Fersht, A.R., *Nucleation mechanisms in protein folding.* Current opinion in structural biology, 1997. **7**(1): p. 3-9.
27. Lazaridis, T. and M. Karplus, *" New view" of protein folding reconciled with the old through multiple unfolding simulations.* Science, 1997. **278**(5345): p. 1928-1931.
28. Dill, K.A. and H.S. Chan, *From Levinthal to pathways to funnels.* Nature Structural & Molecular Biology, 1997. **4**(1): p. 10-19.
29. Onuchic, J.N., Z. Luthey-Schulten, and P.G. Wolynes, *Theory of protein folding: the energy landscape perspective.* Annual review of physical chemistry, 1997. **48**(1): p. 545-600.
30. Dobson, C.M. and M. Karplus, *The fundamentals of protein folding: bringing together theory and experiment.* Current opinion in structural biology, 1999. **9**(1): p. 92-101.
31. Dunker, A.K., et al., *What's in a name? Why these proteins are intrinsically disordered: Why these proteins are intrinsically disordered.* Intrinsically Disordered Proteins, 2013. **1**(1): p. e24157.
32. Uversky, V.N., *Intrinsically disordered proteins from A to Z.* The international journal of biochemistry & cell biology, 2011. **43**(8): p. 1090-1103.
33. Fink, A.L., *Natively unfolded proteins.* Current opinion in structural biology, 2005. **15**(1): p. 35-41.
34. Babu, M.M., et al., *Intrinsically disordered proteins: regulation and disease.* Current opinion in structural biology, 2011. **21**(3): p. 432-440.
35. Hardy, J.A. and G.A. Higgins, *Alzheimer's disease: the amyloid cascade hypothesis.* Science, 1992. **256**(5054): p. 184.
36. Dauer, W. and S. Przedborski, *Parkinson's disease: mechanisms and models.* Neuron, 2003. **39**(6): p. 889-909.
37. Cooper, G., et al., *Purification and characterization of a peptide from amyloid-rich pancreases of type 2 diabetic patients.* Proceedings of the National Academy of Sciences, 1987. **84**(23): p. 8628-8632.
38. Swift, B., et al., *Examination of insulin injection sites: an unexpected finding of localized amyloidosis.* Diabetic medicine, 2002. **19**(10): p. 881-882.
39. Zingraff, J.J., et al., *Beta 2-microglobulin amyloidosis in chronic renal failure.* N Engl J Med, 1990. **323**(15): p. 1070-1071.
40. Chiti, F., et al., *Kinetic partitioning of protein folding and aggregation.* Nature Structural & Molecular Biology, 2002. **9**(2): p. 137-143.
41. Fändrich, M. and C.M. Dobson, *The behaviour of polyamino acids reveals an inverse side chain effect in amyloid structure formation.* The EMBO journal, 2002. **21**(21): p. 5682-5690.
42. Glenner, G., et al., *β-pleated sheet fibrils a comparison of native amyloid with synthetic protein fibrils.* Journal of Histochemistry & Cytochemistry, 1974. **22**(12): p. 1141-1158.
43. Westermark, P., et al., *Amyloid fibril protein nomenclature--2002.* Amyloid: the international journal of experimental and clinical investigation: the official journal of the International Society of Amyloidosis, 2002. **9**(3): p. 197.
44. Fitzpatrick, A.W., et al., *Atomic structure and hierarchical assembly of a cross-β amyloid fibril.* Proceedings of the National Academy of Sciences, 2013. **110**(14): p. 5468-5473.
45. Glenner, G.G., *Amyloid deposits and amyloidosis. The beta-fibrilloses (first of two parts).* The New England journal of medicine, 1980. **302**(23): p. 1283.
46. Hawe, A., M. Sutter, and W. Jiskoot, *Extrinsic fluorescent dyes as tools for protein characterization.* Pharmaceutical research, 2008. **25**(7): p. 1487-1499.
47. Sunde, M., et al., *Common core structure of amyloid fibrils by synchrotron X-ray diffraction.* Journal of molecular biology, 1997. **273**(3): p. 729-739.
48. Pauling, L. and R.B. Corey, *Configurations of polypeptide chains with favored orientations around single bonds: two new pleated sheets.* Proceedings of the National Academy of Sciences of the United States of America, 1951. **37**(11): p. 729.

49. Asthana, S., et al., *IAPP in type II diabetes: Basic research on structure, molecular interactions, and disease mechanisms suggests potential intervention strategies.* Biochimica et Biophysica Acta (BBA)-Biomembranes, 2018.
50. Serio, T.R., et al., *Nucleated conformational conversion and the replication of conformational information by a prion determinant.* Science, 2000. **289**(5483): p. 1317-1321.
51. Uversky, V.N., et al., *Biophysical Properties of the Synucleins and Their Propensities to Fibrillate inhibition of α-synuclein assembly by β-and γ-synucleins.* Journal of Biological Chemistry, 2002. **277**(14): p. 11970-11978.
52. Lesne, S., et al., *A specific amyloid-beta protein assembly in the brain impairs memory.* Nature, 2006. **440**(7082): p. 352-357.
53. Miller, Y., et al., *Hollow core of Alzheimer's $A\beta_{42}$ amyloid observed by cryoEM is relevant at physiological pH.* Proceedings of the National Academy of Sciences, 2010. **107**(32): p. 14128-14133.
54. Khurana, R., et al., *A general model for amyloid fibril assembly based on morphological studies using atomic force microscopy.* Biophysical journal, 2003. **85**(2): p. 1135-1144.
55. Chiti, F. and C.M. Dobson, *Protein misfolding, functional amyloid, and human disease.* Annu. Rev. Biochem., 2006. **75**: p. 333-366.
56. Uversky, V.N. and A.L. Fink, *Conformational constraints for amyloid fibrillation: the importance of being unfolded.* Biochimica et Biophysica Acta (BBA)-Proteins and Proteomics, 2004. **1698**(2): p. 131-153.
57. Chiti, F. and C.M. Dobson, *Amyloid formation by globular proteins under native conditions.* Nature chemical biology, 2009. **5**(1): p. 15-22.
58. Feynman, R.P., *There's plenty of room at the bottom.* Engineering and science, 1960. **23**(5): p. 22-36.
59. Emerich, D.F. and C.G. Thanos, *Nanotechnology and medicine.* Expert Opinion on Biological Therapy, 2003. **3**(4): p. 655-663.
60. Vauthier, C. and K. Bouchemal, *Methods for the preparation and manufacture of polymeric nanoparticles.* Pharmaceutical research, 2009. **26**(5): p. 1025-1058.
61. Puri, A., et al., *Lipid-based nanoparticles as pharmaceutical drug carriers: from concepts to clinic.* Critical Reviews™ in Therapeutic Drug Carrier Systems, 2009. **26**(6).
62. C Thomas, S., P. Kumar Mishra, and S. Talegaonkar, *Ceramic nanoparticles: fabrication methods and applications in drug delivery.* Current pharmaceutical design, 2015. **21**(42): p. 6165-6188.
63. Cha, C., et al., *Carbon-based nanomaterials: multifunctional materials for biomedical engineering.* ACS nano, 2013. **7**(4): p. 2891-2897.
64. Kamat, P.V., *Photophysical, photochemical and photocatalytic aspects of metal nanoparticles*. 2002, ACS Publications.
65. Liu, Z., F. Kiessling, and J. Gätjens, *Advanced nanomaterials in multimodal imaging: design, functionalization, and biomedical applications.* Journal of Nanomaterials, 2010. **2010**: p. 51.
66. Conde, J., et al., *Revisiting 30 years of biofunctionalization and surface chemistry of inorganic nanoparticles for nanomedicine.* Frontiers in chemistry, 2014. **2**.
67. Dreaden, E.C., et al., *The golden age: gold nanoparticles for biomedicine.* Chemical Society Reviews, 2012. **41**(7): p. 2740-2779.
68. Agnihotri, S., S. Mukherji, and S. Mukherji, *Size-controlled silver nanoparticles synthesized over the range 5–100 nm using the same protocol and their antibacterial efficacy.* RSC Advances, 2014. **4**(8): p. 3974-3983.
69. Pankhurst, Q.A., et al., *Applications of magnetic nanoparticles in biomedicine.* Journal of physics D: Applied physics, 2003. **36**(13): p. R167.
70. Reiss, G. and A. Hütten, *Magnetic nanoparticles: applications beyond data storage.* Nature materials, 2005. **4**(10): p. 725-726.

71. Faivre, D. and M. Bennet, *Materials science: magnetic nanoparticles line up.* Nature, 2016. **535**(7611): p. 235-236.
72. Zhang, L., et al., *Nanoparticles in medicine: therapeutic applications and developments.* Clinical pharmacology & therapeutics, 2008. **83**(5): p. 761-769.
73. Loureiro, A., et al., *Albumin-based nanodevices as drug carriers.* Current pharmaceutical design, 2016. **22**(10): p. 1371-1390.
74. Singh, R. and J.W. Lillard, *Nanoparticle-based targeted drug delivery.* Experimental and molecular pathology, 2009. **86**(3): p. 215-223.
75. Dobson, J., *Magnetic nanoparticles for drug delivery.* Drug development research, 2006. **67**(1): p. 55-60.
76. Soppimath, K.S., et al., *Biodegradable polymeric nanoparticles as drug delivery devices.* Journal of controlled release, 2001. **70**(1): p. 1-20.
77. Saha, K., et al., *Gold nanoparticles in chemical and biological sensing.* Chemical reviews, 2012. **112**(5): p. 2739-2779.
78. Panyam, J. and V. Labhasetwar, *Biodegradable nanoparticles for drug and gene delivery to cells and tissue.* Advanced drug delivery reviews, 2003. **55**(3): p. 329-347.
79. Jain, P.K., I.H. El-Sayed, and M.A. El-Sayed, *Au nanoparticles target cancer.* nano today, 2007. **2**(1): p. 18-29.
80. Li, Y., Y. Tian, and G. Nie, *Antineoplastic activities of Gd@ C 82 (OH) 22 nanoparticles: tumor microenvironment regulation.* Science China Life Sciences, 2012. **55**(10): p. 884-890.
81. AshaRani, P., et al., *Cytotoxicity and genotoxicity of silver nanoparticles in human cells.* ACS nano, 2008. **3**(2): p. 279-290.
82. Nayak, D., et al., *Biologically synthesised silver nanoparticles from three diverse family of plant extracts and their anticancer activity against epidermoid A431 carcinoma.* Journal of colloid and Interface science, 2015. **457**: p. 329-338.
83. Arakha, M., et al., *The effects of interfacial potential on antimicrobial propensity of ZnO nanoparticle.* Scientific reports, 2015. **5**: p. 9578.
84. Nayak, P.S., et al., *An approach towards continuous production of silver nanoparticles using Bacillus thuringiensis.* RSC Advances, 2016. **6**(10): p. 8232-8242.
85. Weir, A., et al., *Titanium dioxide nanoparticles in food and personal care products.* Environmental science & technology, 2012. **46**(4): p. 2242-2250.
86. Zhang, Y., et al., *Biomedical applications of zinc oxide nanomaterials.* Current molecular medicine, 2013. **13**(10): p. 1633-1645.
87. Warheit, D.B., *Nanoparticles: health impacts?* Materials today, 2004. **7**(2): p. 32-35.
88. Buzea, C., I.I. Pacheco, and K. Robbie, *Nanomaterials and nanoparticles: Sources and toxicity.* Biointerphases, 2007. **2**(4): p. MR17-MR71.
89. Hoet, P.H., I. Brüske-Hohlfeld, and O.V. Salata, *Nanoparticles–known and unknown health risks.* Journal of nanobiotechnology, 2004. **2**(1): p. 12.
90. Kim, J.S., et al., *In vivo genotoxicity of silver nanoparticles after 90-day silver nanoparticle inhalation exposure.* Safety and health at work, 2011. **2**(1): p. 34-38.
91. Yu, L.E., et al., *Translocation and effects of gold nanoparticles after inhalation exposure in rats.* Nanotoxicology, 2007. **1**(3): p. 235-242.
92. Navarro, E., et al., *Environmental behavior and ecotoxicity of engineered nanoparticles to algae, plants, and fungi.* Ecotoxicology, 2008. **17**(5): p. 372-386.
93. Bakshi, M.S., et al., *Metal nanoparticle pollutants interfere with pulmonary surfactant function in vitro.* Biophysical journal, 2008. **94**(3): p. 855-868.
94. Maher, B.A., et al., *Magnetite pollution nanoparticles in the human brain.* Proceedings of the National Academy of Sciences, 2016. **113**(39): p. 10797-10801.
95. Colvin, V.L. and K.M. Kulinowski, *Nanoparticles as catalysts for protein fibrillation.* Proceedings of the National Academy of Sciences, 2007. **104**(21): p. 8679-8680.

96. Mahmoudi, M., et al., *Protein fibrillation and nanoparticle interactions: opportunities and challenges.* Nanoscale, 2013. **5**(7): p. 2570-2588.
97. Sear, R.P., *Protein crystals and charged surfaces: interactions and heterogeneous nucleation.* Physical Review E, 2003. **67**(6): p. 061907.
98. Warszyński, P. and Z. Adamczyk, *Calculations of double-layer electrostatic interactions for the sphere/plane geometry.* Journal of colloid and interface science, 1997. **187**(2): p. 283-295.
99. Biesheuvel, P.M., M. van der Veen, and W. Norde, *A Modified Poisson− Boltzmann Model Including Charge Regulation for the Adsorption of Ionizable Polyelectrolytes to Charged Interfaces, Applied to Lysozyme Adsorption on Silica.* The Journal of Physical Chemistry B, 2005. **109**(9): p. 4172-4180.
100. Johnson, C., P. Wu, and A. Lenhoff, *Electrostatic and Van der Waals contributions to protein adsorption: 2. Modeling of ordered arrays.* Langmuir, 1994. **10**(10): p. 3705-3713.
101. Zhou, J., J. Zheng, and S. Jiang, *Molecular simulation studies of the orientation and conformation of cytochrome c adsorbed on self-assembled monolayers.* The Journal of Physical Chemistry B, 2004. **108**(45): p. 17418-17424.
102. Roth, C.M. and A.M. Lenhoff, *Electrostatic and van der Waals contributions to protein adsorption: computation of equilibrium constants.* Langmuir, 1993. **9**(4): p. 962-972.
103. Regnier, F.E., *The role of protein structure in chromatographic behavior.* Science, 1987. **238**(4825): p. 319-323.
104. Noh, H., S.T. Yohe, and E.A. Vogler, *Volumetric interpretation of protein adsorption: ion-exchange adsorbent capacity, protein pI, and interaction energetics.* Biomaterials, 2008. **29**(13): p. 2033-2048.
105. Lund, M., T. Åkesson, and B. Jönsson, *Enhanced protein adsorption due to charge regulation.* Langmuir, 2005. **21**(18): p. 8385-8388.
106. Hartvig, R.A., et al., *Protein adsorption at charged surfaces: the role of electrostatic interactions and interfacial charge regulation.* Langmuir, 2011. **27**(6): p. 2634-2643.
107. Alexandrescu, A.T., *Amyloid accomplices and enforcers.* Protein science, 2005. **14**(1): p. 1-12.
108. Cecchi, C. and M. Stefani, *The amyloid-cell membrane system. The interplay between the biophysical features of oligomers/fibrils and cell membrane defines amyloid toxicity.* Biophysical chemistry, 2013. **182**: p. 30-43.
109. Jha, S., et al., *Amyloidogenic propensities and conformational properties of ProIAPP and IAPP in the presence of lipid bilayer membranes.* Journal of molecular biology, 2009. **389**(5): p. 907-920.
110. Janson, J., et al., *The mechanism of islet amyloid polypeptide toxicity is membrane disruption by intermediate-sized toxic amyloid particles.* Diabetes, 1999. **48**(3): p. 491-498.
111. Lee, H.-J., C. Choi, and S.-J. Lee, *Membrane-bound α-synuclein has a high aggregation propensity and the ability to seed the aggregation of the cytosolic form.* Journal of Biological Chemistry, 2002. **277**(1): p. 671-678.
112. Necula, M., C.N. Chirita, and J. Kuret, *Rapid anionic micelle-mediated α-synuclein fibrillization in vitro.* Journal of Biological Chemistry, 2003. **278**(47): p. 46674-46680.
113. Anguiano, M., R.J. Nowak, and P.T. Lansbury, *Protofibrillar islet amyloid polypeptide permeabilizes synthetic vesicles by a pore-like mechanism that may be relevant to type II diabetes.* Biochemistry, 2002. **41**(38): p. 11338-11343.
114. Chirita, C.N., M. Necula, and J. Kuret, *Anionic micelles and vesicles induce tau fibrillization in vitro.* Journal of Biological Chemistry, 2003. **278**(28): p. 25644-25650.
115. Knight, J.D. and A.D. Miranker, *Phospholipid catalysis of diabetic amyloid assembly.* Journal of molecular biology, 2004. **341**(5): p. 1175-1187.
116. Terzi, E., G. Holzemann, and J. Seelig, *Self-association of β-amyloid peptide (1-40) in solution and binding to lipid membranes.* Journal of molecular biology, 1995. **252**(5): p. 633-642.

117. Jayasinghe, S.A. and R. Langen, *Lipid membranes modulate the structure of islet amyloid polypeptide.* Biochemistry, 2005. **44**(36): p. 12113-12119.
118. Knight, J.D., J.A. Hebda, and A.D. Miranker, *Conserved and cooperative assembly of membrane-bound α-helical states of islet amyloid polypeptide.* Biochemistry, 2006. **45**(31): p. 9496-9508.
119. Brender, J.R., et al., *Biphasic effects of insulin on islet amyloid polypeptide membrane disruption.* Biophysical journal, 2011. **100**(3): p. 685-692.
120. Cao, P., et al., *Islet amyloid polypeptide toxicity and membrane interactions.* Proceedings of the National Academy of Sciences, 2013. **110**(48): p. 19279-19284.
121. Jackson, R.L., S.J. Busch, and A.D. Cardin, *Glycosaminoglycans: molecular properties, protein interactions, and role in physiological processes.* Physiological reviews, 1991. **71**(2): p. 481-539.
122. Young, I.D., et al., *Localization of the basement membrane heparan sulfate proteoglycan in islet amyloid deposits in type II diabetes mellitus.* Arch Pathol Lab Med, 1992. **116**(9): p. 951-4.
123. Lindahl, U. and J.-p. Li, *Interactions between heparan sulfate and proteins-"Design and functional implications.* International review of cell and molecular biology, 2009. **276**: p. 105-159.
124. Cohlberg, J.A., et al., *Heparin and other glycosaminoglycans stimulate the formation of amyloid fibrils from α-synuclein in vitro.* Biochemistry, 2002. **41**(5): p. 1502-1511.
125. Fukuchi, K.-i., M. Hart, and L. Li, *Alzheimer's disease and heparan sulfate proteoglycan.* Front. Biosci, 1998. **3**: p. 327-337.
126. Ohashi, K., R. Kisilevsky, and M. Yanagishita, *Affinity binding of glycosaminoglycans with **beta-**2-microglobulin.* Nephron, 2002. **90**(2): p. 158-168.
127. Yamaguchi, I., et al., *Glycosaminoglycan and proteoglycan inhibit the depolymerization of &bgr; 2-microglobulin amyloid fibrils in vitro.* Kidney international, 2003. **64**(3): p. 1080-1088.
128. Potter, K. and K. Park, *Heparin induces amyloid formation in cultured human islets.* Clinical & Investigative Medicine, 2007. **30** (4): p. S92.
129. Castillo, G.M., et al., *Sulfate content and specific glycosaminoglycan backbone of perlecan are critical for perlecan's enhancement of islet amyloid polypeptide (amylin) fibril formation.* Diabetes, 1998. **47**(4): p. 612-620.
130. Castillo, G.M., et al., *The sulfate moieties of glycosaminoglycans are critical for the enhancement of beta-amyloid protein fibril formation.* J Neurochem, 1999. **72**(4): p. 1681-7.
131. Hull, R.L., et al., *Inhibition of glycosaminoglycan synthesis and protein glycosylation with WAS-406 and azaserine result in reduced islet amyloid formation in vitro.* Am J Physiol Cell Physiol, 2007. **293**(5): p. C1586-93.
132. Jha, S., et al., *Mechanism of amylin fibrillization enhancement by heparin.* Journal of Biological Chemistry, 2011. **286**(26): p. 22894-22904.
133. Potter-Perigo, S., et al., *Proteoglycans synthesized and secreted by pancreatic islet β-cells bind amylin.* Archives of biochemistry and biophysics, 2003. **413**(2): p. 182-190.
134. Abedini, A., et al., *Characterization of the heparin binding site in the N-terminus of human pro-islet amyloid polypeptide: implications for amyloid formation.* Biochemistry, 2006. **45**(30): p. 9228-9237.
135. Park, K. and C.B. Verchere, *Identification of a Heparin Binding Domain in the N-terminal Cleavage Site of Pro-islet Amyloid Polypeptide implications for amyloid formation.* Journal of Biological Chemistry, 2001. **276**(20): p. 16611-16616.
136. Castillo, G.M., et al., *The Sulfate Moieties of Glycosaminoglycans Are Critical for the Enhancement of β-Amyloid Protein Fibril Formation.* Journal of neurochemistry, 1999. **72**(4): p. 1681-1687.

137. Fraser, P.E., A.A. Darabie, and J. McLaurin, *Amyloid-β Interactions with Chondroitin Sulfate-derived Monosaccharides and Disaccharides IMPLICATIONS FOR DRUG DEVELOPMENT.* Journal of Biological Chemistry, 2001. **276**(9): p. 6412-6419.
138. Paudel, H.K. and W. Li, *Heparin-induced conformational change in microtubule-associated protein Tau as detected by chemical cross-linking and phosphopeptide mapping.* Journal of Biological Chemistry, 1999. **274**(12): p. 8029-8038.
139. Suk, J.Y., et al., *Heparin accelerates gelsolin amyloidogenesis.* Biochemistry, 2006. **45**(7): p. 2234-2242.
140. Nel, A.E., et al., *Understanding biophysicochemical interactions at the nano–bio interface.* Nature materials, 2009. **8**(7): p. 543-557.
141. Treuel, L., et al., *Protein corona–from molecular adsorption to physiological complexity.* Beilstein journal of nanotechnology, 2015. **6**: p. 857.
142. De, M., et al., *Biomimetic interactions of proteins with functionalized nanoparticles: a thermodynamic study.* Journal of the American Chemical Society, 2007. **129**(35): p. 10747-10753.
143. Casals, E., et al., *Time evolution of the nanoparticle protein corona.* ACS nano, 2010. **4**(7): p. 3623-3632.
144. Dell'Orco, D., et al., *Modeling the time evolution of the nanoparticle-protein corona in a body fluid.* PloS one, 2010. **5**(6): p. e10949.
145. Owens, D.E. and N.A. Peppas, *Opsonization, biodistribution, and pharmacokinetics of polymeric nanoparticles.* International journal of pharmaceutics, 2006. **307**(1): p. 93-102.
146. Lundqvist, M., et al., *The nanoparticle protein corona formed in human blood or human blood fractions.* PloS one, 2017. **12**(4): p. e0175871.
147. Mahmoudi, M., et al., *Protein− nanoparticle interactions: opportunities and challenges.* Chemical reviews, 2011. **111**(9): p. 5610-5637.
148. Shang, L., et al., *pH-dependent protein conformational changes in albumin: gold nanoparticle bioconjugates: a spectroscopic study.* Langmuir, 2007. **23**(5): p. 2714-2721.
149. Satzer, P., et al., *Protein adsorption onto nanoparticles induces conformational changes: Particle size dependency, kinetics, and mechanisms.* Engineering in life sciences, 2016. **16**(3): p. 238-246.
150. Lundqvist, M., et al., *Nanoparticle size and surface properties determine the protein corona with possible implications for biological impacts.* Proceedings of the National Academy of Sciences, 2008. **105**(38): p. 14265-14270.
151. Nasir, I., M. Lundqvist, and C. Cabaleiro-Lago, *Size and surface chemistry of nanoparticles lead to a variant behavior in the unfolding dynamics of human carbonic anhydrase.* Nanoscale, 2015. **7**(41): p. 17504-17515.
152. Piella, J., N.G. Bastús, and V. Puntes, *Size-dependent protein–nanoparticle interactions in citrate-stabilized gold nanoparticles: the emergence of the protein corona.* Bioconjugate chemistry, 2016. **28**(1): p. 88-97.
153. Yadav, I., V.K. Aswal, and J. Kohlbrecher, *Size-dependent interaction of silica nanoparticles with lysozyme and bovine serum albumin proteins.* Physical Review E, 2016. **93**(5): p. 052601.
154. Treuel, L., et al., *The influence of surface composition of nanoparticles on their interactions with serum albumin.* ChemPhysChem, 2010. **11**(14): p. 3093-3099.
155. Podila, R., et al., *Effects of surface functional groups on the formation of nanoparticle-protein corona.* Applied physics letters, 2012. **101**(26): p. 263701.
156. Ritz, S., et al., *Protein corona of nanoparticles: distinct proteins regulate the cellular uptake.* Biomacromolecules, 2015. **16**(4): p. 1311-1321.
157. Gessner, A., et al., *Functional groups on polystyrene model nanoparticles: influence on protein adsorption.* Journal of Biomedical Materials Research Part A, 2003. **65**(3): p. 319-326.
158. Tenzer, S., et al., *Rapid formation of plasma protein corona critically affects nanoparticle pathophysiology.* Nature nanotechnology, 2013. **8**(10): p. 772-781.

159. Valenti, L.E., et al., *The adsorption–desorption process of bovine serum albumin on carbon nanotubes.* Journal of colloid and interface science, 2007. **307**(2): p. 349-356.
160. Zhao, X., et al., *New insights into the behavior of bovine serum albumin adsorbed onto carbon nanotubes: comprehensive spectroscopic studies.* The Journal of Physical Chemistry B, 2010. **114**(16): p. 5625-5631.
161. Schmidt, B., et al., *Quantitative characterization of gold nanoparticles by field-flow fractionation coupled online with light scattering detection and inductively coupled plasma mass spectrometry.* Anal. Chem, 2011. **83**(7): p. 2461-2468.
162. Pfeiffer, C., et al., *Interaction of colloidal nanoparticles with their local environment: the (ionic) nanoenvironment around nanoparticles is different from bulk and determines the physico-chemical properties of the nanoparticles.* Journal of The Royal Society Interface, 2014. **11**(96): p. 20130931.
163. Simoes, T., et al. *Bovine Serum Albumin binding to CoCrMo nanoparticles and the influence on dissolution*. in *Journal of Physics: Conference Series*. 2015. IOP Publishing.
164. Dutta, D., et al., *Adsorbed proteins influence the biological activity and molecular targeting of nanomaterials.* Toxicological Sciences, 2007. **100**(1): p. 303-315.
165. Deng, Z.J., et al., *Differential plasma protein binding to metal oxide nanoparticles.* Nanotechnology, 2009. **20**(45): p. 455101.
166. Gojova, A., et al., *Induction of inflammation in vascular endothelial cells by metal oxide nanoparticles: effect of particle composition.* Environmental health perspectives, 2007. **115**(3): p. 403.
167. Mariam, J., P. Dongre, and D. Kothari, *Study of interaction of silver nanoparticles with bovine serum albumin using fluorescence spectroscopy.* Journal of fluorescence, 2011. **21**(6): p. 2193.
168. Ravindran, A., et al., *Studies on interaction of colloidal Ag nanoparticles with bovine serum albumin (BSA).* Colloids and Surfaces B: Biointerfaces, 2010. **76**(1): p. 32-37.
169. Kittler, S., et al., *Toxicity of silver nanoparticles increases during storage because of slow dissolution under release of silver ions.* Chem. Mater, 2010. **22**(16): p. 4548-4554.
170. Shang, L., et al., *Ultrasmall fluorescent silver nanoclusters: protein adsorption and its effects on cellular responses.* Nano Research, 2012. **5**(8): p. 531-542.
171. Shannahan, J.H., et al., *Silver nanoparticle protein corona composition in cell culture media.* PloS one, 2013. **8**(9): p. e74001.
172. Huang, X.-W., et al., *Monodisperse phase transfer and surface bioengineering of metal nanoparticles via a silk fibroin protein corona.* Nanoscale, 2017. **9**(8): p. 2695-2700.
173. Casals, E., et al., *Hardening of the nanoparticle–protein corona in metal (Au, Ag) and oxide (Fe3O4, CoO, and CeO2) nanoparticles.* Small, 2011. **7**(24): p. 3479-3486.
174. Aggarwal, P., et al., *Nanoparticle interaction with plasma proteins as it relates to particle biodistribution, biocompatibility and therapeutic efficacy.* Advanced drug delivery reviews, 2009. **61**(6): p. 428-437.
175. Mahmoudi, M., et al., *Variation of protein corona composition of gold nanoparticles following plasmonic heating.* Nano letters, 2013. **14**(1): p. 6-12.
176. Fei, L. and S. Perrett, *Effect of nanoparticles on protein folding and fibrillogenesis.* International journal of molecular sciences, 2009. **10**(2): p. 646-655.
177. Vertegel, A.A., R.W. Siegel, and J.S. Dordick, *Silica nanoparticle size influences the structure and enzymatic activity of adsorbed lysozyme.* Langmuir, 2004. **20**(16): p. 6800-6807.
178. Shang, W., et al., *Unfolding of ribonuclease A on silica nanoparticle surfaces.* Nano letters, 2007. **7**(7): p. 1991-1995.
179. Tsai, D.-H., et al., *Adsorption and conformation of serum albumin protein on gold nanoparticles investigated using dimensional measurements and in situ spectroscopic methods.* Langmuir, 2011. **27**(6): p. 2464-2477.

180. Gagner, J.E., et al., *Effect of gold nanoparticle structure on the conformation and function of adsorbed proteins.* Biomaterials, 2012. **33**(33): p. 8503-8516.
181. Zolghadri, S., et al., *Interaction between silver nanoparticle and bovine hemoglobin at different temperatures.* Journal of Nanoparticle Research, 2009. **11**(7): p. 1751.
182. Bhunia, A.K., et al., *Biocompatibility study of protein capped and uncapped silver nanoparticles on human hemoglobin.* Journal of Physics D: Applied Physics, 2015. **48**(23): p. 235305.
183. Ban, D.K. and S. Paul, *Protein corona over silver nanoparticles triggers conformational change of proteins and drop in bactericidal potential of nanoparticles: Polyethylene glycol capping as preventive strategy.* Colloids and Surfaces B: Biointerfaces, 2016. **146**: p. 577-584.
184. Gnanadhas, D.P., et al., *Interaction of silver nanoparticles with serum proteins affects their antimicrobial activity in vivo.* Antimicrobial agents and chemotherapy, 2013. **57**(10): p. 4945-4955.
185. Salvati, A., et al., *Transferrin-functionalized nanoparticles lose their targeting capabilities when a biomolecule corona adsorbs on the surface.* Nature nanotechnology, 2013. **8**(2): p. 137-143.
186. Chakraborti, S., et al., *Interaction of polyethyleneimine-functionalized ZnO nanoparticles with bovine serum albumin.* Langmuir, 2012. **28**(30): p. 11142-11152.
187. Chakraborti, S., S. Sarwar, and P. Chakrabarti, *The effect of the binding of ZnO nanoparticle on the structure and stability of α-lactalbumin: a comparative study.* The Journal of Physical Chemistry B, 2013. **117**(43): p. 13397-13408.
188. Chatterjee, T., et al., *The effect of zinc oxide nanoparticles on the structure of the periplasmic domain of the Vibrio cholerae ToxR protein.* The FEBS journal, 2010. **277**(20): p. 4184-4194.
189. Žūkienė, R. and V. Snitka, *Zinc oxide nanoparticle and bovine serum albumin interaction and nanoparticles influence on cytotoxicity in vitro.* Colloids and Surfaces B: Biointerfaces, 2015. **135**: p. 316-323.
190. Runa, S., et al. *PEGylated nanoparticles: protein corona and secondary structure*. in *SPIE NanoScience+ Engineering*. 2014. International Society for Optics and Photonics.
191. Linse, S., et al., *Nucleation of protein fibrillation by nanoparticles.* Proceedings of the National Academy of Sciences, 2007. **104**(21): p. 8691-8696.
192. Mohammadi, S. and M. Nikkhah, *TiO2 Nanoparticles as Potential Promoting Agents of Fibrillation of α-Synuclein, a Parkinson's Disease-Related Protein.* Iranian Journal of Biotechnology, 2017. **15**(2): p. 87-94.
193. Álvarez, Y.D., et al., *Influence of gold nanoparticles on the kinetics of α-synuclein aggregation.* Nano letters, 2013. **13**(12): p. 6156-6163.
194. Gladytz, A., et al., *Structure-Making Effects of Metal Nanoparticles in Amyloid Peptide Fibrillation.* Particle & Particle Systems Characterization, 2015. **32**(5): p. 573-582.
195. Liu, H., et al., *Negatively charged hydrophobic nanoparticles inhibit amyloid β-protein fibrillation: The presence of an optimal charge density.* Reactive and Functional Polymers, 2016. **103**: p. 108-116.
196. Xiong, N., et al., *Design of LVFFARK and LVFFARK-functionalized nanoparticles for inhibiting amyloid β-protein fibrillation and cytotoxicity.* ACS applied materials & interfaces, 2015. **7**(10): p. 5650-5662.
197. Cabaleiro-Lago, C., et al., *Inhibition of amyloid β protein fibrillation by polymeric nanoparticles.* Journal of the American Chemical Society, 2008. **130**(46): p. 15437-15443.
198. Liao, Y.H., et al., *Negatively Charged Gold Nanoparticles Inhibit Alzheimer's Amyloid-β Fibrillization, Induce Fibril Dissociation, and Mitigate Neurotoxicity.* Small, 2012. **8**(23): p. 3631-3639.
199. Prasad, A. *Discovery and importance of zinc in human nutrition*. in *Federation proceedings*. 1984.

200. Maret, W. and H.H. Sandstead, *Zinc requirements and the risks and benefits of zinc supplementation.* Journal of Trace Elements in Medicine and Biology, 2006. **20**(1): p. 3-18.
201. Bao, P., S.-C. Chen, and K.-Q. Xiao, *Dynamic equilibrium of endogenous selenium nanoparticles in selenite-exposed cancer cells: a deep insight into the interaction between endogenous SeNPs and proteins.* Molecular BioSystems, 2015. **11**(12): p. 3355-3361.
202. Ng, H.T., et al., *Optical properties of single-crystalline ZnO nanowires on m-sapphire.* Applied physics letters, 2003. **82**(13): p. 2023-2025.
203. Smijs, T.G. and S. Pavel, *Titanium dioxide and zinc oxide nanoparticles in sunscreens: focus on their safety and effectiveness.* Nanotechnology, science and applications, 2011. **4**: p. 95.
204. Zvyagin, A.V., et al., *Imaging of zinc oxide nanoparticle penetration in human skin in vitro and in vivo.* Journal of biomedical optics, 2008. **13**(6): p. 064031-064031-9.
205. Sudhagar, S., et al., *Targeting and sensing cancer cells with ZnO nanoprobes in vitro.* Biotechnology letters, 2011. **33**(9): p. 1891-1896.
206. Wang, H., et al., *Fluorescent dye encapsulated ZnO particles with cell-specific toxicity for potential use in biomedical applications.* Journal of Materials Science: Materials in Medicine, 2009. **20**(1): p. 11.
207. Yang, S.-C., et al., *Tumor detection strategy using ZnO light-emitting nanoprobes.* Nanotechnology, 2012. **23**(5): p. 055202.
208. Rasmussen, J.W., et al., *Zinc oxide nanoparticles for selective destruction of tumor cells and potential for drug delivery applications.* Expert opinion on drug delivery, 2010. **7**(9): p. 1063-1077.
209. Ricci-Júnior, E. and J.M. Marchetti, *Zinc (II) phthalocyanine loaded PLGA nanoparticles for photodynamic therapy use.* International journal of pharmaceutics, 2006. **310**(1): p. 187-195.
210. Arakha, M., et al., *Zinc oxide nanoparticle energy band gap reduction triggers the oxidative stress resulting into autophagy-mediated apoptotic cell death.* Free Radical Biology and Medicine, 2017.
211. Nie, L., et al., *Functionalized tetrapod-like ZnO nanostructures for plasmid DNA purification, polymerase chain reaction and delivery.* Nanotechnology, 2006. **18**(1): p. 015101.
212. Wang, J., et al., *Zinc oxide nanocomb biosensor for glucose detection.* Applied physics letters, 2006. **88**(23): p. 233106.
213. Kołodziejczak-Radzimska, A. and T. Jesionowski, *Zinc oxide—from synthesis to application: a review.* Materials, 2014. **7**(4): p. 2833-2881.
214. Control, C.f.D. and Prevention, *National diabetes statistics report: estimates of diabetes and its burden in the United States, 2014.* Atlanta, GA: US Department of Health and Human Services, 2014.
215. Opie, E.L., *The relation oe diabetes mellitus to lesions of the pancreas. hyaline degeneration of the islands oe langerhans.* The Journal of experimental medicine, 1901. **5**(5): p. 527-540.
216. Westermark, P. and L. Grimelius, *The pancreatic islet cells in insular amyloidosis in human diabetic and non-diabetic adults.* Acta Pathologica Microbiologica Scandinavica Section A Pathology, 1973. **81**(3): p. 291-300.
217. Westermark, P., et al., *A novel peptide in the calcitonin gene related peptide family as an amyloid fibril protein in the endocrine pancreas.* Biochemical and biophysical research communications, 1986. **140**(3): p. 827-831.
218. Montane, J., et al., *Metabolic stress, IAPP and islet amyloid.* Diabetes, Obesity and Metabolism, 2012. **14**(s3): p. 68-77.
219. Nishi, M., et al., *Islet amyloid polypeptide. A new beta cell secretory product related to islet amyloid deposits.* J Biol Chem, 1990. **265**(8): p. 4173-4176.
220. Jaikaran, E.T.A.S. and A. Clark, *Islet amyloid and type 2 diabetes : from molecular misfolding to islet pathophysiology.* Biochimica et Biophysica Acta (BBA)-Molecular Basis of Disease, 2001. **1537**(3): p. 179-203.

221. Westermark, P., A. Andersson, and G.T. Westermark, *Islet amyloid polypeptide, islet amyloid, and diabetes mellitus.* Physiological reviews, 2011. **91**(3): p. 795-826.
222. Gulli, G., L. Rossetti, and R. DeFronzo, *Hyperamylinemia is associated with hyperinsulinemia in the glucose-tolerant, insulin-resistant offspring of two Mexican-American non—insulin-dependent diabetic parents.* Metabolism, 1997. **46**(10): p. 1157-1161.
223. O'Rahilly, S., I. Barroso, and N.J. Wareham, *Genetic factors in type 2 diabetes: the end of the beginning?* Science, 2005. **307**(5708): p. 370-373.
224. Jaikaran, E., M. Nilsson, and A. Clark, *Pancreatic beta-cell granule peptides form heteromolecular complexes which inhibit islet amyloid polypeptide fibril formation.* Biochem. J, 2004. **377**: p. 709-716.
225. Brender, J.R., et al., *Role of zinc in human islet amyloid polypeptide aggregation.* Journal of the American Chemical Society, 2010. **132**(26): p. 8973-8983.
226. Ballut, L., et al., *Mapping of heparin/heparan sulfate binding sites on αvβ3 integrin by molecular docking.* Journal of Molecular Recognition, 2013. **26**(2): p. 76-85.
227. Bitomsky, W. and R.C. Wade, *Docking of glycosaminoglycans to heparin-binding proteins: Validation for aFGF, bFGF, and antithrombin and application to IL-8.* Journal of the American Chemical Society, 1999. **121**(13): p. 3004-3013.
228. Watson, D.J., A.D. Lander, and D.J. Selkoe, *Heparin-binding Properties of the Amyloidogenic Peptides Aβ and Amylin dependence on aggregation state and inhibition by congo red.* Journal of Biological Chemistry, 1997. **272**(50): p. 31617-31624.
229. Mcduffie, N., *Heparin: Structure, Cellular Functions, and Clinical Applications*. 2012: Elsevier.
230. Westermark, P., et al., *Islet amyloid polypeptide: pinpointing amino acid residues linked to amyloid fibril formation.* Proceedings of the National Academy of Sciences, 1990. **87**(13): p. 5036-5040.
231. Jha, S., et al., *THE pH-dependence of amylin fibrillization.* Biochemistry, 2014. **53**(2): p. 300-310.
232. Arnold, K., et al., *The SWISS-MODEL workspace: a web-based environment for protein structure homology modelling.* Bioinformatics, 2006. **22**(2): p. 195-201.
233. Berman, H.M., et al., *The Protein Data Bank, 1999–*, in *International Tables for Crystallography Volume F: Crystallography of biological macromolecules*. 2006, Springer. p. 675-684.
234. Colovos, C. and T.O. Yeates, *Verification of protein structures: patterns of nonbonded atomic interactions.* Protein science, 1993. **2**(9): p. 1511-1519.
235. Laskowski, R.A., et al., *PROCHECK: a program to check the stereochemical quality of protein structures.* Journal of applied crystallography, 1993. **26**(2): p. 283-291.
236. Pontius, J., J. Richelle, and S.J. Wodak, *Deviations from standard atomic volumes as a quality measure for protein crystal structures.* Journal of molecular biology, 1996. **264**(1): p. 121-136.
237. Bolton, E.E., et al., *PubChem: integrated platform of small molecules and biological activities.* Annual reports in computational chemistry, 2008. **4**: p. 217-241.
238. Dementiev, A., et al., *Antithrombin− anhydrothrombin− heparin ternary complex structure reveals the basis of inhibitor specificity.* Nat. Struct. Mol. Biol, 2004.
239. Mulloy, B., et al., *Nmr and molecular-modelling studies of the solution conformation of heparin.* Biochem. J, 1993. **293**: p. 849-858.
240. Yuriev, E. and P.A. Ramsland, *Latest developments in molecular docking: 2010–2011 in review.* Journal of Molecular Recognition, 2013. **26**(5): p. 215-239.
241. Ritchie, D.W. and V. Venkatraman, *Ultra-fast FFT protein docking on graphics processors.* Bioinformatics, 2010. **26**(19): p. 2398-2405.
242. Pettersen, E.F., et al., *UCSF Chimera—a visualization system for exploratory research and analysis.* Journal of computational chemistry, 2004. **25**(13): p. 1605-1612.

243. Dunbrack, R.L., *Rotamer Libraries in the 21 st Century.* Current opinion in structural biology, 2002. **12**(4): p. 431-440.
244. SchuÈttelkopf, A.W. and D.M. Van Aalten, *PRODRG: a tool for high-throughput crystallography of protein–ligand complexes.* Acta Crystallographica Section D: Biological Crystallography, 2004. **60**(8): p. 1355-1363.
245. Schrödinger, L., *PyMOL The PyMOL Molecular Graphics System*. 2010, Version.
246. Laskowski, R.A. and M.B. Swindells, *LigPlot+: multiple ligand–protein interaction diagrams for drug discovery.* Journal of chemical information and modeling, 2011. **51**(10): p. 2778-2786.
247. BIOVIA, D.S., *Discovery Studio Modeling Environment.* San Diego, Dassault Systemes, Release, 2013. **4**.
248. Pronk, S., et al., *GROMACS 4.5: a high-throughput and highly parallel open source molecular simulation toolkit.* Bioinformatics, 2013. **29**(7): p. 845-854.
249. Hess, B., *P-LINCS: A parallel linear constraint solver for molecular simulation.* Journal of Chemical Theory and Computation, 2008. **4**(1): p. 116-122.
250. Darden, T., et al., *New tricks for modelers from the crystallography toolkit: the particle mesh Ewald algorithm and its use in nucleic acid simulations.* Structure, 1999. **7**(3): p. R55-R60.
251. Wiltzius, J.J., et al., *Atomic structures of IAPP (amylin) fusions suggest a mechanism for fibrillation and the role of insulin in the process.* Protein science, 2009. **18**(7): p. 1521-1530.
252. Nanga, R.P., et al., *Structure and membrane orientation of IAPP in its natively amidated form at physiological pH in a membrane environment.* Biochim Biophys Acta, 2011. **1808**(10): p. 2337-42.
253. Nanga, R.P., et al., *Three-dimensional structure and orientation of rat islet amyloid polypeptide protein in a membrane environment by solution NMR spectroscopy.* J Am Chem Soc, 2009. **131**(23): p. 8252-61.
254. Gordon, J.C., et al., *H++: a server for estimating pKas and adding missing hydrogens to macromolecules.* Nucleic acids research, 2005. **33**(suppl 2): p. W368-W371.
255. Bhaskaran, R. and P. Ponnuswamy, *Positional flexibilities of amino acid residues in globular proteins.* Int J Pept Protein Res, 1988. **32**(3): p. 241-255.
256. Kyte, J. and R.F. Doolittle, *A simple method for displaying the hydropathic character of a protein.* Journal of molecular biology, 1982. **157**(1): p. 105-132.
257. Gasteiger, E., et al., *Protein identification and analysis tools on the ExPASy server*. 2005: Springer.
258. Lins, L., A. Thomas, and R. Brasseur, *Analysis of accessible surface of residues in proteins.* Protein science, 2003. **12**(7): p. 1406-1417.
259. Ganesh, V.K., et al., *Structure of vaccinia complement protein in complex with heparin and potential implications for complement regulation.* Proceedings of the National Academy of Sciences of the United States of America, 2004. **101**(24): p. 8924-8929.
260. Yadav, V.K., et al., *Structural and Binding Studies of SAP-1 Protein With Heparin.* Chemical biology & drug design, 2015. **85**(3): p. 404-410.
261. Fromm, J., et al., *Differences in the interaction of heparin with arginine and lysine and the importance of these basic amino acids in the binding of heparin to acidic fibroblast growth factor.* Archives of biochemistry and biophysics, 1995. **323**(2): p. 279-287.
262. Capila, I. and R.J. Linhardt, *Heparin–protein interactions.* Angewandte Chemie International Edition, 2002. **41**(3): p. 390-412.
263. Luca, S., et al., *Peptide conformation and supramolecular organization in amylin fibrils: constraints from solid-state NMR.* Biochemistry, 2007. **46**(47): p. 13505-13522.
264. Kajava, A.V., U. Aebi, and A.C. Steven, *The parallel superpleated beta-structure as a model for amyloid fibrils of human amylin.* J Mol Biol, 2005. **348**(2): p. 247-52.
265. Wiltzius, J.J., et al., *Atomic structure of the cross-beta spine of islet amyloid polypeptide (amylin).* Protein Sci, 2008. **17**(9): p. 1467-74.

266. Zhao, J., et al., *Heterogeneous triangular structures of human islet amyloid polypeptide (amylin) with internal hydrophobic cavity and external wrapping morphology reveal the polymorphic nature of amyloid fibrils.* Biomacromolecules, 2011. **12**(5): p. 1781-1794.
267. Soriaga, A.B., et al., *Crystal structures of IAPP amyloidogenic segments reveal a novel packing motif of out-of-register beta sheets.* The Journal of Physical Chemistry B, 2016. **120**(26): p. 5810-5816.
268. Sen, T.Z., et al., *GOR V server for protein secondary structure prediction.* Bioinformatics, 2005. **21**(11): p. 2787-2788.
269. He, L., et al., *Effects of gold complexes on the assembly behavior of human islet amyloid polypeptide.* Journal of inorganic biochemistry, 2015. **152**: p. 114-122.
270. Wang, M., et al., *Differential effects of silver and iron oxide nanoparticles on IAPP amyloid aggregation.* Biomaterials Science, 2017.
271. Cabaleiro-Lago, C., et al., *Inhibition of IAPP and IAPP (20− 29) fibrillation by polymeric nanoparticles.* Langmuir, 2009. **26**(5): p. 3453-3461.
272. Gurzov, E.N., et al., *Inhibition of hIAPP Amyloid Aggregation and Pancreatic β-Cell Toxicity by OH-Terminated PAMAM Dendrimer.* Small, 2016.
273. Guo, J., et al., *Exploring the influence of carbon nanoparticles on the formation of β-sheet-rich oligomers of IAPP 22–28 peptide by molecular dynamics simulation.* PLoS One, 2013. **8**(6): p. e65579.
274. Nedumpully-Govindan, P., et al., *Graphene oxide inhibits hIAPP amyloid fibrillation and toxicity in insulin-producing NIT-1 cells.* Physical Chemistry Chemical Physics, 2016. **18**(1): p. 94-100.
275. Pourrahimi, A.M., et al., *Water-based synthesis and cleaning methods for high purity ZnO nanoparticles–comparing acetate, chloride, sulphate and nitrate zinc salt precursors.* RSC Advances, 2014. **4**(67): p. 35568-35577.
276. ToolKit, A., *QuantumWise A/S: Copenhagen*. 2016, Denmark.
277. Abraham, M.J., et al., *GROMACS: High performance molecular simulations through multi-level parallelism from laptops to supercomputers.* SoftwareX, 2015. **1**: p. 19-25.
278. Schmid, N., et al., *Definition and testing of the GROMOS force-field versions 54A7 and 54B7.* European biophysics journal, 2011. **40**(7): p. 843.
279. Tankhiwale, R. and S. Bajpai, *Preparation, characterization and antibacterial applications of ZnO-nanoparticles coated polyethylene films for food packaging.* Colloids and Surfaces B: Biointerfaces, 2012. **90**: p. 16-20.
280. Zhang, X., et al., *Effect of aspect ratio and surface defects on the photocatalytic activity of ZnO nanorods.* Scientific reports, 2014. **4**: p. 4596.
281. Habibi, M.H. and B. Karimi, *Preparation, characterization, and application of zinc oxide nanoparticles by sol-gel pyrrolysis method: influence of annealing temperature on crystalline phases.* Synthesis and Reactivity in Inorganic, Metal-Organic, and Nano-Metal Chemistry, 2014. **44**(9): p. 1291-1298.
282. V. Manzano, C., et al., *ZnO morphology control by pulsed electrodeposition.* The Journal of Physical Chemistry C, 2013. **117**(3): p. 1502-1508.
283. Xiong, H.M., et al., *Sonochemical synthesis of highly luminescent zinc oxide nanoparticles doped with magnesium (II).* Angewandte Chemie International Edition, 2009. **48**(15): p. 2727-2731.
284. Ramimoghadam, D., M.Z.B. Hussein, and Y.H. Taufiq-Yap, *Synthesis and characterization of ZnO nanostructures using palm olein as biotemplate.* Chemistry Central Journal, 2013. **7**(1): p. 71.
285. Degen, A. and M. Kosec, *Effect of pH and impurities on the surface charge of zinc oxide in aqueous solution.* Journal of the European Ceramic Society, 2000. **20**(6): p. 667-673.
286. Khurana, R., et al., *Mechanism of thioflavin T binding to amyloid fibrils.* Journal of structural biology, 2005. **151**(3): p. 229-238.

287. Yanagi, K., et al., *Hexafluoroisopropanol induces amyloid fibrils of islet amyloid polypeptide by enhancing both hydrophobic and electrostatic interactions.* Journal of Biological Chemistry, 2011. **286**(27): p. 23959-23966.
288. Greenfield, N.J., *Applications of circular dichroism in protein and peptide analysis.* TrAC Trends in Analytical Chemistry, 1999. **18**(4): p. 236-244.
289. Kayed, R., et al., *Conformational transitions of islet amyloid polypeptide (IAPP) in amyloid formation in vitro.* Journal of molecular biology, 1999. **287**(4): p. 781-796.
290. Kao, P.-Y., et al., *Inhibition of toxic IAPP amyloid by extracts of common fruits.* Journal of Functional Foods, 2015. **12**: p. 450-457.
291. Yan, L.-M., et al., *Design of a mimic of nonamyloidogenic and bioactive human islet amyloid polypeptide (IAPP) as nanomolar affinity inhibitor of IAPP cytotoxic fibrillogenesis.* Proceedings of the National Academy of Sciences of the United States of America, 2006. **103**(7): p. 2046-2051.
292. Greenfield, N.J., *Using circular dichroism spectra to estimate protein secondary structure.* Nature protocols, 2006. **1**(6): p. 2876-2890.
293. Wu, J., et al., *Imaging and elemental mapping of biological specimens with a dual-EDS dedicated scanning transmission electron microscope.* Ultramicroscopy, 2013. **128**: p. 24-31.
294. Padrick, S.B. and A.D. Miranker, *Islet amyloid: phase partitioning and secondary nucleation are central to the mechanism of fibrillogenesis.* Biochemistry, 2002. **41**(14): p. 4694-703.
295. Buchanan, L.E., et al., *Mechanism of IAPP amyloid fibril formation involves an intermediate with a transient β-sheet.* Proceedings of the National Academy of Sciences, 2013. **110**(48): p. 19285-19290.
296. Williamson, J.A. and A.D. Miranker, *Direct detection of transient α-helical states in islet amyloid polypeptide.* Protein science, 2007. **16**(1): p. 110-117.
297. Abedini, A. and D.P. Raleigh, *A role for helical intermediates in amyloid formation by natively unfolded polypeptides?* Physical biology, 2009. **6**(1): p. 015005.
298. Goldsbury, C., et al., *Amyloid fibril formation from full-length and fragments of amylin.* Journal of structural biology, 2000. **130**(2-3): p. 352-362.
299. Gilead, S. and E. Gazit, *The role of the 14–20 domain of the islet amyloid polypeptide in amyloid formation.* Experimental diabetes research, 2008. **2008**.
300. Nilsson, M.R. and D.P. Raleigh, *Analysis of amylin cleavage products provides new insights into the amyloidogenic region of human amylin.* Journal of molecular biology, 1999. **294**(5): p. 1375-1385.
301. Scrocchi, L.A., et al., *Identification of minimal peptide sequences in the (8–20) domain of human islet amyloid polypeptide involved in fibrillogenesis.* Journal of structural biology, 2003. **141**(3): p. 218-227.
302. Abedini, A., F. Meng, and D.P. Raleigh, *A single-point mutation converts the highly amyloidogenic human islet amyloid polypeptide into a potent fibrillization inhibitor.* Journal of the American Chemical Society, 2007. **129**(37): p. 11300-11301.
303. Porat, Y., et al., *Inhibition of islet amyloid polypeptide fibril formation: a potential role for heteroaromatic interactions.* Biochemistry, 2004. **43**(45): p. 14454-14462.
304. Levy, M., et al., *Phenolsulfonphthalein, but not phenolphthalein, inhibits amyloid fibril formation: implications for the modulation of amyloid self-assembly.* Biochemistry, 2008. **47**(22): p. 5896-5904.
305. Mishra, A., et al., *Conformationally restricted short peptides inhibit human islet amyloid polypeptide (hIAPP) fibrillization.* Chemical Communications, 2013. **49**(26): p. 2688-2690.
306. Tatarek-Nossol, M., et al., *Inhibition of hIAPP amyloid-fibril formation and apoptotic cell death by a designed hIAPP amyloid-core-containing hexapeptide.* Chemistry & biology, 2005. **12**(7): p. 797-809.

307. Paul, A., et al., *Disaggregation of amylin aggregate by novel conformationally restricted aminobenzoic acid containing α/β and α/γ hybrid peptidomimetics.* Scientific reports, 2017. **7**: p. 40095.
308. Xiao, L., et al., *Inhibition of beta 1–40 amyloid fibrillation with N-acetyl-l-cysteine capped quantum dots.* Biomaterials, 2010. **31**(1): p. 91-98.
309. Gladytz, A., B. Abel, and H.J. Risselada, *Gold-Induced Fibril Growth: The Mechanism of Surface-Facilitated Amyloid Aggregation.* Angewandte Chemie International Edition, 2016. **55**(37): p. 11242-11246.
310. Maroteaux, L., J.T. Campanelli, and R.H. Scheller, *Synuclein: a neuron-specific protein localized to the nucleus and presynaptic nerve terminal.* Journal of Neuroscience, 1988. **8**(8): p. 2804-2815.
311. Spillantini, M.G., et al., *Î±-Synuclein in filamentous inclusions of Lewy bodies from Parkinsonâ€™s disease and dementia with Lewy bodies.* Proceedings of the National Academy of Sciences, 1998. **95**(11): p. 6469-6473.
312. Baba, M., et al., *Aggregation of alpha-synuclein in Lewy bodies of sporadic Parkinson's disease and dementia with Lewy bodies.* The American journal of pathology, 1998. **152**(4): p. 879.
313. Fink, A.L., *The aggregation and fibrillation of α-synuclein.* Accounts of chemical research, 2006. **39**(9): p. 628-634.
314. Bendor, J.T., T.P. Logan, and R.H. Edwards, *The function of α-synuclein.* Neuron, 2013. **79**(6): p. 1044-1066.
315. Clayton, D.F. and J.M. George, *The synucleins: a family of proteins involved in synaptic function, plasticity, neurodegeneration and disease.* Trends in neurosciences, 1998. **21**(6): p. 249-254.
316. George, J.M., et al., *Characterization of a novel protein regulated during the critical period for song learning in the zebra finch.* Neuron, 1995. **15**(2): p. 361-372.
317. Uversky, V.N., J.R. Gillespie, and A.L. Fink, *Why are "natively unfolded" proteins unstructured under physiologic conditions?* Proteins: structure, function, and bioinformatics, 2000. **41**(3): p. 415-427.
318. Weinreb, P.H., et al., *NACP, a protein implicated in Alzheimer's disease and learning, is natively unfolded.* Biochemistry, 1996. **35**(43): p. 13709-13715.
319. Eliezer, D., et al., *Conformational properties of α-synuclein in its free and lipid-associated states.* Journal of molecular biology, 2001. **307**(4): p. 1061-1073.
320. Uversky, V.N., J. Li, and A.L. Fink, *Metal-triggered structural transformations, aggregation, and fibrillation of human α-synuclein a possible molecular link between parkinson' s disease and heavy metal exposure.* Journal of Biological Chemistry, 2001. **276**(47): p. 44284-44296.
321. Xue, B., et al., *PONDR-FIT: a meta-predictor of intrinsically disordered amino acids.* Biochimica et Biophysica Acta (BBA)-Proteins and Proteomics, 2010. **1804**(4): p. 996-1010.
322. Dosztányi, Z., et al., *IUPred: web server for the prediction of intrinsically unstructured regions of proteins based on estimated energy content.* Bioinformatics, 2005. **21**(16): p. 3433-3434.
323. Uversky, V.N., J. Li, and A.L. Fink, *Evidence for a partially folded intermediate in α-synuclein fibril formation.* Journal of Biological Chemistry, 2001. **276**(14): p. 10737-10744.
324. Uversky, V.N., J. Li, and A.L. Fink, *Trimethylamine-N-oxide-induced folding of α-synuclein.* FEBS letters, 2001. **509**(1): p. 31-35.
325. Davidson, W.S., et al., *Stabilization of α-synuclein secondary structure upon binding to synthetic membranes.* Journal of Biological Chemistry, 1998. **273**(16): p. 9443-9449.
326. de Laureto, P.P., et al., *Conformational properties of the SDS-bound state of α-synuclein probed by limited proteolysis: unexpected rigidity of the acidic C-terminal tail.* Biochemistry, 2006. **45**(38): p. 11523-11531.
327. Conway, K.A., et al., *Acceleration of oligomerization, not fibrillization, is a shared property of both α-synuclein mutations linked to early-onset Parkinson's disease: implications for*

pathogenesis and therapy. Proceedings of the National Academy of Sciences, 2000. **97**(2): p. 571-576.

328. Ding, T.T., et al., *Annular α-synuclein protofibrils are produced when spherical protofibrils are incubated in solution or bound to brain-derived membranes.* Biochemistry, 2002. **41**(32): p. 10209-10217.
329. Souza, J.M., et al., *Dityrosine Cross-linking Promotes Formation of Stable α-Synuclein Polymers Implication Of Nitrative And Oxidative Stress In The Pathogenesis Of Neurodegenerative Synucleinopathies.* Journal of Biological Chemistry, 2000. **275**(24): p. 18344-18349.
330. Sawaya, M.R., et al., *Atomic structures of amyloid cross-[beta] spines reveal varied steric zippers.* Nature, 2007. **447**(7143): p. 453.
331. Uversky, V.N., et al., *Accelerated α-synuclein fibrillation in crowded milieu.* FEBS letters, 2002. **515**(1-3): p. 99-103.
332. Giehm, L., et al., *Low-resolution structure of a vesicle disrupting α-synuclein oligomer that accumulates during fibrillation.* Proceedings of the National Academy of Sciences, 2011. **108**(8): p. 3246-3251.
333. Van Rooijen, B.D., M.M. Claessens, and V. Subramaniam, *Membrane permeabilization by oligomeric α-synuclein: in search of the mechanism.* PLoS One, 2010. **5**(12): p. e14292.
334. Kayed, R., et al., *Permeabilization of lipid bilayers is a common conformation-dependent activity of soluble amyloid oligomers in protein misfolding diseases.* Journal of Biological Chemistry, 2004. **279**(45): p. 46363-46366.
335. Volles, M.J. and P.T. Lansbury, *Zeroing in on the pathogenic form of α-synuclein and its mechanism of neurotoxicity in Parkinson's disease.* Biochemistry, 2003. **42**(26): p. 7871-7878.
336. Hong, D.-P., A.L. Fink, and V.N. Uversky, *Structural characteristics of α-synuclein oligomers stabilized by the flavonoid baicalein.* Journal of molecular biology, 2008. **383**(1): p. 214-223.
337. Ehrnhoefer, D.E., et al., *EGCG redirects amyloidogenic polypeptides into unstructured, off-pathway oligomers.* Nature structural & molecular biology, 2008. **15**(6): p. 558-566.
338. Pandey, N., et al., *Curcumin inhibits aggregation of α-synuclein.* Acta neuropathologica, 2008. **115**(4): p. 479-489.
339. Frederickson, C.J., et al., *Importance of zinc in the central nervous system: the zinc-containing neuron.* The Journal of nutrition, 2000. **130**(5): p. 1471S-1483S.
340. Dexter, D., et al., *Alterations in the levels of iron, ferritin and other trace metals in Parkinson's disease and other neurodegenerative diseases affecting the basal ganglia.* Brain, 1991. **114**(4): p. 1953-1975.
341. Xie, H. and J. Wu, *Silica nanoparticles induce alpha-synuclein induction and aggregation in PC12-cells.* Chemico-biological interactions, 2016. **258**: p. 197-204.
342. Coelho-Cerqueira, E., et al., *α-Synuclein as an intrinsically disordered monomer–fact or artefact?* The FEBS journal, 2013. **280**(19): p. 4915-4927.
343. Huang, C., et al., *A new method for purification of recombinant human α-synuclein in Escherichia coli.* Protein expression and purification, 2005. **42**(1): p. 173-177.
344. Morris, G.M., et al., *AutoDock4 and AutoDockTools4: Automated docking with selective receptor flexibility.* Journal of computational chemistry, 2009. **30**(16): p. 2785-2791.
345. Kathiravan, A., G. Paramaguru, and R. Renganathan, *Study on the binding of colloidal zinc oxide nanoparticles with bovine serum albumin.* Journal of Molecular Structure, 2009. **934**(1): p. 129-137.
346. Li, L., et al., *Analytical strategies for detecting nanoparticle–protein interactions.* Analyst, 2010. **135**(7): p. 1519-1530.
347. Cedervall, T., et al., *Understanding the nanoparticle–protein corona using methods to quantify exchange rates and affinities of proteins for nanoparticles.* Proceedings of the National Academy of Sciences, 2007. **104**(7): p. 2050-2055.

348. Ross, P.D. and S. Subramanian, *Thermodynamics of protein association reactions: forces contributing to stability.* Biochemistry, 1981. **20**(11): p. 3096-3102.
349. Beechem, J.M. and L. Brand, *Time-resolved fluorescence of proteins.* Annual review of biochemistry, 1985. **54**(1): p. 43-71.
350. Khalaf, O., et al., *The H50Q mutation enhances α-synuclein aggregation, secretion, and toxicity.* Journal of Biological Chemistry, 2014. **289**(32): p. 21856-21876.
351. Perni, M., et al., *A natural product inhibits the initiation of α-synuclein aggregation and suppresses its toxicity.* Proceedings of the National Academy of Sciences, 2017. **114**(6): p. E1009-E1017.
352. Zhu, M., et al., *The flavonoid baicalein inhibits fibrillation of α-synuclein and disaggregates existing fibrils.* Journal of Biological Chemistry, 2004. **279**(26): p. 26846-26857.
353. Ardah, M.T., et al., *Structure activity relationship of phenolic acid inhibitors of α-synuclein fibril formation and toxicity.* Frontiers in aging neuroscience, 2014. **6**.
354. Chan, F.T., et al., *Structure-specific intrinsic fluorescence of protein amyloids used to study their kinetics of aggregation.* Bio-nanoimaging: protein misfolding and aggregation, 2014.
355. Lee, J. and R.T. Ross, *Absorption and fluorescence of tyrosine hydrogen-bonded to amide-like ligands.* The Journal of Physical Chemistry B, 1998. **102**(23): p. 4612-4618.
356. Szabo, A., et al., *Tyrosinate fluorescence maxima at 345 nm in proteins lacking tryptophan at pH 7.* FEBS letters, 1978. **94**(2): p. 249-252.
357. Serpell, L.C., et al., *Fiber diffraction of synthetic α-synuclein filaments shows amyloid-like cross-β conformation.* Proceedings of the National Academy of Sciences, 2000. **97**(9): p. 4897-4902.
358. Breydo, L., J.W. Wu, and V.N. Uversky, *α-Synuclein misfolding and Parkinson's disease.* Biochimica et Biophysica Acta (BBA)-Molecular Basis of Disease, 2012. **1822**(2): p. 261-285.
359. Yang, J.A., et al., *α-Synuclein's adsorption, conformation, and orientation on cationic gold nanoparticle surfaces seeds global conformation change.* The Journal of Physical Chemistry B, 2014. **118**(13): p. 3559-3571.
360. Tcherkasskaya, O., *Slow phase separation–preliminary stages in the filament formation.* Nanomedicine: Nanotechnology, Biology and Medicine, 2006. **2**(4): p. 314.
361. Ghavami, M., et al., *Physiological temperature has a crucial role in amyloid beta in the absence and presence of hydrophobic and hydrophilic nanoparticles.* ACS chemical neuroscience, 2013. **4**(3): p. 375.
362. Wang, X., et al., *Influence of cell size on cellular uptake of gold nanoparticles.* Biomaterials science, 2016. **4**(6): p. 970-978.
363. Zraika, S., et al., *Toxic oligomers and islet beta cell death: guilty by association or convicted by circumstantial evidence?* Diabetologia, 2010. **53**(6): p. 1046-56.
364. Klegeris, A., et al., *α-Synuclein activates stress signaling protein kinases in THP-1 cells and microglia.* Neurobiology of aging, 2008. **29**(5): p. 739-752.
365. Salata, O.V., *Applications of nanoparticles in biology and medicine.* Journal of nanobiotechnology, 2004. **2**(1): p. 3.
366. Liu, J.-H., et al., *Low toxicity and accumulation of zinc oxide nanoparticles in mice after 270-day consecutive dietary supplementation.* Toxicology Research, 2017. **6**(2): p. 134-143.
367. Morimoto, Y., et al., *Evaluation of pulmonary toxicity of zinc oxide nanoparticles following inhalation and intratracheal instillation.* International journal of molecular sciences, 2016. **17**(8): p. 1241.
368. Pati, R., et al., *Zinc-oxide nanoparticles exhibit genotoxic, clastogenic, cytotoxic and actin depolymerization effects by inducing oxidative stress responses in macrophages and adult mice.* Toxicological Sciences, 2016. **150**(2): p. 454-472.
369. Chue, P. and S. Valiyaveettil, *Toxicity Studies of Zinc oxide Nanoparticles in Human cells.* Science Drive, 2009. **117543**.

370. Cedillos, R.O., *Alpha-synuclein aggregates activate the Nlrp3 Inflammasome following vesicle rupture.* 2013.
371. Sipe, J.D., et al., *Amyloid fibril proteins and amyloidosis: chemical identification and clinical classification International Society of Amyloidosis 2016 Nomenclature Guidelines.* Amyloid, 2016. **23**(4): p. 209-213.
372. Westermark, P., et al., *Amyloid fibrils in human insulinoma and islets of Langerhans of the diabetic cat are derived from a neuropeptide-like protein also present in normal islet cells.* Proceedings of the National Academy of Sciences, 1987. **84**(11): p. 3881-3885.
373. Störkel, S., et al., *Iatrogenic, insulin-dependent, local amyloidosis.* Laboratory investigation; a journal of technical methods and pathology, 1983. **48**(1): p. 108-111.
374. Dische, F., et al., *Insulin as an amyloid-fibril protein at sites of repeated insulin injections in a diabetic patient.* Diabetologia, 1988. **31**(3): p. 158-161.
375. Brange, J., et al., *Toward understanding insulin fibrillation.* Journal of pharmaceutical sciences, 1997. **86**(5): p. 517-525.
376. Blundell, T., et al., *Atomic positions in rhombohedral 2-zinc insulin crystals.* Nature, 1971. **231**: p. 506-511.
377. Bryant, C., et al., *Acid stabilization of insulin.* Protein Engineering, 1993. **6**(Supplement): p. 8-8.
378. Nielsen, L., et al., *Effect of environmental factors on the kinetics of insulin fibril formation: elucidation of the molecular mechanism.* Biochemistry, 2001. **40**(20): p. 6036-6046.
379. Noormägi, A., et al., *Insulin Fibrillization at Acidic and Physiological pH Values is Controlled by Different Molecular Mechanisms.* The protein journal, 2015. **34**(6): p. 398-403.
380. Ahmad, A., et al., *Stimulation of insulin fibrillation by urea-induced intermediates.* Journal of Biological Chemistry, 2004. **279**(15): p. 14999-15013.
381. Ahmad, A., et al., *Early events in the fibrillation of monomeric insulin.* Journal of Biological Chemistry, 2005. **280**(52): p. 42669-42675.
382. Hua, Q.-x. and M.A. Weiss, *Mechanism of insulin fibrillation the structure of insulin under amyloidogenic conditions resembles a protein-folding intermediate.* Journal of Biological Chemistry, 2004. **279**(20): p. 21449-21460.
383. Nielsen, L., et al., *Probing the mechanism of insulin fibril formation with insulin mutants.* Biochemistry, 2001. **40**(28): p. 8397-8409.
384. Bouchard, M., et al., *Formation of insulin amyloid fibrils followed by FTIR simultaneously with CD and electron microscopy.* Protein Science, 2000. **9**(10): p. 1960-1967.
385. Ivanova, M.I., et al., *Molecular basis for insulin fibril assembly.* Proceedings of the National Academy of Sciences, 2009. **106**(45): p. 18990-18995.
386. Jiménez, J.L., et al., *The protofilament structure of insulin amyloid fibrils.* Proceedings of the National Academy of Sciences, 2002. **99**(14): p. 9196-9201.
387. Yoshihara, H., et al., *Characterization of Novel Insulin Fibrils That Show Strong Cytotoxicity Under Physiological pH.* Journal of pharmaceutical sciences, 2016. **105**(4): p. 1419-1426.
388. Selkoe, D.J., *Folding proteins in fatal ways.* Nature, 2003. **426**(6968): p. 900-904.
389. Koziara, J.M., et al., *In situ blood–brain barrier transport of nanoparticles.* Pharmaceutical research, 2003. **20**(11): p. 1772-1778.
390. Wang, J., et al., *Time-dependent translocation and potential impairment on central nervous system by intranasally instilled TiO 2 nanoparticles.* Toxicology, 2008. **254**(1): p. 82-90.
391. Tiwari, A., et al., *Passive membrane penetration by ZnO nanoparticles is driven by the interplay of electrostatic and phase boundary conditions.* Nanoscale, 2018.
392. Moyano, D.F. and V.M. Rotello, *Nano meets biology: structure and function at the nanoparticle interface.* Langmuir, 2011. **27**(17): p. 10376-10385.
393. Hsieh, S., C.-w. Chang, and H.-h. Chou, *Gold nanoparticles as amyloid-like fibrillogenesis inhibitors.* Colloids and Surfaces B: Biointerfaces, 2013. **112**: p. 525-529.

394. Palmal, S., N.R. Jana, and N.R. Jana, *Inhibition of amyloid fibril growth by nanoparticle coated with histidine-based polymer.* The Journal of Physical Chemistry C, 2014. **118**(37): p. 21630-21638.
395. Vinardell, M.P., et al., *In Vitro Comparative Skin Irritation Induced by Nano and Non-Nano Zinc Oxide.* Nanomaterials, 2017. **7**(3): p. 56.
396. Klunk, W.E., R.F. Jacob, and R.P. Mason, *Quantifying amyloid β-peptide (Aβ) aggregation using the Congo Red-Aβ (CR–Aβ) spectrophotometric assay.* Analytical biochemistry, 1999. **266**(1): p. 66-76.
397. Böhm, G., R. Muhr, and R. Jaenicke, *Quantitative analysis of protein far UV circular dichroism spectra by neural networks.* Protein Engineering, Design and Selection, 1992. **5**(3): p. 191-195.
398. Jacob, D., et al., *Synthesis and identification of FITC-insulin conjugates produced using human insulin and insulin analogues for biomedical applications.* Journal of fluorescence, 2016. **26**(2): p. 617-629.
399. Shi, X., et al., *Spectroscopic investigation of the interactions between gold nanoparticles and bovine serum albumin.* Chinese Science Bulletin, 2012. **57**(10): p. 1109-1115.
400. Goy-López, S., et al., *Physicochemical characteristics of protein–NP bioconjugates: the role of particle curvature and solution conditions on human serum albumin conformation and fibrillogenesis inhibition.* Langmuir, 2012. **28**(24): p. 9113-9126.
401. Lacerda, S.H.D.P., et al., *Interaction of gold nanoparticles with common human blood proteins.* ACS nano, 2009. **4**(1): p. 365-379.
402. Zhang, Y., et al., *Stability of commercial metal oxide nanoparticles in water.* Water research, 2008. **42**(8): p. 2204-2212.
403. Arakha, M., et al., *Interfacial assembly at silver nanoparticle enhances the antibacterial efficacy of nisin.* Free Radical Biology and Medicine, 2016. **101**: p. 434-445.
404. Saikia, N., A.N. Jha, and R.C. Deka, *Interaction of pyrazinamide drug functionalized carbon and boron nitride nanotubes with pncA protein: a molecular dynamics and density functional approach.* RSC Advances, 2013. **3**(35): p. 15102-15107.
405. Ruvinsky, A.M., et al., *Structure fluctuations and conformational changes in protein binding.* Journal of bioinformatics and computational biology, 2012. **10**(02): p. 1241002.
406. Milani, S., et al., *Reversible versus irreversible binding of transferrin to polystyrene nanoparticles: soft and hard corona.* ACS nano, 2012. **6**(3): p. 2532-2541.
407. Juárez, J., et al., *Influence of electrostatic interactions on the fibrillation process of human serum albumin.* The Journal of Physical Chemistry B, 2009. **113**(30): p. 10521-10529.
408. Lim, B.T. and T. Kimura, *Conformation-associated anomalous tyrosine fluorescence of adrenodoxin.* J. Biol. Chem, 1980. **255**(6): p. 2440-2444.
409. Smaoui, M.R., H. Orland, and J. Waldispühl, *Probing the binding affinity of amyloids to reduce toxicity of oligomers in diabetes.* Bioinformatics, 2015. **31**(14): p. 2294-2302.
410. Vega-Avila, E. and M.K. Pugsley. *An overview of colorimetric assay methods used to assess survival or proliferation of mammalian cells*. in *Proc West Pharmacol Soc*. 2011.
411. Li, Y.V., *Zinc and insulin in pancreatic beta-cells.* Endocrine, 2014. **45**(2): p. 178-189.
412. Wang, N., et al., *Lifetime and dissolution kinetics of zinc oxide nanoparticles in aqueous media.* Nanotechnology, 2016. **27**(32): p. 324001.
413. Shen, C., et al., *Relating cytotoxicity, zinc ions, and reactive oxygen in ZnO nanoparticle–exposed human immune cells.* toxicological sciences, 2013. **136**(1): p. 120-130.
414. Ohsugi, M., et al., *Reduced expression of the insulin receptor in mouse insulinoma (MIN6) cells reveals multiple roles of insulin signaling in gene expression, proliferation, insulin content, and secretion.* Journal of Biological Chemistry, 2005. **280**(6): p. 4992-5003.
415. Liu, Y., et al., *Insulin regulates multiple signaling pathways leading to monocyte/macrophage chemotaxis into the wound tissue.* Biology open, 2017: p. bio. 026187.

416. Zhao, Y., et al., *Mesoporous silica nanoparticle-based double drug delivery system for glucose-responsive controlled release of insulin and cyclic AMP.* Journal of the American Chemical Society, 2009. **131**(24): p. 8398-8400.
417. Babu, E.P., et al., *Size Dependent Uptake and Hemolytic Effect of Zinc Oxide Nanoparticles on Erythrocytes and Biomedical Potential of ZnO-Ferulic acid Conjugates.* Scientific reports, 2017. **7**(1): p. 4203.
418. Yang, L., et al., *Se/Ru nanoparticles as inhibitors of metal-induced Aβ aggregation in Alzheimer's disease.* Journal of Materials Chemistry B, 2014. **2**(14): p. 1977-1987.
419. Dubey, K., et al., *Tyrosine-and tryptophan-coated gold nanoparticles inhibit amyloid aggregation of insulin.* Amino acids, 2015. **47**(12): p. 2551.
420. Bekard, I.B. and D.E. Dunstan, *Tyrosine autofluorescence as a measure of bovine insulin fibrillation.* Biophysical journal, 2009. **97**(9): p. 2521-2531.
421. Becker, J.W., et al., *The covalent and three-dimensional structure of concanavalin A. III. Structure of the monomer and its interactions with metals and saccharides.* Journal of Biological Chemistry, 1975. **250**(4): p. 1513-1524.
422. Przytycka, T., R. Srinivasan, and G.D. Rose, *Recursive domains in proteins.* Protein Science, 2002. **11**(2): p. 409-417.
423. Vijayan, M. and N. Chandra, *Lectins.* Current opinion in structural biology, 1999. **9**(6): p. 707-714.
424. Loris, R., et al., *Legume lectin structure.* Biochimica et Biophysica Acta (BBA)-Protein Structure and Molecular Enzymology, 1998. **1383**(1): p. 9-36.
425. Reeke, G., J. Becker, and G. Edelman, *The covalent and three-dimensional structure of concanavalin A. IV. Atomic coordinates, hydrogen bonding, and quaternary structure.* Journal of Biological Chemistry, 1975. **250**(4): p. 1525-1547.
426. Mitra, N., et al., *Conformational stability of legume lectins reflect their different modes of quaternary association: solvent denaturation studies on concanavalin A and winged bean acidic agglutinin.* Biochemistry, 2002. **41**(29): p. 9256-9263.
427. Sinha, S. and A. Surolia, *Oligomerization endows enormous stability to soybean agglutinin: a comparison of the stability of monomer and tetramer of soybean agglutinin.* Biophysical journal, 2005. **88**(6): p. 4243-4251.
428. Lee, Y.-C., et al., *One-step isolation of plasma membrane proteins using magnetic beads with immobilized concanavalin A.* Protein expression and purification, 2008. **62**(2): p. 223-229.
429. Pratt, J., R. Roy, and B. Annabi, *Concanavalin-A-induced autophagy biomarkers requires membrane type-1 matrix metalloproteinase intracellular signaling in glioblastoma cells.* Glycobiology, 2012. **22**(9): p. 1245-1255.
430. Bittiger, H. and H.P. Schnebli, *Concanavalin A as a Tool.* 1976.
431. Ohyama, Y., et al., *Frontal affinity chromatography of ovalbumin glycoasparagines on a concanavalin A-sepharose column. A quantitative study of the binding specificity of the lectin.* Journal of Biological Chemistry, 1985. **260**(11): p. 6882-6887.
432. Go, N., *Theoretical studies of protein folding.* Annual review of biophysics and bioengineering, 1983. **12**(1): p. 183-210.
433. Freire, E., et al., *Chemical denaturation as a tool in the formulation optimization of biologics.* Drug discovery today, 2013. **18**(19): p. 1007-1013.
434. Makhatadze, G.I. and P.L. Privalov, *Protein interactions with urea and guanidinium chloride: a calorimetric study.* Journal of molecular biology, 1992. **226**(2): p. 491-505.
435. Bhuyan, A.K., *Protein stabilization by urea and guanidine hydrochloride.* Biochemistry, 2002. **41**(45): p. 13386-13394.
436. Manning, M. and W. Colon, *Structural basis of protein kinetic stability: resistance to sodium dodecyl sulfate suggests a central role for rigidity and a bias toward beta-sheet structure.* Biochemistry, 2004. **43**(35): p. 11248-11254.

437. Relkin, P., *Differential scanning calorimetry: a useful tool for studying protein denaturation.* Thermochimica acta, 1994. **246**(2): p. 371-386.
438. Diwu, Z., et al., *Fluorescent molecular probes II. The synthesis, spectral properties and use of fluorescent solvatochromic dapoxyl dyes.* Photochemistry and photobiology, 1997. **66**(4): p. 424-431.
439. Agrawal, B. and I.J. Goldstein, *Protein-carbohydrate interaction: VI. Isolation of concanavalin a by specific adsorption on cross-linked dextran gels.* Biochimica et Biophysica Acta (BBA)-Protein Structure, 1967. **147**(2): p. 262-271.
440. Kong, J. and S. Yu, *Fourier transform infrared spectroscopic analysis of protein secondary structures.* Acta biochimica et biophysica Sinica, 2007. **39**(8): p. 549-559.
441. Vivian, J.T. and P.R. Callis, *Mechanisms of tryptophan fluorescence shifts in proteins.* Biophysical journal, 2001. **80**(5): p. 2093-2109.
442. Goto, Y. and A.L. Fink, *Conformational states in. beta.-lactamase: molten-globule states at acidic and alkaline pH with high salt.* Biochemistry, 1989. **28**(3): p. 945-952.
443. Semisotnov, G.V., et al., *Study of the "molten globule"□ intermediate state in protein folding by a hydrophobic fluorescent probe.* Biopolymers, 1991. **31**(1): p. 119-128.
444. Ghosh, G. and D.K. Mandal, *Differing structural characteristics of molten globule intermediate of peanut lectin in urea and guanidine-HCl.* International journal of biological macromolecules, 2012. **51**(3): p. 188-195.
445. Pflumm, M.N. and S. Beychok, *Alkali and urea induced conformation changes in concanavalin A.* Biochemistry, 1974. **13**(24): p. 4982-4987.
446. Arrondo, J.L., N.M. Young, and H.H. Mantsch, *The solution structure of concanavalin A probed by FT-IR spectroscopy.* Biochimica et Biophysica Acta (BBA)-Protein Structure and Molecular Enzymology, 1988. **952**: p. 261-268.
447. Zand, R., B. Agrawal, and I. Goldstein, *pH-dependent conformational changes of concanavalin A.* Proceedings of the National Academy of Sciences, 1971. **68**(9): p. 2173-2176.
448. Auer, H.E. and T. Schilz, *pH-dependent changes in properties of concanavalin A in the acid pH range.* International journal of peptide and protein research, 1984. **24**(5): p. 462-471.
449. Vetri, V., et al., *Amyloid fibrils formation and amorphous aggregation in concanavalin A.* Biophysical chemistry, 2007. **125**(1): p. 184-190.
450. Royer, C.A., *Probing protein folding and conformational transitions with fluorescence.* Chemical reviews, 2006. **106**(5): p. 1769-1784.
451. Ghisaidoobe, A.B. and S.J. Chung, *Intrinsic tryptophan fluorescence in the detection and analysis of proteins: A focus on Förster resonance energy transfer techniques.* International journal of molecular sciences, 2014. **15**(12): p. 22518-22538.
452. Reynolds, J.A. and C. Tanford, *The gross conformation of protein-sodium dodecyl sulfate complexes.* Journal of Biological Chemistry, 1970. **245**(19): p. 5161-5165.
453. Nielsen, M.M., et al., *Unfolding of β-sheet proteins in SDS.* Biophysical journal, 2007. **92**(10): p. 3674-3685.
454. Fuguet, E., et al., *Critical micelle concentration of surfactants in aqueous buffered and unbuffered systems.* Analytica Chimica Acta, 2005. **548**(1): p. 95-100.
455. Jirgensons, B., *Factors determining the reconstructive denaturation of proteins in sodium dodecyl sulfate solutions. Further circular dichroism studies on structural reorganization of seven proteins.* Journal of Protein Chemistry, 1982. **1**(1): p. 71-84.
456. Vallée-Bélisle, A. and S.W. Michnick, *Multiple tryptophan probes reveal that ubiquitin folds via a late misfolded intermediate.* Journal of molecular biology, 2007. **374**(3): p. 791-805.
457. Bhuyan, A.K., *On the mechanism of SDS-induced protein denaturation.* Biopolymers, 2010. **93**(2): p. 186-199.
458. Otzen, D.E., *Protein unfolding in detergents: effect of micelle structure, ionic strength, pH, and temperature.* Biophysical journal, 2002. **83**(4): p. 2219-2230.

459. Greenfield, N.J., *Determination of the folding of proteins as a function of denaturants, osmolytes or ligands using circular dichroism.* Nature protocols, 2006. **1**(6): p. 2733-2741.
460. Chatterjee, A. and D.K. Mandal, *Denaturant-induced equilibrium unfolding of concanavalin A is expressed by a three-state mechanism and provides an estimate of its protein stability.* Biochimica et Biophysica Acta (BBA)-Proteins and Proteomics, 2003. **1648**(1): p. 174-183.
461. Khurana, R., et al., *Partially folded intermediates as critical precursors of light chain amyloid fibrils and amorphous aggregates.* Biochemistry, 2001. **40**(12): p. 3525-3535.
462. Militello, V., V. Vetri, and M. Leone, *Conformational changes involved in thermal aggregation processes of bovine serum albumin.* Biophysical chemistry, 2003. **105**(1): p. 133-141.
463. Vaiana, S., et al., *Irreversible formation of intermediate BSA oligomers requires and induces conformational changes.* Proteins: Structure, Function, and Bioinformatics, 2004. **55**(4): p. 1053-1062.
464. Booth, D.R., et al., *Instability, unfolding and aggregation of human lysozyme variants underlying amyloid fibrillogenesis.* Nature, 1997. **385**(6619): p. 787-793.
465. Marek, P.J., et al., *Ionic strength effects on amyloid formation by amylin are a complicated interplay among Debye screening, ion selectivity, and Hofmeister effects.* Biochemistry, 2012. **51**(43): p. 8478-8490.
466. Pepys, M., et al., *Human serum amyloid P component is an invariant constituent of amyloid deposits and has a uniquely homogeneous glycostructure.* Proceedings of the National Academy of Sciences, 1994. **91**(12): p. 5602-5606.
467. Emsley, J., et al., *Structure of pentameric human serum amyloid P component.* Nature, 1994. **367**(6461): p. 338-345.
468. Santangelo, M., et al., *Back to the oligomeric state: pH-induced dissolution of concanavalin A amyloid-like fibrils into non-native oligomers.* Rsc Advances, 2016. **6**(79): p. 75082-75091.
469. Carrotta, R., et al., *Amyloid fibrils formation of concanavalin A at basic pH.* The Journal of Physical Chemistry B, 2011. **115**(12): p. 2691-2698.
470. Piccirilli, F., et al., *Decoding vibrational states of Concanavalin A amyloid fibrils.* Biophysical chemistry, 2015. **199**: p. 17-24.
471. Vetri, V., et al., *Unlocked concanavalin A forms amyloid-like fibrils from coagulation of long-lived "Crinkled" intermediates.* PloS one, 2013. **8**(7): p. e68912.
472. Asthana, S., et al., *Chaotropes trigger conformational rearrangements differently in Concanavalin A.* Journal of Chemical Sciences, 2017. **129**(8): p. 1267-1276.
473. Bhunia, A., et al., *ZnO nanoparticle-protein interaction: Corona formation with associated unfolding.* Applied Physics Letters, 2013. **103**(14): p. 143701.
474. Karim, Z., R. Adnan, and M.S. Ansari, *Low concentration of silver nanoparticles not only enhances the activity of horseradish peroxidase but alter the structure also.* PloS one, 2012. **7**(7): p. e41422.
475. Peng, X., et al., *Elucidating the influence of gold nanoparticles on the binding of salvianolic acid B and rosmarinic acid to bovine serum albumin.* PloS one, 2015. **10**(4): p. e0118274.
476. Lin, W., et al., *Control of protein orientation on gold nanoparticles.* The Journal of Physical Chemistry C, 2015. **119**(36): p. 21035-21043.
477. Yang, J.A., et al., *Study of wild-type α-synuclein binding and orientation on gold nanoparticles.* Langmuir, 2013. **29**(14): p. 4603-4615.
478. Afrin, S., G. Rabbani, and R.H. Khan, *Spectroscopic and calorimetric studies of interaction of methimazole with human serum albumin.* Journal of Luminescence, 2014. **151**: p. 219-223.
479. Harel, M., et al., *Crystal structure of thioflavin T bound to the peripheral site of Torpedo californica acetylcholinesterase reveals how thioflavin T acts as a sensitive fluorescent reporter of ligand binding to the acylation site.* Journal of the American Chemical Society, 2008. **130**(25): p. 7856-7861.

480. Biancalana, M., et al., *Molecular mechanism of thioflavin-T binding to the surface of β-rich peptide self-assemblies.* Journal of molecular biology, 2009. **385**(4): p. 1052-1063.
481. Wu, C., et al., *Binding modes of thioflavin-T to the single-layer β-sheet of the peptide self-assembly mimics.* Journal of molecular biology, 2009. **394**(4): p. 627-633.
482. Wu, C., et al., *The binding of thioflavin T and its neutral analog BTA-1 to protofibrils of the Alzheimer's disease Aβ 16–22 peptide probed by molecular dynamics simulations.* Journal of molecular biology, 2008. **384**(3): p. 718-729.
483. Kudou, M., K. Shiraki, and M. Takagi, *Characterization of heat-induced aggregates of concanavalin A using fluorescent probes.* Science and Technology of Advanced Materials, 2004. **5**(3): p. 339-341.

Dissemination

Education

- PhD (Life Science), National Institute of Technology (Oct 2013-present)
- GATE (2013)
- M.Sc (Biotechnology), Ravenshaw University (2010-2012)

Experience

- Junior research fellow (April to October 2013), National Institute Science and Educational research (NISER, Department of Energy, Govt of India),
- BCIL research Trainee (November 2012 to April 2013), Abgenex India Private Limited, Bhubaneswar
- M.Sc dissertation (January to June 2012), Department of Zoology, Ravenshaw University, Cuttack
- Summer Research Fellowships, Indian Academy of Sciences (June- July 2011), IICB, Kolkata

Publications (in internationally indexed journals)

- **Asthana, S**., Bhutia, S. K., Sahoo, H., & Jha, S. (2017). Chaotropes trigger conformational rearrangements differently in Concanavalin A. *Journal of Chemical Sciences*, *129*(8), 1267-1276.
- **Asthana, S**., Sahu, M., Nayak, P. S., Mallick, B., & Jha, S. (2018). The smaller heparin fragments bind non-specifically through the IAPP sequence: An *in silico* study. *International journal of biological macromolecules*, *113*, 1092-1104.
- **Asthana, S**., Mallick, B., Alexandrescu, A. T., & Jha, S. (2018). IAPP in type II diabetes: Basic research on structure, molecular interactions, and disease mechanisms suggests potential intervention strategies. *Biochimica et Biophysica Acta (BBA)-Biomembranes*.
- **Asthana, S.,** Hazarika, Z., Nayak, P. S., Roy, J., Jha, A. N., Mallick, B., & Jha, S. (2018). Insulin adsorption onto zinc oxide nanoparticle mediates conformational rearrangement into amyloid-prone structure with enhanced cytotoxic propensity. *Biochimica et Biophysica Acta (BBA)-General Subjects*.
- Nayak, P. S., Arakha, M., Kumar, A., **Asthana, S**., Mallick, B. C., & Jha, S. (2016). An approach towards the continuous production of silver nanoparticles using *Bacillus thuringiensis*. *RSC Advances*, *6*(10), 8232-8242
- Sharma, M., Nayak, P. S., **Asthana, S**., Mahapatra, D., Arakha, M., & Jha, S. (2018). Biofabrication of silver nanoparticles using bacteria from mangrove swamp. *IET Nanobiotechnology*.

Manuscript (submitted/under preparation)

- **Asthana, S**., Kumari S., P.S. Nayak, Mohammed S., Jha S., α-Synuclein interaction with ZnONP ameliorate the protein fibrillation and the particle-mediated cytotoxicity (submitted).

Conferences

- **Asthana S**, Hazaraika Z, Nayak P.S., Roy J, Jha A.N., Mallick B and Jha S, Insulin adsorption onto zinc oxide nanoparticle mediates conformational rearrangement into amyloid-prone structure with enhanced cytotoxic propensity (Meeting of the Indian Biophysical Society, 9-11th March 2018, IISER, Pune)
- **Asthana S**, Sahu M, Nayak P.S., Mallick B and Jha S, Interaction of monomeric IAPP with heparin oligomers: an *in silico* study (Biomolecular Dynamics: Experimental and Theoretical Perspectives, 18-20th December 2017, National Institute of Technology, Rourkela, India)
- **Asthana S**, Nayak P.S., Roy J, Mallick B and Jha S, Effect of zinc oxide on the conformational, amyloidogenic and cytotoxic propensities of insulin (19th IUPAB Congress and 11th EBSA Congress,16th to 20th July 2017, Edinburgh, Scotland, United Kingdom)
- **Asthana S** and Jha S, Conformational propensities of peanut agglutinin in presence of different chaotropes (International symposium on protein folding and dynamics, 8-11th Nov 2016 at National Centre for Biological Sciences, Bengaluru, India)
- **Asthana S** and Jha S, Using ANS as a tool to study structural dynamics in Concanavalin A (International conference on proteomics,7-9th December 2014 at Indian Institute of Technology, Bombay, India)

Personal details

- **Name** Shreyasi Asthana
- **E mail id** shreya.asthana2@gmail.com